UNIVERSITY OF OKLAHOMA

GRADUATE COLLEGE

ELECTRIFICATION AND LIGHTNING IN SIMULATED SUPERCELL AND NON-SUPERCELL THUNDERSTORMS

A Dissertation

SUBMITTED TO THE GRADUATE FACULTY

in partial fulfillment of the requirements for the

degree of

Doctor of Philosophy

By

Edward R. Mansell

Norman, Oklahoma

2000

UMI Number: 9960908

ELECTRIFICATION AND LIGHTNING IN SIMULATED SUPERCELL AND NON-SUPERCELL THUNDERSTORMS

A Dissertation APPROVED FOR THE

DEPARTMENT OF PHYSICS AND ASTRONOMY

BY

ACKNOWLEDGMENTS

First of all, I would like to thank Donald MacGorman for his guidance, extreme patience, depth of knowledge, and lots of green marks on the draft of this dissertation, which vastly improved its quality. This research was made possible through our many discussions and his helpful suggestions.

Thanks also go to Jerry Straka for allowing me to use his superb thunderstorm model, for all the useful feedback, and for the airplane trivia. And a thank you to Conrad Ziegler for being an unofficial committee member, a willing resource, and for helping to guide my research.

Thanks to my committe members Stewart Ryan (thanks for the loan of the cinder blocks, too), Kieran Mullen (great comics on the door), William Beasley, and Mark Morrissey for their time and encouragement.

To the National Severe Storms Laboratory (Norman, OK) for its computing resources, library, copy machines, and printers. And Loretta McKibben, Clinton Bunch, and Kevin "The Wizard" Thomas for keeping Ork alive.

To Grettie, Danette, and Linda in the Physics & Astronomy office.

To the creators of the Vis5D visualization software, which made analysis of the model output a whole lot easier.

To space charge!

Support for this research was provided under National Science Foundation grants ATM 9617318 and ATM 9807179. This work was also supported in part by a grant from the National Oceanic and Atmospheric Administration for high performance computing resources at the Arctic Region Supercomputing Center. The majority of production simulations were carried out on a multiprocessor SGI Origin 2000 at the National Severe Storms Laboratory.

Hey, Dad! It's finally done!

Contents

List of Tables

List of Figures

ABSTRACT

Thunderstorm simulations were performed for a strong, airmass storm and three types of supercell storms, and several different electrification parameterizations were used for each type of storm. The main focus of our analysis was characteristics of the resulting charge distributions and lightning, with two major goals: (1) Examine how sensitive the characteristics are to changes in the parameterizations. (2) Begin analyzing how the characteristics are affected by variations in the kinematic and microphysical structure of storms.

The numerical cloud model used for the simulations is three dimensional and includes detailed bulk microphysics, with separate categories for cloud water, rain, cloud ice (columns, plates, and rimed), snow aggregates, three graupel densities, two size ranges for hail, and frozen drops. Lightning discharges were produced by a stochastic dielectric breakdown model that extends flashes bidirectionally in a step- by-step manner and creates realistic, fractal-like branch structure. The simulations produced a wide variety of lightning types, including horizontally extensive bilevel intracloud flashes, positive and negative cloud-to-ground flashes, and intracloud discharges involving charge layers at the cloud boundary. Simulated flashes sometimes reversed the net charge density locally, and this added complexity to the charge structure of the storm.

Three parameterizations of a noninductive graupel-ice mechanism and various strengths of inductive graupel-droplet charging were tested. For a given storm type, the charge distribution and lightning produced by the different parameterizations had several similarities, but also important differences. For example, choices of average impact angle and separation efficiency that gave greater inductive charging tended to cause earlier development of a lower positive charge region and were more likely to produce enough lower positive charge to cause negative cloud-to-ground lightning.

One important result was that all lightning originated between regions of opposite charge, as has been inferred previously for cloud flashes and negative cloud-to-ground

flashes. However, in many cases, enough charge was in anvils for initiation to occur several tens of kilometers from deep convection, a behavior not yet documented in published observations. Furthermore, positive cloud-to-ground flashes also were initiated between opposite charges in our simulations, a relationship not suggested previously. Positive cloud-to-ground lightning occurred only when the lowest significant charge region near the initiation point was negative.

Chapter 1

Introduction

For millenia, lightning has inspired fear, awe, and fascination. Once people discovered in the eighteenth century that lightning is an electrical phenomenon, they began asking questions about its electrical nature: How do storms become electrified enough to produce lightning? What factors influence lightning characteristics? These remain fundamental questions of thunderstorm research. Answering them has been the ultimate objective of many laboratory experiments, field programs, and numerical modeling simulations. Though there has been considerable progress addressing these questions in recent years, much about lightning and the electrical development of thunderstorms is still not understood.

A particular example of an unresolved mystery is the occurrence of cloud-to-ground (CG) lightning flashes which effectively bring positive charge to ground. For thunderstorms in the United States, the statistics compiled by Orville (1994) indicate that overall more than 90% of ground flashes bring negative charge to ground. In some individual thunderstorms, however, more than 50% of ground flashes bring positive charge to ground. Of particular interest in motivating the current research is the association of dominant positive ground flash activity with severe weather, such as large hail and tornadoes (e.g. MacGorman and Burgess 1994, Stolzenburg 1994, Reap and MacGorman 1989, Carey and Rutledge 1998).

One type of storm that is often associated with severe weather, especially tornadoes, is the *supercell* storm. A supercell storm is characterized by a persistent *mesocyclone*, which is a deep rotation coincident with or in the vicinity of the main updraft. MacGorman and Burgess (1994) presented a number of supercell storm cases in which positive ground flashes were dominant for at least part of the storm's lifetime. An intriguing aspect of many of these storms is a switch in the dominant ground stroke polarity near the time of a tornado. The causes of such polarity switching are unknown, and one goal of our present modeling research is to make progress toward identifying processes that may be involved. As in studies of general storm dynamics, there is an interaction between observations and models: Observations provide data and ideas for the models, which in turn are used to test hypotheses and to develop a framework of concepts to direct new observations and laboratory experiments.

The research to be presented here uses a three-dimensional thunderstorm model that incorporates parameterizations of electrification and lightning to investigate the electrical characteristics of isolated strong thunderstorms. Four different storm environments were chosen for the simulations to provide a spectrum of storm types. One environment produces a strong thunderstorm that is not a supercell, and the other three environments produce various types of supercell storms. These simulations are used to explore the sensitivity of the storm's charge distribution and lightning to (1) different electrification schemes and (2) the different storm environments.

We expect that a successful simulation of thunderstorm electrification will produce charge structures and lightning characteristics within the range of observations. Real thunderstorms can exhibit complex vertical distributions of charge, though the updraft region is sometimes roughly characterized by a tripole structure (main negative charge region with an upper positive charge and additional lower positive charge region) (Stolzenburg et al. 1998a, 1998b). The simulated storms in the present study all have strong updrafts, so cloud flashes are expected to comprise a large percentage (>90%) of the total number of flashes because of increased elevation of the main charge regions

(MacGorman et al. 1989, MacGorman 1993, Carey and Rutledge 1998, MacGorman and Rust 1998).

1.1 Numerical Models in Thunderstorm Electrification Research

Numerically modeling the electrical development of clouds is a natural outgrowth of modeling microphysical development. Three-dimensional models have become the standard for simulation studies of the microphysics and kinematics of storms. However, a search through the reviewed literature reveals only one study of thunderstorm electrification that used a three dimensional model (Ziegler and MacGorman, 1994). Electrification modeling studies have lagged far behind microphysical modeling studies in terms of breadth of application and sensitivity studies.

A primary hindrance to electrification modeling has been the increase in computational resources required to incorporate electrical processes. Ice-phase microphysics with several hydrometeor categories are required to treat noninductive charge separation during particle collisions (chapter 3), a process thought to be important for electrifying storms. (A hydrometeor is any particle composed of water in liquid or solid phase.) The number of types of microphysical interactions increases rapidly as new hydrometeor categories are added. At each grid point where hydrometeors interact, the effects of these interactions must be treated and tracked. Furthermore, charge density becomes yet another property that must be treated and tracked for each hydrometeor category. Last, the effect of lightning must also be represented if simulations are to be continued beyond initial electrification. To do all of this in sufficient detail in three dimensions sometimes strains the capabilities of present supercomputers. For example, a majority of the simulations for this study were performed on a Silicon Graphics Origin2000 computer with multiple 250 MHz R10000 processors. Typical ratios of total CPU-time to model time were as low as 16:1 for the early stage of the smallest storm

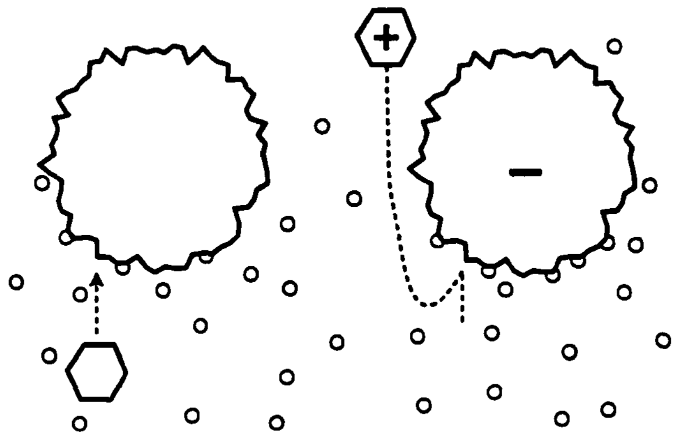

Figure 1.1: Schematic of a noninductive charging interaction. A larger precipitation ice particle (graupel) and smaller ice crystal are shown before and after a rebounding collision that separates charge. The graupel particle is collecting cloud droplets (small circles). The sign of charge gained by the graupel may be either positive or negative, depending on conditions.

(real-time ratio of about 4:1 with 4 processors) and as high as 80:1 for a mature storm in the largest model domain with high lightning flash rates. However, the feasibility of sophisticated large-scale storm electrification simulations is increasing as computers continue to improve in speed and memory size.

Two of the main types of mechanisms for electrification that have been incorporated into thunderstorm models are noninductive and inductive processes. Noninductive processes act independently of external electric fields and pre-existing charge on the particles, and charge is separated by means of surface interactions between particles that collide and rebound (Figure 1.1). Inductive mechanisms, on the other hand, are driven by an external electric field which acts to polarize interacting particles (Figure 1.2). In the model used in this research, collisional charging can occur between graupel or hail particles and small particles (snow aggregates, cloud ice, cloud water droplets). Graupel are precipitation ice particles that began as ice crystals and became heavily rimed. Riming (or rime accretion) is the process of collecting and freezing supercooled water droplets, and is the same process which results in icing of aircraft. More details about the charging processes in the model are described in Chapter 3.

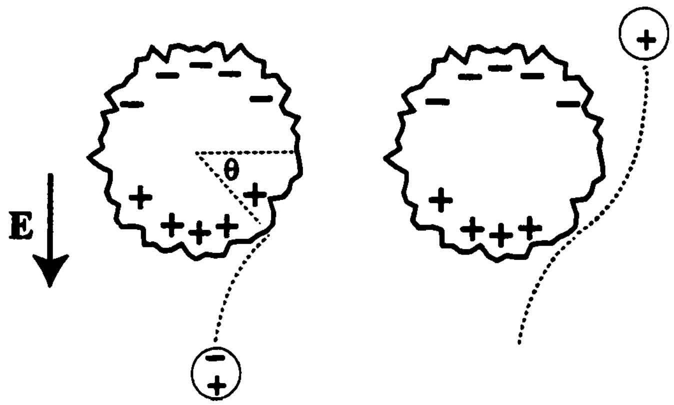

Figure 1.2: Schematic of an inductive charging interaction. A larger precipitation ice particle (graupel) and small cloud droplet are polarized by the external electric field. The sign of charge gained by the graupel depends on the direction of the vertical electric field component.

The rest of this section reviews some previous numerical simulation studies of storm electrification. A number of the studies have used two dimensional axisymmetric or slab-symmetric computational domains. In the former case, charge densities are effectively "rings" of charge around the central axis, and in the latter case, the charge at each point becomes an infinite line charge. The slab-symmetric case thus results in distortion of the electric field toward larger magnitudes. Three-dimensional domains are clearly desirable, not only for electric field calculations, but also for simulating the many asymmetrical characteristics of thunderstorms.

Chiu (1978) developed electrification processes for an axisymmetric model which had only liquid-phase hydrometeors. Electrification was achieved by ion attachment and polarization charging. The model was one of the first to couple particle interactions with electrification in a self-consistent manner. Another axisymmetric model was used by Takahashi (1983,1984). Takahashi's model included ice processes and therefore could incorporate laboratory results for charging due to ice particle collisions (Takahashi, 1978). The model also included ion categories and ion attachment. Takahashi (1984) compared maritime and continental storms by varying the concentrations of cloud condensation nuclei and cloud ice nuclei . He concluded that charging due to ice collisions alone would be sufficient to electrify a storm and produce lightning.

A two dimensional slab-symmetric model was implemented by Helsdon and Farley (1987) to simulate electrification in a Montana thunderstorm. The model included ice-ice charging mechanisms, large and small ions, and ice-rain charging interactions. The simulation produced a charge structure quite similar to the features inferred from observations of the storm by Dye et al. (1986). An intracloud lightning parameterization was described by Helsdon et al. (1992). (Helsdon and Farley, 1987, showed a simulated channel only.) Only one lightning flash was simulated, so the effects of successive flashes over a period of time were not investigated. More details about the lightning parameterization are given in Chapter 4. Helsdon's Storm Electrification Model (SEM) has since been extended to three dimensions (Helsdon et al. 1999), though each lightning flash still consists of a single, unbranched channel.

Ziegler et al. (1991) and Ziegler and MacGorman (1994) employed a three dimensional kinematic model (Ziegler, 1985) to model storm electrification. (A kinematic model ingests observed wind fields and therefore does not integrate the momentum advection equations.) The model included noninductive charging based on Gardiner et al. (1985), inductive charging, and an electrical screening layer parameterization. Ziegler et al. (1991) modeled a small New Mexico thunderstorm and found that the height distribution of charge had a strong sensitivity to the charge reversal temperature. (The reversal temperature is the temperature at which the polarity of charge gained by graupel via the noninductive ice-ice mechanism reverses.) Ziegler and MacGorman (1994) added a simple lightning parameterization to the model, which allowed their simulation of a supercell storm to continue beyond the time of the first flash. In the upper part of the storm, the effect of lightning was mainly to deposit charge on the smallest hydrometeors, thereby acting to mask the charge carried by the larger hydrometeors. The resulting mix of charged particles resulted in new regions of net charge as the large particles fell away from the smaller particles.

Randell et al. (1994) used the two-dimensional SEM (Helsdon and Farley, 1987) for simulations of tropical convection. They used a noninductive ice-ice charging scheme based on the laboratory results of Takahashi (1978) (see Chapter 3). The study did not include lightning, and simulations were terminated if the electric field magnitude approached breakdown values. One of the chief conclusions of the modeling study was the importance of the height distribution of graupel-ice interactions relative to the charge reversal level (CRL). The CRL is a function of temperature and liquid water content and denotes the altitude at which the sign of charge gained by graupel reverses (passes through zero). Graupel colliding with ice particles above the CRL gained negative charge, whereas graupel below the CRL gained positive charge. The efficiency of noninductive charging is high if most of the graupel interactions that transfer charge occur either above or below the CRL. If the CRL lies within the main interaction zone, however, negative charging of graupel above the CRL tends to be offset by positive charging below the CRL. Randell et al. attributed differences in lightning rates in Australian storms to different updraft speeds in regions of riming graupel, because the different updraft speeds affected the location of the CRL relative to the graupel interaction zones. They presented evidence suggesting that this was the reason storms forming in continental air masses are more likely to produce lightning than are storms forming in maritime air masses.

Wojcik (1994) used the two dimensional model of Helsdon and Farley (1987) to study sensitivity to variations in the charge separation parameterization. The storm sounding was the same as in Helsdon and Farley (1987) and Helsdon et al. (1992). Three noninductive parameterizations were used: Helsdon and Farley (HF 1987), Takahashi (1978), and Saunders et al. (1991). Wojcik obtained reasonable results with the HF and Takahashi schemes, but encountered difficulties with the Saunders et al. parameterization: The Saunders et al. equations for noninductive charging at low liquid water content caused the development of strong "anomalous" charge regions which did not at all match the observations. Reducing the charging produced in low liquid water conditions by 80% to

90% effectively removed the anomalous regions. Saunders consented to this strategy because measurements of the magnitude of charging in low liquid water conditions were susceptible to large errors.

Solomon and Baker (1998) combined their one-dimensional lightning parameterization (Solomon and Baker, 1996; described in Chapter 4) with an axisymmetric, kinematic cloud model that ignored horizontal variations in each of two concentric cylindrical regions. The model included various warm and cold cloud microphysical processes. Electrification was achieved by the charging parameterization of Saunders et al. (1991), without any modifications. A screening layer parameterization was also included. The initial charge structure was found to depend on cloud ice concentrations at altitudes in the 0 to $-5°$ C temperature range. The model produced both intracloud flashes and negative cloud-to-ground (CG) flashes. CG flashes did not occur until a positive charge developed below the main negative charge. The lower positive charge was necessary to cause the electric field magnitude just below the main negative charge region to exceed the initiation threshold. The main contributor to lower positive charge was lightning, whose effect may have been exaggerated by the simple geometry of the channel in their model.

1.2 The Supercell Spectrum

A major goal of this research is to investigate electrification and lightning in a variety of supercell storms. Supercell storms have been categorized into three main types: Low Precipitation (LP), Classic (CL), and High Precipitation (HP). Excellent reviews of the characteristics of each type are given by Doswell and Burgess (1993) and Rasmussen and Straka (1998). The nomenclature is somewhat self-explanatory in that precipitation rates are a distinguishing feature, with LP and HP storms at opposite ends of the spectrum and the CL storms in the middle.

A general schematic of a supercell storm is shown in Figure 1.3. As stated above, supercell storms are characterized by a mesocyclone, which is a deep, persistent rotation in the vicinity of the updraft. The mesocyclone typically forms at middle levels and grows upward and downward. When strong tornadoes occur, they generally extend from the mesocyclone. A supercell storm is so-named because it appears to have a single long-lived, quasi-steady updraft cell. This is in contrast to multicell storms, which have multiple, readily distinguishable updraft cells, each of which goes through its own cycle of growth and decay. A supercell storm may last a number of hours and may change from one type to another, usually moving more toward the HP end of the spectrum.

The classic type of supercell storms can produce a variety of severe weather, such as large hail, damaging winds, and major tornadoes. They generally have sufficient precipitation in the updraft to make the mesocyclone observable by radar. The rotation in the mesocylone can move falling precipitation around the updraft region, resulting in a radar "hook echo" at lower levels of the storm. Classic supercell storms may have moderate to heavy rainfall, but are rarely associated with flash flooding.

High precipitation supercell storms are perhaps the most common type of supercell (Moller et al. 1990). They are often surrounded by other clouds and tend not to occur as isolated storms (Rasmussen and Straka, 1998). HP storms can cause flash flooding, hail, and tornadoes. Heavy rain may surround most of the updraft region and mesocyclone and may obscure visual observation of tornadoes. Hook echoes in HP storms generally have greater radar reflectivities than in CL storms.

Low precipitation supercell storms have very little precipitation within the mesocyclone and lack a radar hook echo. (Hook echoes may also be absent from CL and HP storms.) Hail may be produced, but tornadoes are uncommon despite strong rotation. In an LP storm, the mesocyclone may be difficult to detect by radar, because of the lack of precipitation. However, this also gives a clearer view of the cloud in the vicinity of the updraft, and visible cloud features such as striations typically reveal strong rotation in the cloud.

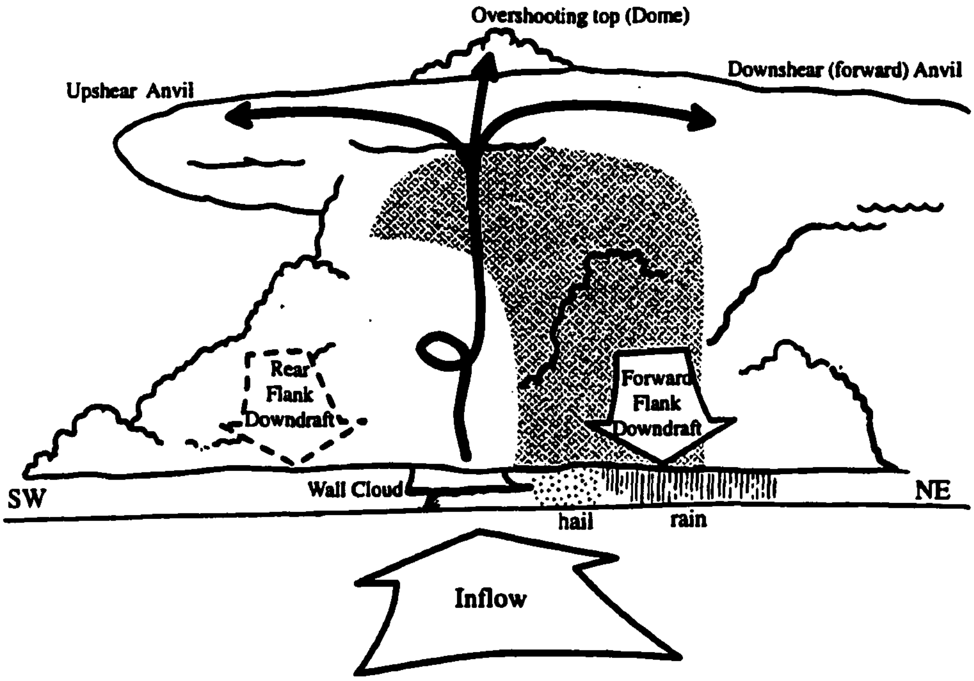

Figure 1.3: Sketch of a supercell thunderstorm. The shaded region indicates higher reflectivity and shows a weak echo region beneath the overhanging reflectivity region. A persistest, rotating wall cloud is a visual manifestation of rotation (mesocyclone) in the storm. (Adapted from MacGorman and Rust, 1998).

Note that these different types of supercell storms are discrete categorizations of a continuously varying spectrum of supercell characteristics. Most supercell storms lie somewhere between the main types, and classification of any particular supercell as a particular type involves subjective judgments. Nevertheless, the three types are useful for identifying the general part of the spectrum in which a storm lies.

1.3 Goals of this study

As stated previously, the general goal of the present research is to investigate electrification in strong storms, particularly supercell storms, through the use of a numerical thunderstorm simulation model. To do this, however, it is also necessary to consider the effects of common variations in the electrical parameterizations. For example, most investigators have used a constant electric field threshold to initiate lightning, instead of a height-varying threshold (see Chapter 4). Though most of our simulations used a height-varying threshold because it is more realistic, one simulation used a constant lightning initiation threshold, to allow an evaluation of the effect of these two assumptions. Similarly, the model has a choice of electrification schemes, each based on a different set of laboratory results. One aspect of the study is concerned with the differences in charge structure and lightning resulting from these various schemes.

Another interest is the significance of inductive (or polarization) charging in rebounding graupel-droplet collisions. Ziegler et al. (1991) found that such inductive charging had little effect, but that study used parameter values that resulted in inductive charging rates at the lower end of the observed range for this mechanism. Helsdon and Farley (1987) used parameter values that gave inductive charging rates more than an order of magnitude larger than that of Ziegler et al. (1991), though still within the observed range. However, Helsdon and Farley allowed inductive charging for collisions between almost all hydrometeor categories except rebounding collisions of cloud droplets with graupel/hail, which is the one interaction most investigators (e.g. Brooks and Saunders,

1994) have found can cause appreciable inductive charge transfer. Thus, in the present study we investigate the effect of a stronger inductive charging mechanism for graupel-droplet interactions.

The main meteorological focus of this study is to investigate the production of charge and lightning in supercell storms, with particular interest in production of positive cloud-to-ground lightning. Three environments were chosen to produce supercell storms that more or less represented the three categories of supercell storms. A fourth environment had low wind shear and produced a strong non-supercell storm. Each simulation continued for at least 105 minutes and produced over 75 minutes of lightning activity. Unfortunately, 105 minutes was not long enough to reach the final decay stage of any of the storms. The four storm environments used in this study provided a basis for comparing simulated electrification and lightning characteristics across a broad spectrum of strong storms. Because one of the key differences in the four environments was the magnitude of wind shear, these simulations also allowed an examination of effects on electrification and lightning caused by increasing wind shear.

Chapter 2

The Thunderstorm Simulation Model

The numerical thunderstorm model employed in this research is three-dimensional, fully compressible, and non-hydrostatic (Straka and Anderson, 1993). The model has a modular structure which allows for relatively easy substitution of subroutines for advection, diffusion, microphysics, etc. Vertical and horizontal gridstretching and topography are supported, though not used in the present study.

2.1 Dynamics

The model integrates prognostic equations for momentum (three components), potential temperature, pressure, turbulent kinetic energy (TKE), and microphysical and charge variables. Scalar variables (potential temperature, TKE, and microphysical and charge variables) are advected with a forward-in-time sixth-order Crowley scheme (constant grid flux form, Trembeck et al. 1987) with a monotonic limiter (Leonard, 1991). Ordering of x and y time-split passes is switched after each timestep (i.e. x-y-z, y-x-z). A time-centered (leapfrog) quadratic-conserving second-order scheme is used for momentum advection. Spatial filtering (sixth order) is applied to the velocity components and scalar variables to remove spurious short wavelengths produced by advection. A time (Asselin) filter is also applied to the momentum components and pressure variable to prevent the separation of the solutions that can result from the leapfrog finite difference formulation.

The diffusion parameterization is based on K-theory, with the mixing coefficient derived from the variable turbulent kinetic energy. Weak Rayleigh damping is applied to the scalar variables and momentum components at the top of the domain. Coriolis forces and radiation physics are disabled for the storm simulations, because their effects are not appreciable for short (< 2 hour) time-scales.

2.2 Microphysics

The model employs a novel microphysics package also developed by Straka (not yet published). The number of water substance categories (hydrometer types and vapor) and the detailed treatments of interactions between the categories make this microphysics package one of the most versatile. It is designed to be used for a broad range of convective situations with a minimum of fine tuning of parameters (Straka et al., 1998). Because electrification mechanisms are sensitive to several of the microphysical properties that are treated in greater detail by this package, there is reason to hope that the electrification produced by this model will be more realistic.

The version of the microphysics package used in this research has twelve hydrometeor categories: cloud droplets, rain, two ice crystal habits (column and plate), rimed cloud ice, snow aggregates, three graupel densities, frozen drops, small hail (5–20 mm), and large hail (>20 mm). Hydrometeor categories are represented by gamma distributions:

$$c_x(D) = c_{ox} D^{\alpha_x} \exp\left(-\frac{D}{\mathcal{D}_x}\right) \tag{2.1}$$

where c_x is the number concentration, D is diameter, α_x is the shape parameter, and $\mathcal{D}_x$ is the characteristic diameter (the inverse of the usual slope parameter, λ_x). The intercepts c_{ox} are constant. In this study, all categories have $\alpha_x = 0$ (i.e., they have typical Marshall-Palmer exponential distributions). Table 2.1 lists the number concentration intercepts and the density of water assumed for each hydrometeor category. Rimed cloud ice has a variable density. More recent versions of the microphysics scheme have an expanded number of ice crystal habits (e.g. sectors, dendrites, bullets), prognostic

Category	Intercept, c_{ox} (m^{-4})	Density ($kg\,m^{-3}$)
cloud droplets	1.0×10^8	1000
column ice	1.0×10^8	300–900
plate ice	1.0×10^8	900
rimed ice	1.0×10^8	300
rain	8.0×10^6	1000
snow agg.	8.0×10^6	100
graupel (low)	4.0×10^5	300
graupel (medium)	4.0×10^5	500
graupel (high)	4.0×10^5	700
frozen drops	4.0×10^5	800
small hail	4.0×10^4	800
large hail	1.0×10^3	900

Table 2.1: Intercept and density values for hydrometeor categories.

equations for number concentration, inclusion of categories for aerosols and chemical species, and other improvements.

One of the unique features of the Straka microphysics scheme is that conversions of ice hydrometeor categories due to riming (collecting and freezing cloud droplets) are based on the riming histories of the particles. The model tracks the length of time τ that a hydrometeor category has been riming. The riming histories are used in calculations of multicomponent conversions between ice categories. The continuity equation (in flux form) for riming time τ of the n^{th} hydrometeor category is

$$\frac{\partial \tau_n}{\partial t} = -\frac{1}{\rho_o}[\nabla \cdot (\rho_o \tau_n \mathbf{U}) - \tau_n \nabla \cdot (\rho_o \mathbf{U})] + \frac{1}{\rho_o}\frac{\partial (V_{t,n}\rho_o \tau_n)}{\partial z} + S_{\tau,n} \tag{2.2}$$

where ρ_o is the base-state air density, $\mathbf{U}$ is the wind vector, and $V_{t,n}$ is the mass-weighted mean terminal speed of hydrometeor category n. The source/sink term S_τ is equal to unity for riming rates above a minimum threshold and represents exponential decay (i.e. is negative and proportional to τ) for riming rates below the threshold. Lookup tables are used to determine conversion rates between ice categories. A similar method is used to determine the average age of cloud droplets in a parcel, which allows setting a minimum existence time for the droplets before autoconversion to rain is allowed.

Many other microphysical processes are treated in similar means as in previous bulk parameterizations (e.g. Lin et al. 1983, Ferrier 1994), with the added complication of extra ice categories. These processes include cloud droplet and cloud ice collection by precipitation particles, primary ice nucleation, homogeneous freezing of droplets, stochastic freezing of raindrops, ice multiplication (Hallett-Mossop process), rain autoconversion, cloud ice aggregation, melting of ice particles, vapor deposition, sublimation, and evaporation. Collection of liquid water particles by ice particles results in multicomponent transforms, which use lookup tables to determine the conversions to the various ice categories.

2.3 Electrification

Each hydrometeor species has an associated charge density ρ_n. Prognostic equations are integrated for all charge densities. The electrification processes are described in Chapter 3. Charge may also be transferred from one category to another as mass is transferred. For example, when a fraction of graupel mass melts to rain, the same fraction of the graupel charge is transferred to the rain category. Although charge continuity is imposed, charge is not conserved when charged particles completely evaporate within a given grid volume, or when charged precipitation reaches the ground. Also, the screening layer parameterization (Section 3.4) introduces charge into the domain be means of assumed ion currents. (The model does not have free ion categories for charge.) The rates at which charge enters or exits the model domain by these processes is not yet tracked. Charge may also enter the domain via cloud-to-ground lightning (Chapter 4).

The charge continuity equation resembles a typical conservation equation (advective form):

$$\frac{\partial \rho_n}{\partial t} = -\mathbf{U} \cdot \nabla \rho_n + \nabla \cdot \left(\frac{K_h}{\rho_o} \nabla (\rho_o \rho_n) \right) + \frac{1}{\rho_o} \frac{\partial (V_{t,n} \rho_o \rho_n)}{\partial z} + S_n \tag{2.3}$$

where K_h is the sub-grid eddy mixing coefficient ($m^2\ s^{-1}$). On the right-hand side, the first term represents advection, the second term is for diffusion, the third term accounts for falling particle motion relative to the air motion (i.e. forces of weight and air resistance), and S_n is the sum of source and sink terms. Noticeably absent is a term for electrical forces, which have not yet been incorporated into the dynamics of the model. Even if the electric force on a particle is a relatively small fraction of the net force, over time it could noticeably affect the trajectory of an individual particle (e.g. Masuelli et al. 1998), but in a bulk scheme the overall effect on a group of particles is expected to be smaller.

The actual equation that is integrated by the model is the flux form, which is mathematically equivalent to the advective form (Equation 2.3):

$$\frac{\partial \rho_n}{\partial t} = -\frac{1}{\rho_o}[\nabla \cdot (\rho_o \rho_n \mathbf{U}) - \rho_n \nabla \cdot (\rho_o \mathbf{U})] + \nabla \cdot \left(\frac{K_h}{\rho_o} \nabla (\rho_o \rho_n) \right) + \frac{1}{\rho_o} \frac{\partial (V_{t,n} \rho_o \rho_n)}{\partial z} + S_n \tag{2.4}$$

For completeness, Equation 2.4 is given in component form:

$$\frac{\partial \rho_n}{\partial t} = -\frac{1}{\rho_o} \frac{\partial (u_i \rho_o \rho_n)}{\partial x_i} + \frac{\rho_n}{\rho_o} \frac{\partial (u_i \rho_o)}{\partial x_i} + \frac{\partial}{\partial x_i} \left(\frac{K_h}{\rho_o} \frac{\partial (\rho_o \rho_n)}{\partial x_i} \right) + \frac{1}{\rho_o} \frac{\partial (V_{t,n} \rho_o \rho_n)}{\partial z} + S_n \tag{2.5}$$

The net charge density ρ_t at a gridpoint is simply the sum of all the individual charge categories,

$$\rho_t = \sum_n \rho_n \tag{2.6}$$

The net charge is then the source term for the Poisson equation,

$$\nabla^2 \phi = -\rho_t / \epsilon, \tag{2.7}$$

where ϕ is the electric potential, and ϵ is the electrical permittivity of air. The presence of hydrometeors in a particular grid volume involves such a small fraction of the air volume that the maximum increase in permittivity is estimated to be less than 1% and is therefore ignored. The Poisson equation is solved using an algorithm which employs Fourier transforms (see section 4.3.1 for details). The electric field is then found as the negative gradient of the potential:

$$\mathbf{E} = -\nabla \phi \tag{2.8}$$

Chapter 3

Electrification Parameterizations

A fundamental requirement for using numerical cloud models is to include parameterizations of mechanisms by which hydrometeors become charged. These mechanisms are the subject of ongoing laboratory experiments (e.g Takahashi 1978, Jayaratne et al. 1983, Saunders et al. 1991, Saunders et al. 1999b). A hydrometeor can acquire a net charge from rebounding collisions with other particles or by capturing charged particles (ions or smaller hydrometeors). An example of the importance of ion capture is the formation of a charge layer at a cloud boundary. Because hydrometeors capture ions, they create a discontinuity in conductivity at cloud boundaries. The resulting divergence of ohmic current at the boundry causes a charge layer to form to enhance the current inside the cloud and to diminish it in clear air until the current is continous across the boundary.

The two main classes of collisional charging mechanisms are inductive and noninductive. Inductive or polarization charging requires a pre-existing electric field to induce charge on the surfaces of the colliding particles. Noninductive mechanisms operate without regard to an external electric field. A number of different microphysical mechanisms have been proposed for noninductive charge transfer, such as thermoelectric effects, rime branch break-off, contact potential between different ice surfaces, and surface layer interactions.

Various hypotheses for noninductive charging mechanisms have been based on contact potential, the thermoelectric effect, surface fragmentation, fragment ejection, graupel growth regime, and graupel surface conditions. A summary of charging hypotheses can be found in MacGorman and Rust (1998). The presentation in the rest of this chapter will focus on the laboratory results and their application to thunderstorm modeling studies. Modeling and laboratory results have suggested that collisions between ice particles in the presence of liquid water droplets can result in noninductive transfers of enough net charge to produce lightning. Ice-ice collisions in the absense of liquid water separate much less or no charge at all. Ice-droplet collisions produce appreciable separation only if there is a pre-existing electric field. There is mounting evidence and general agreement that ice hydrometeors are necessary for strong electrification to occur in most, if not all, circumstances. There are very few observations of lightning activity in warm clouds, and those observations are not without controversy.

3.1 Noninductive Charging in the Laboratory

Laboratory studies of noninductive charging have focused on graupel undergoing riming growth and collisions with ice crystals. Riming, the collection and rapid freezing of supercooled liquid droplets, appears to condition the graupel surface so that more charge is exchanged during collisions with ice crystals. The sign of charge acquired by the rimer appears to be dependent on temperature and liquid water content (or more specifically the rime accretion rate), as well as on other factors such as water droplet contaminants. A *reversal temperature* is the temperature at which charge separation approaches zero and the charge gained by graupel changes sign, all other factors being held constant. The laboratory studies agree that the reversal temperature is dependent on cloud water content or rime accretion rate. However, the results of different studies are in conflict over the details of the charging dependence on temperature and cloud water content.

Takahashi (1978) studied collisional charging with a chamber containing ice crystals and supercooled droplets. Rotating rods inside the chamber acted like graupel

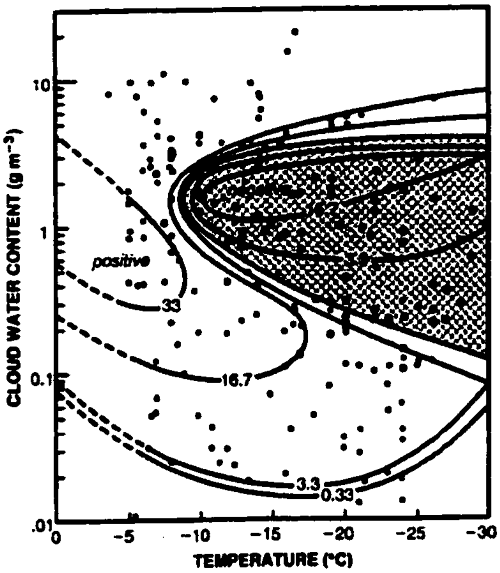

Figure 3.1: Takahashi charging diagram (from Takahashi (1978), and adapted by MacGorman and Rust (1998) to show charge separation in units of fC).

particles by collecting droplets (i.e. riming) and colliding with crystals. He found that the rimed rods gained positive charge from collisions with ice crystals at temperatures above $-10°C$ regardless of liquid water content (Fig. 3.1). At temperatures below $-10°C$, the rime gained positive charge at high and low liquid water contents, but acquired negative charge at intermediate liquid water contents. At a liquid water content of 1 $g\,m^{-3}$, the reversal in the polarity of acquired charge occurred at about $-10°C$. The reversal temperature tended to be lower for other liquid water contents.

Jayaratne, et al. (1983) also studied noninductive charging of a rotating riming rod, but speeds were limited to 4 m/s (Takahashi used 9 m/s). In a variation of the experiment, cloudy air was drawn past a stationary (nonrotating) target at speeds up to 20 m/s for qualitative comparison with the rotating rod results. They tested the effects of various air and water contaminants and found that both could significantly affect the sign of charge gained by the rimer. The air contaminants all affected the droplet size distribution, and the effects on charging ranged from no change to exclusively negative charging of the target. Droplet contaminants could cause either positive or negative charging of the target.

Even when using pure water, as Takahashi (1978) did, Jayaratne et al. (1983)

obtained some results that differed from Takahashi's. Jayaratne et al. saw no positive charging of the rimer at low liquid water content and low temperature. Charging of the rimer at temperatures higher than $-10°C$ was negative for sufficiently low liquid water content. Furthermore, the reversal temperature at a liquid water content of 1.0 g m^{-3} was $-20°C$, or 10°C lower than found by Takahashi (1978).

Three possibilities were suggested by Jayaratne et al. (1983) to explain differences from Takahashi's (1978) results. 1) Takahashi may have overestimated the values of liquid content. 2) The higher rotational forces in Takahashi's experiment may have caused break-up of rime surfaces, resulting in loss of negative charge which could mask the negative charging from crystal impacts. 3) Takahashi allowed outside air into the chamber, and this could have introduced unknown contaminants. Brooks and Saunders (1995) found that higher rotational forces had no effect on charging polarity, but did conclude that Takahashi's liquid water content values were overestimated by up to a factor of six.

The laboratory results of Saunders et al. (1991) (same laboratory as used by Jayaratne et al. 1983) were also at variance with Takahashi (1978), though they reported positive charging at low temperature and liquid water content. Saunders et al. created a parameterization of their results for use in numerical model studies. The charging scheme determined the sign of charging based on the temperature and the effective liquid water content (EW), which is the liquid water content multiplied by the collection efficiency of the riming particle. The magnitude of charging also depended on EW and temperature and had a power-law dependence on both ice-crystal diameter and fall speed difference. Brooks et al. (1997) modified this charging parameterization to use the rime accretion rate, $RAR = EW \times V$ (where V is the graupel fall speed relative to the wind). They omitted the positive charging region at low temperature and low EW for two reasons: 1) They found their simple numerical cloud model was insensitive to that charging regime. 2) They noted that charging tests at very low values of EW were very difficult to perform reliably. Further exploration of the charging dependence on RAR was reported by

Saunders and Peck (1998). The research presented here includes a charge separation parameterization based on Brooks et al. (1997), Saunders and Peck (1998), and Saunders et al. (1999a) and is described in the next section.

Williams et al. (1991) attempted to relate charging to the graupel growth state (e.g. wet or dry growth). They found that the growth state regimes tended to match up with the different charging regimes found by Takahashi, which included charging during wet growth. The equations they used to calculate the growth regimes were appropriate for the higher density rime they expected in the Takahashi (1978) experiment. They suggested that the Jayaratne et al. (1983) results were different because of the lower density rime expected from the lower riming rod speeds. However, Brooks and Saunders (1995) found that the continuous nucleation technique used by Takahashi contributed to a considerable overestimate of the liquid water content and thus wet growth was likely never achieved. Jayaratne (1993) noted that the equations for growth state used by Williams et al. (1991) would not be applicable to the laboratory-grown rime structures which are quite different in shape from natural graupel. When using appropriately modified equations, the hypothesis that the sign of charging depends on the growth state of the graupel appears not to be supported. Williams and Zhang (1996) looked more closely at the expected rime density in the Takahashi (1978) and Saunders et al. (1991) experiments and again suggested that the differences in rime density might preclude direct comparison of the charging results. However, Jayaratne (1998) found that charging was not controlled by rime density.

Baker et al. (1987) suggested that the sign of charging was controlled by which particle was growing faster by vapor diffusion. The particle with faster growth would gain positive charge. Baker and Dash (1994) put forth an explanation in terms of quasi-liquid layers (QLL) at the ice surfaces. The particle growing faster by diffusion would have a thicker QLL and would tend to lose mass during collisions. The mass transfer would then carry off negative ions from the QLL, leaving the particle with net positive charge.

A problem with the QLL theory is that it predicts a thicker liquid-like layer as the temperature is increased. According to QLL theory, heating the target should thicken its surface layer and promote positive charging. However, Saunders et al. (1999b) found that when a riming target was charging positively, applying heat to the target could reverse the charging to negative.

Saunders et al. (1999b) proposed that their results were consistent with the existence of a transition liquid layer (TLL) (Fukuta and Lu, 1994 and 1995). Fukuta and Lu (1995) asserted that a QLL exists only under equilibrium conditions (i.e. that the QLL theory is only valid for equilibrium conditions), and that a surface growing by vapor diffusion at ice supersaturation is properly described by a TLL. The TLL becomes thicker for higher vapor pressure, so that the faster an ice particle is growing by vapor diffusion, the thicker its TLL will be. The TLL theory is thus consistent with the hypothesis that the faster-growing particle will become positively charged in collisions by a net loss of negative ions. Heating an ice particle should cause a thinner TLL because vapor growth is reduced, leading to negative charging, consistent with the Saunders et al. (1999b) results.

Droplets freezing on the graupel surface affect the TLL, because they supply both vapor and latent heat release. Saunders et al. (1999b) hypothesized that at low rime accretion rates the heating effect dominates, causing a thinner TLL than in the crystals and resulting in negative charging. At high rime accretion rates, however, the droplets freeze more slowly and increase the vapor supply, which overcomes the heating effect and causes a thicker TLL and positive charging. The explanation of charging results based on TLL theory assumes that the TLL contains an excess of negative ions, so that the particle with the thicker TLL experiences a net loss of mass and negative ions due to collisions.

3.2 Noninductive charging parameterizations

Three different noninductive charging parameterizations were tested in this research. The first is based on a parameterization by Gardiner et al. (1985) from the laboratory results of

Jayaratne et al. (1983). The second uses results from Takahashi (1978). The third is based on Saunders et al. (1991) as modified by Brooks et al. (1997), Saunders and Peck (1998) and Saunders et al. (1999a). The cloud model has three categories for cloud ice (columns, plates, and rimed ice), one for snow aggregates, three for graupel (low, medium, and high density), and two for hail (small and large). The graupel and hail categories will be referred to collectively as graupel. Charge separation rates are calculated for collisions of graupel and hail with cloud ice and snow aggregates. Interactions between the graupel/hail categories are not yet considered because of the lack of laboratory studies on graupel-graupel collisional charging. Laboratory results to date are directly applicable only to collisions between riming precipitation ice particles and vapor-grown ice crystals. Although small rimed ice crystals are included in the charging equations in the model, it is assumed that the rime accretion rates of the cloud ice are much less than the graupel rime accretion rates and that the laboratory results are still valid. Also, the microphysics package used in this research does not treat graupel-graupel interactions. We expect that lower collision rates and smaller relative fall speeds between the different graupel categories might limit the charge separation.

The general formulation for noninductive charge separation is as follows. The noninductive charge separation rate $\frac{\partial \rho_{xy}}{\partial t}$ between ice hydrometeor clases x and y is

$$\frac{\partial \rho_{xy}}{\partial t} = \frac{\beta}{\rho_0} \int_0^\infty \int_0^\infty \frac{\pi}{4} \delta q'_{xy} (1 - E_{xy})(D_x + D_y)^2 |V_y - V_x| c_x c_y dD_x dD_y \qquad (3.1)$$

where D_x and D_y are the diameters of the colliding particles, E is collection efficiency, $|V_y - V_x|$ is the relative fall speed, c is number concentration, and $\delta q'_{xy}$ charge separated per rebounding collision. In general, $\delta q'_{xy}$ may be a function of ice-crystal diameter, impact speed, liquid water content, and temperature. None of the laboratory studies have given quantitative results on charge separation at temperatures below $-30°$. Therefore we arbitrarily limit charging at low temperature by an arbitrary factor β, where

$$\beta = \begin{cases} 1 & \text{for } T > -30°\text{C} \\ 1 - [(T+30)/13]^2 & \text{for } -43 < T < -30° \\ 0 & \text{for } T < -43°\text{C} \end{cases} \qquad (3.2)$$

As it stands, Equation 3.1 is not a tractable integrand. The equation can be simplified by assuming a form for $\delta q'_{xy}$ that can be pulled out of the integral. Also, the fall speed difference is replaced by the difference of mass-weighted mean fall speeds. The collection efficiency is assumed to be constant. Multiplying and dividing by E_{xy} then isolates the number concentration collection rate integral:

$$\begin{aligned}\frac{\partial \rho_{yx}}{\partial t} &= \beta\, \delta q_{xy}(1 - E_{xy})E_{xy}^{-1} \times \\ &\qquad \frac{1}{\rho_0}|\bar{V}_y - \bar{V}_x| \int_0^\infty \int_0^\infty \frac{\pi}{4} E_{xy}(D_x + D_y)^2 c_x c_y dD_x dD_y \qquad (3.3)\\ &= \beta\, \delta q_{xy}(1 - E_{xy})E_{xy}^{-1} c_{yacx} \qquad (3.4)\end{aligned}$$

where δq_{xy} is now a representative (weighted average) separated charge per collision. The number concentration collection rate c_{yacx} is calculated analytically. (A more complex treatment of the charging equation may be found in Ziegler et al., 1986, and Ziegler et al., 1991.) Each of the noninductive charging schemes uses a representative diameter for cloud ice or snow. Unless otherwise specified, the characteristic diameter $\mathcal{D}_x$ is used. The characteristic diameter comes from the exponential number concentration distribution

$$c(D) = c_0 \exp(-D/\mathcal{D}_x) \qquad (3.5)$$

The maximum magnitude of δq is limited to 200 fC for graupel-snow collisions and 2 fC for graupel-cloud ice interactions.

3.2.1 "Gardiner" Noninductive Charging Parameterization

Gardiner et al. (1985) extrapolated the laboratory results of Jayaratne et al. (1983) to obtain a charge separation equation (in Coulombs) for atmospheric conditions:

$$\delta q' = 7.3 D_\iota^4 \Delta V^3 \,\delta L\, f(\tau) \qquad (3.6)$$

where D_ι is the ice crystal or snow particle diameter in meters and ΔV is the crystal impact speed in m/s. In the model, this equation takes the form of

$$\delta q = \begin{cases} 7.3\mathcal{D}_\iota^4(\bar{V}_g - \bar{V}_\iota)^3\,\delta L\, f(\tau) & \text{for pristine cloud ice crystals} \\ 7.3\frac{\Gamma(8)}{\Gamma(4)}\mathcal{D}_\iota^4(\bar{V}_g - \bar{V}_\iota)^3\,\delta L\, f(\tau) & \text{for snow and rimed cloud ice}\end{cases} \qquad (3.7)$$

where $\bar{V}_g$ and $\bar{V}_\mathrm{I}$ are the mass-weighted mean terminal speeds for graupel/hail and cloud ice/snow, respectively, and $\mathcal{D}_\mathrm{I}$ is the characteristic diameter for the particular cloud ice or snow category being considered. The difference between the two expressions is a constant integration factor (J. Straka, private communication). The dependence on liquid water content (LWC, in $\mathrm{g\,m^{-3}}$) is given by δL as follows:

$$\delta L = \begin{cases} LWC - LWC_\mathrm{crit} & \text{for } T > T_r \\ LWC & \text{for } T < T_r \text{ and } q_c \geq 10^{-6} \text{ kg/kg} \\ 0 & \text{for } q_c < 10^{-6} \text{ kg/kg} \end{cases} \tag{3.8}$$

where $LWC_\mathrm{crit} = 0.1\,\mathrm{g\,m^{-3}}$, q_c is the cloud water mixing ratio (the ratio of the water substance mass to the mass of air in a parcel), and T_r is the reversal temperature. The function $f(\tau)$ was adapted from Gardiner et al. (1985) by Ziegler et al. 1991:

$$f(\tau) = -1.7 \times 10^{-5}\tau^3 - 0.003\tau^2 - 0.05\tau + 0.13 \tag{3.9}$$

where $\tau = (-21/T_r)(T - 273.16)$ is the scaled temperature used by Ziegler et al. (1991) to allow the reversal temperature T_r to be varied. In their modeling study of a small New Mexico thunderstorm, Ziegler et al. (1991) found that using $T_r = -21°\mathrm{C}$ resulted in a charge distribution having negative above positive charge (a so-called "negative dipole"). Measurements in the storm, however, indicated positive charge over negative (a "positive dipole") which is what is typicallly observed in many storms. A change to $T_r = -10°\mathrm{C}$ resulted in positive charge above negative in the simulated charge structure, indicating that the main charging zone was in the -10 to $-20°\mathrm{C}$ layer. The supercell storm study of Ziegler and MacGorman (1994) used the same numerical model as Ziegler et al. and obtained reasonable results with $T_r = -15°\mathrm{C}$, which is the value adopted for the present study.

3.2.2 "Takahashi" Noninductive Charging Parameterization

The Takahashi charging parameterization uses the laboratory data directly from Takahashi (1978). The charge per collision $\delta q'$ is interpolated from a lookup table of Takahashi's data (Wojcik, 1994; reproduced in Appendix C). The table covers a temperature range of 0°C to −30°C and liquid water content from 0.01 to 30 g m^{-3}. For temperatures lower than −30°, the charge separation values at −30° were used. Charging dependence on crystal size and fallspeed are parameterized by multiplying the value obtained from the table by a factor α, as in Takahashi (1984):

$$\alpha = 5.0(\mathcal{D}/D_0)^2\bar{V}_g/V_0 \tag{3.10}$$

where $\mathcal{D}$ is the crystal size (characteristic diameter), $D_0 = 100\,\mu\text{m}$, $\bar{V}_g$ is the terminal fall speed of graupel, and $V_0 = 8\,\text{m/s}$. The value of α is constrained to be no greater than 10.0 (i.e. $\alpha \leq 10.0$). Thus, for the Takahashi scheme we have

$$\delta q = \alpha\delta q' \tag{3.11}$$

where $\delta q'$ is the value from the lookup table.

3.2.3 "Riming Rate" Noninductive Charging Parameterization

The noninductive charging parameterization developed by Saunders et al. (1991) determined the sign of graupel charging from the temperature and the effective liquid water content (*EW*). *EW* is the liquid water content multiplied by the droplet collection efficiency of the graupel. Brooks et al. (1997) reported laboratory results showing that the rime accretion rate (RAR) was better than *EW* as an indicator of charging polarity. Another advantage of using RAR is that experiments at different speeds can be compared more meaningfully. Brooks et al. adapted the Saunders et al. scheme to use RAR instead of EW by the conversion $RAR = EW \times V$. The critical rime accretion rate (RAR_{crit}) is then the riming rate at which the charging of graupel changes sign for a particular temperature. Saunders and Peck (1998) expanded studies of the dependence of charging sign on RAR to a greater temperature range than previously examined. Saunders et al. (1999a) found that a spectrum of smaller droplets allowed negative charging at higher RAR.

Charge sign	Crystal size (μm)	B	a	b
+	< 155	4.9×10^{13}	3.76	2.5
+	155–452	4×10^{6}	1.9	2.5
+	> 452	52.8	0.44	2.5
–	< 253	5.24×10^{8}	2.54	2.8
–	> 253	24	0.5	2.8

Table 3.1: Values of constants for riming rate charging scheme (from Brooks et al. 1997).

The riming rate charging scheme employed in the present study is a hybrid of the results cited above. The mean separated charge per collision is given by

$$\delta q = B\mathcal{D}_{\mathrm{I}}^{a}(\bar{V}_g - \bar{V}_{\mathrm{I}})^b q_{\pm}(RAR) \tag{3.12}$$

where $\mathcal{D}_{\mathrm{I}}$ is the characteristic diameter of the ice or snow crystal , $\bar{V}_g$ and $\bar{V}_{\mathrm{I}}$ are the mass-weighted mean terminal speeds for graupel/hail and cloud ice/snow, respectively, and B, a, and b are constants that depend on crystal size as shown in Table 3.1. The charge separation equations, $q(RAR, T)$ from Brooks et al. (1997) have been altered for the present study so that they smoothly approach zero at $RAR = RAR_{\mathrm{crit}}$:

For positive charging of graupel ($RAR > RAR_{\mathrm{crit}}$),

$$q_{+}(RAR) = 6.74(RAR - RAR_{\mathrm{crit}}) \tag{3.13}$$

For negative charging ($0.1\,\mathrm{g\,m^{-2}s^{-1}} < RAR < RAR_{\mathrm{crit}}$),

$$q_{-}(RAR) = 3.9(RAR_{\mathrm{crit}} - 0.1)\left(-1.0 + 4.0\left[\frac{RAR - (RAR_{\mathrm{crit}} + 0.1)/2.0}{(RAR_{\mathrm{crit}} - 0.1)}\right]^2\right) \tag{3.14}$$

Note that there is an implicit temperature dependence since RAR_{crit} varies with temperature. The negative charging equation q_{-} shifts the parabolic function given in Brooks et al. (1997) to fit between the limits of $0.1\,\mathrm{g\,m^{-2}s^{-1}}$ and RAR_{crit}. Charging is set to zero for $RAR < 0.1\,\mathrm{g\,m^{-2}s^{-1}}$.

The critical RAR curve is shown in Figure 3.2 and given by

$$RAR_{\mathrm{crit}}(T) = \begin{cases} s(T) & \text{for } T > -7.0°\mathrm{C} \\ g(T) & \text{for } -7.0 > T > -16.0°\mathrm{C} \\ h(T) & \text{for } -16.0 > T > -21.7°\mathrm{C} \\ h(-21.7) & \text{for } T < -21.7°\mathrm{C} \end{cases} \tag{3.15}$$

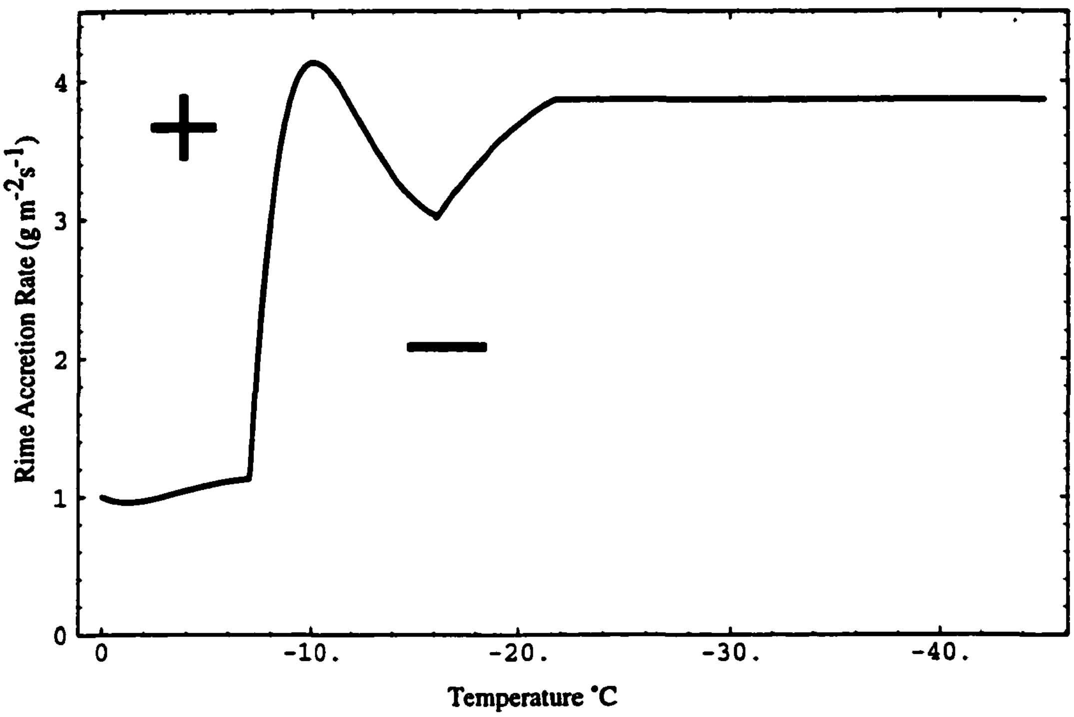

Figure 3.2: Plot of the critical rime accretion rate used in the riming rate noninductive ice-ice parameterization. Graupel charges positively at rime accretion rates above the curve and negatively below.

where $s(T)$ is the sixth-order polynomial functional fit given by Saunders and Peck (1998),

$$\begin{aligned} s(T) &= 1.0 + 7.9262 \times 10^{-2}T + 4.4847 \times 10^{-2}T^2 + 7.4754 \times 10^{-3}T^3 + \\ &\quad 5.4686 \times 10^{-4}T^4 + 1.6737 \times 10^{-5}T^5 + 1.7613 \times 10^{-7}T^6 \end{aligned} \tag{3.16}$$

and

$$g(T) = s(T) + (8/3)|T+7|\exp[(T+7)/3] \tag{3.17}$$

$$h(T) = 4(1.0 - [(T+25)/18]^2) \tag{3.18}$$

are approximate fits to the critical riming rate curve presented in Saunders et al. (1999a). The critical rime accretion rate is kept constant at low temperatures, as was done by Brooks et al. (1997).

3.3 Inductive Charging

Inductive, or polarization, charging results from particle collisions in the presence of an electric field. The electric field forces ions to move to the top and bottom surfaces of the particles. For ice-ice collisions we assume that the lower conductivity of ice makes polarization charging ineffective because contact times are too short for electrical currents to transfer charge. Enhanced coalescence by the electric field makes it unlikely that liquid particles will rebound in regions of even moderate field magnitudes (Jennings, 1975). The only interactions considered in the present model are the rebounding collisions of graupel and cloud droplets, and then only if the graupel is in a dry growth mode. Aufdermauer and Johnson (1972) found a rebound rate of only 1 to 10 per 1000 collisions between droplets and an ice pellet. However, Sartor (1981) pointed out that the ice pellet grown by Aufdermauer and Johnson had many crevices which could capture droplets. Sartor showed photographic evidence that, when the graupel pellet was more rounded with a rough surface, a higher rebound rate could be achieved and droplets could rebound from non-grazing trajectories.

Aufdermauer and Johnson (1972) found that when the droplets did rebound and separate charge they also lost mass. They concluded that the droplets partially froze to the ice pellet surface and the rest of the droplet tore away. If that is the case, then it would appear that it is the droplet which transfers charge to the graupel. When the droplet impacts the surface, the ions in the upper surface become trapped in the frozen portion of the droplet, and the ions of opposite sign are carried off by the liquid that tears away from the graupel surface. Another hypothesis is that the contact time is long enough for the electric field to polarize the joined particles, so that a current flows between the particles before the unfrozen part of the droplet breaks off. Either way, the amount of charge transferred depends on the impact angle, with maximum transfer for rebounding collisions from the bottom of the graupel and minimum transfer for grazing collisions near the equator.

The inductive charging formulation used in the present study is equivalent to that of Ziegler et al. (1991, Equation 7), but is written in terms of characteristic diameter and mass-weighted mean fallspeed:

$$\frac{\partial \rho_g}{\partial t} = (\pi^3/8)\left(\frac{6.0\bar{V}_g}{\Gamma(4.5)}\right) E_{gc}E_r c_{t,c} c_{0g} D_c^2 \cdot \left[\pi\Gamma(3.5)\epsilon\langle\cos\theta\rangle E_z \mathcal{D}_g^2 - \Gamma(1.5)\rho_g/(3c_{t,g})\right] \tag{3.19}$$

where D_c is the cloud droplet diameter (the model uses $D_c = \mathcal{D}_c$, characteristic diameter of cloud droplets), E_{gc} is the collision efficiency, E_r is the rebound efficiency, $c_{t,c}$ and $c_{t,g}$ are the total cloud water and graupel number densities, $\bar{V}_g$ is the mass-weighted mean fall speed of graupel, $\Gamma(x)$ is the complete gamma function, $\mathcal{D}_g$ is the characteristic diameter of graupel, c_{0g} is the number concentration intercept for graupel (Equation 3.5), $\langle\cos\theta\rangle$ is the average cosine of the angle of rebounding collision, E_z is the vertical component of the electric field, and ϵ is the permittivity of air. The second term in the square brackets represents the effect of the pre-existing charge carried by graupel ρ_g on the induced charge on the droplet. Since droplets greatly outnumber graupel, it is assumed that the rebounding droplets are initially neutral and experience only one rebounding collision with graupel. Ziegler et al. (1991) used an effective $E_r = 0.0022$ and $\langle\cos\theta\rangle = 0.1$. These values resulted in very weak inductive charging. Higher values were used in the present study. For "moderate" inductive charging $E_r = 0.007$ and $\langle\cos\theta\rangle = 0.2$. For "strong" charging $E_r = 0.015$ and $\langle\cos\theta\rangle = 0.5$. The assumed rebound probabilities E_r are well within the range of experimental results, which vary from as low as 0.1–1.0% (Aufdermauer and Johnson, 1972) to as large as about 10% (Gaskell, 1981).

3.4 Charge Screening Layer Parameterization

The thunderstorm model used in this research does not explicitly treat ion capture by hydrometeors. Therefore, the formation of electrical screening layers is parameterized as in Ziegler et al. (1991). The difference in conductivity between clear air and cloudy air causes an initial current discontinuity when an electric field is applied. Charge builds up on the cloud boundary due to current divergence, $\partial\rho/\partial t = -\nabla \cdot \vec{J}$, until the current densities in the cloud (J_c) and in clear air (J_a) are balanced:

$$J_a = \sigma_a E_a = \sigma_c E_c = J_c. \tag{3.20}$$

Here the equation has been simplified by considering the cloud boundary as an infinite plane, and J_c and J_a are the currents normal to the cloud boundary, since only the normal component causes the screening layer. The thickness of the screening layer is parameterized as the cube root of the gridpoint volume, $L = (\Delta x\, \Delta y\, \Delta z)^{1/3}$, so the charge is added only to the outermost grid points within the cloud. This thickness is consistent with reports by Marshall et al. (1989).

The currents normal to the surface J_n are found by computing the unit surface normal vector $\hat{n}$ and taking the dot product with the electric field inside and outside of the cloud.

$$\hat{n} = \nabla q_{cld}/|\nabla q_{cld}|$$

$$J_n = \hat{n} \cdot (\sigma \vec{E})$$

where q_{cld} is the sum of the cloud droplets and cloud ice mixing ratios. The cloud boundary is defined by the surface $q_{cld} = 10^{-5}$ kg/kg. Ziegler et al. (1991) showed that the change in charge density at a point on the cloud boundary for a time step Δt is given by

$$\delta\rho = \frac{(2\epsilon/L)(\sigma_a E_a - \sigma_c E_c)}{\sigma_a + \sigma_c}\left\{1 - \exp\left[\frac{-(\sigma_a + \sigma_c)\Delta t}{2\epsilon}\right]\right\} \tag{3.21}$$

The screening charge is distributed to each of the cloud particle categories q_i according to its fraction of the total cloud mass q_{cld} by the formula $\delta\rho_i = \delta\rho(q_i/q_{cld})$. Following Ziegler et al. (1991), it is assumed that the conductivity of cloudy air is 10% of the value for clear air, on the basis of measurements by Rust and Moore (1974).

3.5 Surface Corona Layer

A diagnostic surface corona layer was added to the model in the course of this research. The "corona layer" is simply a persistent charge layer that is confined to the lowest model level above ground. The corona charge serves to limit the magnitude of the vertical electric field component E_z at the ground to a set threshold value. (The threshold used in the simulations is 10 kV/m, which is a reasonable limit for realistic magnitudes at ground level.) Charge of the appropriate sign is added where the surface E_z exceeds the threshold. Just enough charge is added to prevent $|E_z|$ from exceeding the threshold value. The corona layer is not advected and does not interact with any hydrometeors. An exponential decay with a time constant of about 1.5 minutes is applied to the corona layer, so that the charge can disappear when it is no longer forced by E_z. The presence of the surface charge layer has very little influence at higher altitudes because of the close proximity of its image charge.

The effect of corona charge on descending raindrops is included as a very simple parameterization of Wilson ion capture. This parameterization operates independently of the surface corona layer described above. It is assumed that the raindrops will be discharged by attracting ions of opposite sign. The scheme reduces to the charge density on raindrops (ρ_r) below 1.5 km at a rate given by

$$\frac{\partial \rho_r}{\partial t} = -0.1(1 - (z/z_{\text{top}})^5)\rho_r \tag{3.22}$$

where z is the altitude (for $z < 1500$ m) and $z_{\text{top}} = 1500$ m. (Note that the differential equation is for an exponential function.)

Chapter 4

Lightning Parameterization

Lightning parameterizations are required for storm electrification simulations beyond initial electrification. Without lightning discharges, the electric field can reach unrealistic magnitudes. The simulated lightning should also produce realistic lightning characteristics, such as spatial extent and flash frequency. A number of lightning parameterizations have been developed previously, and each has some advantages as well as shortcomings. A new lightning parameterization was developed in the course of the present research. The new parameterization, the stochastic lightning model (SLM), is based on the dielectric breakdown model originally developed by Niemeyer, Pietronero, and Wiesmann (NPW, 1984) and Wiesmann and Zeller (WZ, 1986). The SLM can produce realistic-looking, branched, three-dimensional intracloud (IC) and cloud-to-ground (CG) lightning discharges. (In this dissertation, IC lightning refers simply to any discharge which does not connect to ground.) This chapter provides an overview of lightning parameterizations in the literature and then a description of the Wiesmann-Zeller dielectric breakdown model and the adaptations made to turn it into the SLM.

4.1 Previous Lightning Parameterizations

Two early lightning parameterizations were quite simple. Rawlins (1982) reduced the charge density on all categories everywhere in the domain by 70% when the electric field exceeded 500 kV/m. Takahashi (1987) delineated positive and negative regions with just over 20 Coulombs of net charge and neutralized the same fraction of charge on all hydrometeors in those regions to reduce the net charge by 20 Coulombs. Both of these parameterizations are physically unrealistic in that they reduce the charge on *all* hydrometeor species by the same rate. Different hydrometeor categories often carry opposite signs of charge at the same location, so that an overall reduction involves much more charge than a change in net charge alone.

The lightning parameterization of Helsdon et al. (1992) makes a single, unbranched channel which traces the electric field line from an initiation point. The channel is extended until the ambient field falls below a certain threshold. A relatively simple analytical model is used to calculate the positive and negative linear charge densities that are induced by the external electric field along the channel. The charges at the ends of channel are adjusted to maintain net charge neutrality of the flash. Charge carried by the channel is released to the small ion category of the storm model, which explicitly treats ion capture by hydrometeors. The discharge can result in the sign reversal of the net charge density at affected points. The Helsdon lightning parameterization was used within a two-dimensional electrified numerical thunderstorm model (Helsdon and Farley, 1987) which has since been extended to three dimensions. The shortcomings of the Helsdon et al. parameterization include the lack of branching and controlling the structure and extent based only on the ambient electric field with no contribution from the channel itself.

Solomon and Baker (1996) developed a one-dimensional lightning parameterization. Like the Helsdon et al. (1992) parameterization, there are electric field thresholds for both initiating and stopping flash propagation. However, Solomon and Baker used analytical equations to calculate the contribution to the electric field from the charge induced on the channel, which is an improvement over the Helsdon et al. parameterization. Thus it is the total electric field which controls propagation. (The total electric field is the superposition of the ambient field plus the "local" field from the channel.) Both intracloud and ground flashes can be produced. The main limitation of their parameterization is the constraint that channels develop only vertically and only on the axis of the cylindrical storm. Thus, the simulated flashes have no tortuosity or branching, and the parameterization would not be realistic in a less symmetrical storm geometry. The lightning parameterization was modified when used in the modeling study of Solomon and Baker (1998). Here the channel was simply extended until the charge induced at the tips reversed sign or was reduced to zero, implying a zero field stopping threshold. The criterion of an explicit nonzero critical electric field at the channel tip was dropped, although such a threshold for propagation arguably has a more physical basis.

Another one-dimensional lightning model was presented by Mazur and Ruhnke (1998). Like the Solomon and Baker (1996) parameterization, their modeled lightning channel accounted for the charge induced on the channel, and the continued growth of the channel was based on the total electric field near the tips of the developing flash. They did not use a storm model, but instead used a simple axisymmetric 'tripole' charge distribution (main negative charge with a main positive charge above and lower positive charge below). From this distribution they modeled both an intracloud flash and a ground flash. In each case the channel was treated as a perfect conductor, and its electric potential was adjusted to maintain overall charge neutrality during growth. Mazur and Ruhnke also determined the charge distribution on the lightning channel. They found that the return stroke deposited a nearly constant linear charge density on the vertical channel.

MacGorman et al. (1998) presented a lightning parameterization which may be considered to be an extension of the Helsdon et al. (1992) parameterization. It creates an initial lightning channel by tracing the electric field line passing through the chosen initiation point. The trace continues in each direction until the field magnitude drops below a preset stopping threshold, at which point the channel is assumed to become highly branched if the endpoint is in a cloudy region with sufficient space charge. The discharge volume is extended from the channel endpoint to contiguous points which contain a minimum magnitude of space charge density. The branching regions are also bounded by the equipotential surfaces defined by the electric potential at the respective vertical channel endpoints. The charge deposited by the flash is calculated as a fraction of the net charge in excess of a threshold at each gridpoint in a branching volume. Some other details of this parameterization were incorporated into the new model and are described below.

Petrov and Petrova (1993 and 1999) used the dielectric breakdown model of Wiesmann and Zeller (1986) (see the next section) to simulate branched lightning discharges. These studies were apparently two dimensional and used simple arrangements of conductors at fixed electric potentials as representations of regions of net charge. Thus the discharges were propagated through neutral regions and were in effect unidirectional. This and the arbitrary arrangement and electric potentials of the conductors in their studies limit the conclusions that can be drawn from their results. The Wiesmann-Zeller model does account for the effect of the lightning channel itself on the total electric field, as described in the next section. Petrov and Petrova (1999) showed the effect of using a pressure-dependent threshold for conventional breakdown instead of a constant threshold. When the propagation electric field threshold decreased with height, discharges extended to higher altitudes than they did when the threshold was constant.

The lightning model of Hager (1998) also produces branched lightning channels and bears some similarity to the SLM but is different in a number of respects. Both models extend lightning channels in a discrete step-by-step fashion until the electric field no longer exceeds breakdown threshold at grid points adjacent to the flash. Hager's model requires the lightning channels to be equipotential surfaces (i.e. perfect conductors), whereas the SLM allows the potential to vary along the channels. Hager's model appears limited to propagation along the coordinate directions, but the SLM allows propagation along any direction of the unit cube, including diagonals. Furthermore, Hager's model has no random element as in the SLM (see below), and breakdown extends to all points at which the electric field exceeds the threshold in any given step.

4.2 Dielectric Breakdown Models

The research in this dissertation used a dielectric breakdown model developed by Niemeyer, Pietronero, and Wiesmann (NPW) (1984) and Wiesmann and Zeller (WZ) (1986). The breakdown model was used to simulate the discharge experiments of Williams et al. (1985), and this led to the application of the model as a lightning parameterization. Dielectric breakdown models basically determine only where to place channel steps and do not deal directly with the microscopic processes of breakdown. Though the formulation is rather simple, it is possible to produce complex structures that realistically mimic actual electrical discharges.

NPW introduced a dielectric breakdown model to examine the tortuous, branched patterns of breakdown in neutral dielectrics. WZ made the NPW model more physical by adding a critical field threshold for propagation and allowing for an internal electric field in the discharge channel. The common application of the WZ model has been to map breakdown through an insulating material in a gap between two conductors (planes or concentric spheres) to which a voltage difference is applied. The discharge is often initiated unidirectionally from one of the conductors. Dissado and Sweeny (1993) formulated a new model specifically for solid dielectrics and achieved results similar to those of the WZ model. They simulated two-dimensional electrical channels that originated bidirectionally from a defect within the dielectric and were driven by an AC field.

The essence of the WZ model is to propagate a discharge from an initiation point by creating a new breakdown connection, or bond, to one gridpoint per step. Figure 4.1 shows a sample two-dimensional grid with part of a discharge. Each new bond is chosen at random from all possible new bonds. A bond is possible to any adjoining gridpoint at which the electric field favors forward propagation and exceeds a critical field magnitude, E_{crit}. Once all possible bonds have been identified, the probability of choosing a particular bond is given by

$$p_i(E) = \frac{(E_i - E_{crit})^\eta}{\sum_k (E_k - E_{crit})^\eta}, \tag{4.1}$$

where η is a weighting exponent.

NPW did not have a critical field in their model and found that the density of branching decreased with increasing values of η. When $E_{crit} = 0$, "bush" type (densely packed) discharges resulted for $\eta \leq 1$, and "branched" structures resulted for $\eta \geq 3$. Wiesmann (1988) found that introducing $E_{crit} > 0$ had an effect similar to that of setting $\eta > 1$, since doing either tends to limit side branching. Dissado and Sweeny (1993) point out the difficulty in physically justifying any exponent other than $\eta = 1$. Pietronero and Wiesmann (1988) argued that η can be derived from the relationship between the electron avalanche velocity and the local electric field in gas discharges. In our research, we assume that the relationship is linear (i.e. $\eta = 1$).

In the WZ model, channels can be treated as perfect conductors (zero internal electric field) or as having a resistance (non-zero internal field). A non-zero internal field tends to limit the overall extent of the discharge structure. When a new gridpoint is added to the discharge, the potential at that point is set as will be described. The electric potential is then updated everywhere in the domain by solving Poisson's equation,

$$\nabla^2 \phi = -\frac{\rho}{\epsilon}. \tag{4.2}$$

(In the literature on dielectric breakdown models, breakdown occurs in neutral dielectrics so that $\rho = 0$ and the problem reduces to the Laplace equation.) The potential of the new point is calculated from the potential, ϕ_b, of the point from which the bond extends:

$$\phi_{new} = \phi_b - s\, E_{int}\, d, \tag{4.3}$$

where E_{int} is the internal field, d is the length of the new bond and s is the sign of charge carried by the channel. The discharge structure is treated as a boundary with Dirichlet conditions. Because of the complex geometry of the boundary, Poisson's equation is most

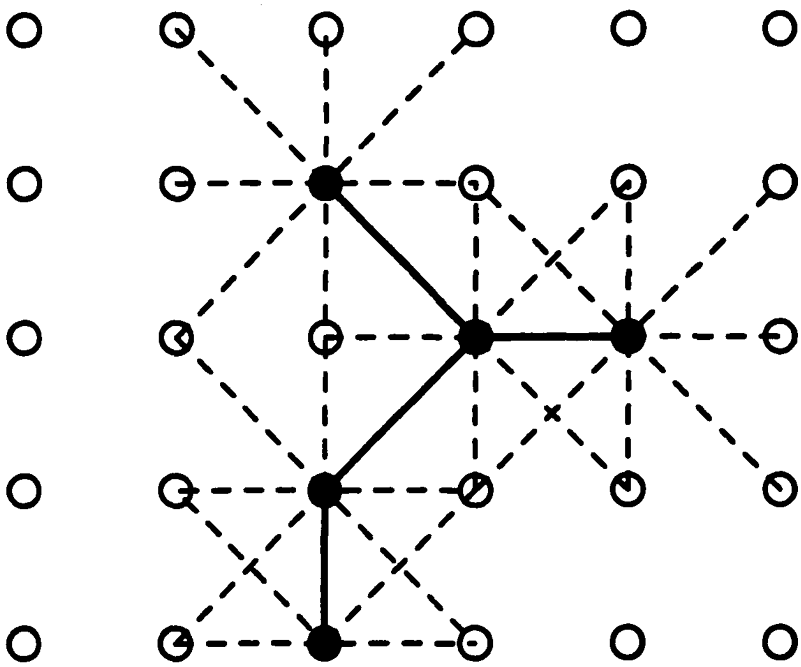

Figure 4.1: Sample grid showing a portion of a discharge in two dimensions. Open circles represent grid points not connected to the discharge. Filled circles and heavy lines indicate the discharge path. Dashed lines indicate possible new bonds. In three dimensions, connections are allowed along all of the unit cube directions.

easily solved numerically with a relaxation technique such as successive overrelaxation (SOR).

Discharge simulations generally add only one new bond per propagation step, whereas in reality growth may occur simultaneously on different branches. In the lightning simulations for the present research, most growth was near the outer ends of the branches. Inner branches tended to be cut off from growth because of the screening effect of the outer branches.

No time scale is assumed for the discharge development. The sequence in which segments are added can be considered a kind of time-ordering, but it would be problematic to assign an actual time scale. Part of the difficulty is that real discharges would be expected to have simultaneous extentions from different branches, but the model adds only one extention at a time. For lightning simulations, one could estimate the elapsed time by using average measurements of positive and negative leader velocities (Mazur and Ruhnke, 1998), but this has not been attempted here. An estimate of elapsed time would also be useful for approximating the electric currents in channels, and this may be attempted in the future.

4.2.1 Simulations of Unipolar Discharges

An initial test of the WZ model was to attempt simulations of the unipolar discharges produced in the laboratory by Williams et al. (1985). Williams et al. exposed plastic slabs to an electron beam to create various horizontal charge distributions in the plastic. A discharge was then initiated to a ground plane, which supported the plastic slab. They found that the discharges became more extensive as the charge density in the plastic increased. Figures 4.2 and 4.3 show simulations of sparks into slabs of horizontally uniform charge. The only difference between the two figures is that in Figure 4.2 there is no internal electric field (i.e. the channels are treated as perfect conductors), and in Figure 4.3 there is a small internal field (i.e. the channels have non-zero resistance).

Figure 4.3 compares well with the laboratory discharges through slabs filled uniformly with different charge densities (Williams et al. 1985, Fig. 1), which is reproduced in Figure 4.4. As the charge density increased, the maximum propagation distance and degree of branching increased in both the experiment and the simulation. Both also showed the tapering in structure with increasing distance from the initiation point. A more quantitative comparison might be to calculate the fractal dimension of the experimental and simulated discharges, but this has not yet been done.

Another aspect of Williams et al.'s work was to show discharges for arrangements of two different charge densities (Williams et al. 1985, Fig. 6). The first one had pockets of higher charge density surrounded by lower charge density, and the second had the same pattern but switched the charge densities (i.e. lower density charge pockets surrounded by higher density charge). They observed that the discharge traveled preferentially into the

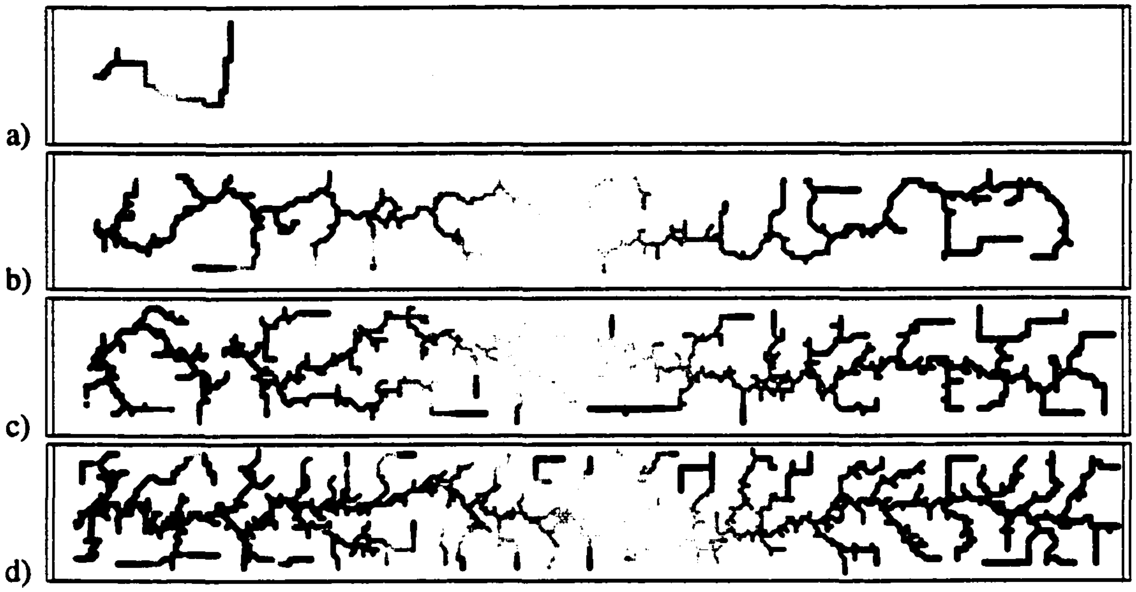

Figure 4.2: Numerical simulations of unidirectional discharges into a rectangular region of charge, $\alpha = 0.0$ (no internal field) Charges densities are a) 0.5, b) 0.7, c) 0.9, d) 1.1 nC m^{-3}. The simulated slabs are 30 grid points wide, 240 points long, and 7 points thick (border regions are not shown). The colors indicate the sequence of the discharge development: from green for early stage to red for later.

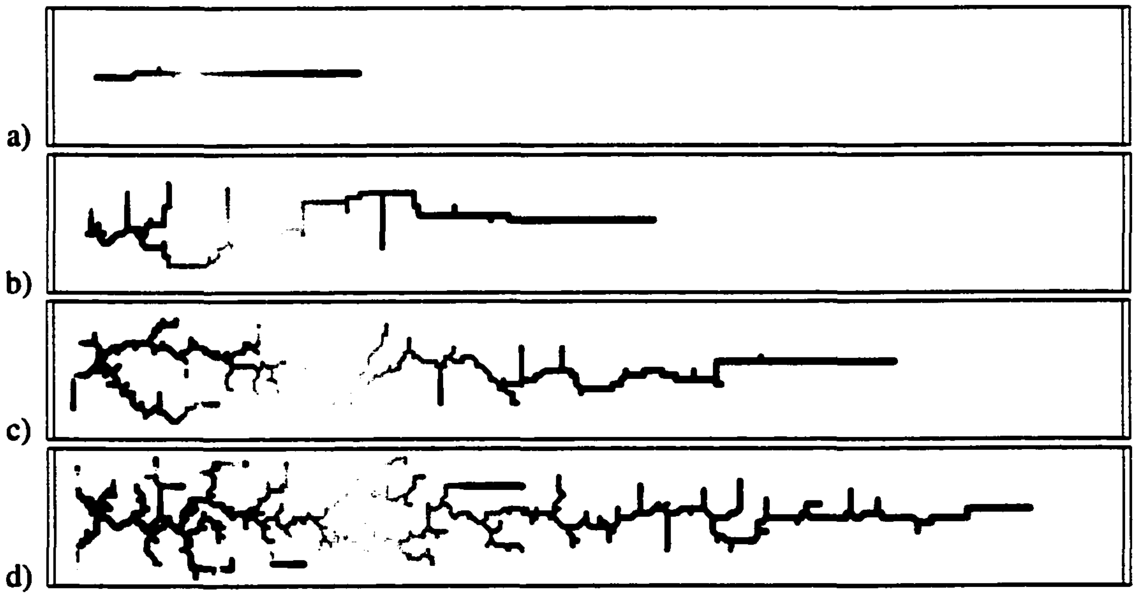

Figure 4.3: As in Figure 4.2, but with $\alpha = 0.01$ (internal electric field of 1 kV/m).

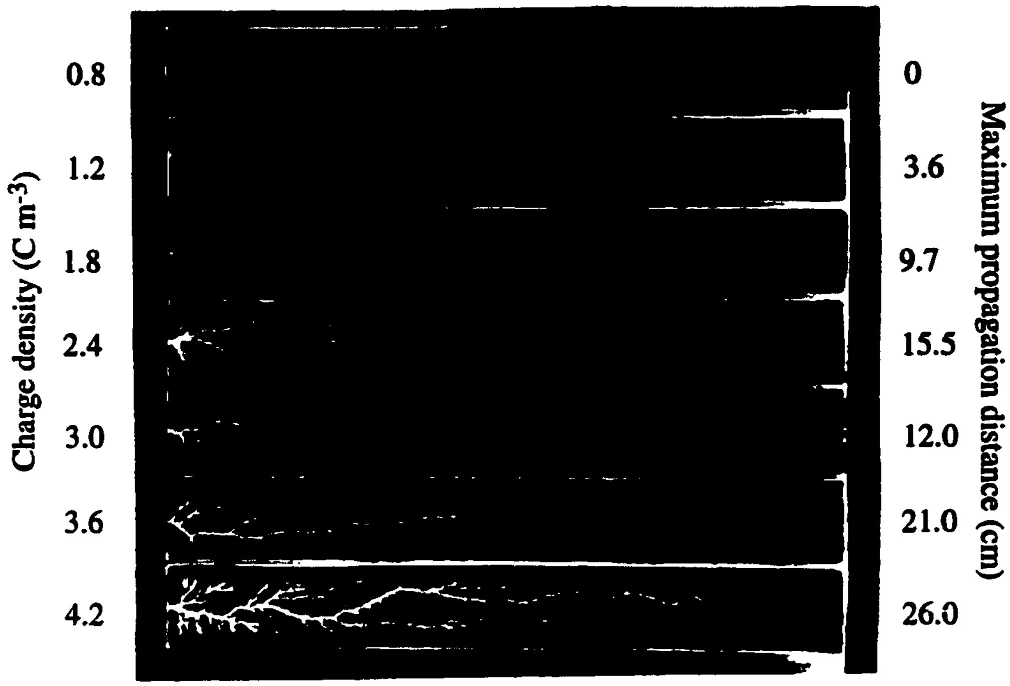

Figure 4.4: Discharges through plastic with uniform charge densities. Reproduced from Williams et al. (1985), Figure 1. The slabs were 35.0 cm long.

regions of larger density, where it also had denser branching. A simulation with similar enhanced regions showed the same behavior (Figure 4.6).

The simulations in Figures 4.2, 4.3, and 4.6 were scaled to atmospheric dimensions. The grid spacing was 125 m in all three dimensions. The space charge densities were in the range of values determined from electric field and particle charge measurements in thunderstorms. The charge regions were confined to a layer that was 7 grid points in thickness. The central layer had the given charge density and was 3 grid points in thickness. The charge density decreased linearly above and below the central layer to zero at the outermost grid points. This distribution approximates the assumed gaussian distribution of charge in the laboratory experiments (Williams et al. 1985). The simulated discharges were initiated by extending a 'needle' conductor from the ground plane. The propagation threshold was set at 100 kV/m, the value suggested by Griffiths and Phelps (1976) for an altitude of 9 km above mean sea level.

One might the question, of course, how comparable discharges in plastic slabs are

Figure 4.5: Discharges through plastic with two charge densities. (a) Isolated regions of higher charge density ($-1.2\,\mathrm{C\,m^{-3}}$) are surrounded by lower charge density ($-0.6\,\mathrm{C\,m^{-3}}$). (b) Isolated regions of lower charge density ($-0.6\,\mathrm{C\,m^{-3}}$) are surrounded by higher charge density ($-1.2\,\mathrm{C\,m^{-3}}$). Reproduced from Williams et al. 1985, Figure 6.

a)

b)

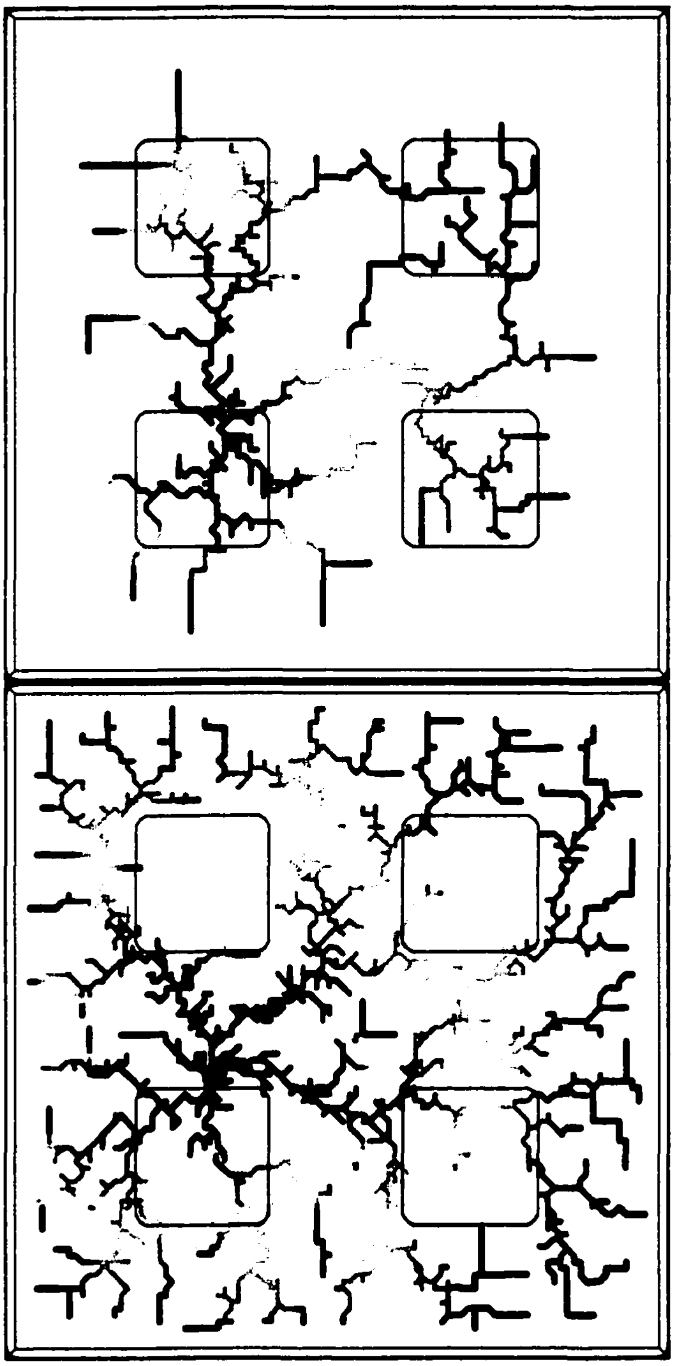

Figure 4.6: Simulations of unidirectional discharges with regions of enhanced or reduced charge density. In (a) the small square regions have $\rho = -1.2\,\mathrm{nC\,m^{-3}}$ surrounded by $\rho = -0.6\,\mathrm{nC\,m^{-3}}$, and in (b) The charge densities are exchanged. The discharges were propagated in a three dimensional domain and had an internal electric field of 1 kV/m. The initiation point is at the top edge of the lower-left small square from a needle protrusion from the simulated ground plane. The area shown is 100 by 100 grid points (12.5 × 12.5 km).

to lightning discharges. However, it probably is reasonable to extrapolate the general behaviors, such as faster and more branched propagation in regions of higher charge density. A more questionable conclusion is that the internal field for a small laboratory discharge would be comparable to that of a lightning leader. Certainly there is no one value of internal field valid for the complete development of any particular discharge, and the choice is necessarily an approximation. Recent results indicate that lightning channels have at least a small resistance (private communication, Vlad Rakov). However, the choice of internal field is not particularly critical to the model,since the effect of including it is primarily to limit the extent of the simulated discharges, not to change their basic character.

4.3 Stochastic Lightning Model

4.3.1 Description

The stochastic lightning model (SLM) is an application of the WZ model to simulate bidirectional discharges in regions of varying net charge density. The lightning model can run either as a subroutine within the electrified thunderstorm model or as a separate application. This section will describe the details of the SLM and the procedure for simulating lightning flashes in the context of a thunderstorm model.

The decision process for initiating a lightning flash follows the procedure of MacGorman et al. (1998). A flash occurs when the electric field magnitude exceeds the initiation threshold E_{init} somewhere in the model domain. There are two options for the initiation threshold: 1) a constant value throughout the domain and 2) a height-varying threshold. The only height-varying threshold included so far is the "breakeven" or "runaway election" electric field threshold given in Marshall et al. (1995):

$$E_{be}(z) = \pm 167\,\rho(z) \tag{4.4}$$

$$\rho(z) = 1.208\ \exp(-z/8.4) \tag{4.5}$$

where E_{be} has units of kilovolts per meter, and ρ is the air density (kg m^{-3}) as a function of altitude, z, in kilometers. In the current study, E_{be} was limited to the range of 30 to 125 kV/m. The actual initiation point is then chosen at random from among all the points at which the electric field magnitude is greater than a chosen percentage of the initiation threshold. For the present study a value of 90% was used. The secondary threshold and random element are an attempt to allow lightning to occur over a larger range of locations and to account for some of the natural variability of lightning due to unresolved sub-grid fluctuations in a cloud model.

The maximum number of lightning flashes allowed per time step is set by user input. In the present research, maximum allowed flash rates ranged from 96 to 120 per minute (8 to 10 per 5-second time step). Some of the thunderstorm cases did reach the maximum rate of 120 flashes per minute.

The initial breakdown process is not treated at all, and the discharge is started as a leader channel between two grid points. The first point is chosen as described above, and the second one is the adjacent grid point with the maximum electric field magnitude (i.e. maximum value of $|\phi_2 - \phi_1|/d_{12}$, where d_{12} is the distance between the points). Positive and negative leaders are propagated from opposite ends of the initial channel. Positive leaders carry net positive charge and propagate toward and through regions of lower electric potential (generally negative charge regions). Negative leaders do the opposite, carrying net negative charge and extending preferentially into and through regions of net positive charge and higher potential.

Although the physics are different for negative and positive leader development, both types of leader are treated in the same way in the SLM. The positive and negative parts of the flash are propagated independently so that up to two new channel segments (one positive and one negative) may be added per step. The channels are assumed to have an internal electric field, typically set to $0.01 \cdot E_{init}$ in our simulations. The value of $0.01 \cdot E_{init}$ was used because it yielded the best qualitative agreement between the simulated (Figures 4.2 and 4.3) and experimental (Figure 4.4) discharges in slabs of uniform charge density. The reference potential for the branches is taken as the average of the ambient potentials of the two initial grid points. In effect, each end is treated as a unipolar leader but with some constraints (outlined below). If one part has no growth possibilities, the other part is still allowed to propagate. If a channel encounters the top or side boundaries of the model domain, all flash propagation is halted. The procedure for ground flashes is described below. Otherwise, the growth process continues until all growth probabilities become zero, unless charge imbalance conditions (described below) stop the flash.

At the start of the SLM routine, an initial solution to Poisson's equation (Equation 4.2) is calculated by a direct method which uses Fast Fourier Transforms (FFT) in the horizontal directions and solves the resulting tridiagonal system of equations in the vertical direction. The bottom of the domain (ground) is set at zero potential, and the top and sides have the Neumann condition of $\partial\phi/\partial n = 0$. The domain in which the potential is solved is actually wider than the thunderstorm domain. The extension of the lateral boundaries increases the accuracy of the solution by reducing the influence of the mirror charges which necessarily result from the boundary condition. A future improvement will be to extend the top boundary as well.

After each step has added up to two channel segments, the previous values of the potential are passed along with values at the new point(s) to a successive overrelaxation (SOR) subroutine. At the beginning of each iteration, or sweep, this routine calculates the residual r (the estimated error in the solution to the potential) at each grid point by using the equation

$$r = (\Delta s)^2(\nabla^2\phi^{old} + \rho/\epsilon), \tag{4.6}$$

where Δs is the uniform grid spacing, ϕ^{old} is the solution to the potential from the most recent iteration, and ρ and ϵ are again the net charge density and permittivity, respectively. The Laplacian, $\nabla^2\phi$, is calculated by a standard 7-point finite difference formulation (second-order accuracy), which is the sum of the second derivatives in each direction:

$$\nabla^2\phi \equiv \sum_{i=1}^{3} \frac{\partial^2\phi}{\partial x_i^2} \tag{4.7}$$

where

$$\frac{\partial^2\phi}{\partial x_i^2} \cong \frac{\phi[x_i - \Delta x_i] - 2\phi[x_i] + \phi[x_i + \Delta x_i]}{(\Delta x_i)^2} \tag{4.8}$$

Each SOR sweep updates the solution to the potential from the residual by

$$\phi_{ijk}^{new} = \phi_{ijk}^{old} + \frac{1}{6}\omega r_{ijk}, \tag{4.9}$$

where ω is the overrelaxation parameter and has a value in the range 1–2. After updating, r is calculated at each grid point, and the maximum fractional residual $\varepsilon = \mathrm{Max}[r]/\mathrm{Max}[\phi]$ is determined. If $\varepsilon \leq 5 \times 10^{-3}$, the SOR routine stops. If $\varepsilon > 5 \times 10^{-3}$, the routine goes through another sweep.

The domain for lightning propagation uses grid spacing of 500 m in all three dimensions. The equal spacing not only simplifies the numerics, but also limits any bias in the electric field calculations in different directions. This differed from the thunderstorm domain, which used 500 m vertical spacing and 1000–1500 m horizontal spacing. When a flash is initiated, the net charge density of the thunderstorm is interpolated linearly in three dimensions from the thunderstorm domain to the SLM grid.

Once the lightning flash begins, Dirichlet boundary conditions are applied at the channel points, where the potential is set according to Equation 4.3. The conducting channel significantly affects the potential at nearby grid points. Thus, after each step of channel development the modified potential of the domain is determined by using the SOR method.

An increase in computational efficiency was achieved by adjusting the domain in which the Poisson equation is solved. When a new channel segment is added to the discharge structure, only the nearby points of the model domain are significantly affected. Therefore it is sufficient to recalculate the potential by the SOR method in a relatively small domain around the new point. After every ten propagation steps, relaxation is also performed in a domain which encompasses the entire lightning flash. This "local/global" method is effective in solving for the important short wavelengths (Fourier components of the solution to the potential). The long wavelengths are not as relevant to the process since the solution at points far from the flash is not important to the propagation of the discharge. The "local" solution is performed in a subdomain that is 21 grid points (10 km) wide in each direction and is centered on the new point. The "global" solution is calculated in a domain which contains the entire flash and which is increased in size by two grid points on each side after each SOR sweep. In both the global and the local calculations, the domain boundaries usually use Dirichlet conditions. However, if boundary of the local or global domain is within 10 grid points of a storm domain boundary, then the smaller domain is expanded all the way to that boundary and uses the corresponding condition for the storm domain (Neumann for top and sides, Dirichlet for bottom). This strategy of using a limited domain does not appear to introduce any obvious instabilities to the solution.

Following the theory of Kasemir (1960), we assume that the channel structure should maintain overall charge neutrality as long as neither end reaches ground. A physically realistic treatment would involve an iterative process in which the reference potential (at the starting point) is shifted until the net charge on the channel branches is zero after each step, but this is not done now. Such a treatment would add to the computational expense and may be tested at a later time.

For the present time, a less realistic but faster approach has been implemented to encourage charge neutrality on flashes as they develop. Both ends have default propagation thresholds of $0.75 \cdot E_{init}(z)$. After every fifth propagation step, the charge carried by positive and negative channels is calculated from Poisson's equation ($\rho = -\epsilon \nabla^2 \phi$) and summed separately over the positive and negative parts of the flash. If the charge magnitude on one part is greater than the other by more than 10%, then the propagation threshold is increased for the end with more charge, to retard its growth, and likewise the threshold is reduced on the end carrying less charge to promote its growth. If the difference in charge subsequently falls below 10%, then the propagation thresholds are incremented back toward the default values. Adjustments are made in increments of $0.05 \cdot E_{init}(z)$, with a minimum possible value of $0.60 \cdot E_{init}(z)$. No maximum limiting value is specified, but after completion of the simulations it was discovered that an unrelated condition inadvertently limited the propagation threshold in regions of clear air.

A flash is never halted because of charge imbalance if fewer than 40 propagation steps have been made since initiation. However, if more than 40 propagation steps have been taken, the flash is halted if the charge imbalance ever becomes greater than a factor of two. The choice of 40 steps was arbitrary and was intended to allow some time for the correction of charge imbalances that arise early in the flash growth. On average, about 10% of all IC flashes are stopped as a result of the charge imbalance condition.

Early tests of the SLM revealed a propensity for flashes sometimes to extend well above the top of the cloud. At the time, this behavior was considered undesirable, and it was partly caused by improper boundary conditions in the "local/global" solution technique. The boundary condition problem was corrected. To inhibit propagation above clouds, the lightning propagation threshold was increased in clear air above 5 km to the smaller of $|2.0 \cdot E_{init}(z)|$ and 150 kV/m. (This condition had the unintended side-effect of also occasionally *limiting* the propagation threshold in clear air. It has since been corrected so that it will not set a lower threshold than the one set by the charge balancing process described above.) This inhibiting of propagation through clear air was justified by the ad hoc hypothesis that the presence of hydrometeors is needed to locally enhance the electric field for further breakdown. However, this hypothesis has no experimental or observational basis and could very well be invalid. This extra propagation limitation reduced but did not eliminate above-cloud lightning.

Cloud-to-ground (CG) flashes are handled in a simple manner. When a lightning channel reaches below 2 km, it is extended to ground, and its polarity determines the polarity of the CG. In other words, a negative leader reaching ground results in a negative CG (−CG) and effectively lowers negative charge to ground from the storm. Similarly, a positive leader to ground makes a positive cloud-to-ground flash (+CG). Propagation is stopped for all branches of the same polarity as the one that reached ground. The upward-growing (i.e. opposite polarity) leaders, however, are allowed to continue propagating until they stop naturally (or reach a domain boundary). Furthermore, if the propagation threshold of the upward branches had been increased because of a charge imbalance, it is reset to the default value. The continued growth acts as a crude parameterization of growth caused by all return strokes. The charge on the branches of the grounded end of the flash is set to zero, and the charge on the upward-developing part of the flash is computed as described previously, without forcing charge neutrality overall. In the future, we will attempt to model the effect of a return stroke by setting the potential to zero everywhere along the channels, recomputing the potential at nearby grid points, and then determining the final charge on the channels by using Poisson's equation.

The locations of charge centroids are found for both IC and CG flashes. For IC flashes two centroids are computed, one for each channel polarity. For CG flashes, the centroid is determined only for the charge on the upward developing channels. (The charge on the downward channels of CG flashes is set to zero.) The electric dipole moment of the charge is also calculated for IC flashes. The dipole location is set equal to the midpoint between the positive and negative charge centroids.

The charge carried by lightning channels is presumably captured quickly by atmospheric molecules to form ions, which are captured by hydrometeors more slowly. Since the thunderstorm model does not have a category for ions, the lightning charge is distributed directly among the hydrometeor categories. Each hydrometeor category receives charge in proportion to its total surface area, as in the MacGorman et al. (1998)

parameterization:

$$\delta\rho_i = \frac{\sigma_i}{\sum_k \sigma_k}\delta\rho, \tag{4.10}$$

where $\delta\rho$ is the charge density at a grid point on the lightning channel and $\delta\rho_i$ is the charge density deposited on the i^{th} hydrometeor category having a total surface area σ_i. If branches extend outside the cloud to regions with no hydrometeors, the charge on branches outside the cloud is considered lost to ions, and overall charge neutrality of the flash is not maintained by the model.

The development of the SLM began as a stand-alone model which used a charge density field output from the thunderstorm model. Tests of the dependence of flash characteristics on grid resolution were made at grid spacings of 250 m and 500 m. For the grid with 250 m spacing the propagation threshold was set equal to the initiation threshold, and this yielded fairly extensive, well-branched flashes. To achieve the same spatial extent at 500 m resolution it was necessary to reduce the propagation threshold by about 25%. This is because the coarser resolution does not represent gradients in the potential as well as the finer resolution, so calculated electric field values tend to be smaller.

The effect of grid resolution on the charge carried by the channels was also tested. A flash was first propagated at 500 m resolution. The channel was then interpolated onto the higher resolution grid by adding channel points at the midpoint of each channel segment. When the Poisson equation was again solved around the channel, it turned out that the charge carried by the channels changed by no more than 4-10%. Tests at even higher resolution would have been computationally prohibitive. The 500 m resolution seems to be a good compromise between detail and computational efficiency.

4.3.2 Examples of Simulated Lightning Flashes

The stochastic lightning model can produce a wide variety of lightning structures, including both intracloud and cloud-to-ground flashes. The model has produced both positive and negative CG flashes, with the polarity depending on the storm type and resulting charge distribution. The simulated IC flashes are often characterized by a bilevel structure like that which has been inferred from lightning observations (e.g. Shao and Krehbiel, 1996; MacGorman et al. 1981). Simulated flashes also produce observed features such as negative leaders extending above the cloud near the overshooting top (private communication, Paul Krehbiel) and cloud-to-air discharges in which part of the flash reaches out from the side of the thunderstorm. The charge deposited by single or repeated flashes is often sufficient to reverse the net charge density in localized regions, an effect also seen in the Helsdon et al. (1992) lightning parameterization.

Two intracloud flashes are shown in Figures 4.7 and 4.8. Both exhibit two layers of horizontal structure associated with two regions of charge in the storm: an upper positive charge region and a lower negative region (the "main positive" and "main negative" charge regions). The flash in Figure 4.7 is from a strong airmass storm about 30 minutes after the first lightning. The magnitude of the dipole moment of the flash was 118 C km, and the flash deposited 21 C of charge at each end. The second IC flash (Figure 4.8) is from a mature supercell storm (about 75 minutes after first lightning) and shows greater horizontal extent. This larger flash had a dipole moment magnitude of 372 C km and deposited 48.1 C of each charge polarity.

Figure 4.9 depicts a discharge between an upper negative screening charge layer and the positive charge within a supercell anvil. There have been some observations of discharges near the tops of thunderstorms (Taylor et al. 1984), and it has been suggested that these high flashes could be discharging a screening layer. Note that the polarity is inverted from that of "normal" intracloud flashes. A flash observed by Krehbiel et al. (1999) with a VHF lightning mapping system showed a similar inverted polarity and was located high in the storm. As will be seen in the results chapters, the model can produce many discharges in the upper negative screening layers of thunderstorm anvils, and sometimes in lower negative screening layers as well.

An example of a negative CG flash is shown in Figure 4.10. The flash began

Side view:

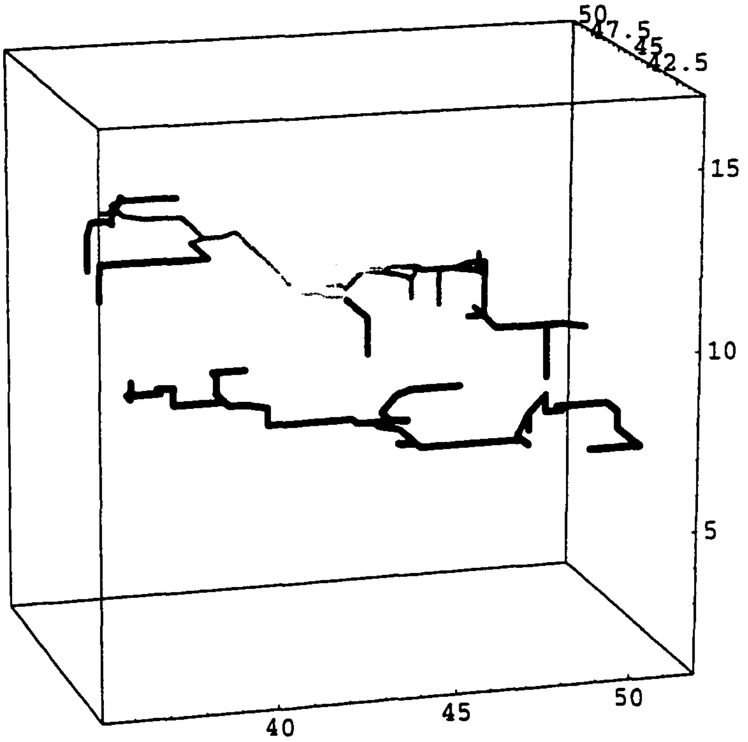

Top view:

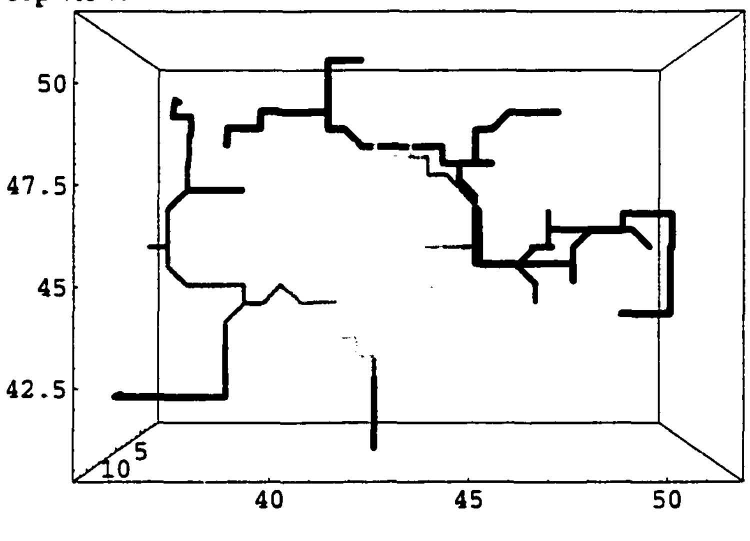

Figure 4.7: A moderate intracloud flash viewed from the side and from above. This flash is from an airmass storm and discharged 21 coulombs. Axes show distance in kilometers within the storm domain. The development of the positive leaders is indicated by blue–dark blue–violet coloring, and green–yellow–orange–red shows the negative leader development. The initial channel segment is not shown, leaving a gap between the positive and negative branches.

Side view:

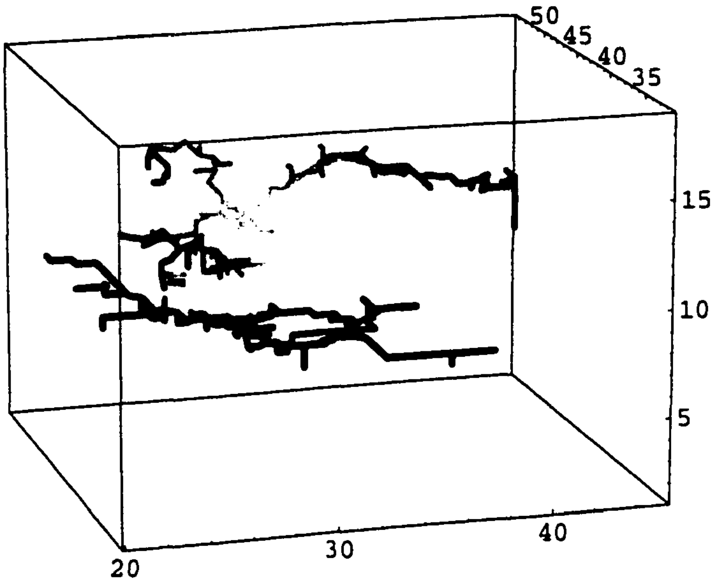

Top view:

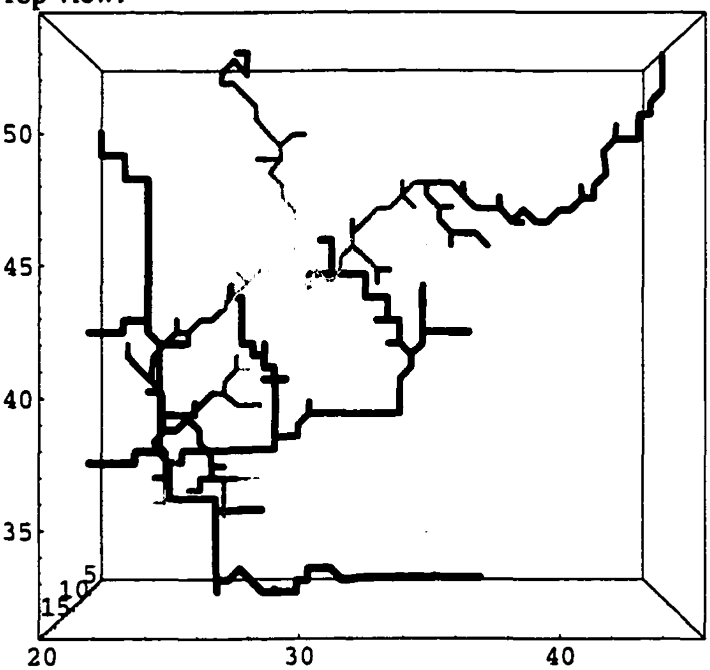

Figure 4.8: A more extensive IC flash from a mature supercell. The flash discharged 48.1 C. The colors are explained in Figure 4.7. Axes show distance in kilometers within the storm domain.

between the main negative region and a lower positive charge region near the base of the updraft. This negative CG occurred in the same simulation as the IC flash in Figure 4.7 and at approximately the same time. The negative, downward-propagating leader has little horizontal extent, though in some cases the horizontal branching is greater. The positive, upward leaders, however, have branching that is nearly exclusively horizontal, as in the IC flashes and in observed flashes (e.g. MacGorman and Rust, 1998).

Some of the supercell simulations produced many positive CG flashes. Figure 4.11 is an example of a fairly extensive positive ground flash. The downward positive leader shows some horizontal branching before connecting to ground. The upward negative leaders branched quite extensively over a 20 km by 20 km area. Some of the negative branches reach into a region of positive charge at the top of the updraft. This CG began downshear of the main updraft, between the main positive charge region and a lower negative region.

An important question to consider is, "What is the difference between IC and CG flashes?" In the SLM, the only physical difference between IC and CG flashes is that CG flashes "happen" to reach the ground. A discussion of the conditions for producing CG flashes will be deferred to Chapter 10. One general observation about both IC and CG flashes is that they appear always to originate between regions of opposite charge. In the model, the electric field magnitude apparently reaches the initiation threshold only at interfaces between charge regions. Figure 4.12 shows lightning branching regions and initiation locations in an east-west plane through two different storms. The slices combine the lightning activity during a 2.5 minutes period, and the lightning is superimposed on the charge density field at the end of the period. The areas of flash initiations (indicated by green outlines) are all located between regions of net positive and negative charge. The positive leaders (blue outlines) propagated into regions of negative charge, and negative leaders (red outlines) propagated into regions of positive charge. Small regions of net charge reversal caused by lightning can be seen in and near the flash volumes.

Side view:

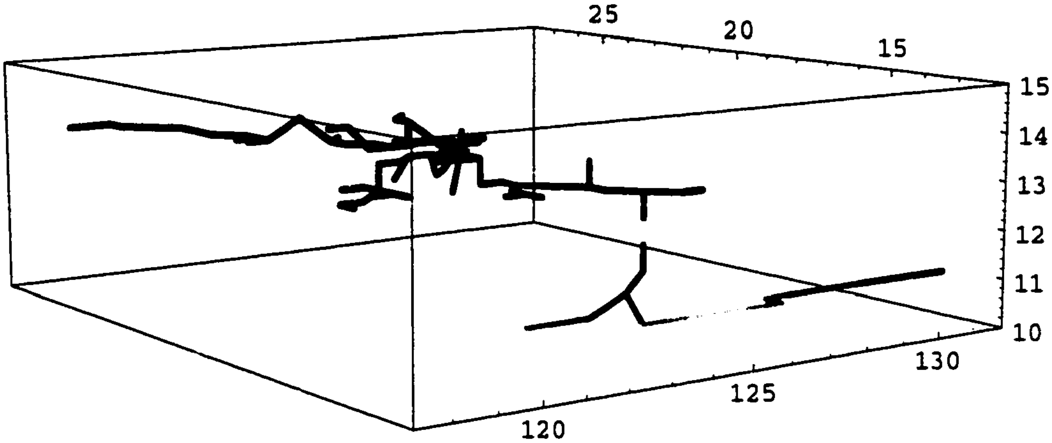

Top view:

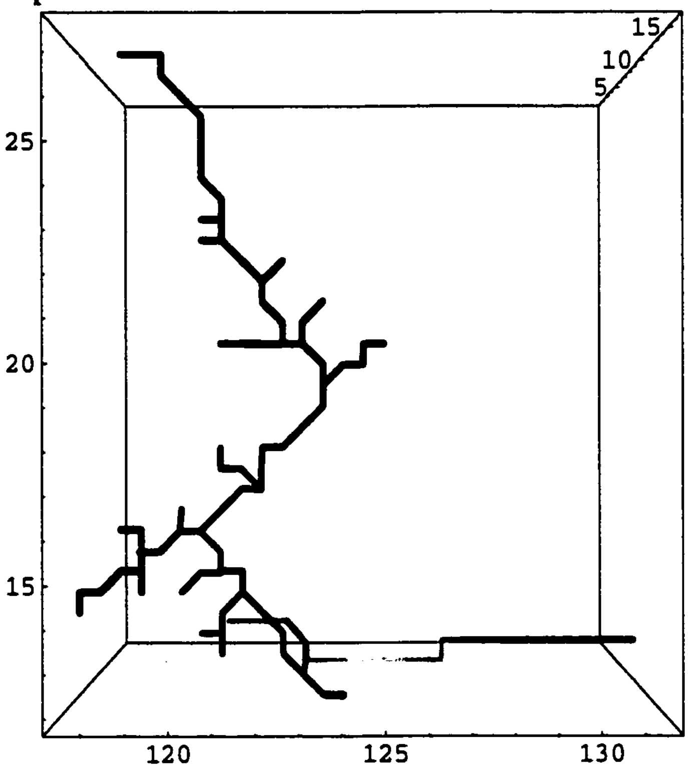

Figure 4.9: A screening layer discharge in a supercell anvil. The colors are explained in Figure 4.7. Axes show distance in kilometers within the storm domain.

Side view:

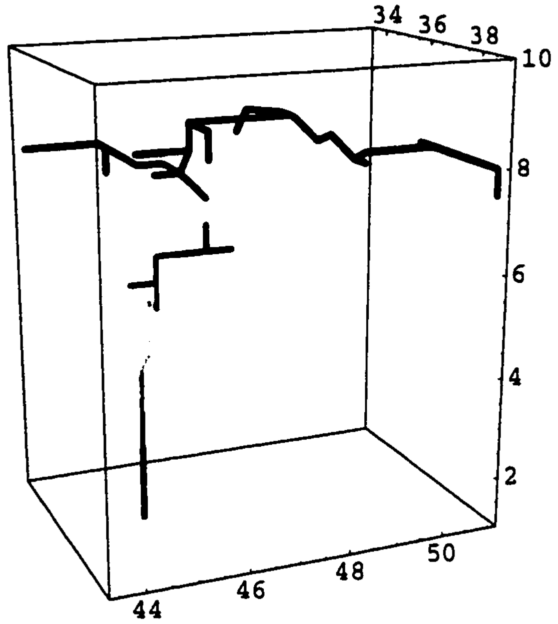

Top view:

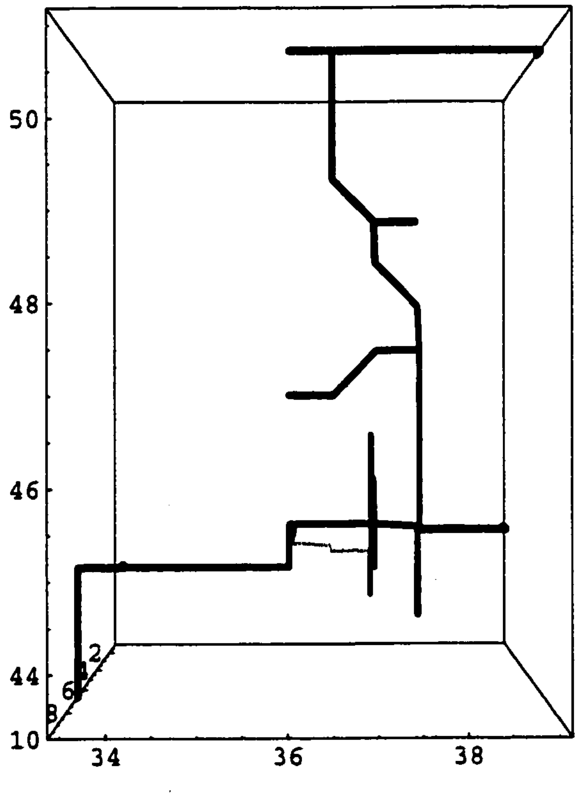

Figure 4.10: A negative CG flash in an airmass storm which lowered -15.8 C to ground. The colors are explained in Figure 4.7. Axes show distance in kilometers within the storm domain.

Side view:

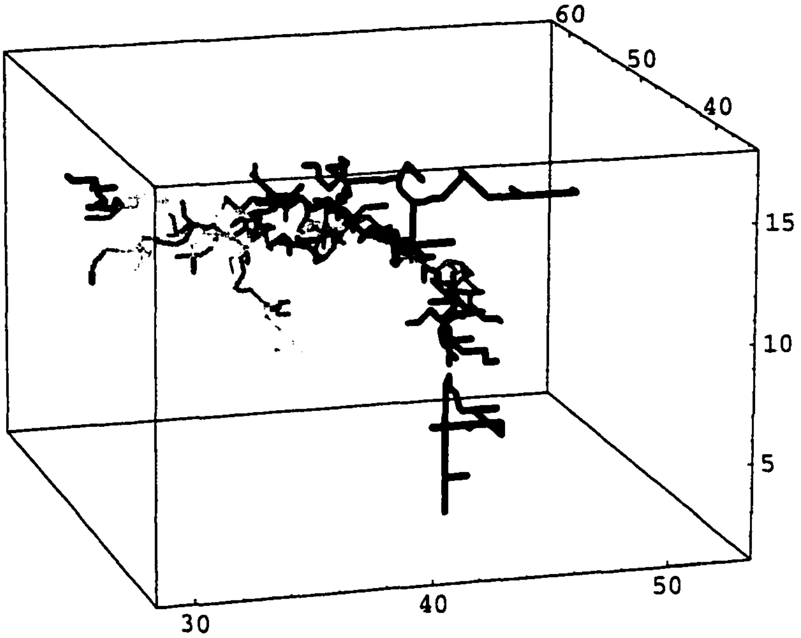

Top view:

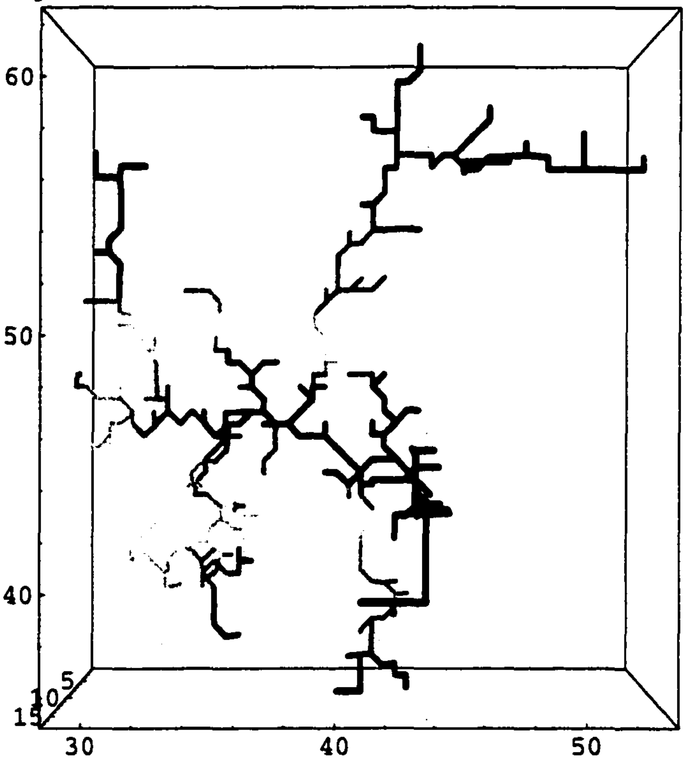

Figure 4.11: A positive CG flash from a supercell simulation. The flash lowered 71.6 C to ground. The colors are explained in Figure 4.7. Axes show distance in kilometers within the storm domain.

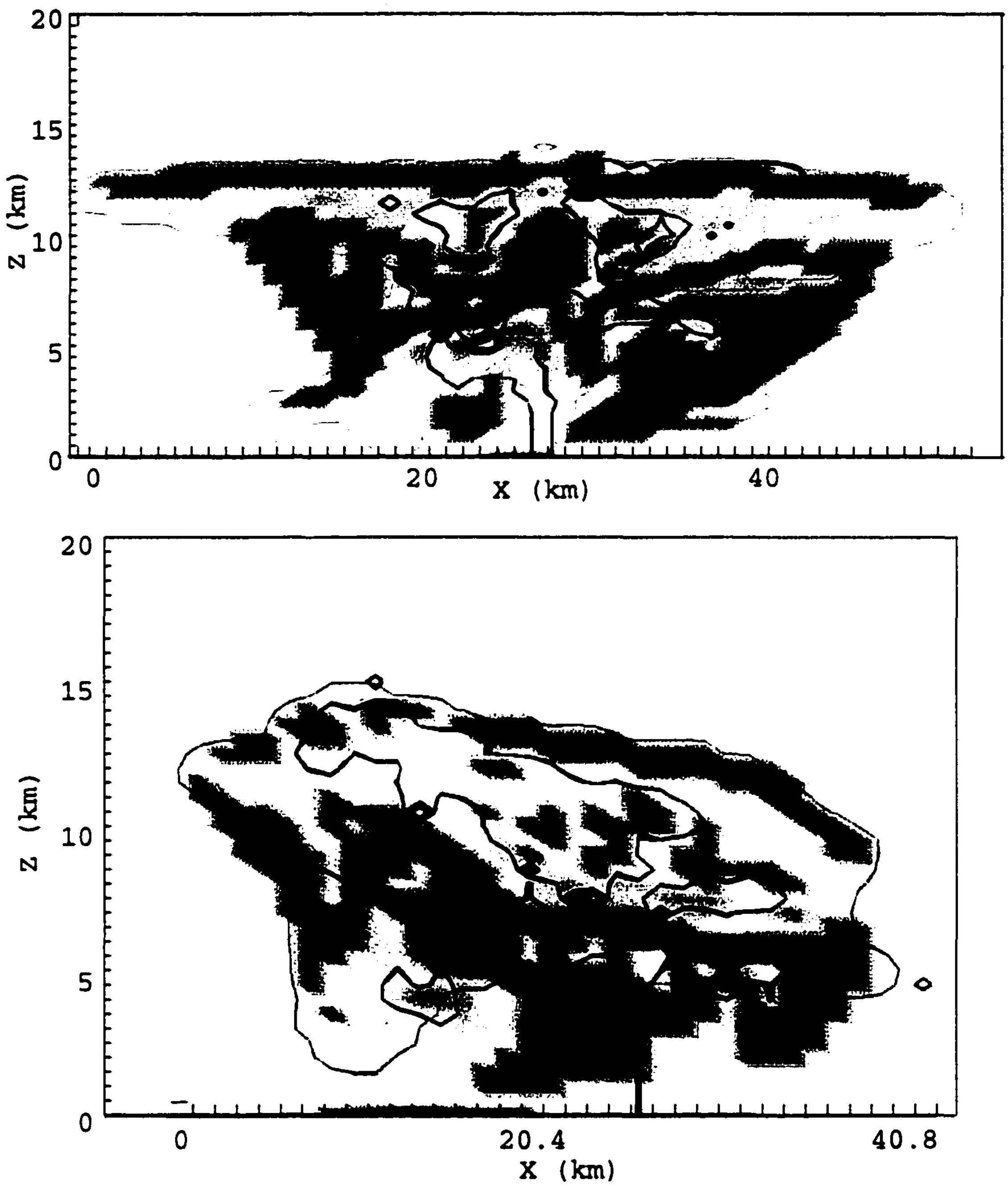

Figure 4.12: Lightning branching regions and initiation locations in east-west planes of two simulated storms. The lightning activity occurred during a 2.5-minute period. Dark blue outlines indicate branching regions of positive leaders, and red outlines show negative leader branching regions. Initiation locations are shown by green contours. Net charge density is indicated by blue (negative) and yellow–orange (positive) solid fill. Both simulations used Gardiner noninductive charging and strong inductive charging. (a) An airmass storm at 62.5 minutes elapsed time with −CG flashes. (b) A supercell storm at 47.5 minutes elapsed time with a +CG flash.

Chapter 5

Case Overview

5.1 Storm Simulation Cases

The eighteen simulations explore various combinations of environment, noninductive charging scheme, and inductive charging strength. Four environments were chosen to produce a range of storm types: an "airmass" storm (weak shear in the horizontal environmental wind with height), a low-precipitation (LP) supercell storm, a classic (CL) supercell storm, and a high precipitation (HP) supercell storm. As discussed in Chapter 1, each supercell type does not refer to a well-defined set of characteristics, but rather to a range of characteristics within the broad spectrum of supercell storms. What is important for this dissertation is not how typical of a particular storm type a simulated storm is, but that the different storm simulations have distinctively different kinematic and electrical characteristics.

All of the simulations were initiated by a warm, moist spheroid within a horizontally homogeneous environment (Weisman and Klemp, 1982). The potential temperature perturbation at the center the spheroid is specified, and the vapor mixing ratio is adjusted to maintain the environmental relative humidity. (The mixing ratio is the ratio of mass of water substance (vapor, rain, hail, etc.) to the mass of air in a given volume. The potential temperature is the temperature a parcel would have if adiabatically expanded or compressed to standard air pressure.) The perturbations reduce toward zero at the surface of the spheroid. The spheroid size was $10 \times 10 \times 1.5$ km except for the classic supercell simulations, which had 12×12 km horizontal radii. The airmass and the HP and LP supercell storms all used analytical thermodynamic soundings following Weisman and Klemp (1982), with a boundary layer vapor mixing ratio of 14 g/kg. All three of these analytical soundings had a Convective Available Potential Energy (CAPE) of about 2200 J/kg. The CL supercell case used an environmental sounding obtained from the vicinity of supercell storms in the Texas panhandle on June 2–3, 1995, and had a CAPE of approximately 3000 J/kg.

The charging schemes were described in Chapter 3. Table 5.1 summarizes the various combinations of parameters. All of the simulations except one used the "breakeven" electric field for lightning initiation (Section 4.3.1).

5.1.1 Airmass and High Precipitation Supercell Storms

The airmass and HP supercell storms used the same temperature and moisture profiles (shown in Figure 5.1) which are the analytical functions used by Weisman and Klemp (1982). Both storm environments used half-circle hodographs (Figure 5.2) with the wind shear confined to the lowest 5 km, as in Weisman and Klemp (1984). The only difference in the environment of the two storms was the arc length of the hodograph: The airmass storm had a shear vector magnitude of $0.2 \times 10^{-2}\,s^{-1}$, and a hodograph arc length (U_s) of 10 m/s. The HP supercell storm had a shear vector magnitude of $1 \times 10^{-2}\,s^{-1}$ and $U_s = 50$ m/s.

The same number of domain grid points were used for the airmass and HP supercell storms. The grid spacing was adjusted according to storm size. For the airmass storm, a domain of $80 \times 80 \times 20$ km was used with a grid resolution of $1000 \times 1000 \times 500$ m. For the HP supercell storm a wider domain was used ($94 \times 94 \times 20$ km) with coarser resolution ($1200 \times 1200 \times 500$ m). The warm moist spheroid used to initiate both storms had a potential temperature perturbation of 1.5 K.

All four storm environments were used to compare the electrification resulting

Table 5.1: List of model runs with charging options.

Environment	Run Name	Noninductive Scheme[a]	Inductive strength[b]
Airmass	wk20b	RR	moderate
	wk20c	RR	strong
	wk21a	Gard.	moderate
	wk21c	Gard.	strong
	wk21d[c]	Gard.	strong
	wk22a	Taka.	moderate
	wk22c	Taka.	strong
HP Supercell	wk30e	RR	strong
	wk30f	RR[d]	strong
	wk31e	Gard.	strong
	wk32e	Taka.	strong
LP Supercell	lp00a	RR	strong
	lp02a	Gard.	strong
	lp01a	Taka.	half-strong
Classic Supercell	jun2a	RR	moderate
	jun2f	RR	strong
	jun2c	Gard.	strong
	jun2e	Taka.	moderate

[a]Riming Rate (RR), Gardiner (Gard.), or Takahashi (Taka) as in Chapter 3.

[b]"moderate" settings: $E_r = 0.007$, $\langle\cos\theta\rangle = 0.2$
"strong" settings: $E_r = 0.015$, $\langle\cos\theta\rangle = 0.5$
"half-strong" settings: $E_r = 0.007$, $\langle\cos\theta\rangle = 0.5$

[c]Used constant E_{init} instead of breakeven.

[d]Enhanced RR: uses median-volume diameter D_o instead of characteristic diameter ($\mathcal{D}$) for crystal/snow size.

from each of the three noninductive charging parameterizations, but the airmass storm environment was used also to examine the sensitivity of electrification to two other changes: First, it was used to test the effect of "moderate" ($E_r = 0.007$, $\langle\cos\theta\rangle = 0.2$; see Section 3.3) versus "strong" ($E_r = 0.015$, $\langle\cos\theta\rangle = 0.5$) inductive charging. Second, this environment was used to compare the effects of using a uniform threshold for lightning initiation versus the breakeven (height-varying) electric field.

One of the HP supercell runs tested a variation of the strength of the 'riming rate' noninductive charging scheme (Chapter 3). This particular run used the median volume

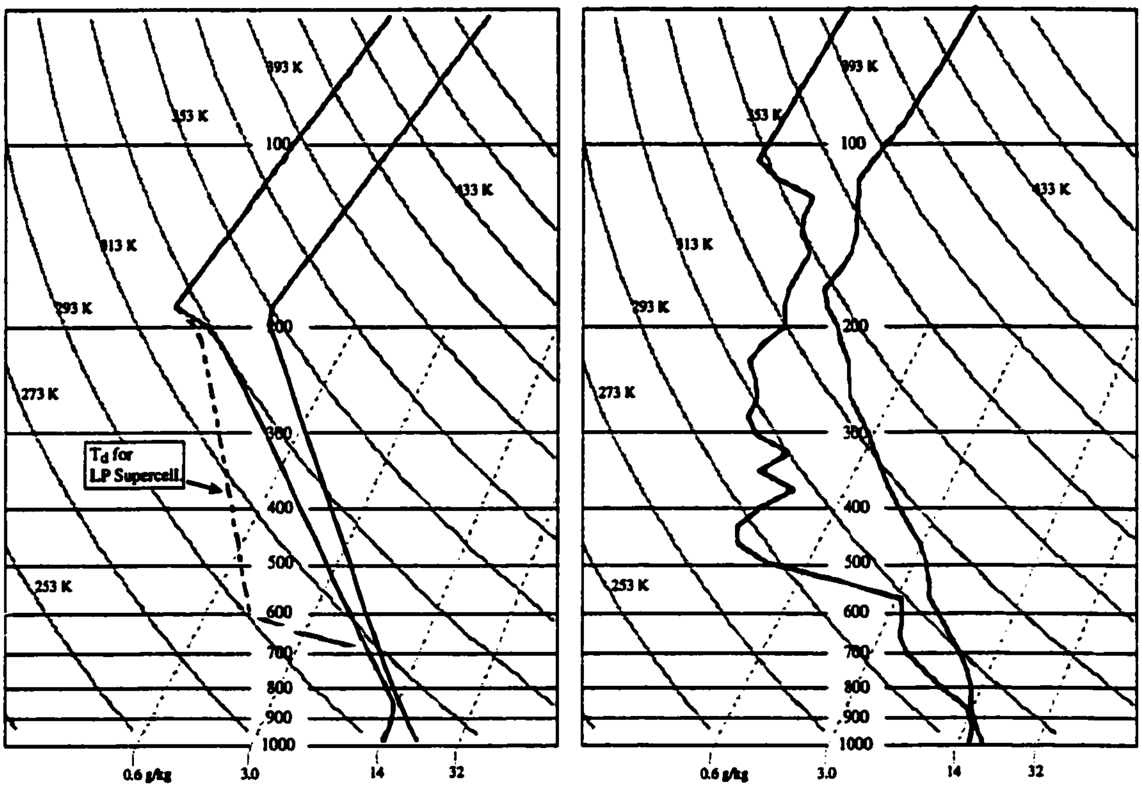

Figure 5.1: Skew-*T* diagrams of temperature and moisture (dewpoint temperature T_d) soundings of the storm simulation initial conditions. Dashed sloping lines from lower left to upper right are constant vapor mixing ratio, and the gray curves from lower right to upper left are dry adiabats. Left: Airmass and HP and LP supercell storms. LP storm differs only in the moisture profile (heavy dashed line). Right: Classic supercell (composite sounding).

diameter D_o to represent the sizes of snow aggregates and cloud ice crystals instead of the characteristic diameter ($\mathcal{D}$). By definition, the particles with $D < D_o$ account for half of the net volume of the hydrometeor category. The median volume and characteristic diameters are related by $D_o = 3.67\mathcal{D}$. This difference is important to the riming rate scheme, because a larger crystal size results in greater charge separation per collision.

5.1.2 Low Precipitation Supercell

The LP supercell environment is distinguished from the HP environment in two respects. The first is the wind shear profile, shown for the LP environment in Figure 5.3. This hodograph was constructed by Straka based on the results of a study of isolated supercells by Rasmussen and Straka (1998) and ongoing numerical modeling work (J. Straka,

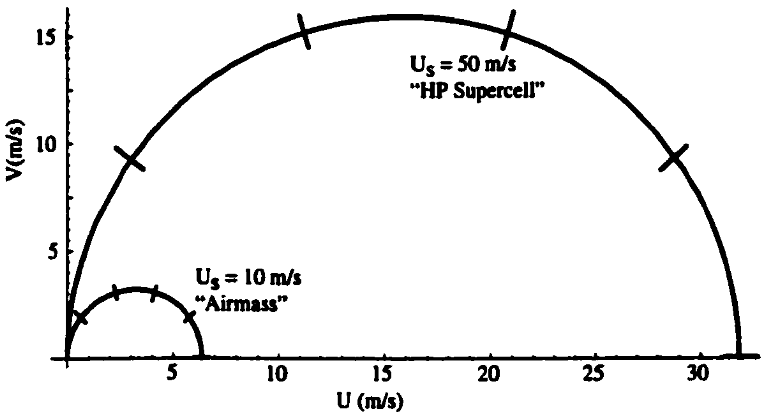

Figure 5.2: Hodographs for airmass and HP supercell storms. These hodographs show the 0–5 km winds. Winds remain constant above 5 km (i.e. maintain 5 km values). Tick marks indicate 1 km height intervals. (Weisman and Klemp, 1984).

personal communication). Whereas the HP environment has no wind shear above 5 km, the LP hodograph has very strong 5–10 km shear. The second difference is the moisture profile, which has reduced relative humidity above 3 km. The drier air aloft is more typical of the dryline environment where many LP storms form. (LP storms have also been called "dryline storms.") The temperature profile for the LP cases (Figure 5.1) is the same as for the airmass and HP supercell cases.

A larger domain size (100 × 140 × 20 km) was used for the LP storm simulations because of the elongated anvils produced in the highly sheared environment. The vertical resolution was 500 m, as in all the simulations, but the horizontal resolution was 1500 m. The bubble temperature perturbation was 2.5 K, an increase over the HP supercell and airmass cases. The higher bubble temperature helped the initial storm to survive in the highly sheared environment.

5.1.3 Classic Supercell

The storm case that we have labeled as a classic supercell used an environmental sounding from the Texas panhandle on June 2, 1995, during the VORTEX field program (Verifications of the Origins of Rotation in Tornadoes Experiment, Rasmussen et al., 1994). Storms on that day produced several tornadoes, including one that passed through

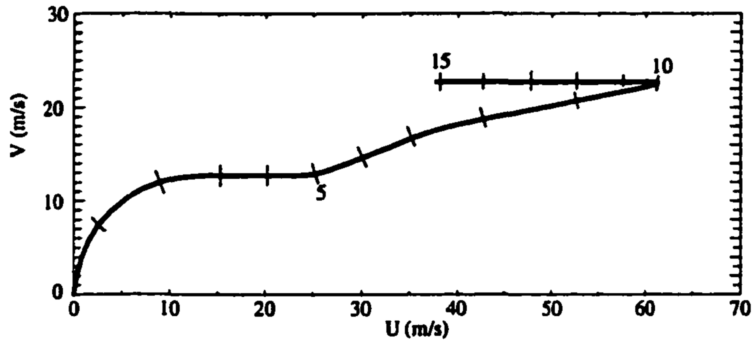

Figure 5.3: Hodograph of horizontal wind for the LP supercell storm. The tick marks along the curve indicate 1 km height intervals.

Dimmitt, Texas. The sounding used here (Figures 5.1 and 5.4) is from Gilmore (2000) who created a composite from two environmental soundings. Data for the low levels (0–4.3 km) were from a sounding at Floydada, Texas, and data for the upper levels (above 4.3 km) were from a sounding at Lubbock, Texas. Gilmore (2000) performed numerical simulations with this and other soundings for comparison with observations. He also analyzed lightning observations for several of the storms that occurred on this day, and this analysis could be used for comparisons in a future electrification modeling study. Unfortunately, more than a cursory comparison of our model results with observations is beyond the scope of this research project.

The classic supercell used the largest domain of all the cases ($140 \times 140 \times 22.5$ km) and had a horizontal resolution of 1500 m and a vertical resolution of 500 m. A larger bubble perturbation temperature (4.5 K) and size ($12 \times 12 \times 1.5$ km) were used to sustain the initial convection.

5.2 Analysis Methods

Such a large set of thunderstorm simulations had a considerable amount of output to be processed and interpreted. The simulations are presented in separate chapters according to storm type (airmass, HP supercell, LP supercell, and CL supercell). For each storm type the general characteristics of the storm are discussed first, and then the versions with

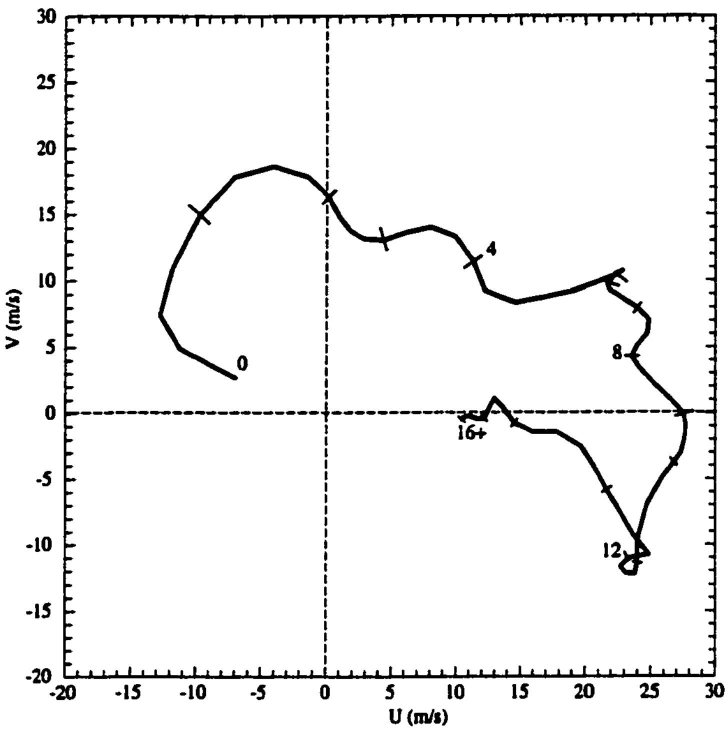

Figure 5.4: Hodograph of horizontal wind for the classic supercell storm. The tick marks along the curve indicate 1 km height intervals.

different noninductive charging parameterizations are discussed individually. Analysis of the simulation results was greatly facilitated by three-dimensional visualizations using the Vis5D software package.

A number of plots and figures were devised to present the simulation results. Within each chapter there are figures showing the lightning activity and the charge structure relative to the cloud boundary at particular times. Further figures show vertical distributions of lightning channel segments and time-histories of lightning activity and charging. Contour plots of lightning activity versus height and time are found in Appendix A, and histograms of discharge magnitudes are grouped together in Appendix B to facilitate comparisons among the many cases. Each of the figure types are described below in greater detail. Although an effort has been made to keep consistent scales, care should be taken to when comparing plots since the scales can vary from storm to storm. (One of the simulations was run very recently, so only the time-history plots were generated because of time constraints.)

5.2.1 Lightning Composites

The lightning composites shown for each case are snapshots from the visualization program. The composites show the extent of lightning activity during a 2.5 minute time period at a time when the storms are mature but still fairly well contained within the domain. Surface contours of cloud water and cloud ice outline the cloud. The regions containing positive and negative leaders are contoured separately. Since the leaders propagate preferentially into charge regions, the leader contours also serve as a rough indication of a storm's charge structure, with positive leaders indicating negative charge regions and vice versa. The highest densities of lightning channels generally were found in the convective regions, where charge separation was most active. Lightning in the anvil regions, by contrast, tended to be much less dense but occurred over a larger region.

5.2.2 Charge Density Contour Plots

The contour plots of charge density show one or two slices through the storms and were selected to highlight as many features as possible. The charge structures can be quite complex and can evolve rapidly, especially in the updraft regions. For all of the supercell storms, the charge slices are taken at about the same time as the lightning composites. The supercell storms all have two slices: one parallel to the anvil and another that is nearly perpendicular to the first slice and cuts through the updraft region(s). Vertical dashed gray lines indicate where the two slices intersect. All of the charge density plots use gray solid fill to indicate regions of charge density more negative than $-0.15\,\mathrm{nC\,m^{-3}}$. Contour intervals are always $0.3\,\mathrm{nC\,m^{-3}}$. Maximum and minimum charge densities for the particular contour slice are given in units of $\mathrm{nC\,m^{-3}}$.

5.2.3 Lightning Channel Segments and Lightning Initiations Histograms

For each storm, a nine-panel figure displays histograms of lightning channel segments and initiations as a function of height and summed over the duration of the simulation. (One case was run out to 120 minutes, but only 105 minutes were used for the totals, as in all the other cases.) These histograms give some idea how the simulated lightning might appear to different lightning mapping systems. Acoustic mapping is presumably equally responsive to both the positive and negative lightning leaders (e.g. MacGorman et al., 1981). Lightning mappers that detect lightning-produced VHF electromagnetic noise, however, respond preferentially to the negative leaders (Shao and Krehbiel, 1996), which have much more impulsive breakdown than the positive leaders. Thus the histogram of negative leader channel segments shows what might be seen by a VHF lightning detection system.

The histograms for total segments were also decomposed into histograms for "convective" and "anvil" regions. Delineation of the convective region was made rather crudely by estimating a horizontal box that encompassed the main graupel volume. Any activity outside the box was considered to be in an 'anvil' region. The same box was applied to both the channel segments and lightning initiation locations. Another histogram also shows the total charge deposited by lightning. The deposited charge is the sum of the absolute values of charge carried by positive and negative channels in each altitude bin.

5.2.4 Time-Series Plots

Three time-series plots are shown in a second figure. The first plot shows the intracloud flash rate and domain maxima of updraft speed and electric field magnitude. Updraft speed and electric field are sampled at one minute intervals. The electric field maxima are the values just after the charge separation calculations and before lightning flashes. The IC flash rates are simply one-minute totals (i.e. flashes per minute). The second plot again shows IC flash rate along with graupel charging rates. The charging rates are the domain-integrated totals for positive charging of graupel/hail by all noninductive (NONIp) and inductive (INDp) charging interactions and for negative charging of graupel/hail (NONIn and INDn). The third plot displays CG flash rates (positive and negative; one-minute totals) with the net charge in the domain (excluding the corona layer). Note that the net charge of the domain sums over all of the storms that are present. A storm-by-storm net charge analysis has not yet been attempted.

5.2.5 Lightning Activity by Altitude and Time

These contour plots, grouped together in Appendix A, give a rough idea of the time evolution of the simulated lightning activity as a function height. Each figure has two contour plots: The first shows total lightning channel segments as a function of altitude and time, and the second has lightning initiations by height and time. The channel segments and initiation points were summed for each model level (0.5 km thick) over time-intervals of 2.5 minutes (i.e. values are 2.5-minute totals).

5.2.6 Lightning Discharge Magnitude Distributions

Appendix B has histograms of IC and CG discharge magnitudes. The discharge magnitude is the amount of charged transported by a flash. The histogram bins are always five coulombs wide (i.e. 0–5 C for the first bin, 5–10 C for the second, etc.). The IC histograms are plotted on a logarithmic vertical axis. No CG histogram was created for those few cases that had only one or two CG flashes. Furthermore, when a storm had many CG flashes of one polarity, but only a few of the opposite sign, only the dominant polarity CG flashes were included.

Chapter 6

Airmass Storm Simulations

6.1 General Characteristics of the Airmass Storms

The environment used for the airmass storm simulations had low wind shear, so the updraft grew rapidly and had very little tilt. The updraft exhaust was fairly symmetric, though the weak shear slightly favored output toward the southeast. The anvil extended a little farther east and south than north or west. The volume of strong precipitation (>5 g/kg) stayed within a 20 km by 20 km horizontal region. The initial surge of high cloud water mixing ratios (>1.3 g/kg) faded by about 45 minutes, and about 10 minutes later the updraft split. Then at about 57 minutes there was a new growth of cloud water, which increased in volume until about 65 minutes. Two small precipitation cores were apparent by 90 minutes. Surface clouds formed along the nearly circular gust front, and the cells remained close to each other in a 25 km by 25 km region. The anvil reached the eastern domain boundary by 75 minutes and was exiting all sides by 90 minutes.

In all of the airmass storm simulations, a significant fraction of lightning activity occurred in the electrical screening layers of the anvil. The anvil lightning did become restricted during the last ten minutes of the simulations, as the anvil propagated out of the domain. The vertical distributions of lightning segments for these cases all exhibited a strong peak at an altitude of about 13 km, indicating extensive horizontal branching in thin charge layers (Figures 6.5, 6.7, 6.9, 6.11, 6.13, 6.15, and 6.17). The height-time contours in Figures A.1–A.7 (Appendix A) reveal that the high-altitude lightning becomes evident sometime after an hour and generally dominates the overall lightning activity by the end of the simulations.

In addition to testing sensitivity to the three noninductive charging parameterizations, the airmass storm was used to test the effect of varying inductive charging strength for rebounding graupel-droplet collisions with each of the three noninductive schemes. An additional test changed the lightning initiation threshold (see Section 6.5 below). The main effect of increasing the inductive charging from moderate to strong was a dramatic enhancement of the lower positive charge region. Figure 6.3 shows representative slices of charge density for the simulations with moderate inductive charging. Of the moderate induction cases, only the Takahashi case exhibited much of a lower positive charge region (see section 6.4). Contour plots for the strong induction cases (Figure 6.4) show charge densities at the same model time, and the lower positive charge is significantly intensified in the lower part of the updraft for all three noninductive parameterizations. Note that the surrounding negative charge regions are also enhanced by the lofting of negatively charged cloud droplets.

The effect of an enhanced lower positive charge on the lightning is evident from a comparison of Figures 6.1 and 6.2. With moderate induction and a weak lower positive charge, the electric field magnitnde rarely, if ever, reached the lightning initiation threshold underneath the main negative charge region. Thus, the cases in Figure 6.1 produced little or no lightning (IC or CG) beneath the main negative charge region. With the strong inductive charging and a strong lower positive charge, however, the cases in Figure 6.2 had significant IC and −CG lightning activity between the main negative and lower positive charge regions.

Another interesting general feature of these simulations is that the storms developed a net negative charge before −CG flashes commenced. Krehbiel (1986) suggested that a build-up of net negative charge in a storm would lead to negative ground flashes. In the model simulations, a net negative charge may indeed be a necessary condition, but it is certainly not a sufficient condition for −CG lightning. For example, compare Figures 6.6c and 6.8c. In the former case, the net charge was even more negative than in the latter, yet no CG flashes occurred. The converse may also apply: The few +CG flashes produced by the airmass storms occurred when the net charge in the domain was positive (e.g. Figures 6.10c and 6.12c).

6.2 'Riming Rate' Noninductive Charging

6.2.1 'Riming Rate' With Moderate Inductive Charging

The initially high cloud water contents and high rime accretion rates resulted in positive charging of graupel in the riming rate noninductive parameterization. The initial positive charging is seen in Figure 6.6b at about 20 minutes. Consequently, the initial charge structure was an 'inverted-polarity' ('negative') dipole (negative over positive charge). The first IC flashes occurred high in the storm in the inverted dipole. By 28–30 minutes, the structure switched to a 'normal-polarity' ('positive') dipole. A weak lower positive charge developed, but it was never involved in any lightning activity. No cloud-to-ground flashes were produced (Figure 6.6c).

The first IC flashes involving the upper negative screening layer occurred around 47 minutes on the eastern side of updraft (the usual location for the first screening layer discharge in the airmass storms). The rear (westward) anvil had a negative screening layer on its underside, but little on its top (Figure 6.3a), possibly because the positive charge densities were smaller than in the forward anvil and convective region. Later in the simulation (after 75 minutes elapsed time), a positive charge layer appeared below the negative screening layer under the forward (southeast) anvil. The new layer was the result of positively charged snow falling out beneath the cloud ice, which carried the screening layer charge.

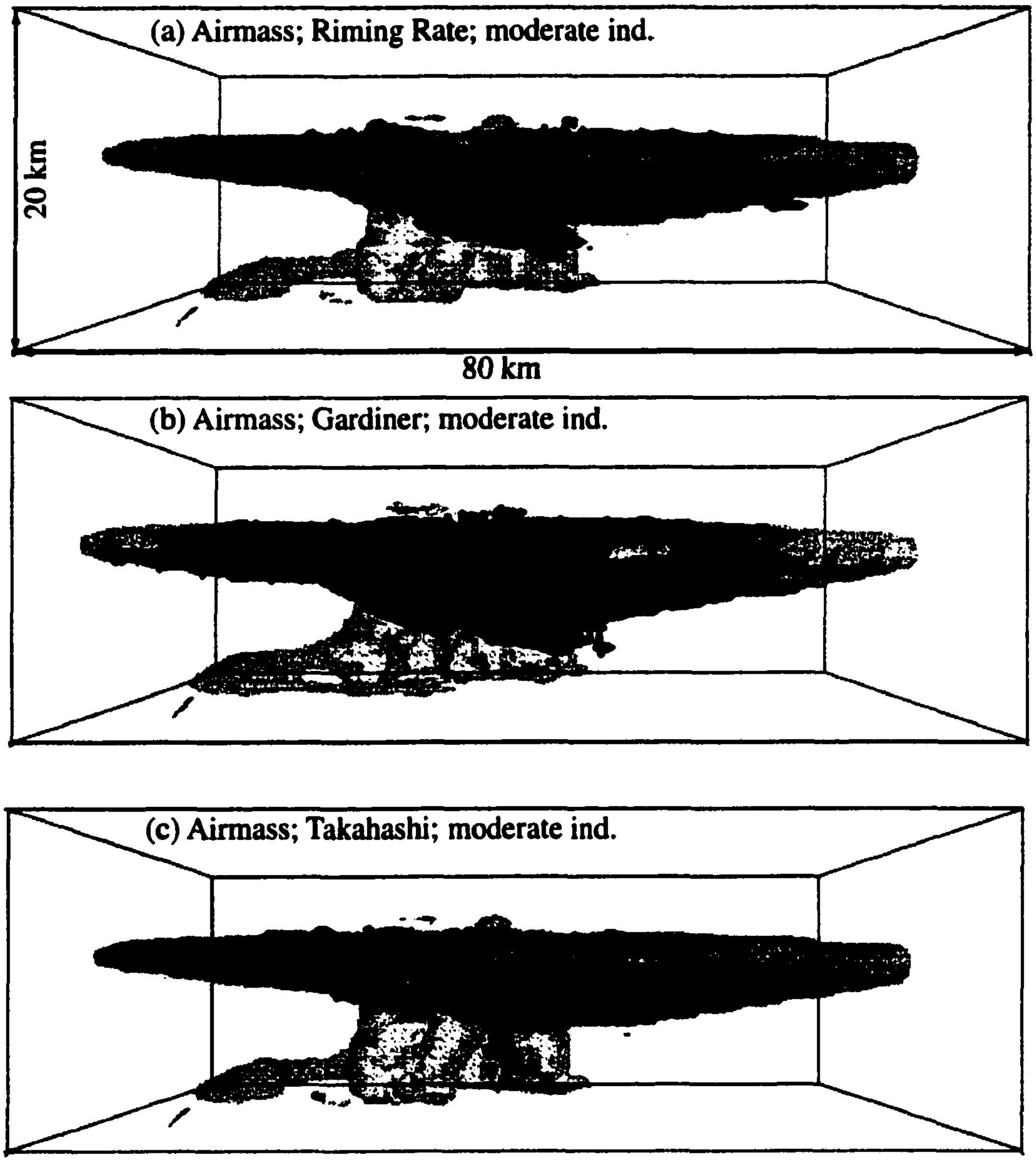

Figure 6.1: Airmass storm lightning composites for three noninductive parameterizations with 'moderate' inductive charging. The view is from the south at 85 minutes elapsed time. Contours outline lightning channels occurring over a 2.5-minute period. Negative leaders are colored orange, and positive leaders are blue. Cloud ice and cloud water contours are gray and yellow, respectively. Green contours indicate where lightning flashes were initiated.

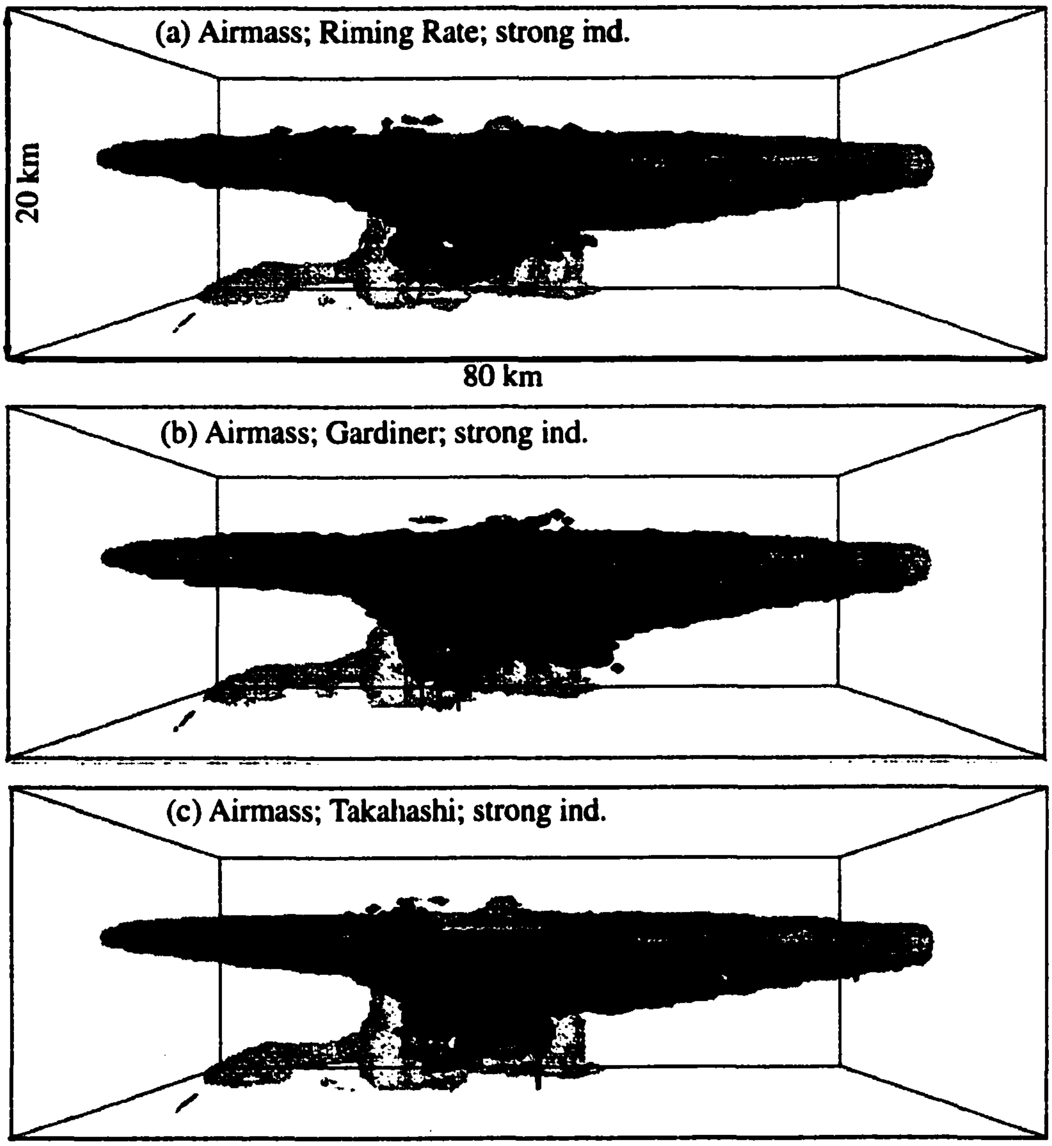

Figure 6.2: Airmass storm lightning composites for three noninductive parameterizations with 'strong' inductive charging. The view is from the south at 85 minutes elapsed time. Contours outline lightning channels occurring over a 2.5-minute period. Negative leaders are colored orange, and positive leaders are blue. Cloud ice and cloud water contours are gray and yellow, respectively. Green contours indicate where lightning flashes were initiated (missing from panel b).

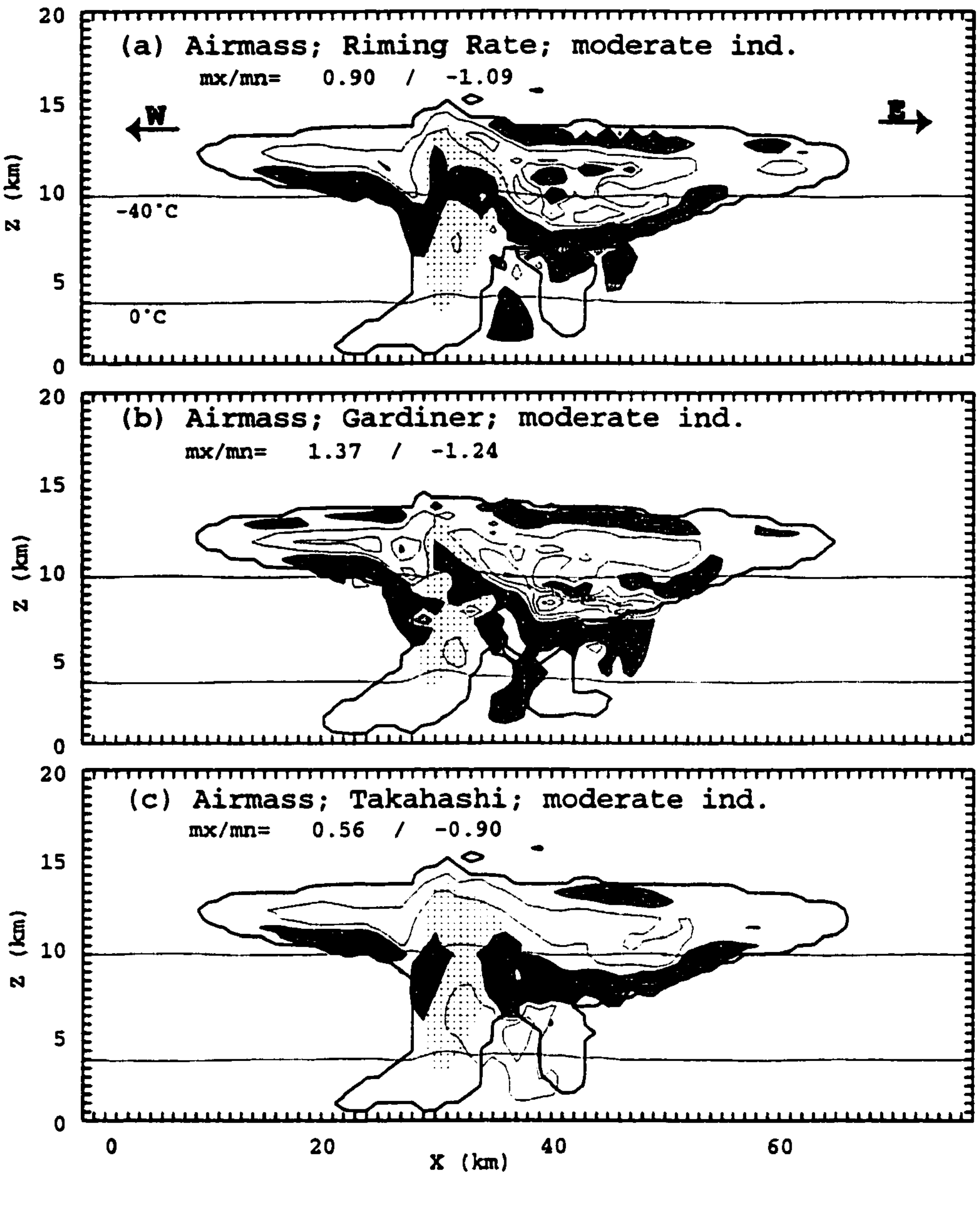

Figure 6.3: Charge density contours for the airmass storms with moderate inductive charging. The east-west slices are taken through the middle of the domain and are viewed from the south at a time of 55 minutes. Negative charge regions are gray. Contour intervals are 0.3 $\mathrm{nC\,m^{-3}}$, starting at ± 0.15. The heavy line outlines the cloud boundary (not including precipitation). Dotted regions indicate updraft of 10 m/s or greater. Maximum and minimum values for the charge slice are given in each panel in $\mathrm{nC\,m^{-3}}$.

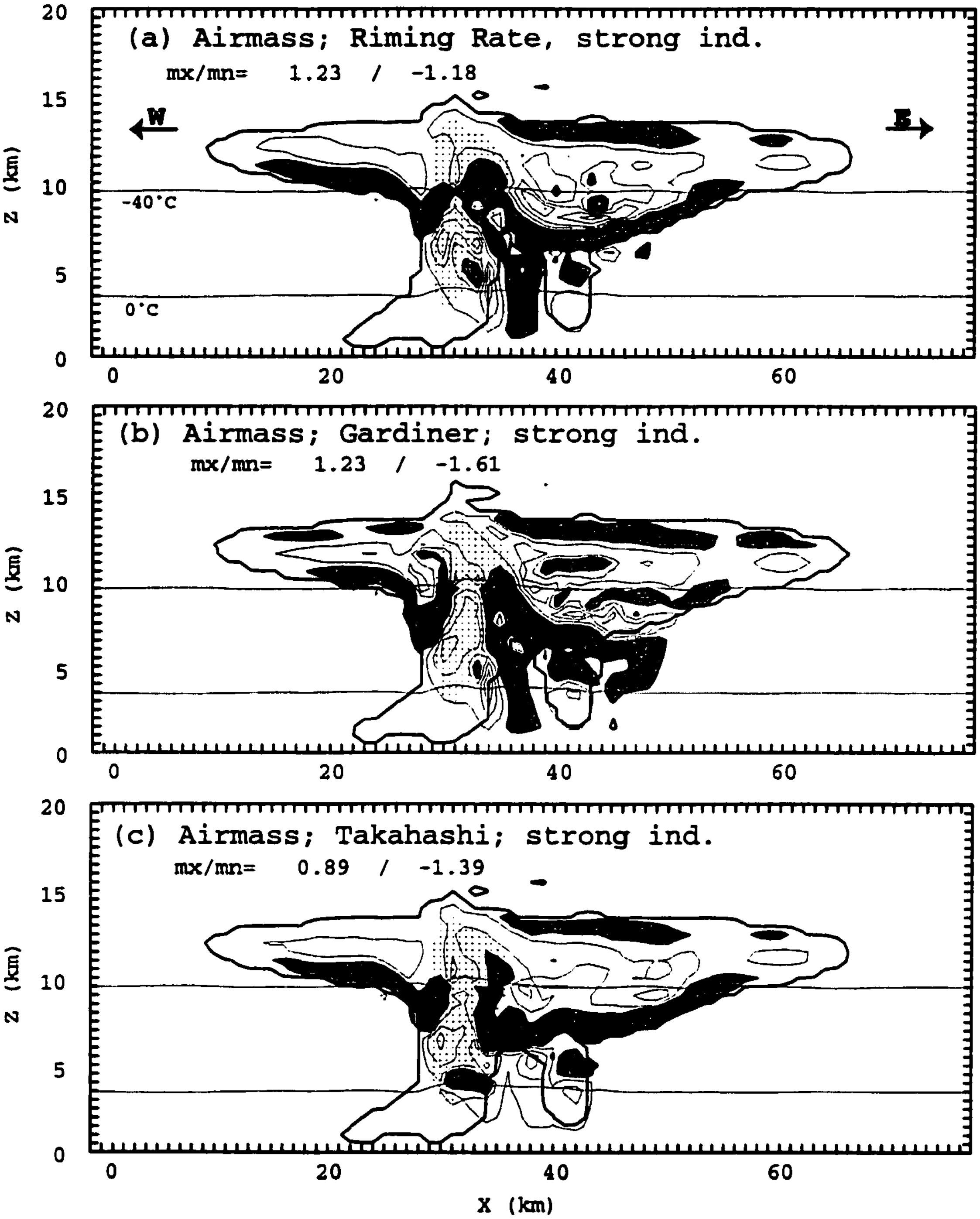

Figure 6.4: Charge density contours for the airmass storms with strong inductive charging. Plot details are the same as in Figure 6.3.

6.2.2 'Riming Rate' With Strong Inductive Charging

With strong induction, the initial charge structure was again an inverted dipole, and the initial intracloud flashes again reflected the inverted vertical charge structure. (Note the initial positive charging of graupel again in Figure 6.8b.) The inductive charging, however, produced a lower *negative* charge region which was involved in some IC flashes. As the rime accretion rates decreased and caused the noninductive charging to switch to mostly negative charging of graupel, the lower negative charge quickly disappeared and was replaced by a lower positive charge. By about 30 minutes, the gross charge structure was a so-called 'tripole', with main positive and negative regions plus a strong lower positive charge. The main difference in the charge structure compared with the moderate induction case was the strong lower positive charge produced in the strong induction case. Only a weak lower positive charge developed in the moderate induction case.

The strong lower positive charge promoted both IC and −CG flashes involving the main negative charge region. As a result, lightning flash rates were larger in the case with strong induction (Figure 6.8a) than in the case with moderate induction (Figure 6.6a) throughout most of the simulation. Even so, the riming rate case with strong induction had fewer −CG flashes than any of the other airmass simulations using strong inductive charging. Also, the CG ground strike points tended to be closer to the low-level precipitation core than in the other cases. Unlike the Gardiner and Takahashi storms with strong induction (discussed next), which had steady or increasing average −CG rates for the last half-hour of simulation, the riming rate case had no CG flashes during the final 20 minutes. There was, however, continued IC activity involving the lower positive charge.

The charge contour slices for both the moderate and strong induction cases (Figures 6.3a and 6.4a) show pockets of negative charge within the positive charge region in the eastern anvil near the −40°C isotherm. These pockets are the result of charge deposited by lightning. In Figure 6.4a there are similar reversals within the lower positive charge and nearby main negative charge regions as a result of IC lightning activity

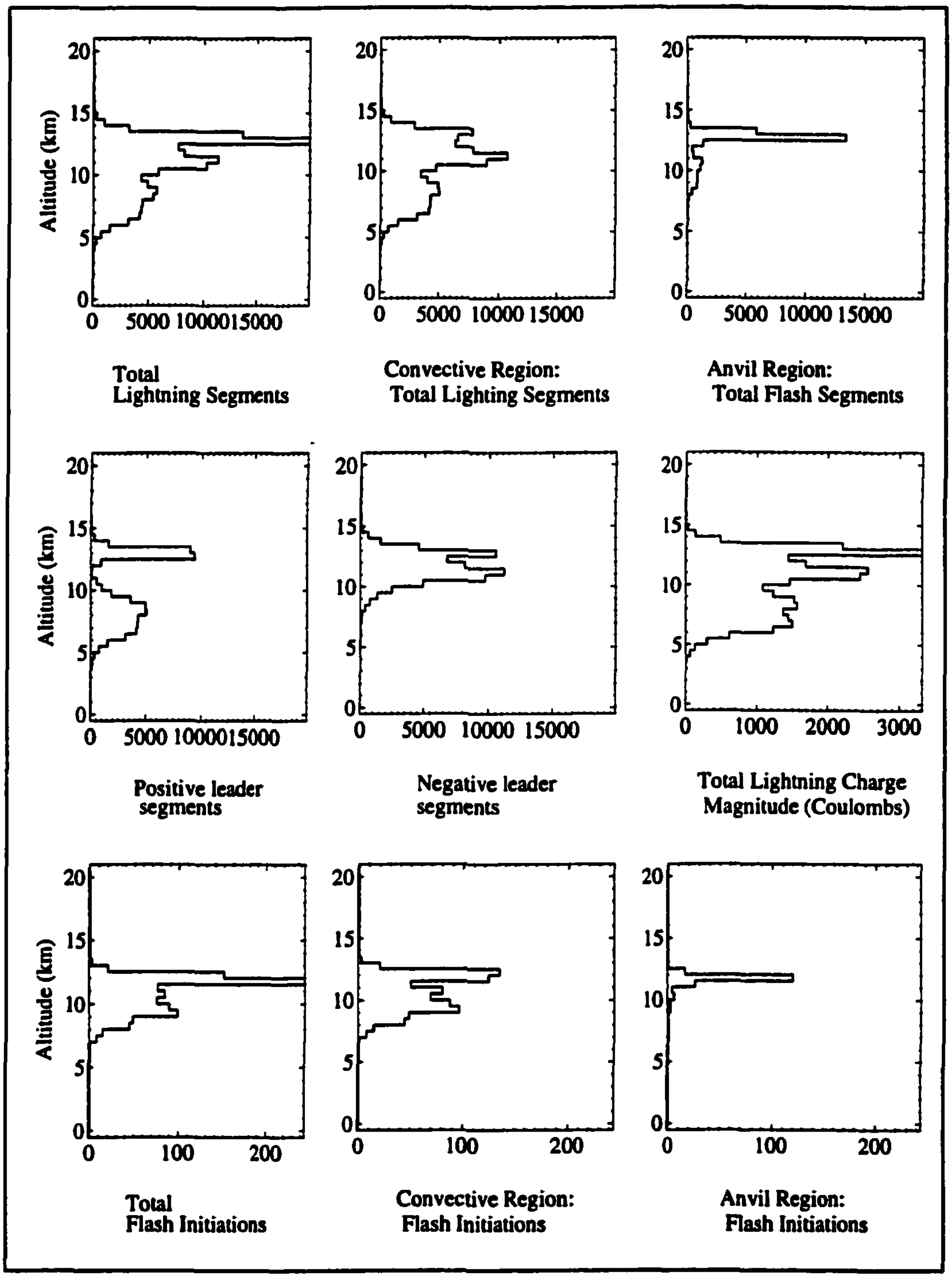

Figure 6.5: Total lightning channel segments and initiations versus height: airmass, riming rate, moderate induction. Values are integrated up to 105 minutes simulation time. Lightning segments are split into positive and negative leaders or into convective and and anvil regions. Total charge is sum of absolute values of charge deposited by lightning.

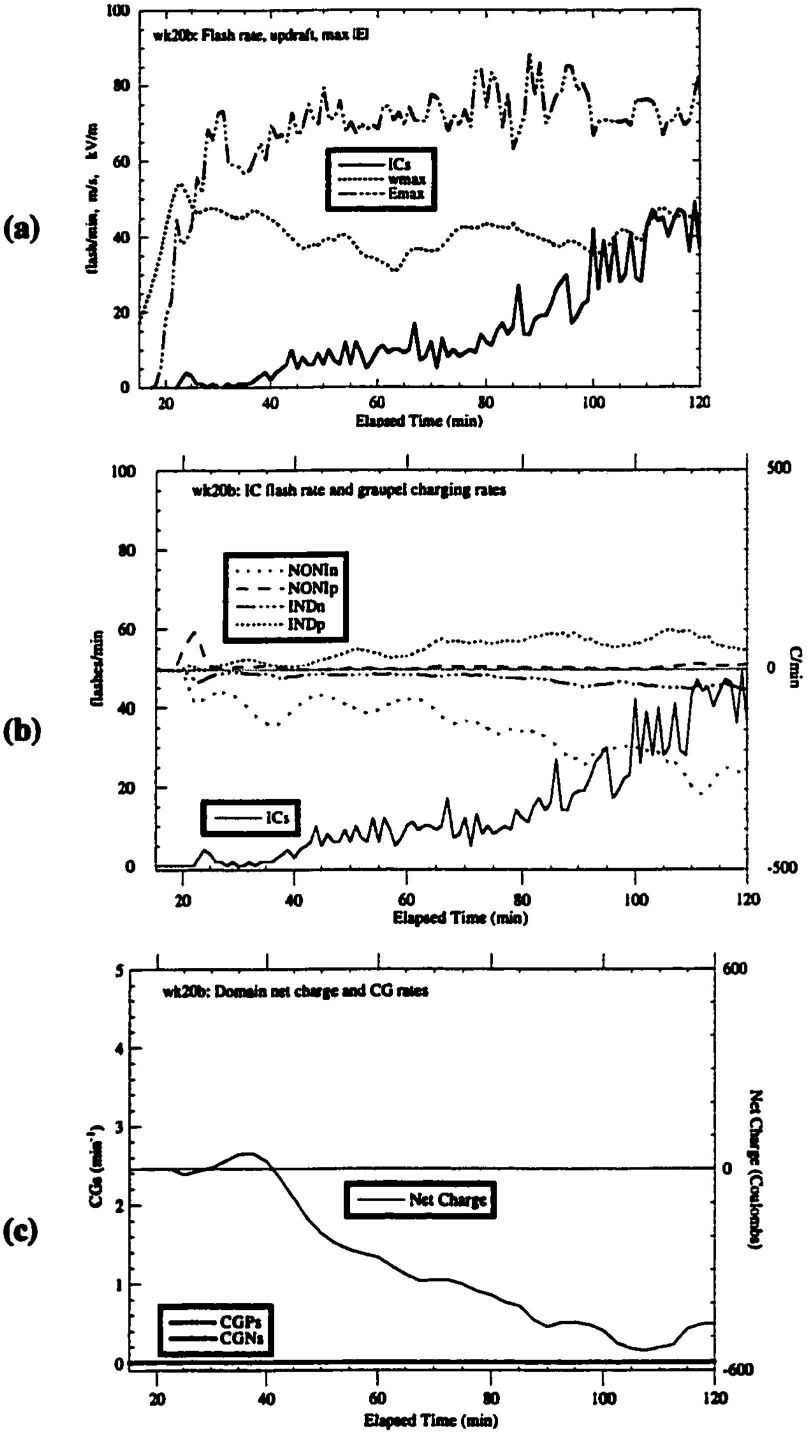

Figure 6.6: Lightning time series plots: airmass, riming rate, moderate induction. (a) IC flash rate (min^{-1}), maximum updraft, and maximum electric field magnitude at one-minute intervals. (b) Domain-integrated graupel charging rates (C/min), positive and negative values of noninductive (NONIp, NONIp) and inductive (INDp, INDn) are summed separately. (c) Domain net charge and CG flash rates. All values are sampled at 1-minute intervals except domain net charge, which has 2.5-minute intervals. (Flash rates are 1-minute totals.)

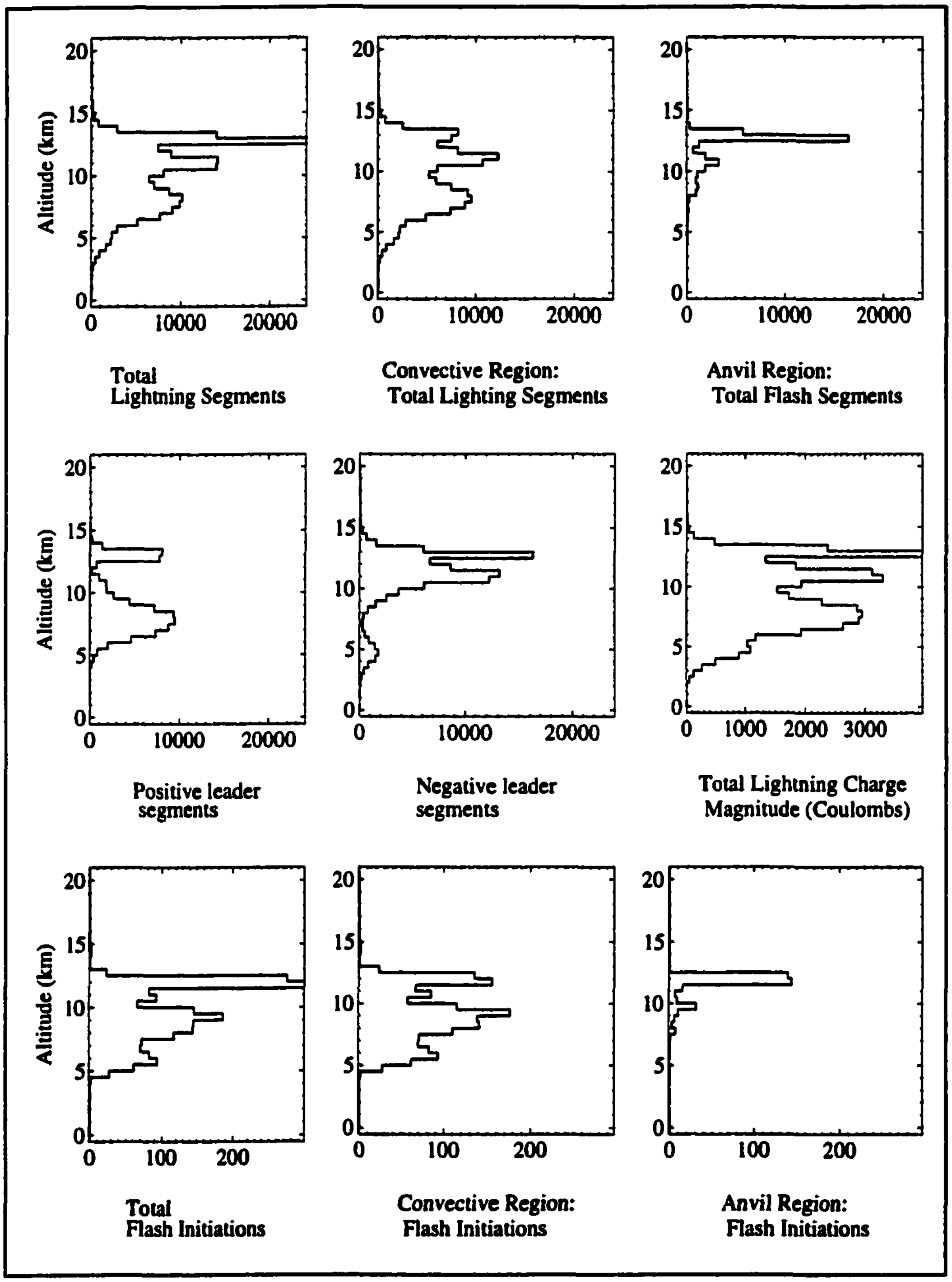

Figure 6.7: Total lightning channel segments and initiations versus height: airmass, riming rate, strong induction. Values are integrated over the whole simulation time (105 minutes). Lightning segments are split into positive and negative leaders or into convective and and anvil regions. Total charge is sum of absolute values of charge deposited by lightning.

(a)
(b)
(c)

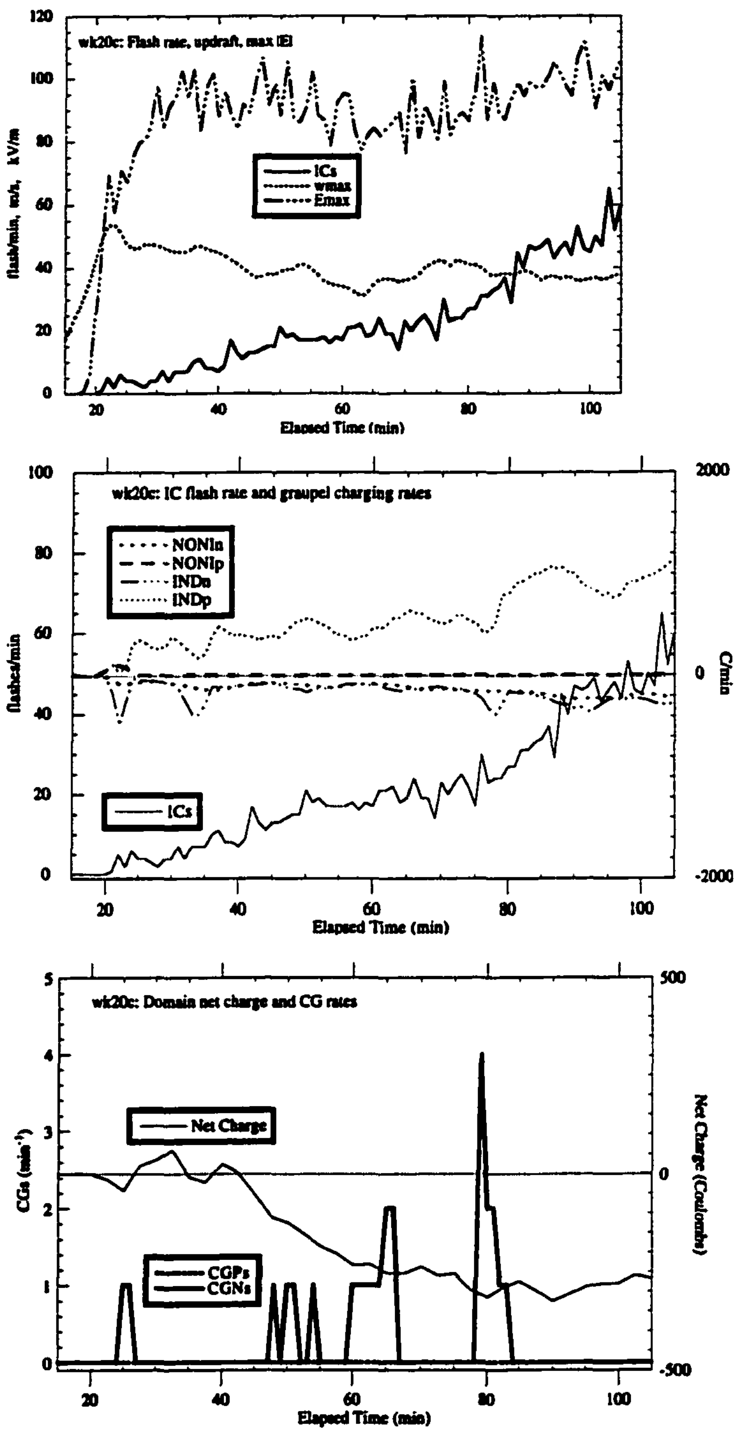

Figure 6.8: Lightning time series plots: airmass, riming rate, strong induction. (a) IC flash rate (min^{-1}), maximum updraft, and maximum electric field magnitude at one-minute intervals. (b) Domain-integrated noninductive and inductive graupel charging rates (C/min), positive and negative values are summed separately. (c) Domain net charge and CG flash rates. All values are sampled at 1-minute intervals except domain net charge, which has 2.5-minute intervals. (Flash rates are 1-minute totals.)

between these two regions.

6.3 Gardiner Noninductive Charging

The airmass storms using Gardiner noninductive charging and moderate or strong inductive charging differ primarily in the strength of the lower positive charge. In other respects, the simulations were quite similar. Thus, the discussion that follows applies to both the moderate and strong inductive versions except as noted.

The runs with the Gardiner noninductive charging parameterization had an initial peak in the IC flash rate at 40–45 minutes (Figures 6.10b and 6.12b) (The actual magnitude of the peak flash rate is not known in the moderate induction case (Figure 6.10b) because the maximum allowed flash rate, set at 60 min^{-1} for that portion of the simulation, was attained.) This peak IC flash rate was coincident with a relative maximum in the extent of the graupel volume, i.e. the graupel volume expanded until about 42 minutes and then went into a period of contraction. The graupel expansion is manifested in the charging as a shallow relative maximum in negative charging of graupel at about 40 minutes elapsed time (Figures 6.10b and 6.12b). The peak in IC flash rate occurred after the maximum in charging because the negatively-charged larger graupel particles needed some time to fall away from the positively-charged smaller snow and cloud ice particles. The graupel volume began to expand again after 70 minutes, again resulting in increased negative charging and flash rates. This later increase in the noninductive charging rate was also seen in the simulations with the riming rate parameterization (e.g. Figure 6.6b, negative charging). For the Takahashi scheme there also was increased *positive* noninductive charging of graupel (Figure 6.14b).

As in the riming rate cases, the net charge density in some regions was reversed by lightning, especially in the convective region to the east of the updraft (Figures 6.3b and 6.4b). The lightning flash rate was greater than in the riming rate case, and eventually a new negative charge layer developed in the anvil: As found by Ziegler and MacGorman

(1994), most of the negative charge deposited by lightning in the main upper positive charge is captured by ice crystals, while most of the positive charge is carried by snow aggregates. The snow falls faster than the ice crystals as both advect into the anvil, thus unmasking the negative charge and expanding and enhancing the negative charge layer. The strong positive layer of snow at the anvil base and the lightning-induced negative layer caused lightning not seen with the other two noninductive parameterizations. This lightning caused the secondary peak appears at 8 km in the vertical distribution of lightning initiations in the anvil region (Figures 6.9 and 6.11, bottom right panels) which was not seen in the other cases.

At about 65 minutes, IC flashes began to occur between the lightning-induced negative charge layer and the positive charge layer below it. The lightning composites in Figures 6.1b and 6.2b show some activity in the negative layer, though the view is obscured. Positive leaders that propagated through the new negative layer can be seen in these figures as blue-colored contours at midlevel in the eastern (right) third of the panels.

The simulated airmass storms with Gardiner noninductive charging developed a strong negative screening layer almost everywhere along the top of the anvil. The screening layers on the anvil undersides had a less simple evolution. As the anvil grew outward, a negative screening layer developed on the underside (seen in Figures 6.3b and 6.4b). After about an hour of simulation time, though, a positive screening layer developed under the leading edges of the anvil (not shown). It is possible that the positive screening layer is a response to the upper negative screening layer and lightning-induced negatively charged ice particles as they are carried outward with the anvil. Subsequent outward spreading of the anvil maintained the lower positive screening layer. The negative screening layer that existed on the underside of the inner part of the anvil is not readily seen in the net charge density contours (Figures 6.3b and 6.4b) because of masking by positively charged falling snow.

A distinguishing feature of the Gardiner charging scheme is that it allows

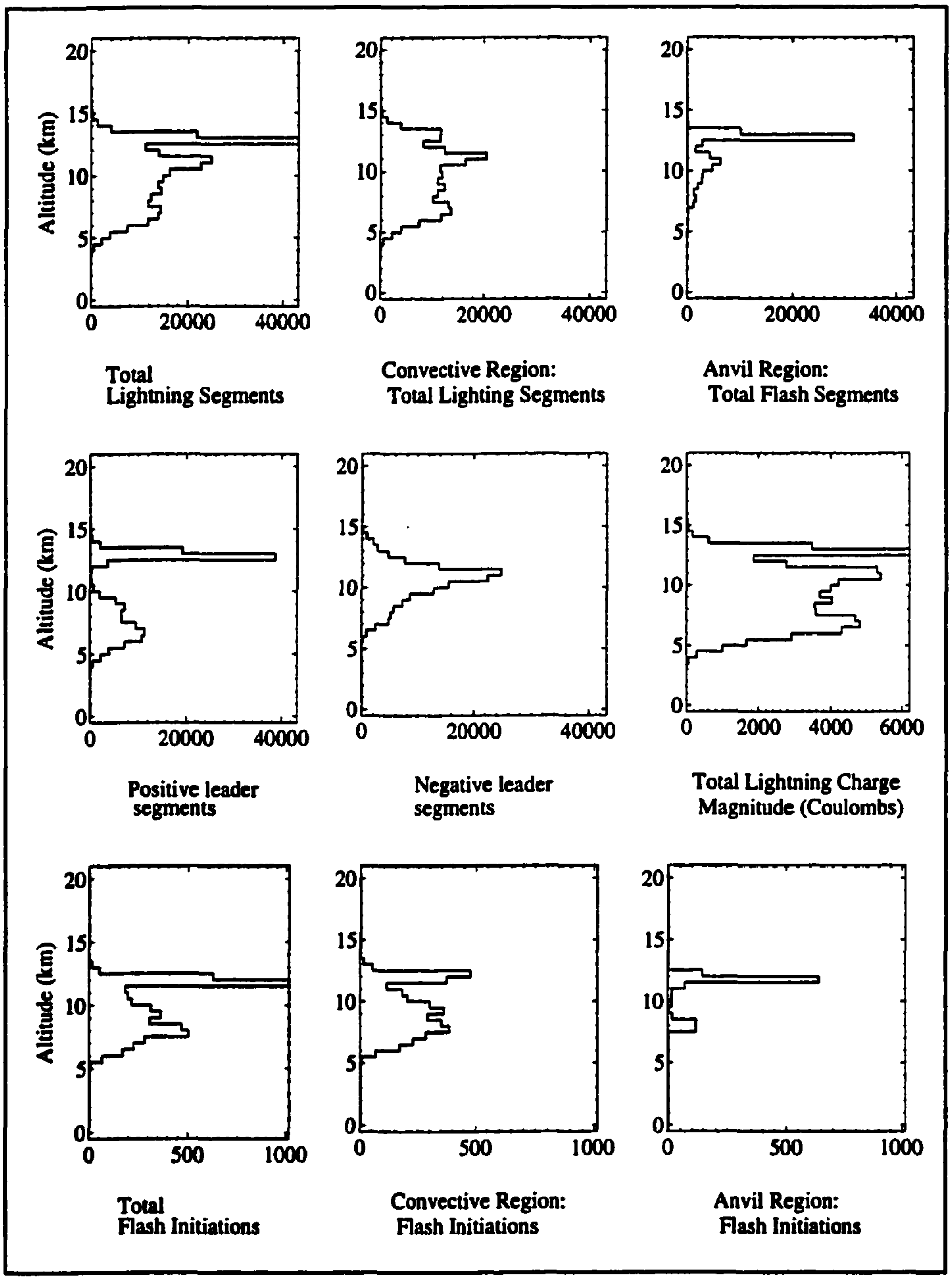

Figure 6.9: Total lightning channel segments and initiations versus height: airmass, Gardiner, moderate induction. Values are integrated over the whole simulation time. Lightning segments are split into positive and negative leaders or into convective and and anvil regions. Total charge is sum of absolute values of charge deposited by lightning.

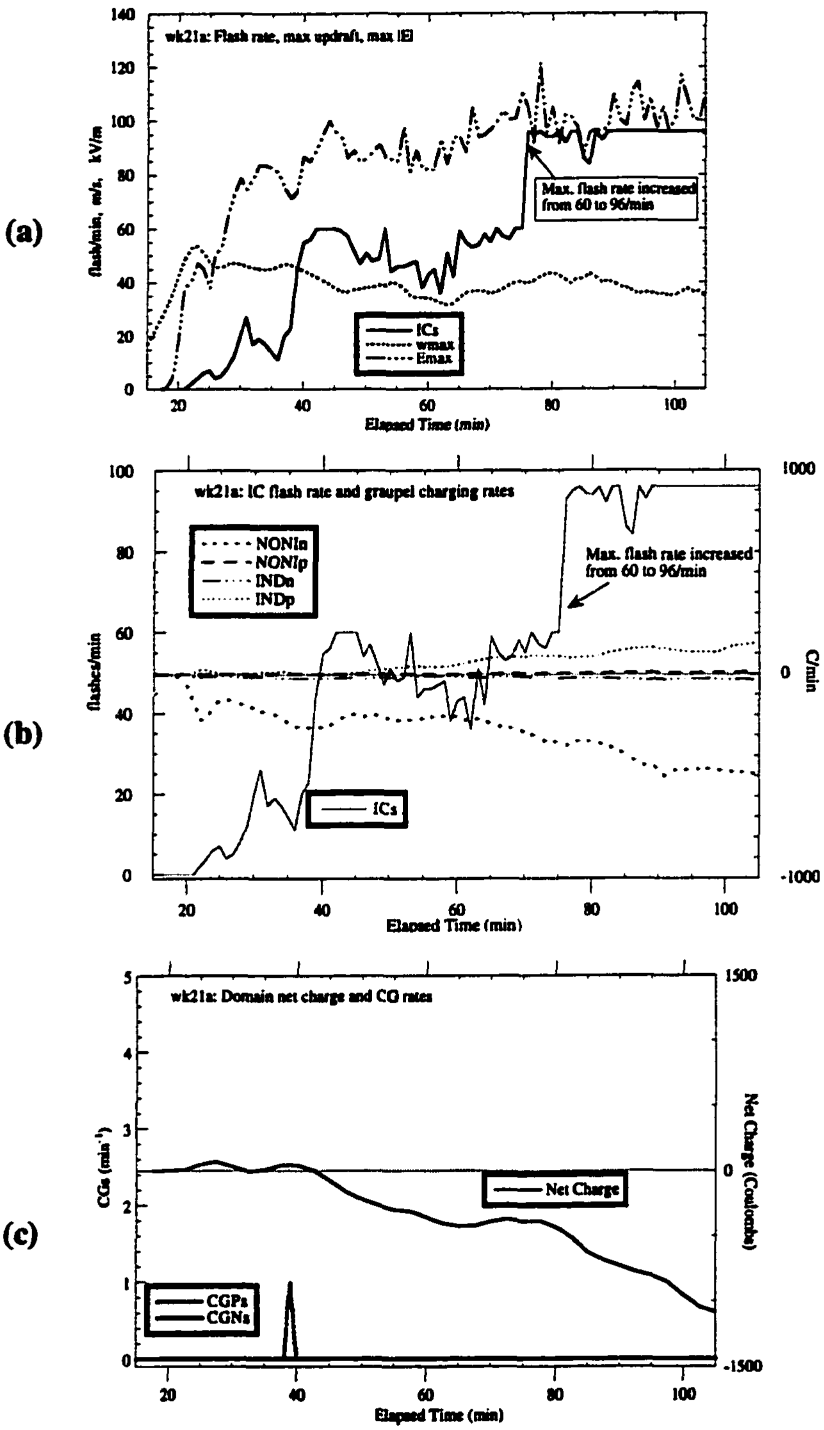

Figure 6.10: Lightning time series plots: airmass, Gardiner, moderate induction. (a) IC flash rate (min^{-1}), maximum updraft, and maximum electric field magnitude at one-minute intervals. (b) Domain-integrated noninductive and inductive graupel charging rates (C/min), positive and negative values are summed separately. (c) Domain net charge and CG flash rates. All values are sampled at 1-minute intervals except domain net charge, which has 2.5-minute intervals. (Flash rates are 1-minute totals.)

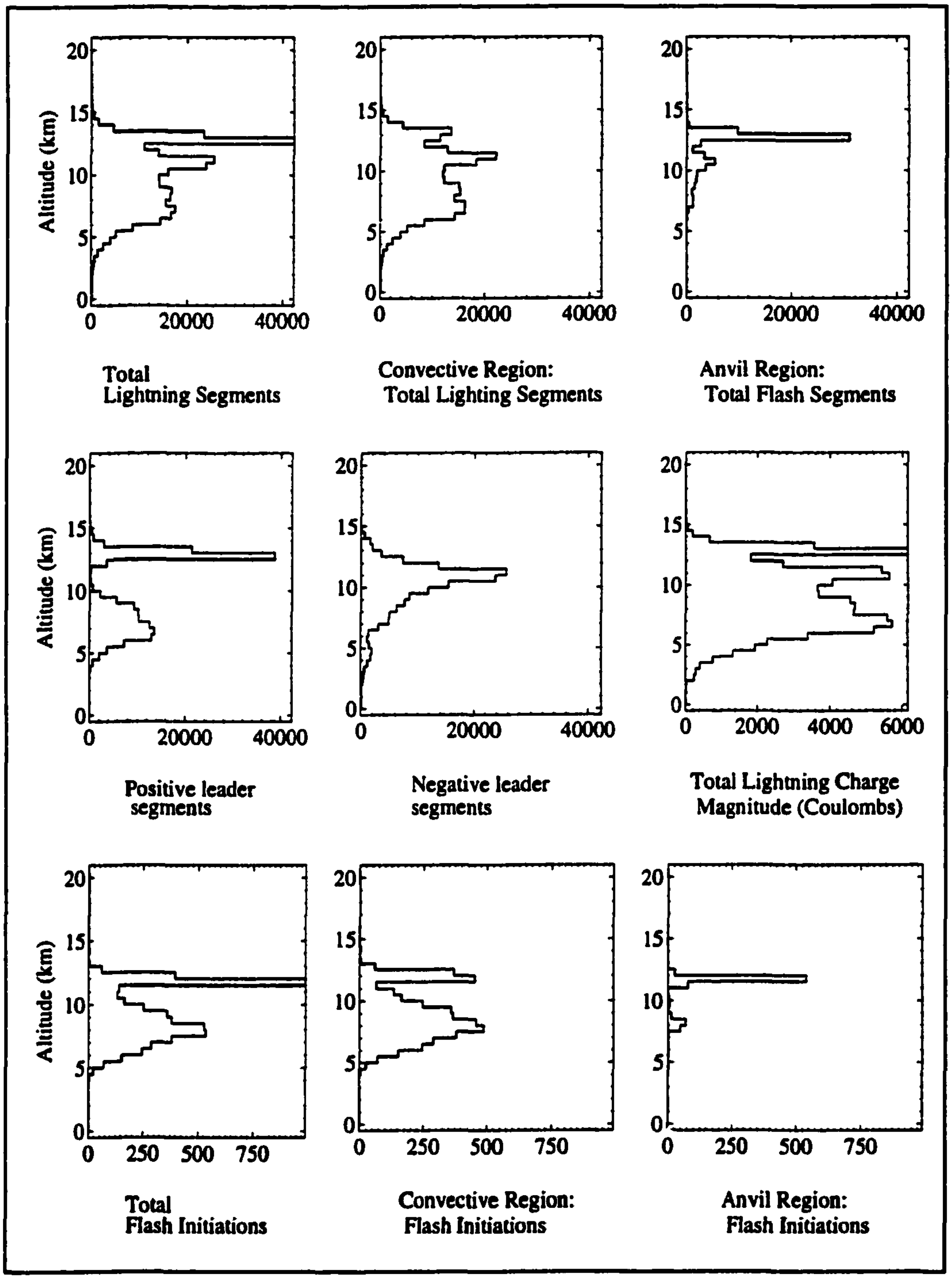

Figure 6.11: Total lightning channel segments and initiations versus height: airmass, Gardiner, strong induction. Values are integrated over the whole simulation time. Lightning segments are split into positive and negative leaders or into convective and and anvil regions. Total charge is sum of absolute values of charge deposited by lightning.

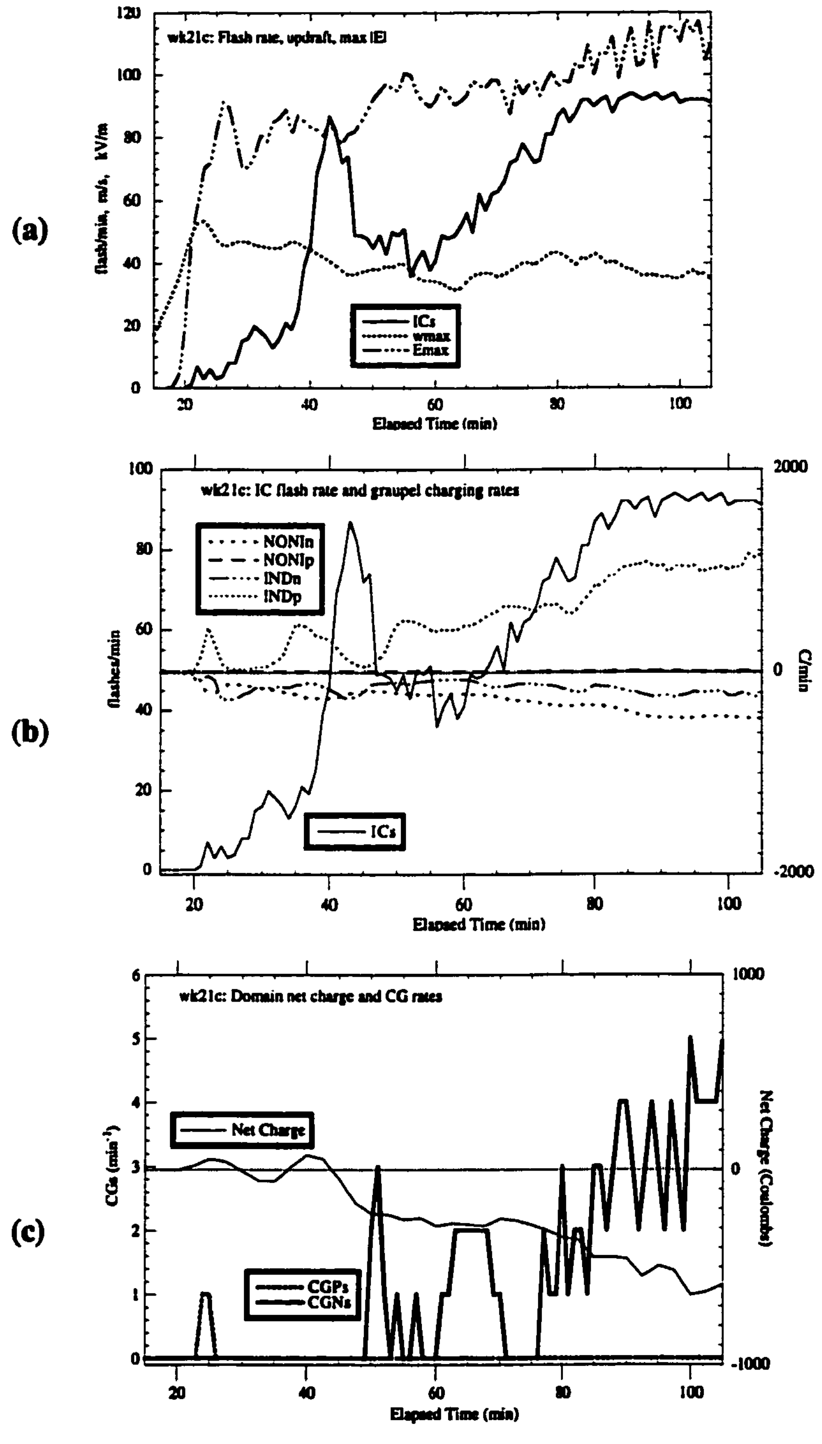

Figure 6.12: Lightning time series plots: airmass, Gardiner, strong induction. (a) IC flash rate (min^{-1}), maximum updraft, and maximum electric field magnitude at one-minute intervals. (b) Domain-integrated noninductive and inductive graupel charging rates (C/min), positive and negative values are summed separately (note different scale). (c) Domain net charge and CG flash rates. All values are sampled at 1-minute intervals except domain net charge, which has 2.5-minute intervals. (Flash rates are 1-minute totals.)

appreciable negative charging of graupel to occur at quite small cloud water mixing ratios (down to 10^{-3} g/kg). The base of the anvil in the forward flank region (the right side of the storm in Figures 6.3 and 6.4) had a thin layer in which there were enough liquid cloud droplets for noninductive charging. The result of the charge separation is seen in Figures 6.3b and 6.4b as a strong positive layer (snow) near or around the cloud boundary and a negative charge region (graupel) underneath. The positively charged snow advected outward with the anvil and maintained the positive charge layer at and a little below the cloud boundary. This was the positively charged snow that masked the negative screening layer carried by cloud ice (mentioned above).

As in the cases with riming rate charging, lightning activity in the lower positive charge region occurred only with the strong inductive charging. The enhanced lower positive charge that resulted again made −CG flashes possible. The Gardiner parameterization with strong inductive charging produced more CG flashes than the riming rate or Takahashi parameterizations, as well as more IC flashes. The −CG ground strike points occurred over a somewhat wider range than they did in the riming rate case, but still remained close to the strong surface precipitation, with a few strikes near the edges of precipitation.

6.4 Takahashi Noninductive Charging

The simulations using Takahashi charging had the lowest total lightning counts of the airmass storms (Table 10.1). However, of the cases using moderate inductive charging, only Takahashi produced any −CG flashes. (Gardiner with moderate induction made a single +CG flash.) Also, with strong induction, the simulations with Takahashi charging had more than twice as many −CG flashes as the simulation with riming rate charging, but about half as many as the simulation with Gardiner charging.

In both cases with Takahashi noninductive charging, IC flash initiations between the main negative and positive regions occurred higher in the storm on average and were fewer in number than in the riming rate and Gardiner cases. Note the strong minimum in total flash initiations at 7–9 km in Figure 6.15 (lower-left corner) and compare with Figures 6.7 and 6.11. The initiation heights were still within the range of altitudes seen in the other cases, however.

As in the riming rate cases, a strong upper negative screening layer developed only on the eastern (forward) half of the anvil. In the western (rear) half, flashes were initiated between the positive charge and the negative screening layer on the bottom of the rear anvil. Also, negative leaders from the convective region occasionally propagated into positive charge in the rear anvil.

The Takahashi parameterization produced a respectable lower positive charge and negative CG flashes even with moderate inductive charging, because of positive noninductive charging of graupel at low liquid water content and low temperature (down to about −25°C). The positive noninductive charging of graupel helped enhance the electric field beneath the main negative charge region, which in turn increased the effectiveness of the inductive charging. Thus, graupel gained positive charge in the forward flank region where the Gardiner parameterization charged graupel negatively. The resulting difference in charge distribution is seen in Figures 6.3 and 6.4: To the east (right) of the updraft base in the sub-anvil region there is a region of positive charge in the Takahashi cases that is not present in the corresponding riming rate and Gardiner cases.

The Takahashi cases had lower positive charge regions that were more horizontally extensive, leading to roughly stratified charge layers. The lightning reflected the different charge structure, e.g. the discernible peak at 5 km in the vertical distribution of total lightning segments in Figure 6.15 compared with the relative lack of such a peak in Figures 6.7 and 6.11. (Similar features consistently appeared when using the Takahashi parameterization in the supercell storms, as well.)

In the simulation with moderate induction, the negative CG flashes during 50–60 minutes elapsed time struck within regions having greater surface precipitation.

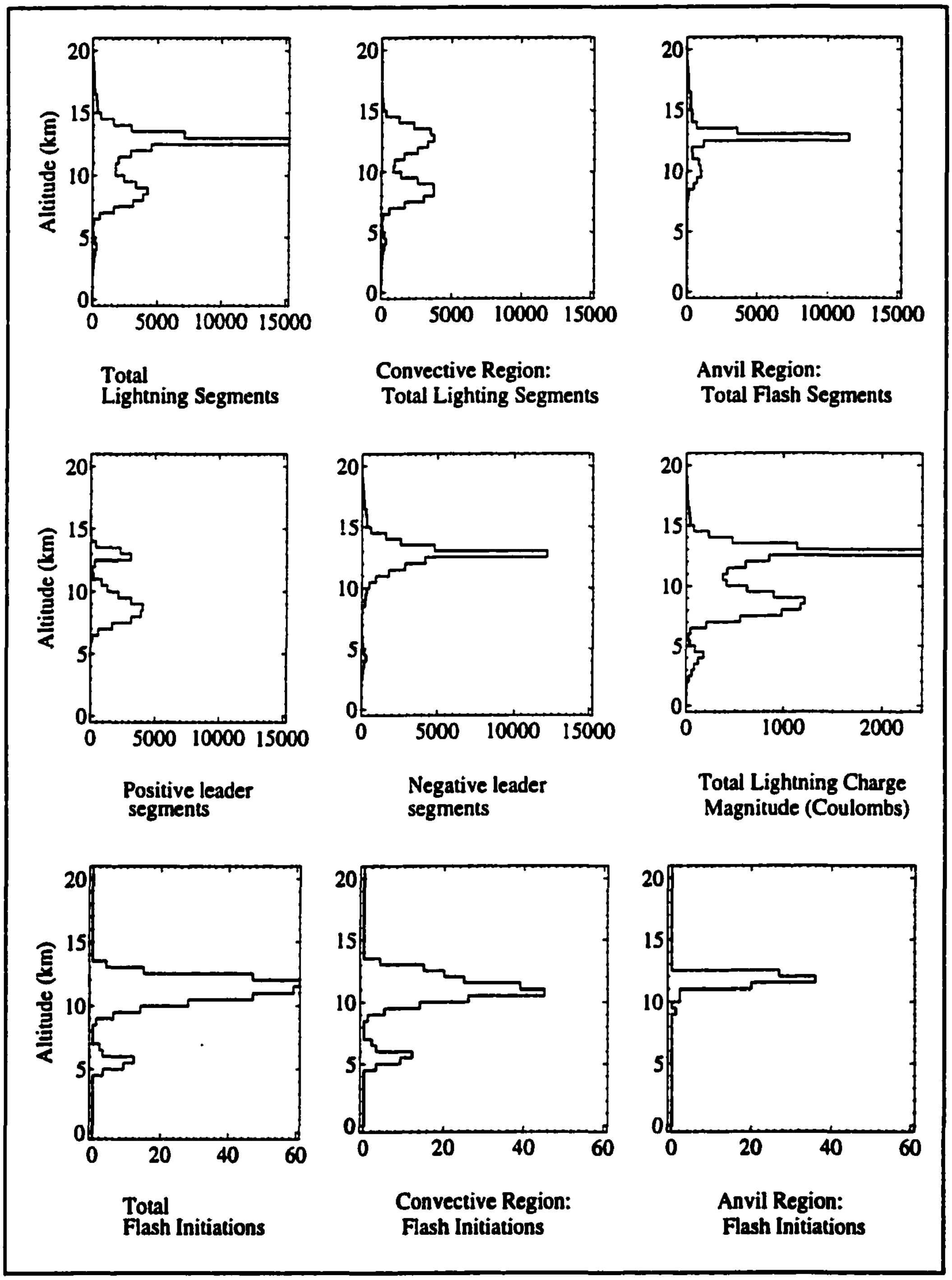

Figure 6.13: Total lightning channel segments and initiations versus height: airmass, Takahashi, moderate induction. Values are integrated over the whole simulation time. Lightning segments are split into positive and negative leaders or into convective and and anvil regions. Total charge is sum of absolute values of charge deposited by lightning.

(a)
(b)
(c)

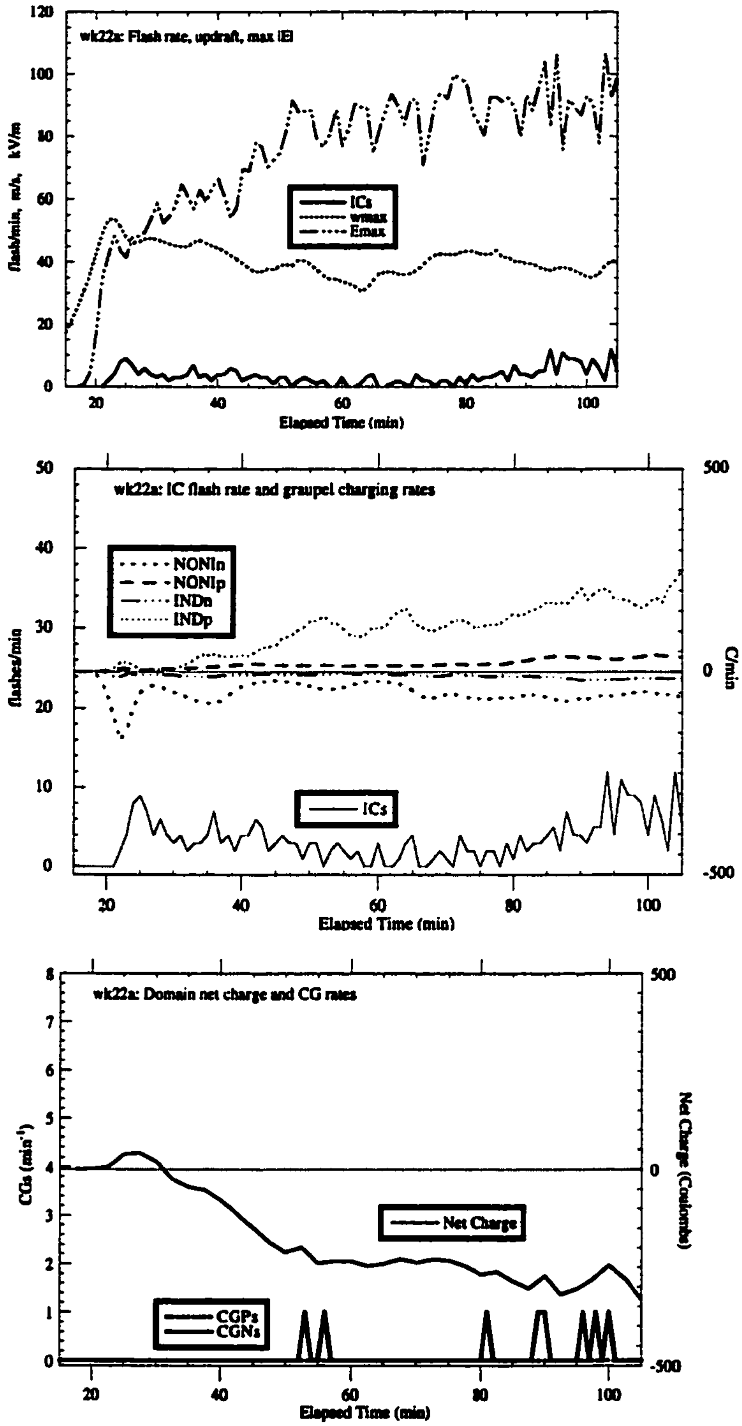

Figure 6.14: Lightning time series plots: airmass, Takahashi, moderate induction. (a) IC flash rate (min^{-1}), maximum updraft, and maximum electric field magnitude at one-minute intervals. (b) Domain-integrated noninductive and inductive graupel charging rates (C/min), positive and negative values are summed separately. (c) Domain net charge and CG flash rates. All values are sampled at 1-minute intervals except domain net charge, which has 2.5-minute intervals. (Flash rates are 1-minute totals.)

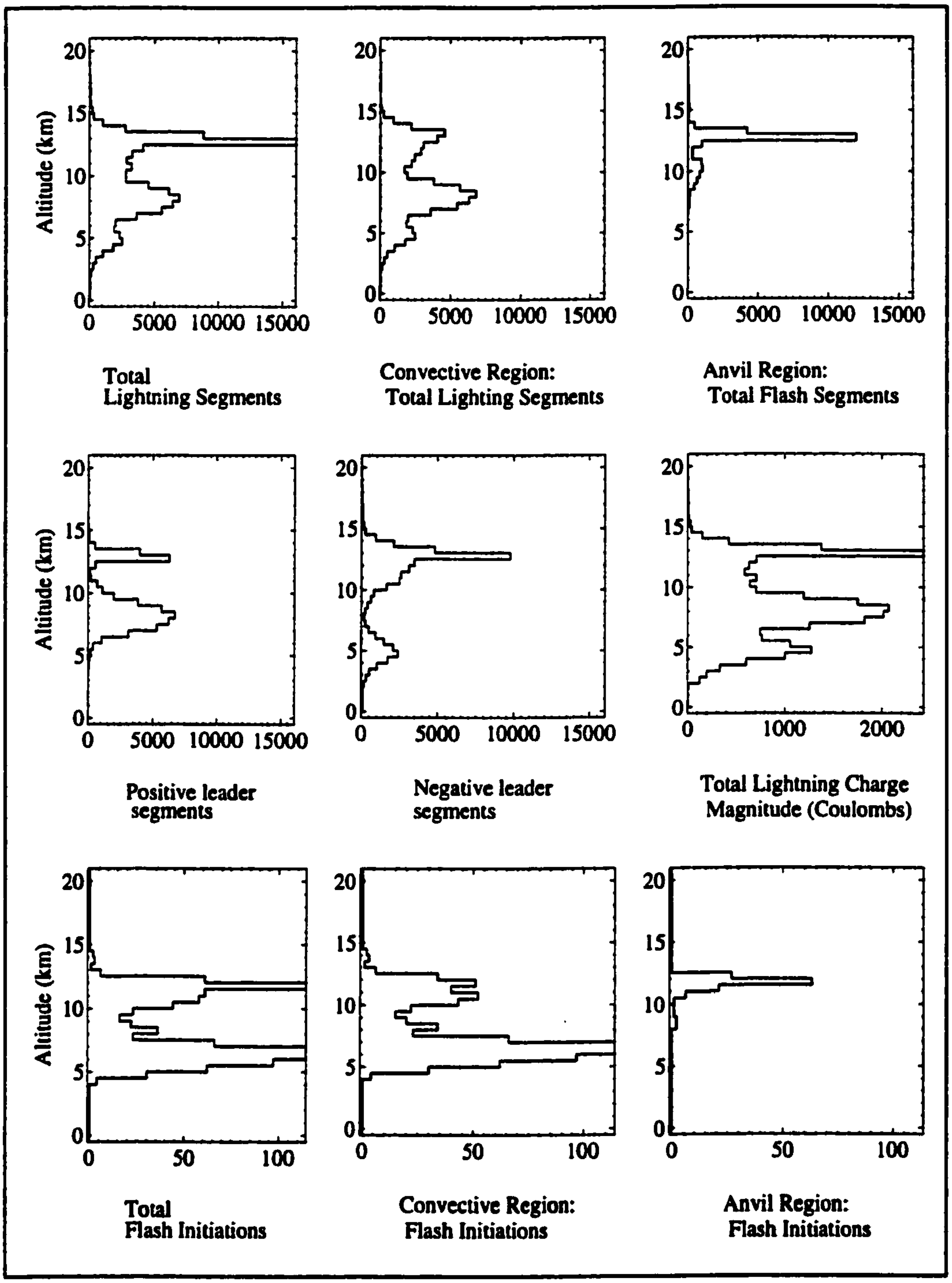

Figure 6.15: Total lightning channel segments and initiations versus height: airmass, Takahashi, strong induction. Values are integrated over the whole simulation time. Lightning segments are split into positive and negative leaders or into convective and and anvil regions. Total charge is sum of absolute values of charge deposited by lightning.

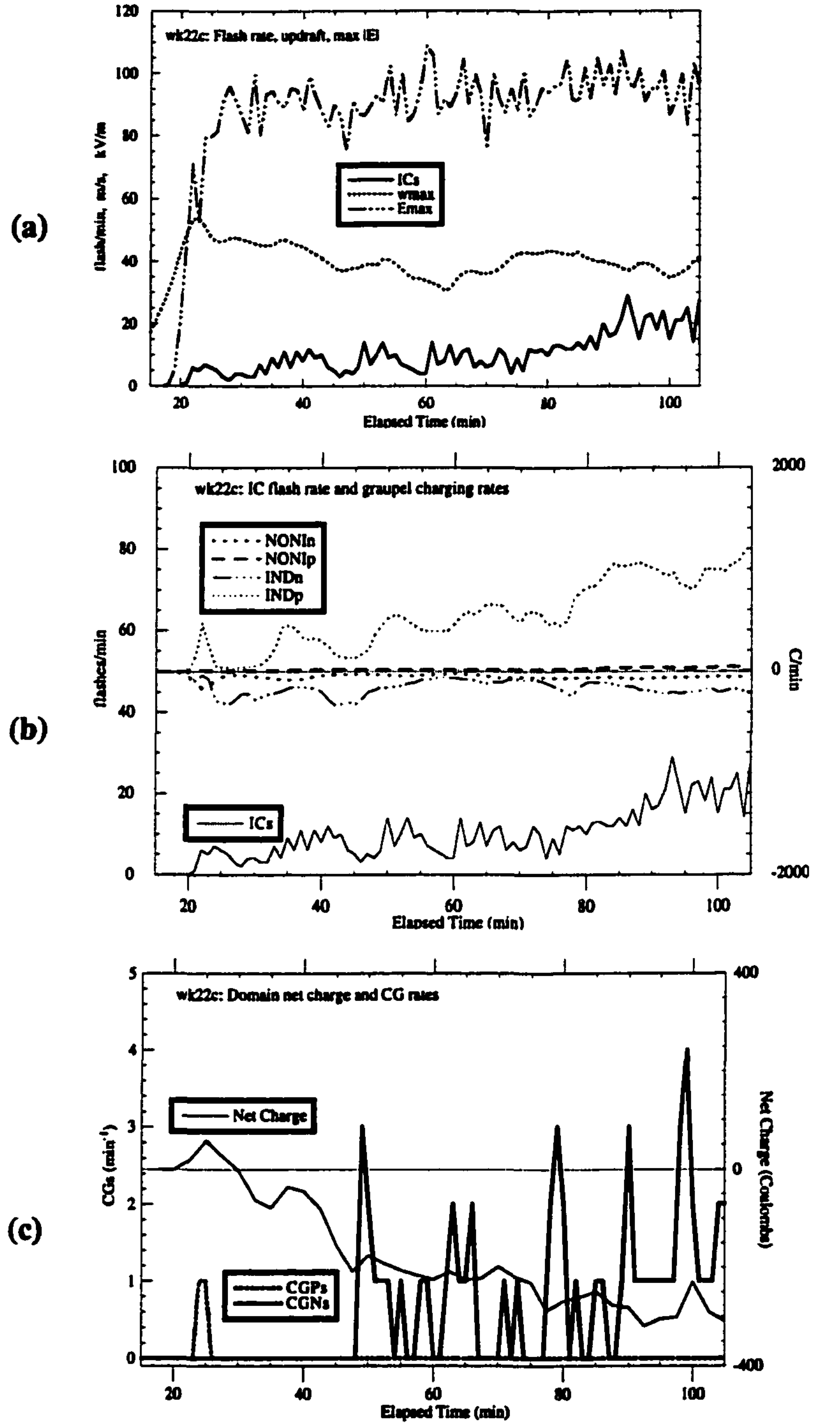

Figure 6.16: Lightning time series plots: airmass, Takahashi, strong induction. (a) IC flash rate (min^{-1}), maximum updraft, and maximum electric field magnitude at one-minute intervals. (b) Domain-integrated noninductive and inductive graupel charging rates (C/min), positive and negative values are summed separately. (c) Domain net charge and CG flash rates. All values are sampled at 1-minute intervals except domain net charge, which has 2.5-minute intervals. (Flash rates are 1-minute totals.)

Subsequent CG flashes occurred in the lighter surface precipitation on the southeast (forward) flank. With strong inductive charging, −CG flashes were more numerous. A few −CG flashes also struck noticeably farther out from the forward flank than in any of the other airmass cases, thanks to the forward extension of the lower positive charge region.

6.5 Case with Constant Lightning Initiation Threshold

The few published studies of electrification and lightning in numerical models have almost all used a constant threshold of electric field magnitude for lightning initiation throughout the domain. Solomon and Baker (1998) merely mentioned preliminary tests with a height-varying threshold. In this study it was decided to use the 'breakeven' electric field profile (E_{be}) as the default choice for lightning initiation (Section 4.3.1). The use of this profile is somewhat controversial, but appears to be consistent with numerous electric field soundings through many types of thunderstorms (Marshall et al. 1995).

One simulation was run with a constant lightning initiation threshold for comparison with the breakeven field results. This test used the airmass storm with Gardiner noninductive and strong inductive charging. The lightning initiation threshold was set at $E_{init} = 150$ kV/m, which was larger than the breakeven threshold even at at low altitudes (125 kV/m at $z \leq 4$ km). The lightning propagation threshold was not adjusted with regard to cloudy or clear air, as it was when using the breakeven electric field.

Many differences resulting from the constant E_{init} are notable between the time-history plots in Figures 6.18 and 6.12. The onset of lightning was delayed slightly, since the electric field had to reach a larger magnitude. After 40 minutes the IC flash rates were smaller. However, the −CG flash rates were larger than in the E_{be} case (note the different scale in Figure 6.18c). The larger electric field values imply greater charge density magnitudes and promote stronger inductive charging.

Lightning was still initiated at high altitudes and in the anvil despite the increased threshold, as seen in the lower-left panel of Figure 6.17 (total lightning initiations).

Having more lightning at lower levels clearly did not prevent the electric field at higher altitudes from reaching the initiation threshold. With the uniform threshold of 150 kV/m, vertical electric field profiles through the simulated storm indicated that the electric field reached much larger values over a wide horizontal area in the upper part of the anvil than were reached with the breakeven threshold for lightning (e.g. Figure 6.19). It seems that, if such large fields persist over wide regions, they ought to be observed, in spite of the relatively sparse soundings that have been obtained in real storms. However, large electric fields have not been observed at these altitudes. Instead, the observed electric fields have been similar to those produced by simulations using the breakeven field.

Another obvious effect of a constant E_{init} is seen in the histogram of the charge magnitudes (Q) discharged by lightning (Figure B.5a). The histogram has a shape that is markedly different from the corresponding case that used E_{be} (Figure B.4a). There is a much steeper slope in the range $0 < Q < 25$ C, but a much more gradual slope for the higher magnitude discharges. Thus for the uniform E_{init} case there were fewer discharges in the 5–40 C range but more flashes with $Q > 45$ C than in the breakeven field case. The usual behavior with E_{be} is a roughly exponential distribution for $Q > 5$ C, sometimes with a slight decrease in the 0–5 C bin or a relatively flat distribution across a few of the bins with the smallest charges.

The constant initiation threshold also resulted in some bizarre lightning behavior. After about 70 minutes, negative leaders began to propagate beneath the forward anvil and often descended to about 5 km altitude, wandering in the clear air. Some of these leaders reached the ground as −CG flashes. By the end of the run, the space under the forward anvil became full of these wandering leaders down to about 5 km. The last 15 minutes of the corresponding simulation with the breakeven threshold was run again without the restriction on propagation outside the cloud to see if the wandering leaders would be reproduced. The result was intriguing: The wandering leaders did not appear when the breakeven threshold was used. Although a few leaders did descend out of the anvil, they

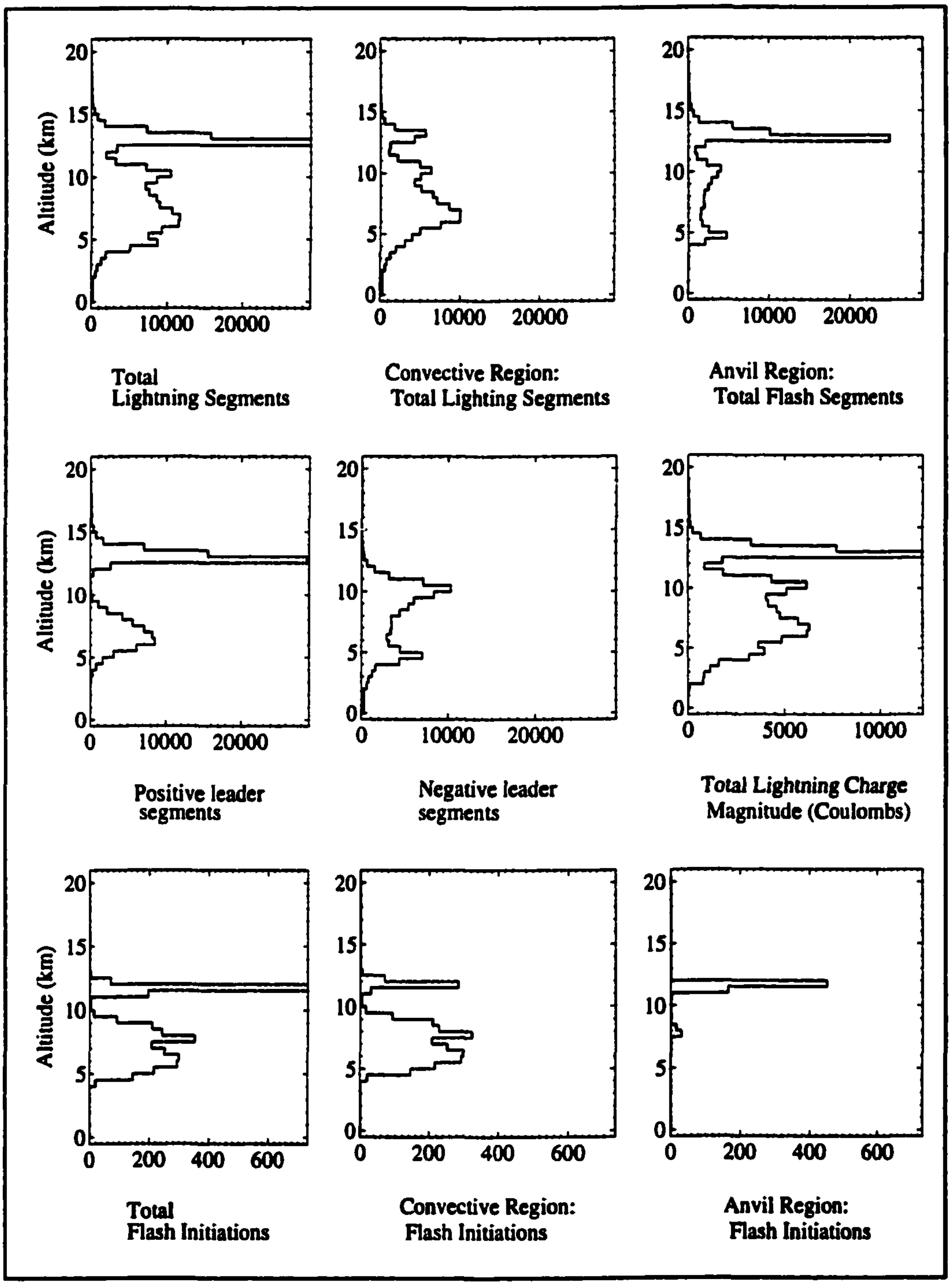

Figure 6.17: Total lightning channel segments and initiations versus height for airmass storm with E_{init} = 150 kV/m (Charging by Gardiner, strong). Values are integrated over the whole simulation time. Lightning segments are split into positive and negative leaders or into convective and and anvil regions. Total charge is sum of absolute values of charge deposited by lightning.

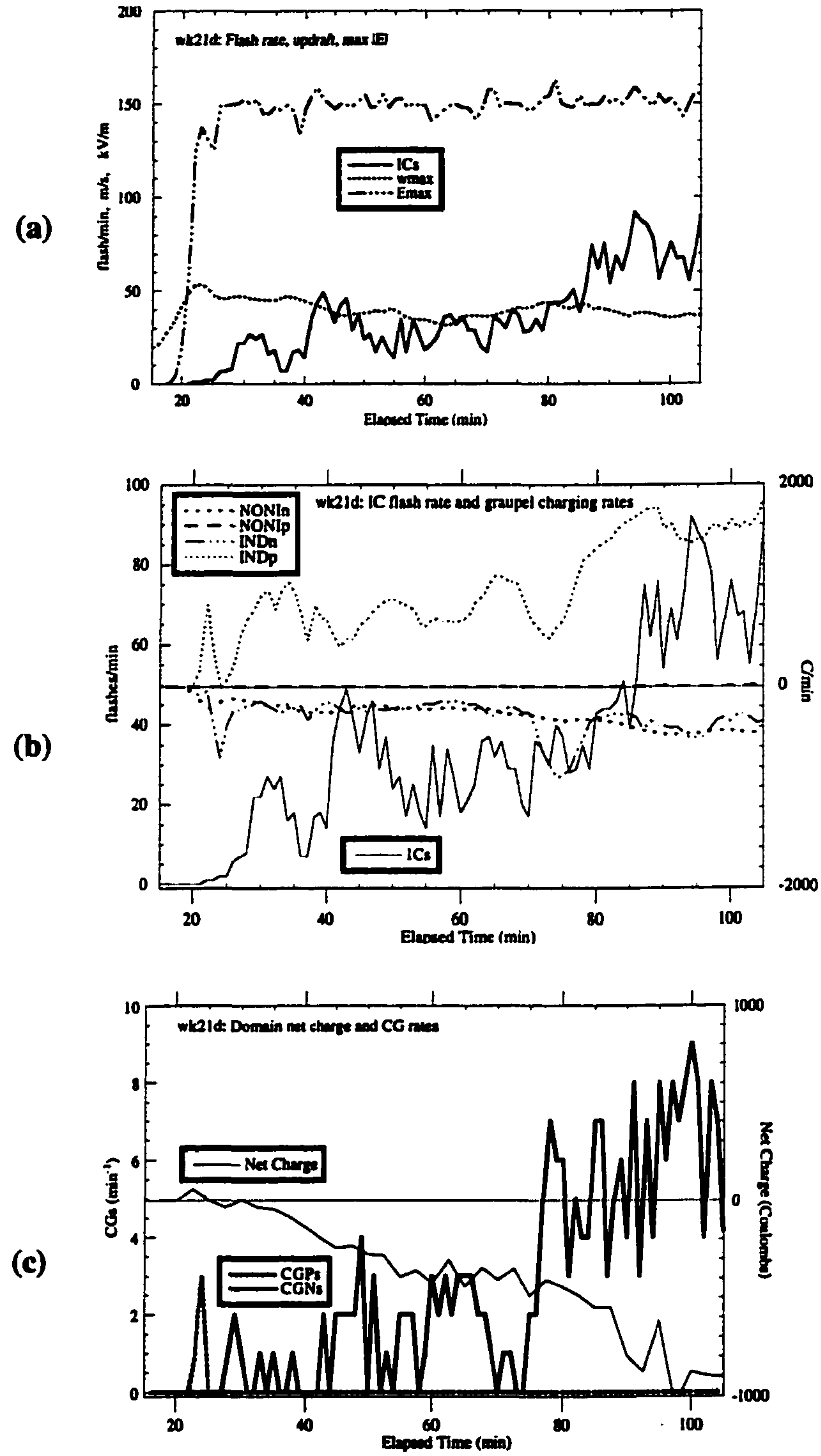

Figure 6.18: Lightning time series plots for airmass storm with E_{init} = 150 kV/m and Gardiner, strong induction. (a) IC flash rate (min^{-1}), maximum updraft, and maximum electric field magnitude at one-minute intervals. (b) Domain-integrated noninductive and inductive graupel charging rates (C/min), positive and negative values are summed separately. (c) Domain net charge and CG flash rates. All values are sampled at 1-minute intervals except domain net charge, which has 2.5-minute intervals. (Flash rates are 1-minute totals.)

either stopped just below the cloud or went straight down all the way to the ground. Additionally, there was an increase in the number of positive leaders that propagated upward above the cloud top.

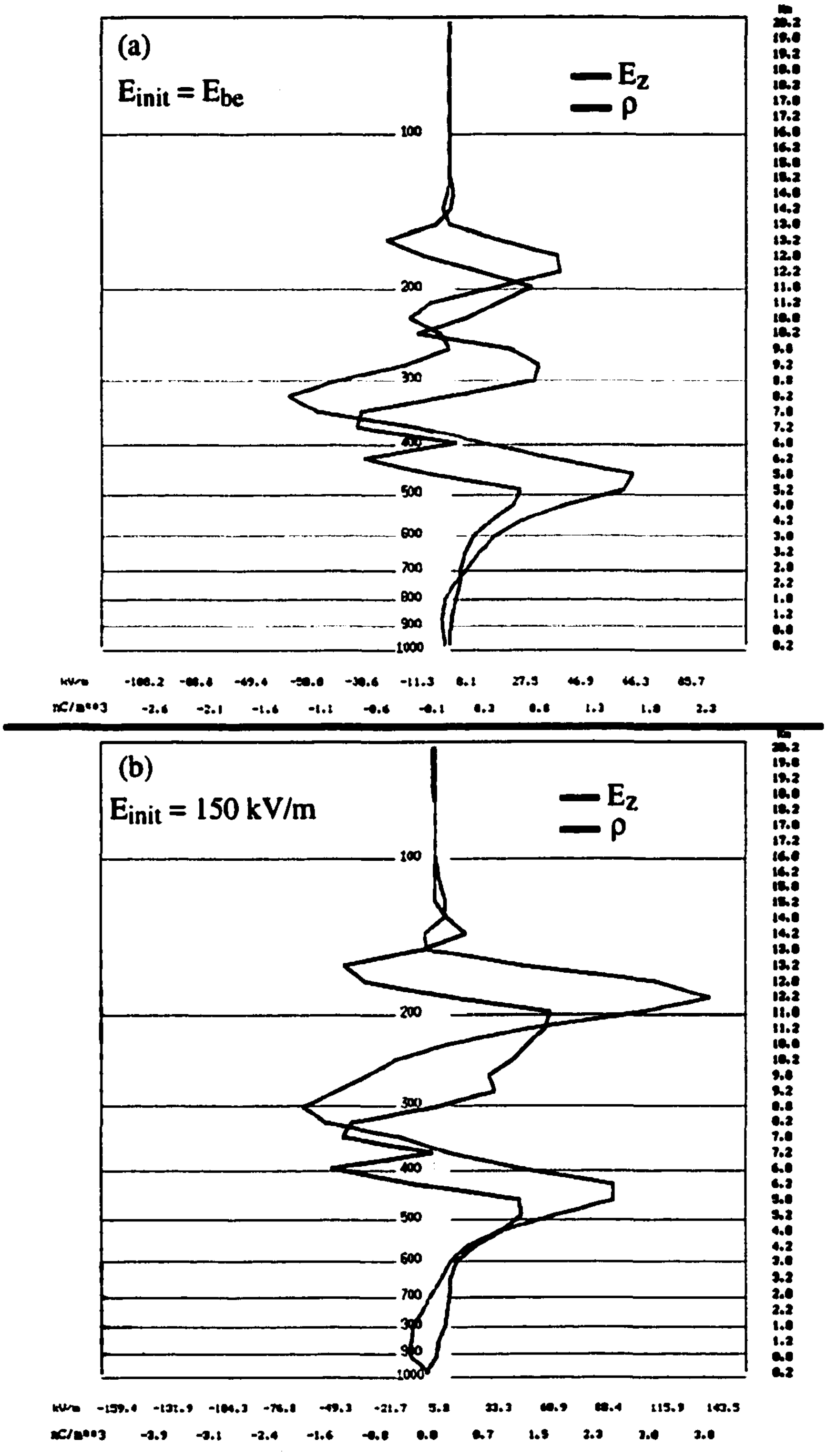

Figure 6.19: Vertical soundings at the same time and location for the airmass storm with Gardiner noninductive charging and lightning initiation thresholds of (a) breakeven electric field and (b) constant value of 150 kV/m. Shown are vertical airspeed (w), vertical electric field component (E_z), and net charge density (ρ). Pressure is indicated in increments of 100 mb.

Chapter 7

High Precipitation Supercell Storm Simulations

7.1 HP Supercell General Characteristics

The environment for this storm is characterized by strong 0–5 km wind shear and no shear at higher altitudes (refer to Section 5.1.1). The temperature and moisture profiles are the same as for the airmass storms. The HP supercell storm simulation was run four times, once with each of the three noninductive charging schemes and once with an 'enhanced' version of the riming rate parameterization. The run with the enhanced riming rate charging is not included in general comparisons because it was only partially analyzed. All the HP simulations used the strong inductive charging option.

The stronger low-level wind shear caused the initial updraft to grow more slowly than in the airmass case and to be tilted slightly downshear (eastward). The initial storm split into northern and southern storms at about 50 minutes elapsed time. The original southern storm was always the strongest storm in the model domain, with the largest updraft speeds and widest updraft area. Within five minutes of the initial split, the southern storm exhibited a precipitation hook structure at low levels (e.g., 1 km) around the updraft in the southern storm. The hook persisted throughout the rest of the simulation. A bounded weak echo region was evident in the southern storm by 70 minutes.

The northern storm developed a weak echo region on its southern flank as it split again at about 85–90 minutes. The southern storm split off additional small and relatively short-lived updraft cells from its northern side during the rest of the simulation. The anvils of the northern storms never separated from that of the southern storm during the entire time that the anvils were completely contained in the simulation domain. By 85 minutes the merged anvil was roughly heart-shaped and began to penetrate all four domain walls (Figure 7.1).

Certain similarities in charge structure are found in the three simulations. For example, at 85 minutes of model time, Figure 7.3 shows negative screening layers on the top of the forward (eastern) anvil and on the underside of the rear (upshear) anvil. All three simulations show relatively thin regions of large charge density below 10 km and generally weaker charge densities above. Negative screening layers are also seen underneath the southern anvil of all three simulations in Figure 7.4. Regions of net charge reversal caused by lightning are seen in all three runs.

The lightning composites at 85 minutes also have general similarities (Figures 7.1 and 7.2). All three simulations show negative leaders in the upper part of the storm and positive leaders below, indicating roughly positive charge above negative. Intracloud flashes involving the upper negative screening layer on the forward anvil are also evident in all the simulations. Figure 7.1 also shows a few negative leaders that propagated up out of the cloud near the overshooting top. Recent VHF lightning mapping observations have recorded similar lightning activity (P. Krehbiel, personal communication).

Another common feature of the HP simulations is the oscillations of inductive charging seen in Figures 7.6b, 7.8b and 7.10b. The oscillations are more regularly spaced and more constant in amplitude than seen in the airmass storms. Similar behavior is seen in the other supercell simulations (LP and Classic) that use strong inductive charging. A possible explanation of this behavior is discussed in Chapter 10.

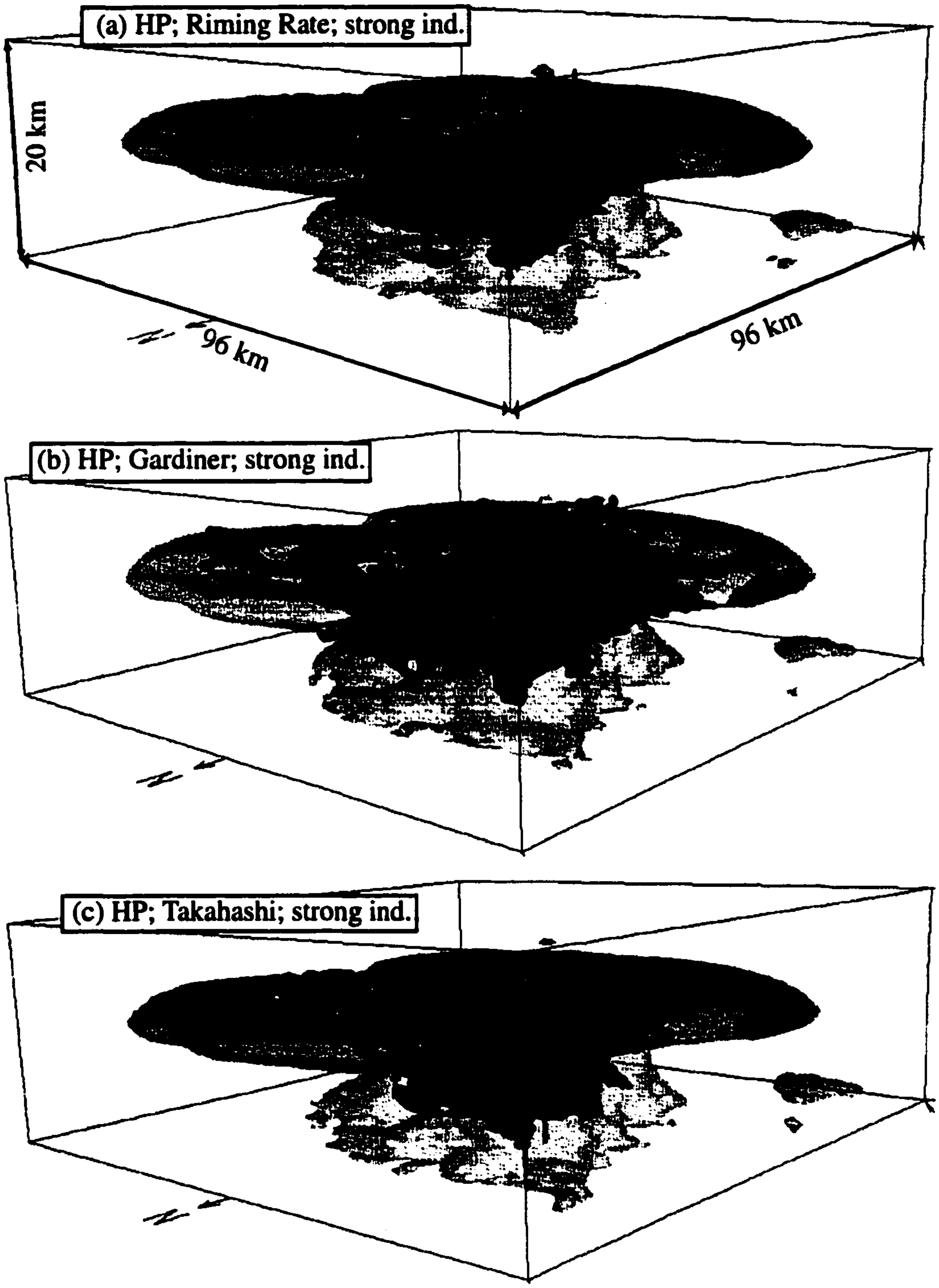

Figure 7.1: HP supercell lightning composites for three noninductive mechanisms. The view is from the northwest at 85 minutes elapsed time. Contours outline lightning channels occurring over a 2.5-minute period. Negative leaders are colored orange, and positive leaders are blue. Cloud ice and cloud water contours are gray and yellow, respectively. Green contours indicate where lightning flashes were initiated.

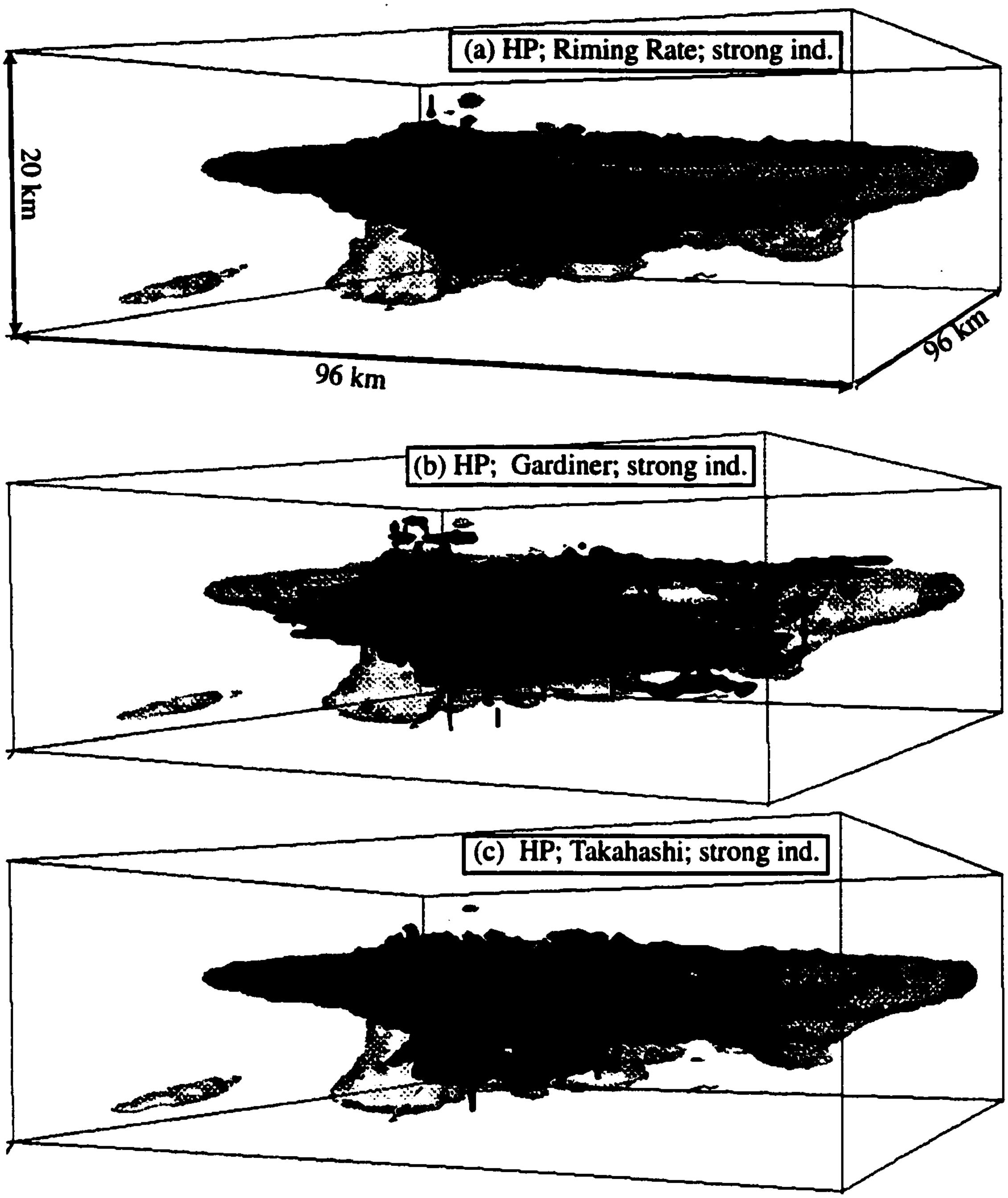

Figure 7.2: HP supercell lightning composites for three noninductive mechanisms. The view is from the southeast at 85 minutes elapsed time. Contours outline lightning channels occurring over a 2.5-minute period. Negative leaders are colored orange, and positive leaders are blue. Cloud ice and cloud water contours are gray and yellow, respectively. Green contours indicate where lightning flashes were initiated.

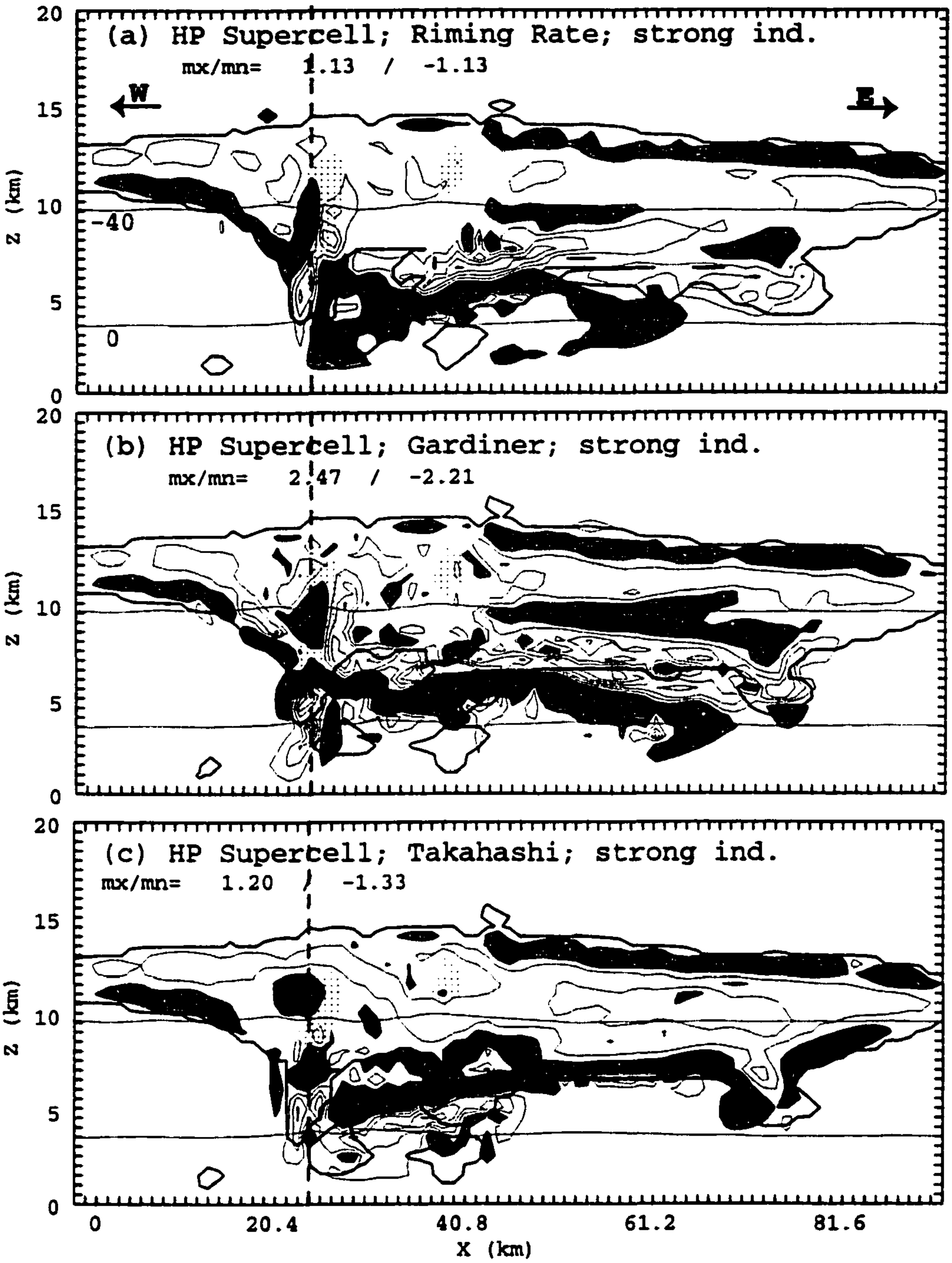

Figure 7.3: Charge density contours (east-west) for the HP supercell storms. All cases use strong inductive charging. The slices are taken through the southernmost storm at the northern edge of the updraft region (y = 51.6 km). The view is from the south at a time of 85 minutes. Negative charge regions are gray. Contour intervals are 0.3 nC m^{-3}, starting at ±0.15. The heavy line outlines the cloud boundary (not including precipitation). Dotted regions indicate updraft of 10 m/s or greater. Maximum and minimum values for the charge slice are given in each panel.

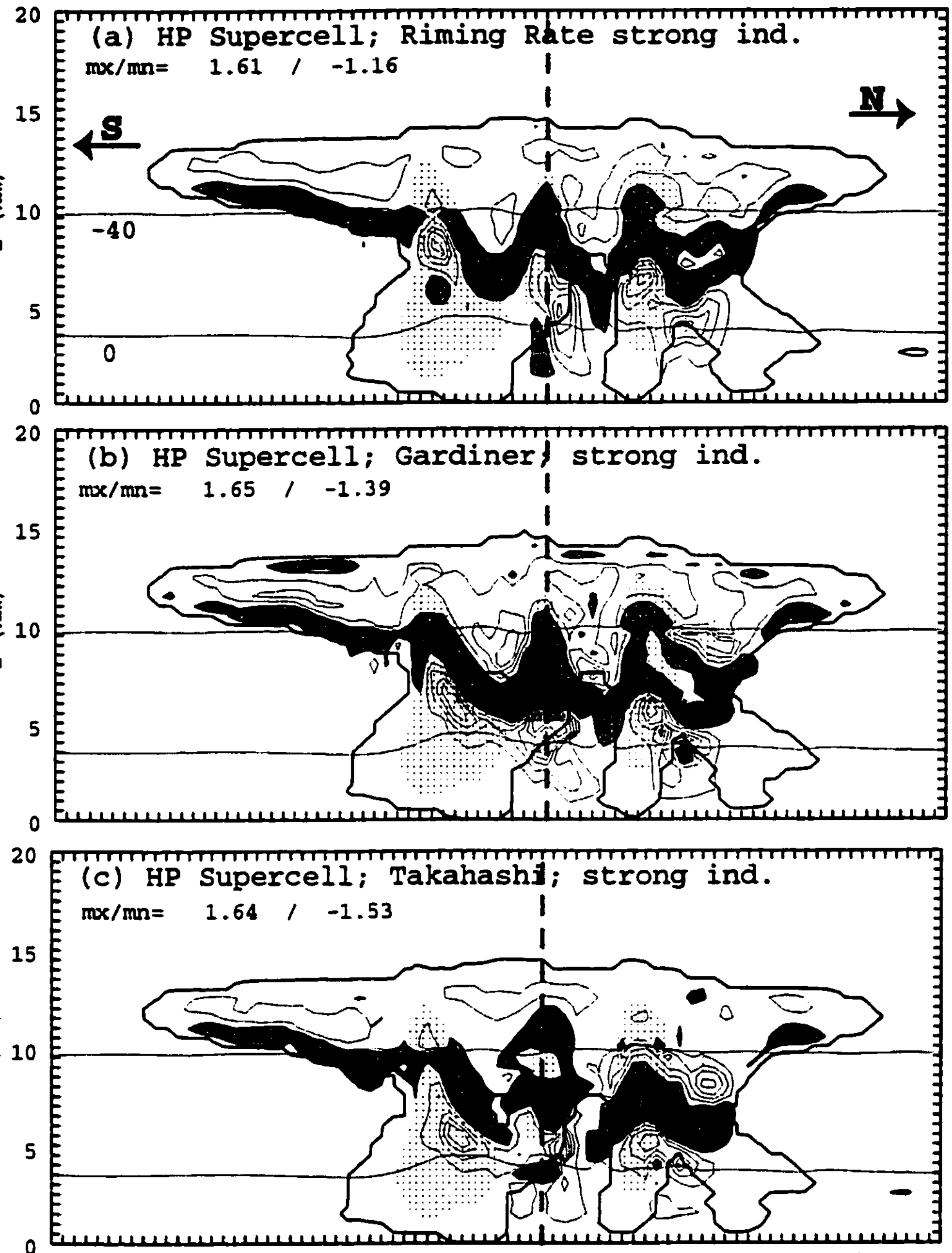

Figure 7.4: Charge density contours (north-south) for the HP supercell storms. The slices go through three updraft regions (x = 25.2 km) The view is from the east at a time of 85 minutes. Negative charge regions are gray. Contour intervals are 0.3 nC m^{-3}, starting at $\pm$0.15. The heavy line outlines the cloud boundary (not including precipitation). Dotted regions indicate updraft of 10 m/s or greater. Maximum and minimum values for the charge slice are given in each panel.

7.2 Riming Rate Noninductive Charging

The initial charge structure was somewhat complicated, but could be described grossly as a positive dipole (positive charge over negative). Two +CG flashes were produced during the early dipole stage. A significant lower positive charge did not develop until about 40 minutes, when it began to be involved in IC flashes.

An upper negative screening layer formed only on the northeast half of the cloud top and anvil. A positive screening layer developed on the underside of the northeast quarter of the anvil, but a lower negative screening layer formed on the southwestern part of the anvil. IC flashes involving the upper negative layer occurred in the eastern/northeastern quadrants of the anvil. The southern and western quadrants were marked by flashes between the negative screening layer on the anvil underside and the positive charge above. The lightning-induced negative layer in the anvil eventually promoted a few IC flashes with the lower positive layer of snow which appeared below the anvil by sedimentation.

Inductive charging rates were quite similar to those of the Gardiner run, though noninductive rates were smaller in magnitude (compare Figures 7.6b and 7.8b). Also, notice that the inductive charging oscillations (Figure 7.6b) tended to be 180 degrees out of phase from those in the Gardiner case (Figure 7.8b). This fact may explain some of the different charge structures in the southern storm updraft (Figure 7.4a and b), where inductive charging has the greatest effect.

7.3 Gardiner Noninductive Charging

The Gardiner noninductive charging produced the strongest electrification and the most lightning activity of the HP supercell simulations. A prominent feature was the substantial number of positive ground strikes produced. Most of the +CG flashes occurred near the forward flank of the storms, and some struck closer to and within the surface precipitation.

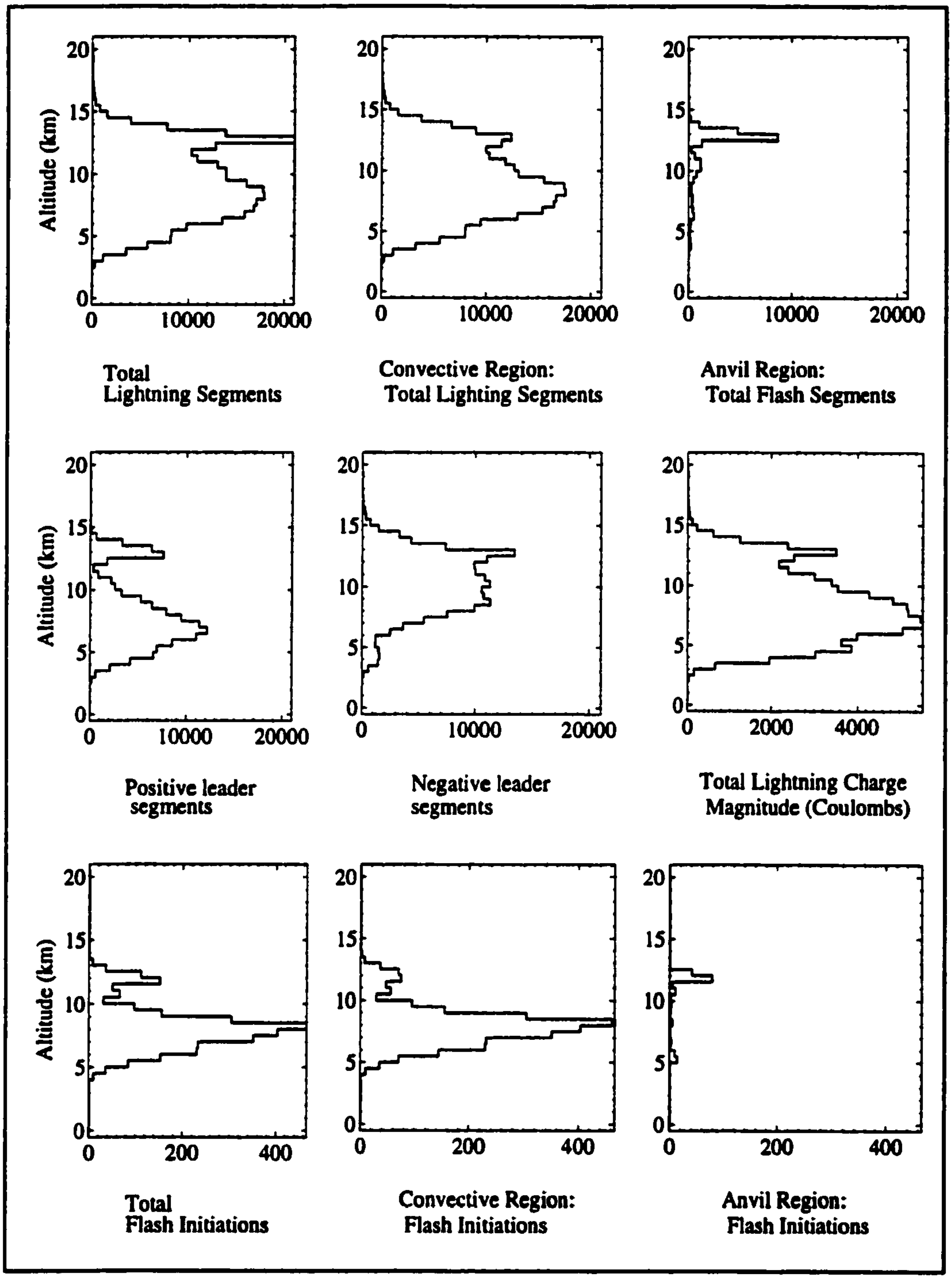

Figure 7.5: Total lightning channel segments and initiations versus height (HP supercell, riming rate noninductive, strong inductive). Values are integrated over the whole simulation time. Lightning segments are split into positive and negative leaders or into convective and and anvil regions. Total charge is sum of absolute values of charge deposited by lightning.

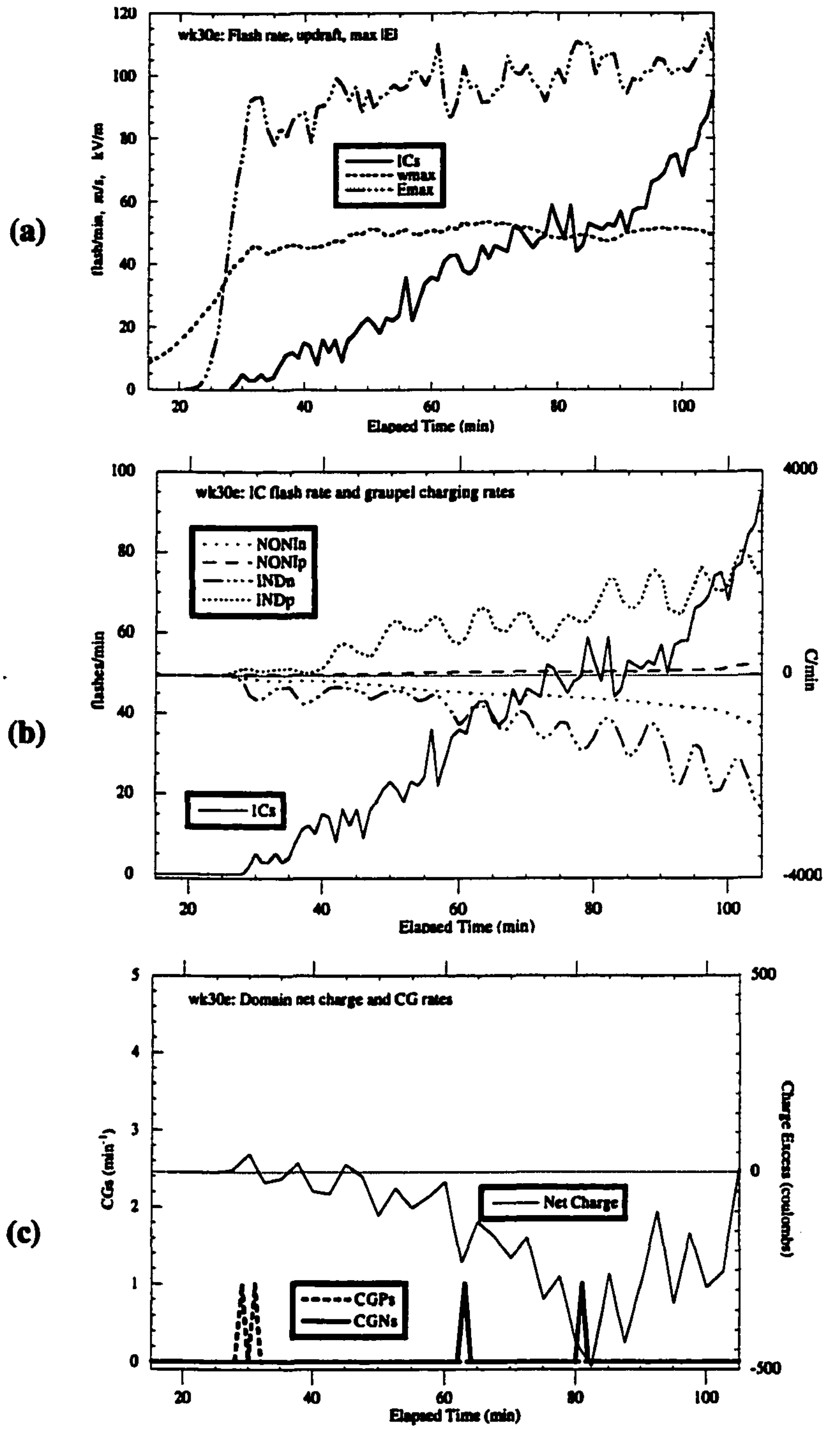

Figure 7.6: Lightning time series plots for HP supercell (riming rate noninductive, strong inductive). (a) IC flash rate (min^{-1}), maximum updraft, and maximum electric field magnitude at one-minute intervals. (b) Domain-integrated noninductive and inductive graupel charging rates (C/min), positive and negative values are summed separately. (c) Domain net charge and CG flash rates. All values are sampled at 1-minute intervals except domain net charge, which has 2.5-minute intervals. (Flash rates are 1-minute totals.)

Also, some of the +CG flashes occurred close to the bounded weak echo region.

Near the end of the simulation, one of the +CG flashes occurred in the precipitation core of the northwestern storm. The strike was preceded by the elevation of the lower positive charge and the appearance of a negative charge region below. The new lower negative region was at about the same altitude as the lower positive charge had been. This polarity switch was caused by inductive charge separation and will be discussed further in Chapter 10. Inductive charging produced negatively charged graupel and hail below positively charged cloud droplets. The cloud droplets were carried by the updraft and intensified the positive charge region. The +CG flash was then initiated between the new negative region and the positive charge region above it.

7.4 Takahashi Noninductive Charging

The lightning layer structure produced by the Takahashi parameterization was noticeably different from that produced by the riming rate and Gardiner parameterizations. The vertical distribution of negative leader segments (Figure 7.9, center-center) had two peaks instead of the one broader peak seen in Figures 7.5 and 7.7 for the other two parameterizations. The lower peak in negative leader segments at 4.5 km was a result of a lower positive charge layer that was more horizontally extensive than with the other noninductive schemes. The lightning composite in Figure 7.2c clearly shows the greater stratification of the lightning. Also, there was much less overlap between the lower positive leader segment peak (5–10 km) and the upper negative leader peak (10–15 km), indicating that the altitudes of the main positive and negative charge regions were more distinctly separate (Figure 7.9, center-left and center-center).

The −CG flashes during 80–90 minutes occurred mostly within the 3 g/kg surface precipitation contours. Subsequent −CG flashes (90–105 minutes) all occurred in the northern half of the storm complex and at the western edge of the 1 g/kg contour of surface precipitation.

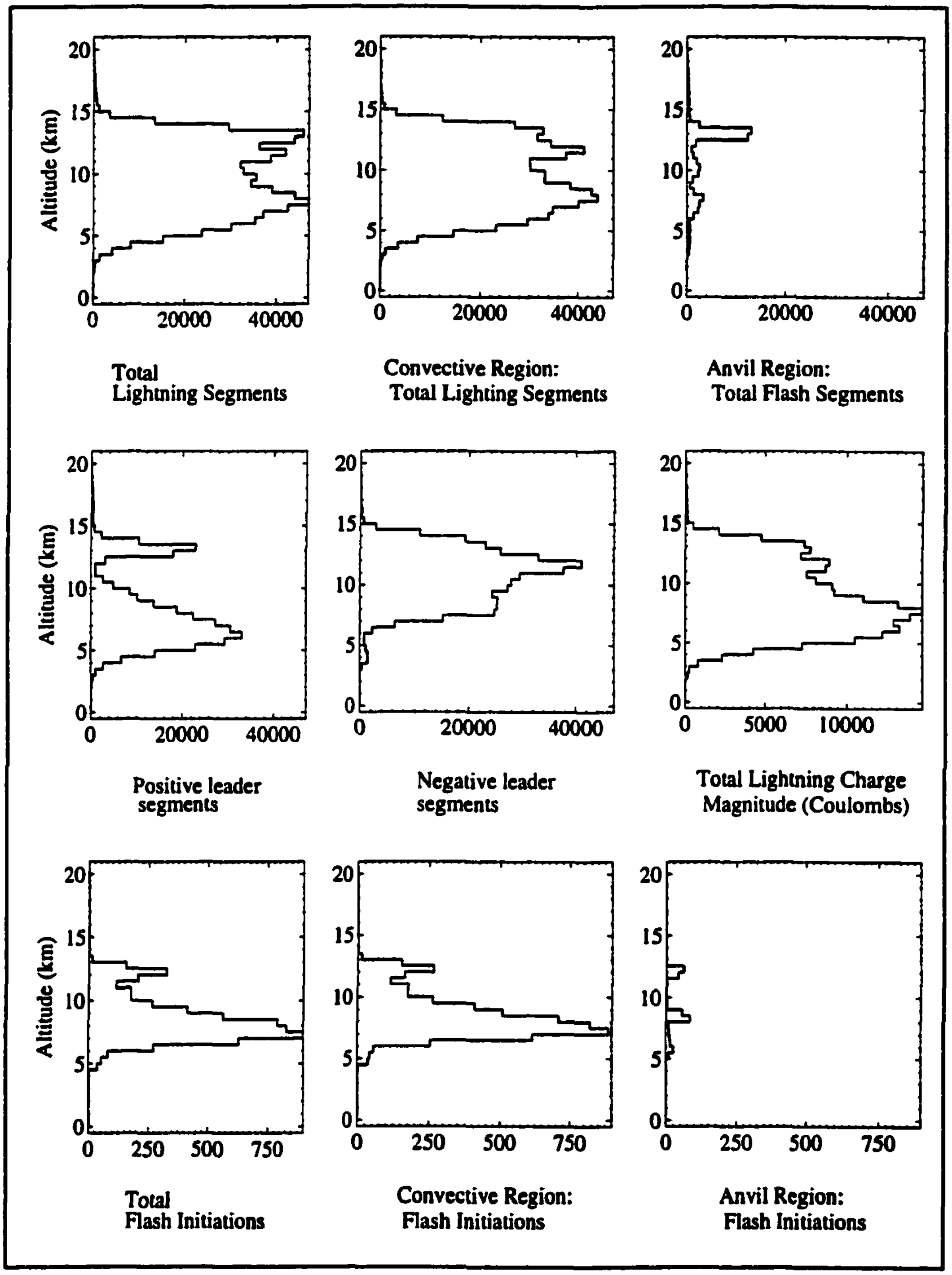

Figure 7.7: Total lightning channel segments and initiations versus height for HP supercell (Gardiner noninductive, strong inductive). Values are integrated over the whole simulation time. Lightning segments are split into positive and negative leaders or into convective and and anvil regions. Total charge is sum of absolute values of charge deposited by lightning.

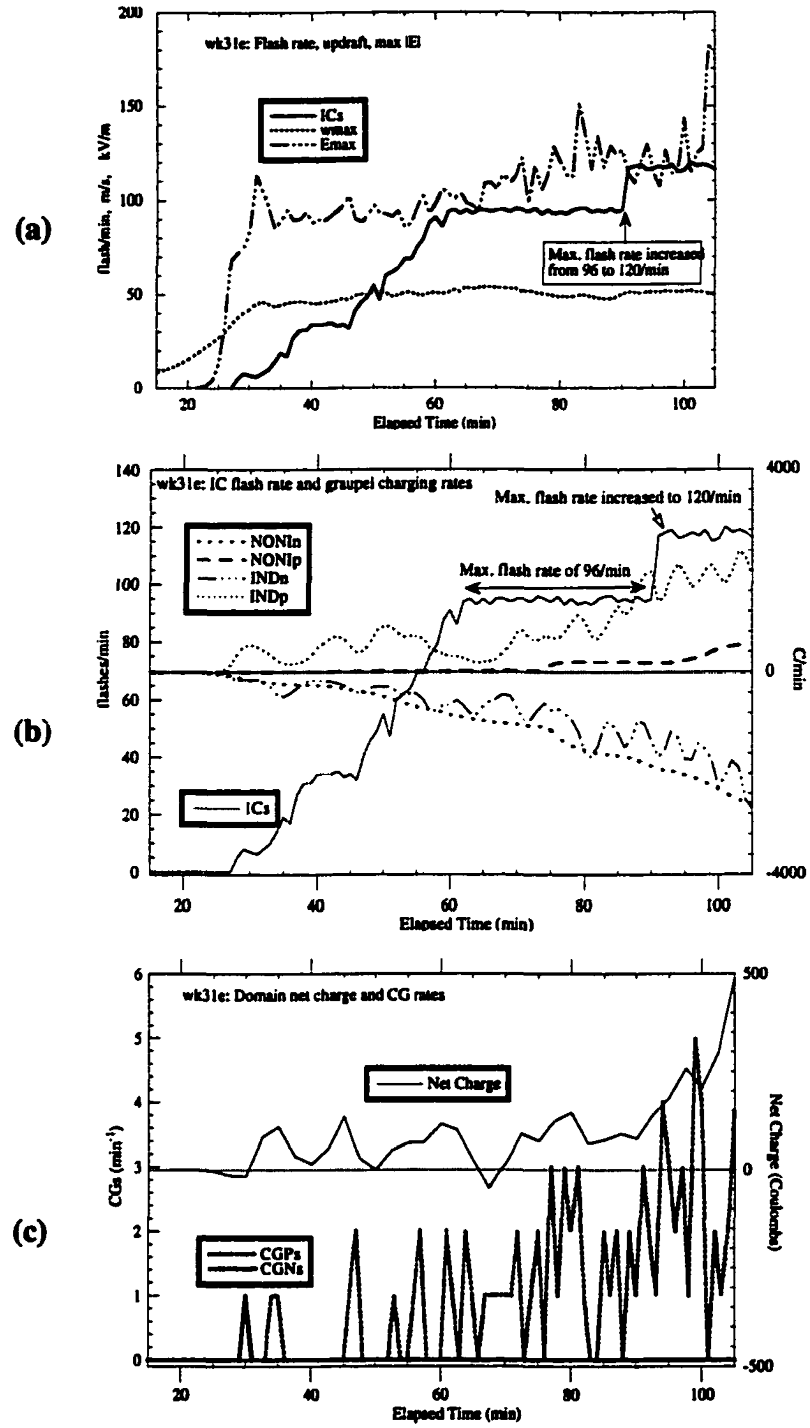

Figure 7.8: Lightning time series plots for HP supercell (Gardiner noninductive, strong inductive). (a) IC flash rate (min^{-1}), maximum updraft, and maximum electric field magnitude at one-minute intervals. (b) Domain-integrated noninductive and inductive graupel charging rates (C/min), positive and negative values are summed separately. (c) Domain net charge and CG flash rates. All values are sampled at 1-minute intervals except domain net charge, which has 2.5-minute intervals. (Flash rates are 1-minute totals.)

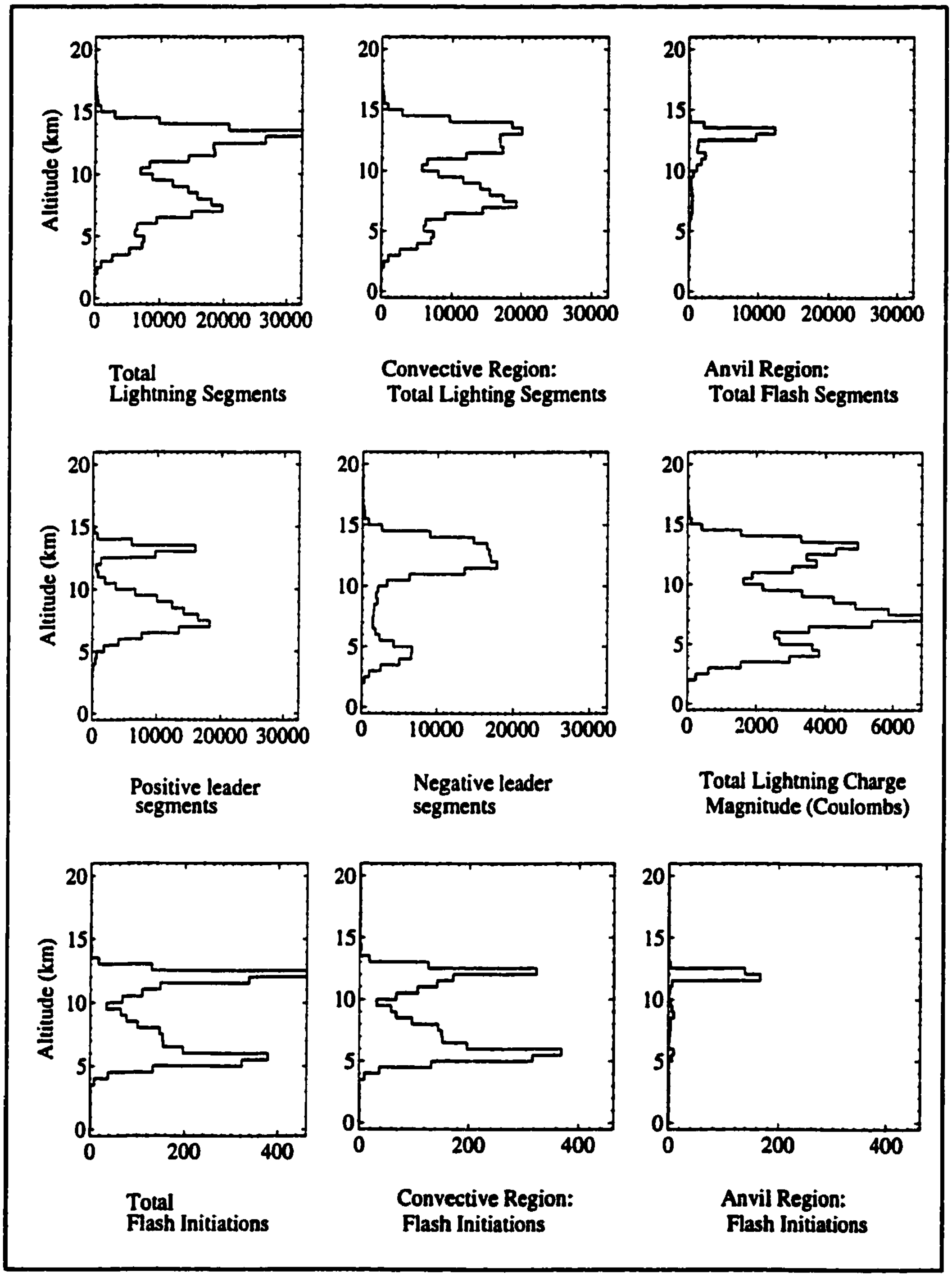

Figure 7.9: Total lightning channel segments and initiations versus height for HP supercell (Takahashi noninductive, strong inductive). Values are integrated over the whole simulation time. Lightning segments are split into positive and negative leaders or into convective and and anvil regions. Total charge is sum of absolute values of charge deposited by lightning.

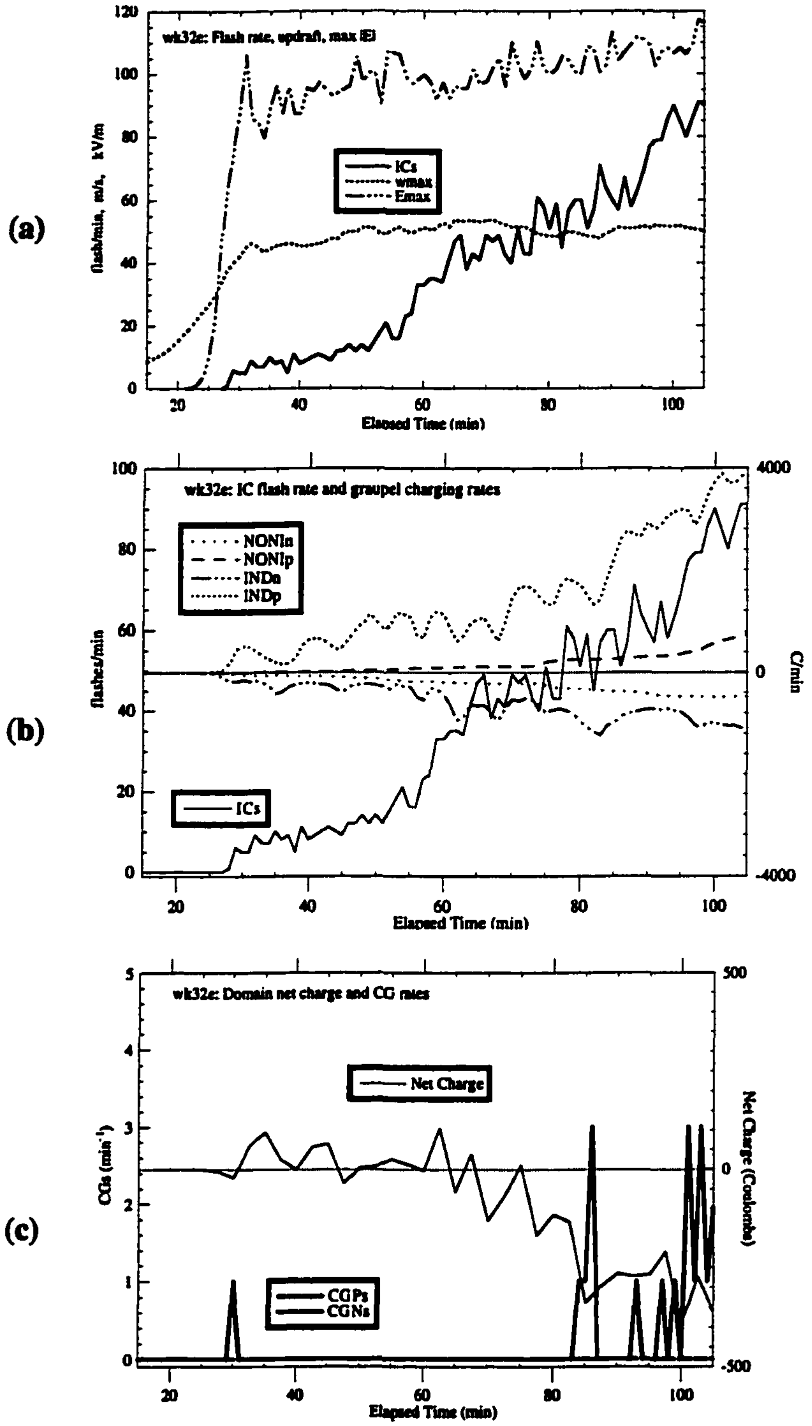

Figure 7.10: Lightning time series plots for HP supercell (Takahashi noninductive, strong inductive). (a) IC flash rate (min^{-1}), maximum updraft, and maximum electric field magnitude at one-minute intervals. (b) Domain-integrated noninductive and inductive graupel charging rates (C/min), positive and negative values are summed separately. (c) Domain net charge and CG flash rates. All values are sampled at 1-minute intervals except domain net charge, which has 2.5-minute intervals. (Flash rates are 1-minute totals.)

7.5 Enhanced Riming Rate Noninductive Charging

An extra simulation also used strong induction, but with a version of the riming rate noninductive scheme with enhanced charge separation (i.e. increased separated charge per collision; refer to Section 5.1.1). Time constraints prevented a detailed analysis of this simulation, so it is excluded from any general comparisons of the HP supercell simulations unless it is explicitly mentioned.

Some results from the test with enhanced riming rate charging are shown in Figure 7.11. As expected, the noninductive charging rates were higher than for the regular riming rate scheme (Figure 7.6) and IC flash rates were about 50% higher. The net charge of the domain also changed more quickly to positive values during the final 25 minute period, and some +CG flashes were produced in the last five minutes. The general effect appeared to be to nudge the results from the regular riming rate noninductive charging scheme toward the results of the Gardiner charging scheme.

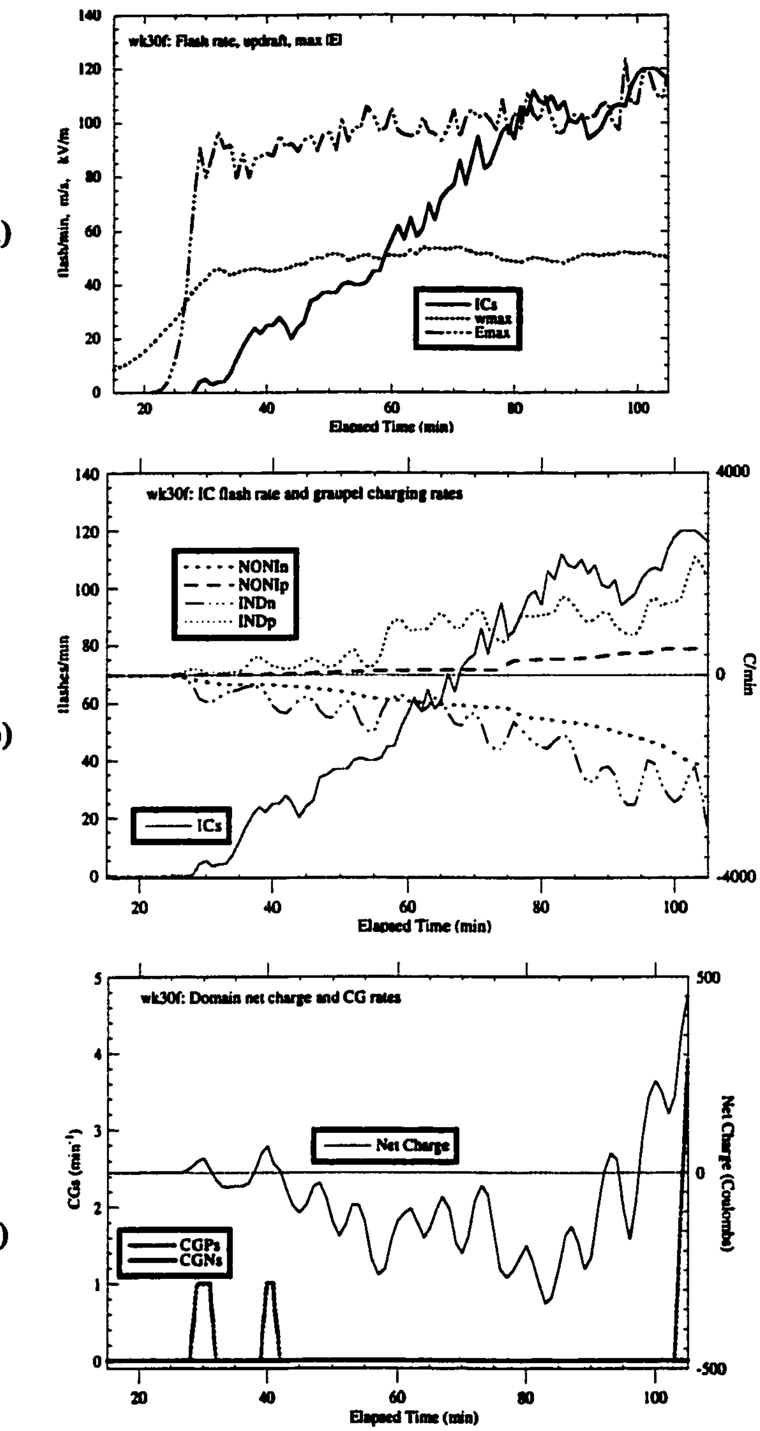

Figure 7.11: Lightning time series plots for HP supercell (enhanced riming rate noninductive, strong inductive). (a) IC flash rate (min^{-1}), maximum updraft, and maximum electric field magnitude at one-minute intervals. (b) Domain-integrated noninductive and inductive graupel charging rates (C/min), positive and negative values are summed separately. (c) Domain net charge and CG flash rates. All values are sampled at 1-minute intervals (including domain net charge). Flash rates are 1-minute totals.

Chapter 8

Low Precipitation Supercell Simulations

8.1 LP Supercell General Characteristics

The environmental temperature profile was again the same as for the airmass storm, but the moisture profile was modified by reducing the water vapor aloft (refer to Section 5.1.2). The extreme wind shear prevented an upshear anvil from forming and limited the maximum updraft speeds, which were the lowest of the supercell storms. The LP storm anvils were long and narrow and propagated quickly across the domain. The precipitation fields had no discernible hook structures. The initial storm began splitting approximately 40 minutes after convection was initiated. The split had progressed enough 20 minutes later that two distinct convective towers were visible. The northern storm remained slightly weaker than the southern storm, which had a wider updraft region. The horizontal component of wind in the southern storm had cyclonic (counterclockwise) rotation throughout the updraft, with an obvious weak echo region on the southern flank. The winds in the updraft of the northern storm were clearly anticyclonic at midlevels of the storm.

The northern storm intensified slowly until it encountered the northern boundary. The updraft region of the northern storm was elongated, and a new updraft center developed at its western end. The northern storm developed a weak echo region at its northern flank in the vicinity of its main (eastern) updraft.

The anvils reached the eastern boundary of the model domain by 60 minutes of elapsed time. By 80 minutes, they were also exiting through the northern boundary (northeast corner). Then by 97 minutes the convective region of the northern storm also began to exit through the northern boundary. Most of its anvil had already left the domain. The edge of its updraft also encountered the northern boundary at the end of the simulation (105 minutes). The influence of the northern boundary (an artifact of the finite domain) had different effects in the three simulations: For the Takahashi and riming rate cases, snow aggregates developed in the updraft of the northern storm during the final 3–6 minutes. The snow had little effect on charging rates in the riming rate run, but it caused a noticeable increase in positive noninductive charging of graupel in the Takahashi case (Figure 8.8b). There was no comparable effect in the simulation using Gardiner charging.

As noted for the HP supercell simulation (Section 7.2), oscillations in the inductive charging for the riming rate and Gardiner cases tended to be out of phase. Strong inductive charging caused complex charge evolution in the updraft regions (see Chapter 10) and was a likely cause for the different charge structures found for the riming rate and Gardiner cases in the updrafts in Figures 8.4a and 8.4b.

8.2 Riming Rate Noninductive Charging

The gross charge distribution produced by the riming rate parameterization early in the simulated LP supercell storm was an inverted dipole (negative charge over positive). The inverted dipole resulted from the initially high rime accretion rates, which caused graupel to acquire positive charge. However, no lightning occurred until 23 minutes elapsed time, after the charge structure had flipped to the more commonly observed positive charge over negative. After about 60 minutes elapsed time, positive leaders of IC flashes occasionally propagated 20–30 km through negative charge along the underside of the anvil. Anvil flashes in the upper negative screening layer began around 80 minutes elapsed time, and by 90 minutes the anvil flashes were restricted by the northern and eastern domain boundaries. Many of the flashes in the anvil were completely outside the convective

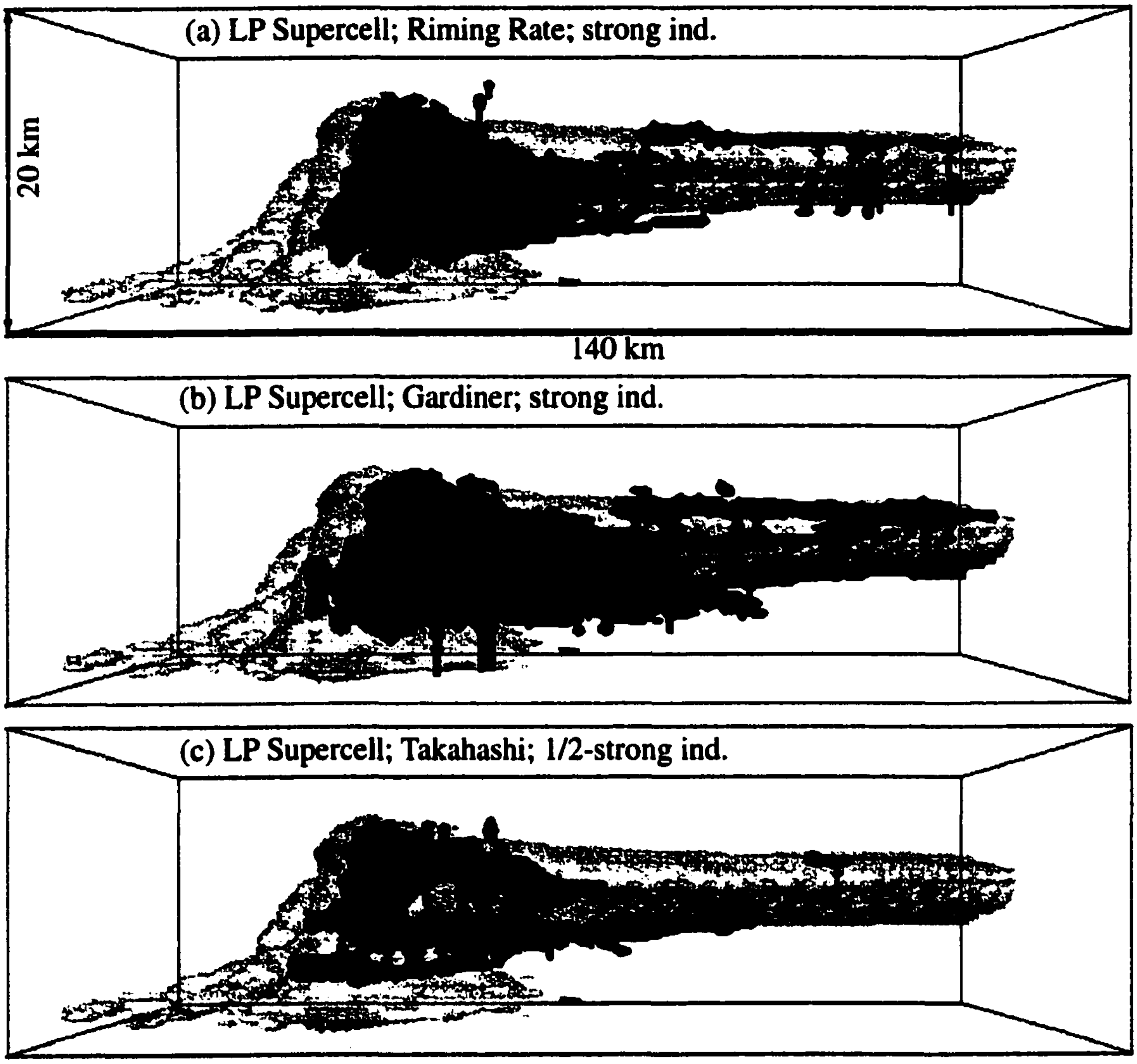

Figure 8.1: LP supercell lightning composites for three noninductive mechanisms. The view is from the south at 92.5 minutes elapsed time. Contours outline lightning channels occurring over a 2.5-minute period. Negative leaders are colored orange, and positive leaders are blue. Cloud ice and cloud water contours are pale gray. Green contours indicate where lightning flashes were initiated.

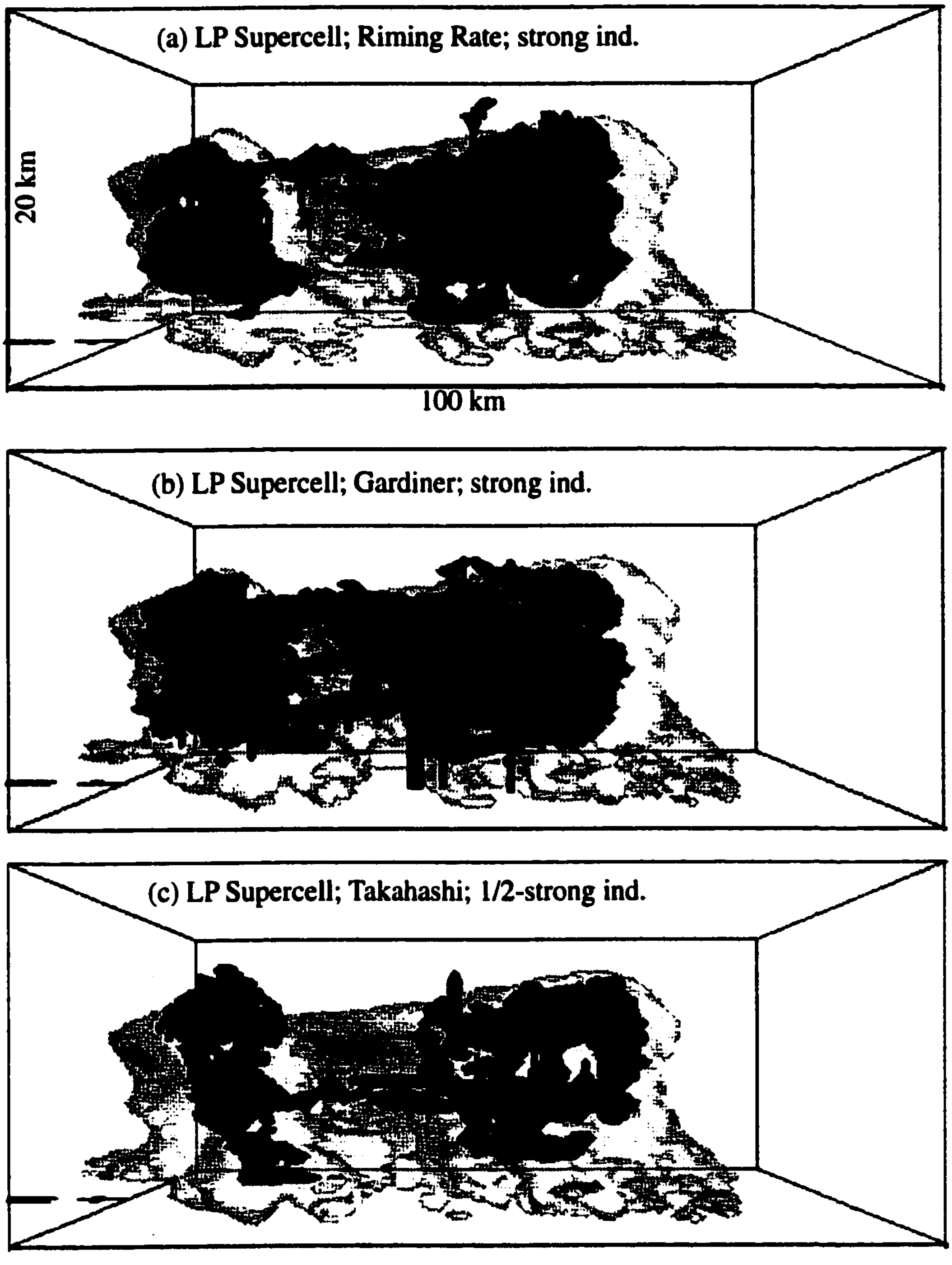

Figure 8.2: LP supercell lightning composites for three noninductive mechanisms. The view is from the west at 92.5 minutes elapsed time. Contours outline lightning channels occurring over a 2.5-minute period. Negative leaders are colored orange, and positive leaders are blue. Cloud ice and cloud water contours are pale gray. Green contours indicate where lightning flashes were initiated.

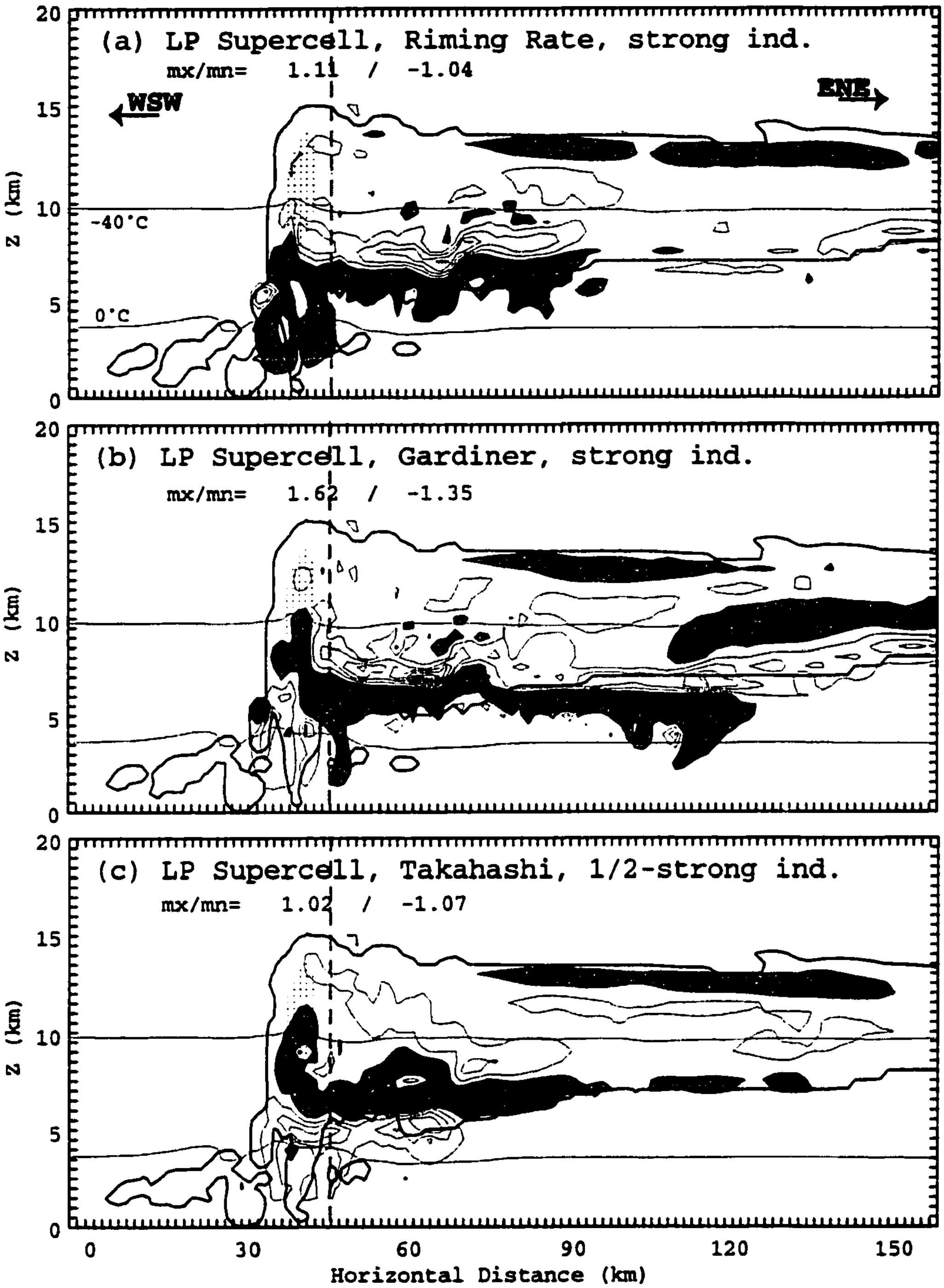

Figure 8.3: Charge density contours (parallel to southern storm anvil) for the LP supercell storms. Gardiner and riming rate versions use strong inductive charging, but Takahashi version is with $\frac{1}{2}$-strong induction. The slices are taken through the southern storm, just to the north of the main updraft. The view is from the south-SE at a time of 92.5 minutes. Negative charge regions are gray. Contour intervals are 0.3 nC m^{-3}, starting at ± 0.15. The heavy line outlines the cloud boundary (not including precipitation). Dotted regions indicate updraft of 10 m/s or greater. Maximum and minimum values for the charge slice are given in each panel.

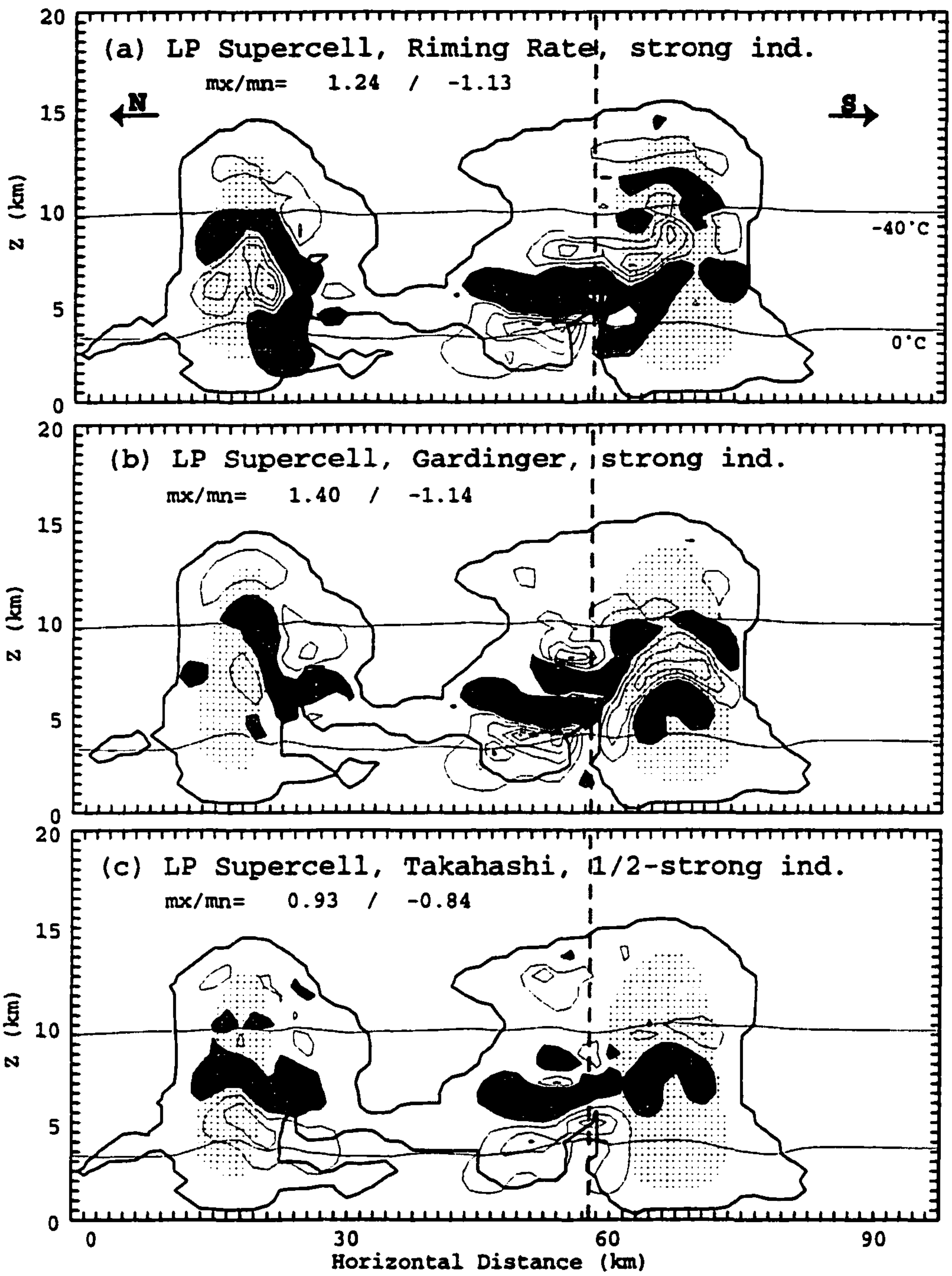

Figure 8.4: Charge density contours (north-south) for the LP supercell storms. The slices go through three updraft regions ($x \approx 35$ km) The view is from the west at a time of 92.5 minutes. Negative charge regions are gray. Contour intervals are 0.3 nC m^{-3}, starting at ± 0.15. The heavy line outlines the cloud boundary (not including precipitation). Dotted regions indicate updraft of 10 m/s or greater. Maximum and minimum values for the charge slice are given in each panel.

region and did not overlap the lightning from the convective region.

A few CG flashes of both polarities occurred early in the simulation (25–45 minutes elapsed time), but most of the CG flashes occurred after 60 minutes. The burst of +CG flashes starting at about 65 minutes had two main clusters, one in each of the two storms that had split apart. In each storm, +CG clusters occurred at the downshear (ENE) edge of the midlevel updraft. The strike points were near the edge of the surface precipitation to the side of the respective updrafts. Additional +CG flashes occurred in the forward flank region ahead of the surface precipitation. The subsequent peak in −CG flashes beginning at 75 minutes also involved both storms. A majority of the −CG flashes in the southern storm occurred within the surface precipitation, and a few struck at the edge of the surface precipitation beneath the weak echo region. The −CG flashes in the northern storm occurred in nearly the same location as the earlier +CG cluster: near the outside edge of the surface precipitation and under the weak echo region.

The rapid switch in CG flash polarity appears to be correlated to reversals of inductive charging. Figures 8.6b and 8.6c show large oscillations of inductive charging and corresponding shifts in CG flash rates and in the net charge of the domain. It is unclear what determines the period of the charging oscillations. Inspection of time-lapse contour plots (not shown) indicated that the southern and northern storms were nearly "in phase" in their charging oscillations during the 60–90 minute time period. This case contrasts with the corresponding HP supercell simulation with riming rate charging, which had smaller and more rapid inductive charging oscillations.

This case was the only one which produced fairly large numbers of both positive and negative CG flashes, with alternating periods in which one or the other polarity dominated.

8.3 Gardiner Noninductive Charging

The Gardiner case had the largest charge separation rates and lightning flash rates of the LP supercell simulations. One difference from the other LP supercell simulations is seen in the anvil lightning in Figure 8.1. In the other cases, anvil flashes were initiated just below the upper negative screening layer. In the Gardiner case, however, most anvil discharges started just above a positive charge layer of strongly charged snow near the lower boundary of the anvil (Figure 8.3b at 100–140 km horizontal distance). The positive charge at the far eastern, thinner part of the anvil is partly due to a positive screening layer on cloud ice. Above the positive layer the net charge was negative because of ice crystals that had gained negative charge from lightning and advected down the anvil. (A short distance below the negative charge, there appears also to be a strong negative screening layer on ice crystals at the lower cloud boundary, but the net charge at the boundary remained net positive because of the high positive charge densities carried by falling snow.) The lightning in the convective region thus indirectly influenced the lightning in the anvil.

With the Gardiner noninductive parameterization, the average altitude of lightning initiations in the anvil was considerably lower than it was with the other two noninductive parameterizations for the LP supercell (mostly between 8.0–9.5 km versus 11.0–12.0 km) (lower, rightmost panel of Figures 8.5, 8.7, and 8.9). This difference is also apparent in the vertical distribution of lightning segments in the anvil, where the Gardiner parameterization is the only one with a sharp lower peak at 7.5 km (compare the top right panel of Figure 8.7 with those of Figures 8.5 and 8.9). The lower peak resulted from lightning (negative leaders) propagating through the thin lower positive charge layer.

The +CG flash activity during the 70–80 minute period (Figure 8.8c) included flashes from both the southern and northern storms. The +CG flashes during the 80–85 minute period were all associated with the northern storm. Then the southern storm produced all but one of the +CG flashes during the 90–100 minute period, and the northern storm produced all of the subsequent ground flashes. Both storms produced +CG flashes in both the forward flank and the weak echo (updraft) regions.

8.4 Takahashi Noninductive Charging

The simulation with the Takahashi noninductive parameterization used "half-strong" inductive charging in an attempt to limit the dominance of inductive charging in the early electrification of the storm. However, even with reduced inductive charging, a majority of the lightning activity occurred between the main negative and lower positive charge regions during the first 30 minutes after the first flash. (Note the generally lower altitude for initiations in Figure A.13b compared with those in Figures A.11b and A.12b.) By one hour of elapsed time, the main lightning activity had shifted to the main negative and upper positive regions, though lightning in the lower positive region remained significant throughout the simulation.

No anvil flashes occurred until 90 minutes after initiation of convection. The single +CG flash at 84 minutes occurred in the northern storm. The +CG flash was initiated in the updraft region (along with a couple IC flashes) when a pocket of lower negative charge developed in the weak echo region. As can be seen in Figure 8.10b, there was a sharp increase in the negative inductive charging (INDn) of graupel shortly before this, at about 80 minutes.

At about 90 minutes, negative leaders began to propagate into the lower positive charge region in the forward flank of the southern storm. As it was for the other simulations using the Takahashi parameterization, positive noninductive charging of graupel was responsible for the lower positive charge layer in the forward flank of the storm (Figure 8.3c). This positive charging contributed to the notably different character of the vertical distribution of lightning segments (compare the top left panel of Figure 8.9 with that of Figures 8.5 and 8.7). There was more distinct layering of lightning activity than was seen with the other two noninductive parameterizations (Figures 8.1 and 8.2).

The Takahashi scheme maintained flatter charge layers (Figures 8.3 and 8.4), resulting in the more distinct layers of lightning segments. A very similar feature was found in the HP supercell simulations.

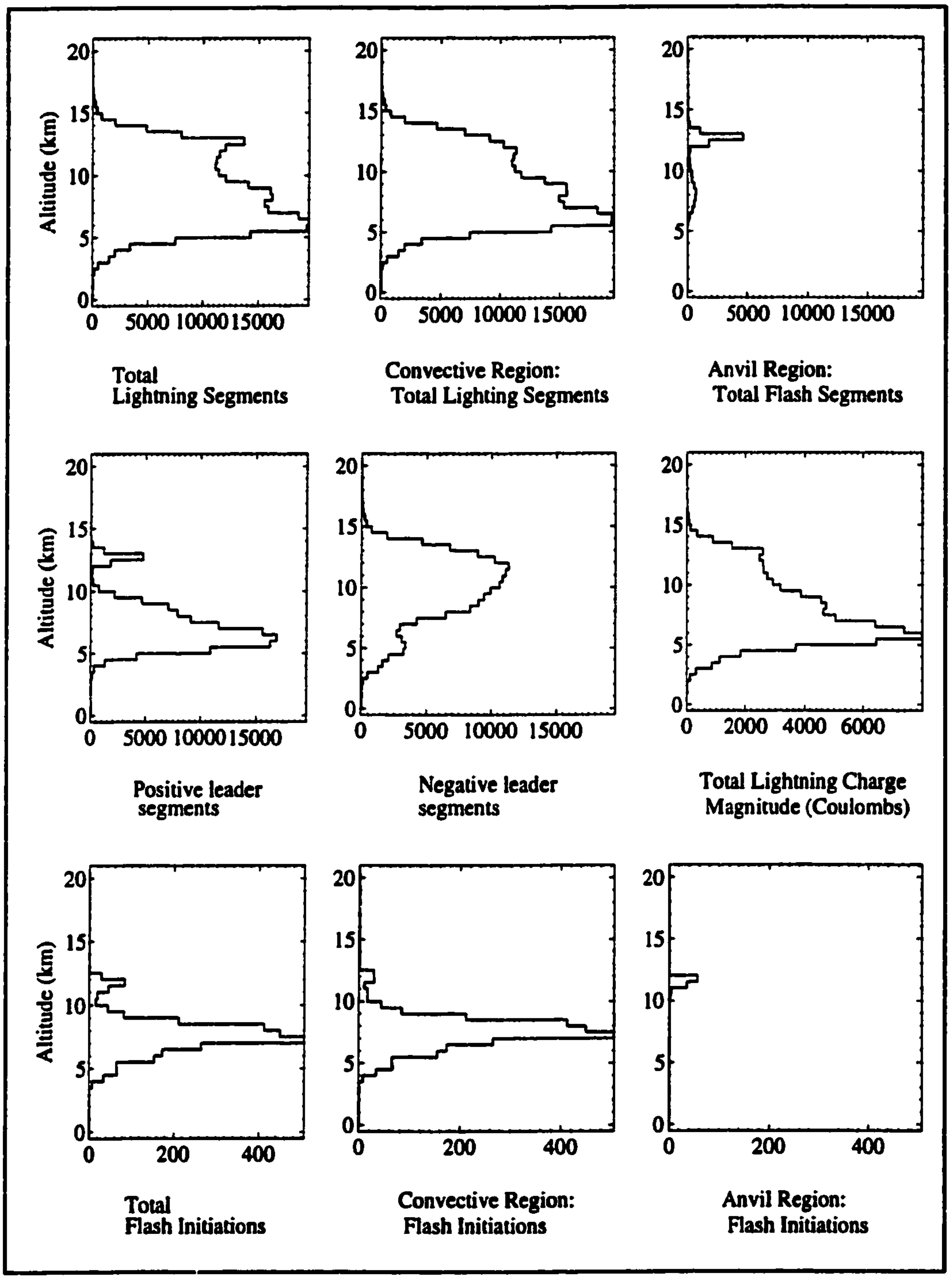

Figure 8.5: Total lightning channel segments and initiations versus height for LP Supercell (riming rate, strong inductive). Values are integrated over the whole simulation time. Lightning segments are split into positive and negative leaders or into convective and and anvil regions. Total charge is sum of absolute values of charge deposited by lightning.

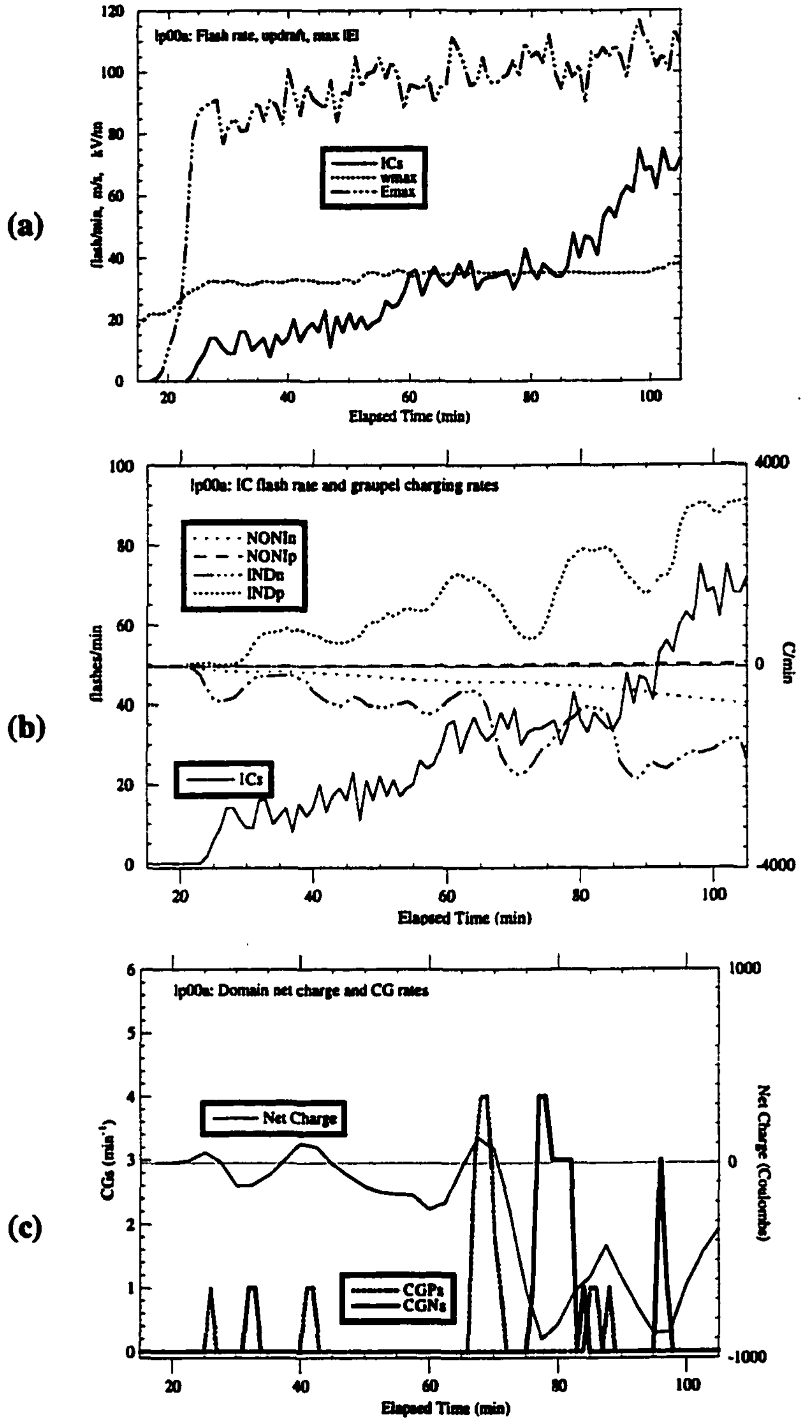

Figure 8.6: Lightning time series plots for LP Supercell (riming rate, strong inductive). (a) IC flash rate ($\min^{-1}$), maximum updraft, and maximum electric field magnitude at one-minute intervals. (b) Domain-integrated noninductive and inductive graupel charging rates (C/min), positive and negative values are summed separately. (c) Domain net charge and CG flash rates. All values are sampled at 1-minute intervals except domain net charge, which has 2.5-minute intervals. (Flash rates are 1-minute totals.)

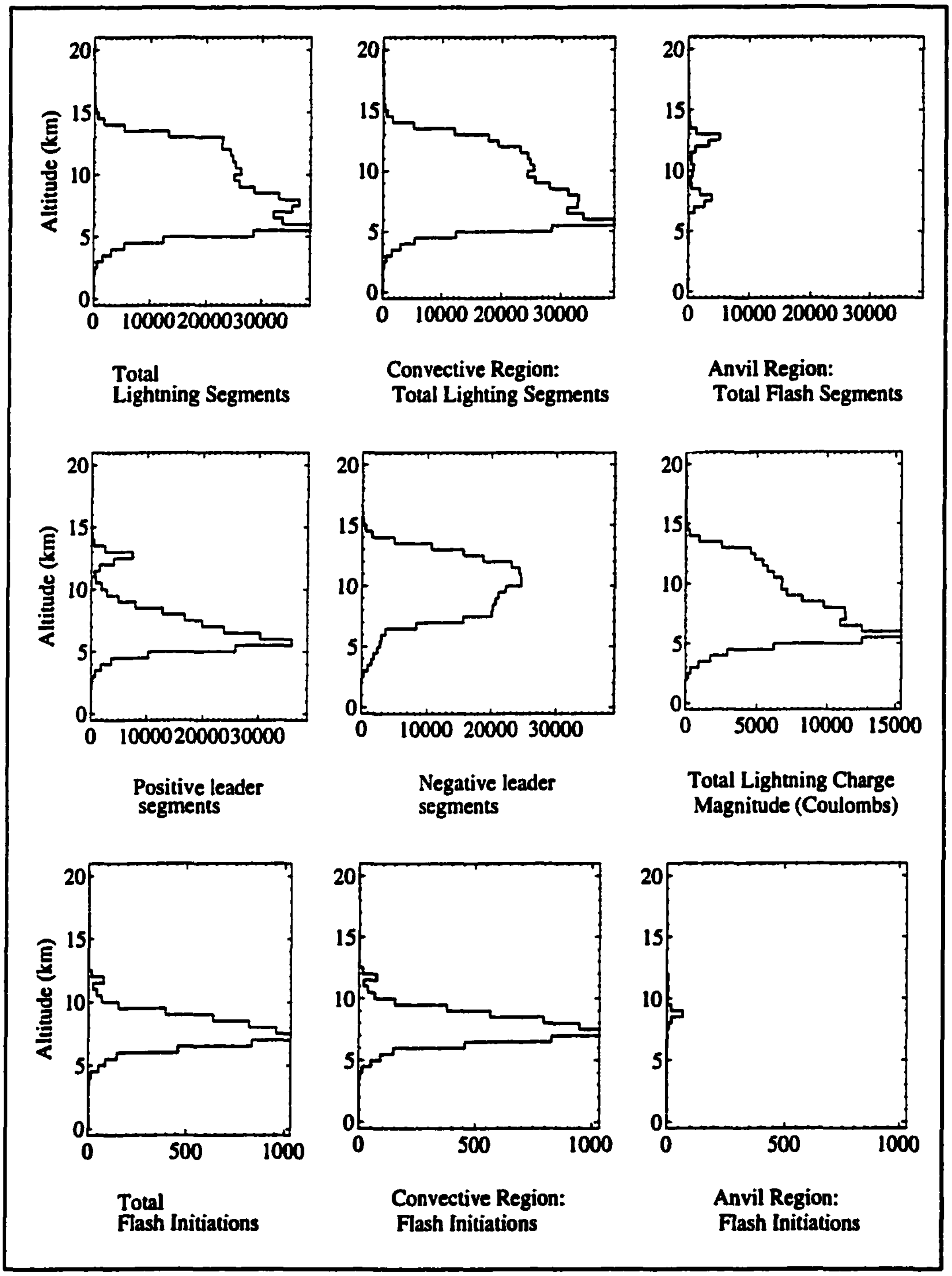

Figure 8.7: Total lightning channel segments and initiations versus height for LP Supercell (Gardiner, strong inductive). Values are integrated over the whole simulation time. Lightning segments are split into positive and negative leaders or into convective and and anvil regions. Total charge is sum of absolute values of charge deposited by lightning.

(a)

(b)

(c)

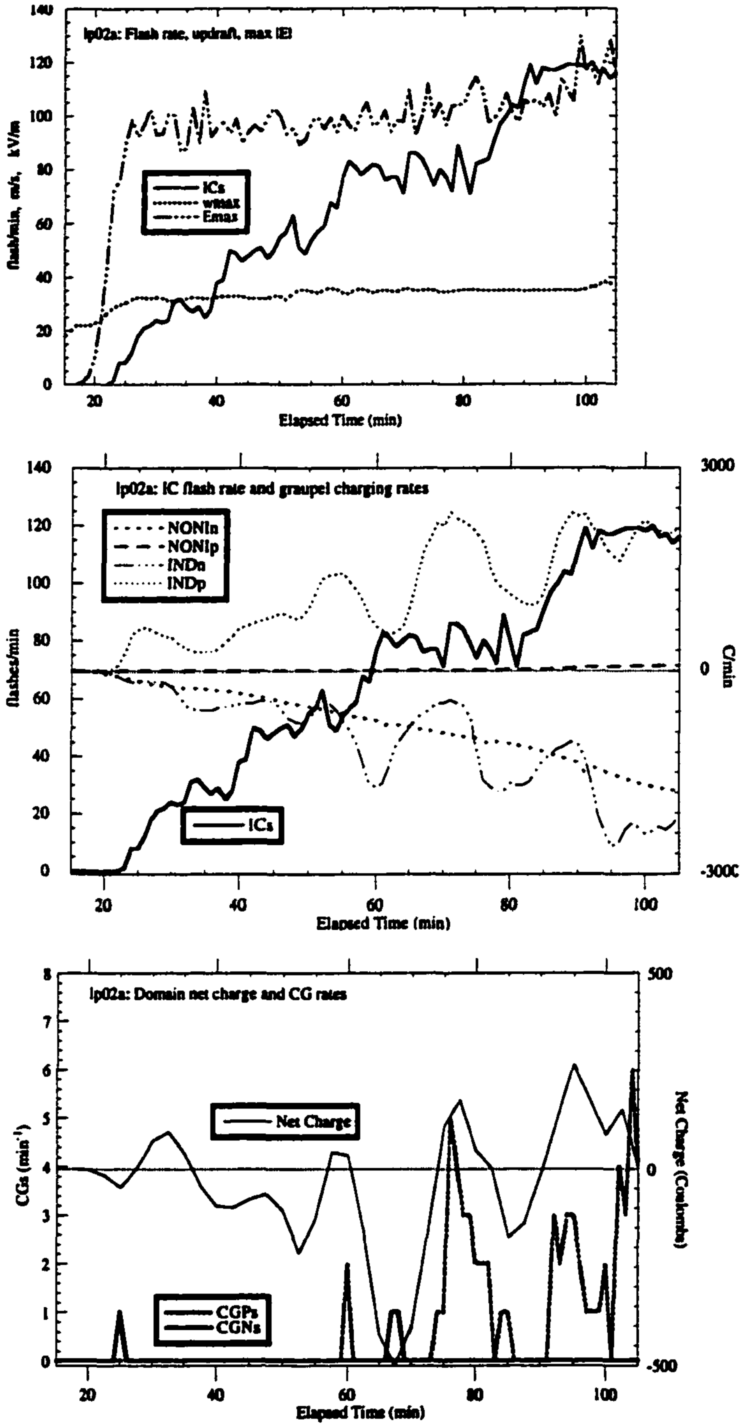

Figure 8.8: Lightning time series plots for LP Supercell (Gardiner, strong inductive). (a) IC flash rate (min^{-1}), maximum updraft, and maximum electric field magnitude at one-minute intervals. (b) Domain-integrated noninductive and inductive graupel charging rates (C/min), positive and negative values are summed separately. (c) Domain net charge and CG flash rates. All values are sampled at 1-minute intervals except domain net charge, which has 2.5-minute intervals. (Flash rates are 1-minute totals.)

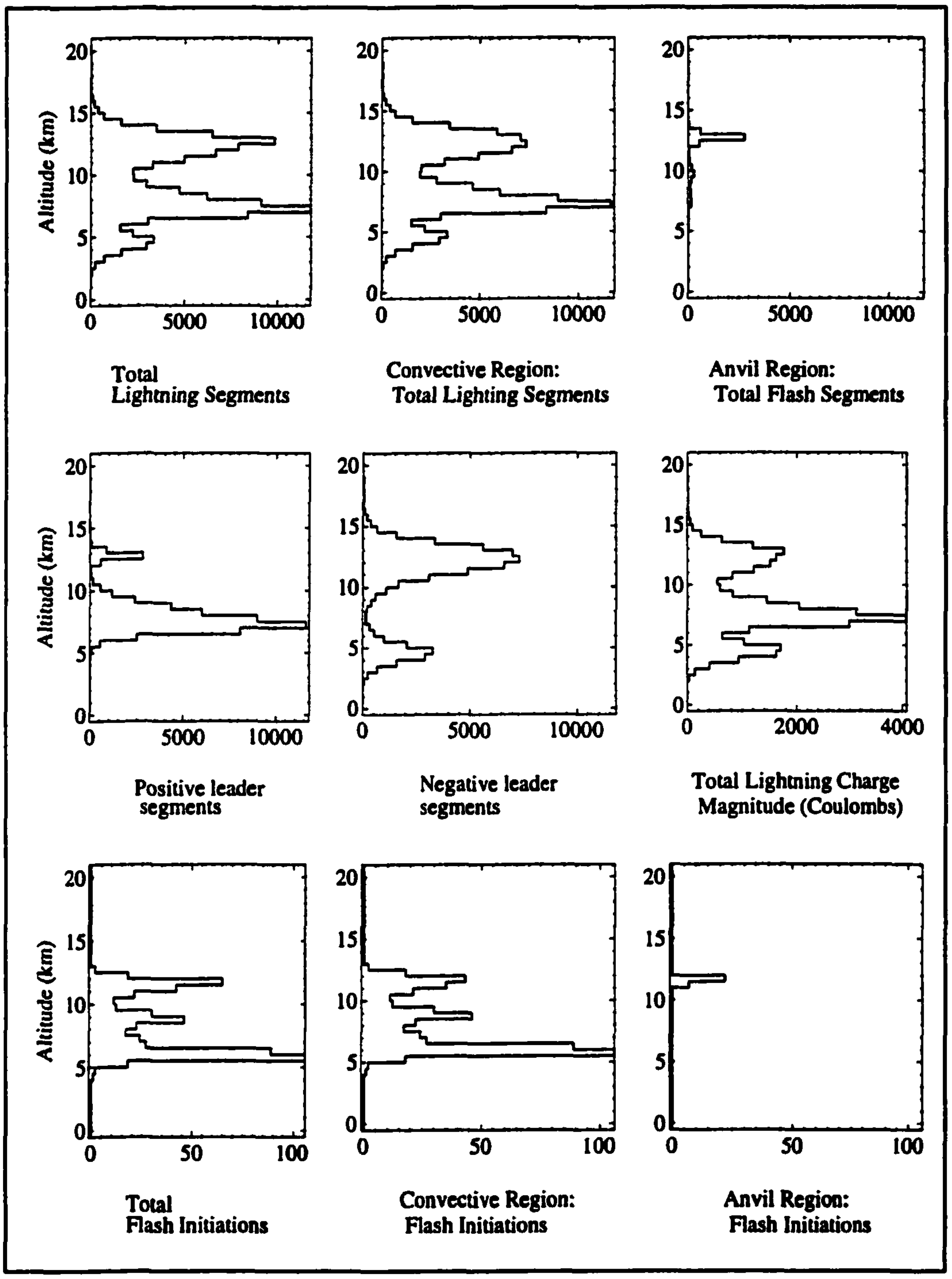

Figure 8.9: Total lightning channel segments and initiations versus height for LP Supercell (Takahashi, $\frac{1}{2}$-strong inductive). Values are integrated over the whole simulation time. Lightning segments are split into positive and negative leaders or into convective and and anvil regions. Total charge is sum of absolute values of charge deposited by lightning.

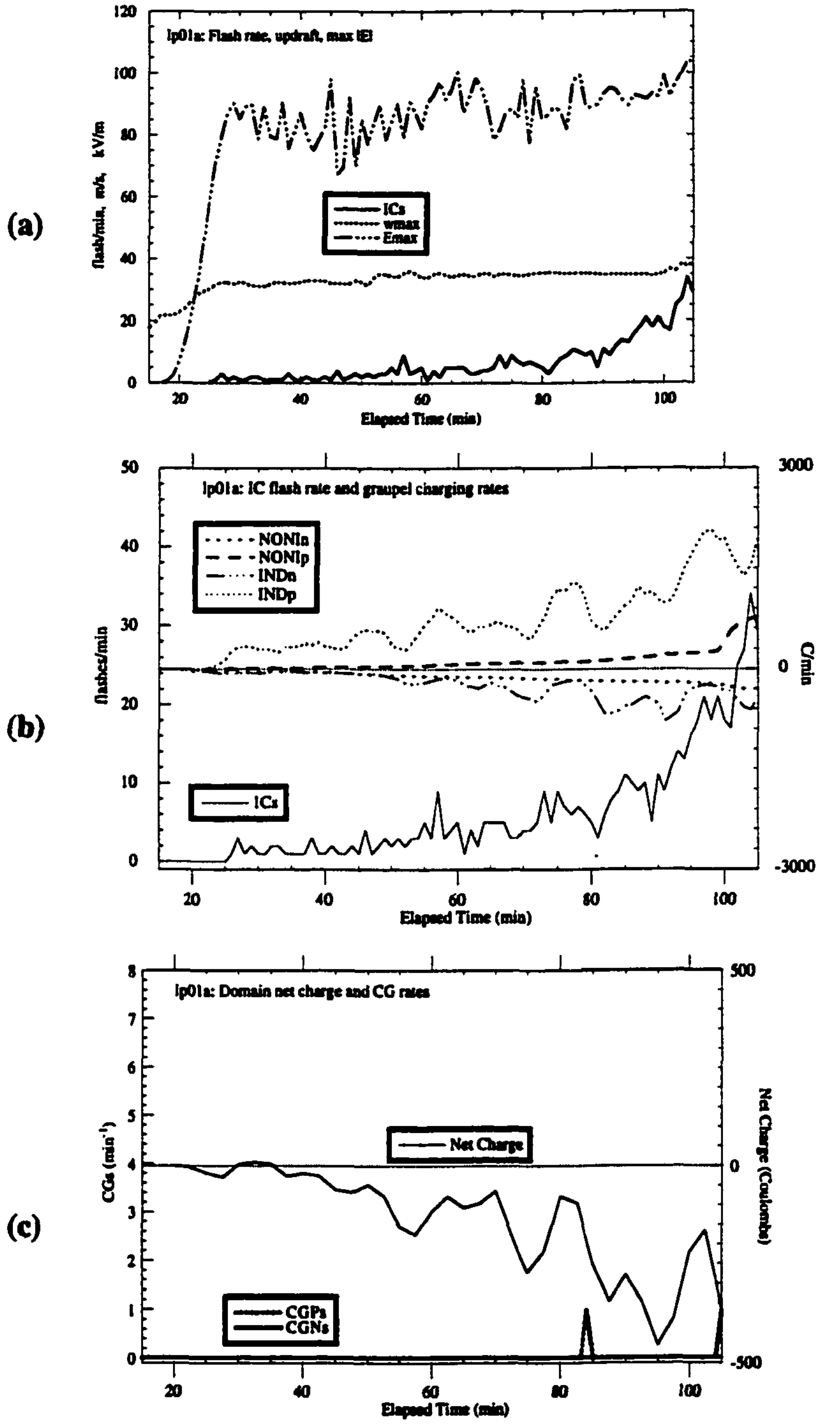

Figure 8.10: Lightning time series plots for LP Supercell (Takahashi, $\frac{1}{2}$-strong inductive). (a) IC flash rate (min^{-1}), maximum updraft, and maximum electric field magnitude at one-minute intervals. (b) Domain-integrated noninductive and inductive graupel charging rates (C/min), positive and negative values are summed separately. (c) Domain net charge and CG flash rates. All values are sampled at 1-minute intervals except domain net charge, which has 2.5-minute intervals. (Flash rates are 1-minute totals.)

Chapter 9

Classic Supercell Simulations

9.1 Classic Supercell General Characteristics

As noted previously in Chapter 5, the sounding for the classic supercell simulation combined features of two soundings (Gilmore, 2000) taken of an environment that produced observed classic supercell storms. The hodograph for this environment had strong curvature to the right. Clockwise turning of the shear vector with height results in dynamic pressure perturbations which favor right-moving storms and retard growth of left-moving storms (Klemp 1987). The convective available potential energy (CAPE) of the sounding was approximately 3000 J/kg, which was about 800 J/kg larger than for the other two supercell environments. The maximum updraft speed in the main right-moving (southern) supercell was about 62 m/s. The outward appearance of the simulated mature right-moving storm certainly fit the term "classic supercell thunderstorm."

The first cell to split from the left flank of the main storm did so approximately 30 minutes after initiation of convection. The left storm remained weak (updraft less than 16 m/s) and had a maximum cloud top significantly lower than that of the southern storm. Its anvil was rather narrow and merged into the underside of the main storm's anvil farther downstream (to the southeast). Because the height of the weaker storm's anvil was appreciably lower than that of the main anvil, the merger resulted in multiple charge layers where the anvils overlapped. Other little storms split from the main storm at roughly 20-minute intervals, and all of them remained very weak. The first left-split storm had completely rained out before it reached the northern boundary at the end of the run (105 min), leaving behind an "orphaned anvil."

By about 30 minutes elapsed time, a precipitation hook was evident at low altitudes in the main storm and a weak echo region had developed. The hook in this storm was weaker than the one in the HP supercell. At about 60 minutes, there was a rapid increase in snow aggregates in the updraft region. A corresponding rise in noninductive charging was seen in all of the runs, especially in the positive noninductive charging of graupel. By about 80 minutes, the weak echo region appeared to become slightly bounded, though not as prominently as in the HP supercell. The main storm anvil spread less quickly than the LP supercell anvil and so did not begin to exit the southeast corner until approximately 77 minutes.

Observations of one of the storms that moved into the region of the soundings are roughly consistent with the model results (Matthew Gilmore, private communication). Gilmore, (2000) analyzed the CG lightning produced by the storms on June 2-3, 1995. One of these storms produced a tornado at Dimmitt, TX, and most of the CG flashes it produced lowered positive charge to ground. The overall CG flash rate was quite low, however. The locations of the positive CG flashes tended to be close to the main reflectivity region, with a few farther out in the forward flank region.

9.2 Riming Rate Noninductive Charging

When the riming rate charging parameterization was used, lightning in the overshooting top (beginning at 60 minutes elapsed time, e.g., Figure 9.1) was dramatically different from that produced by the other two noninductive charging parameterizations. The riming rate with both inductive charging strengths produced positive leaders in this region (indicating overall negative charge), whereas the Gardiner and Takahashi parameterizations produced negative leaders in the same upper part of the convective zone (indicating overall positive charge). The upper negative region was the result of snow

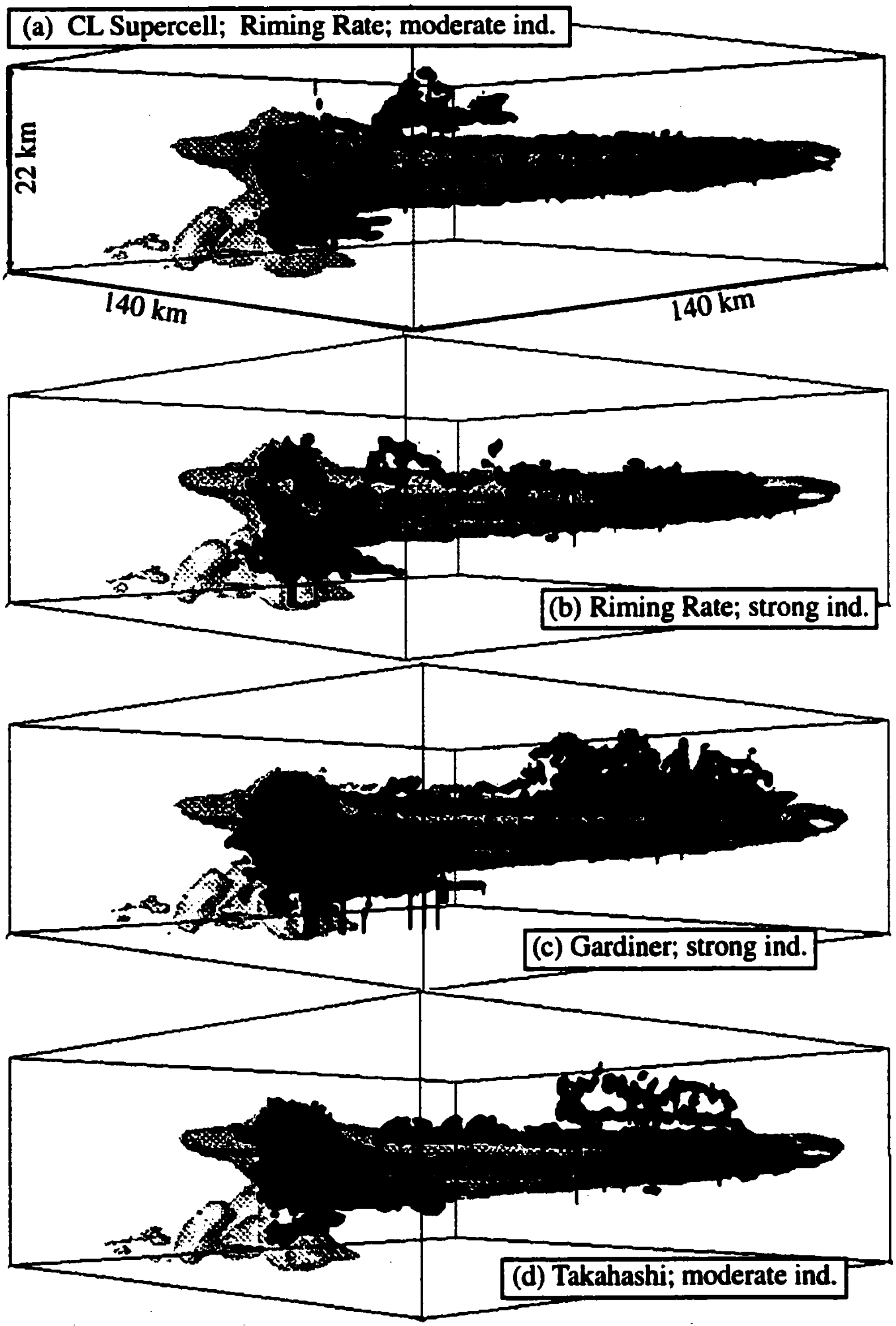

Figure 9.1: Classic supercell storm lightning composites for four runs. The view is from the southwest at 85 minutes elapsed time. Contours outline lightning channels occurring over a 2.5-minute period. Negative leaders are colored orange, and positive leaders are blue. Cloud ice and cloud water contours are gray and yellow, respectively. Green contours indicate where lightning flashes were initiated.

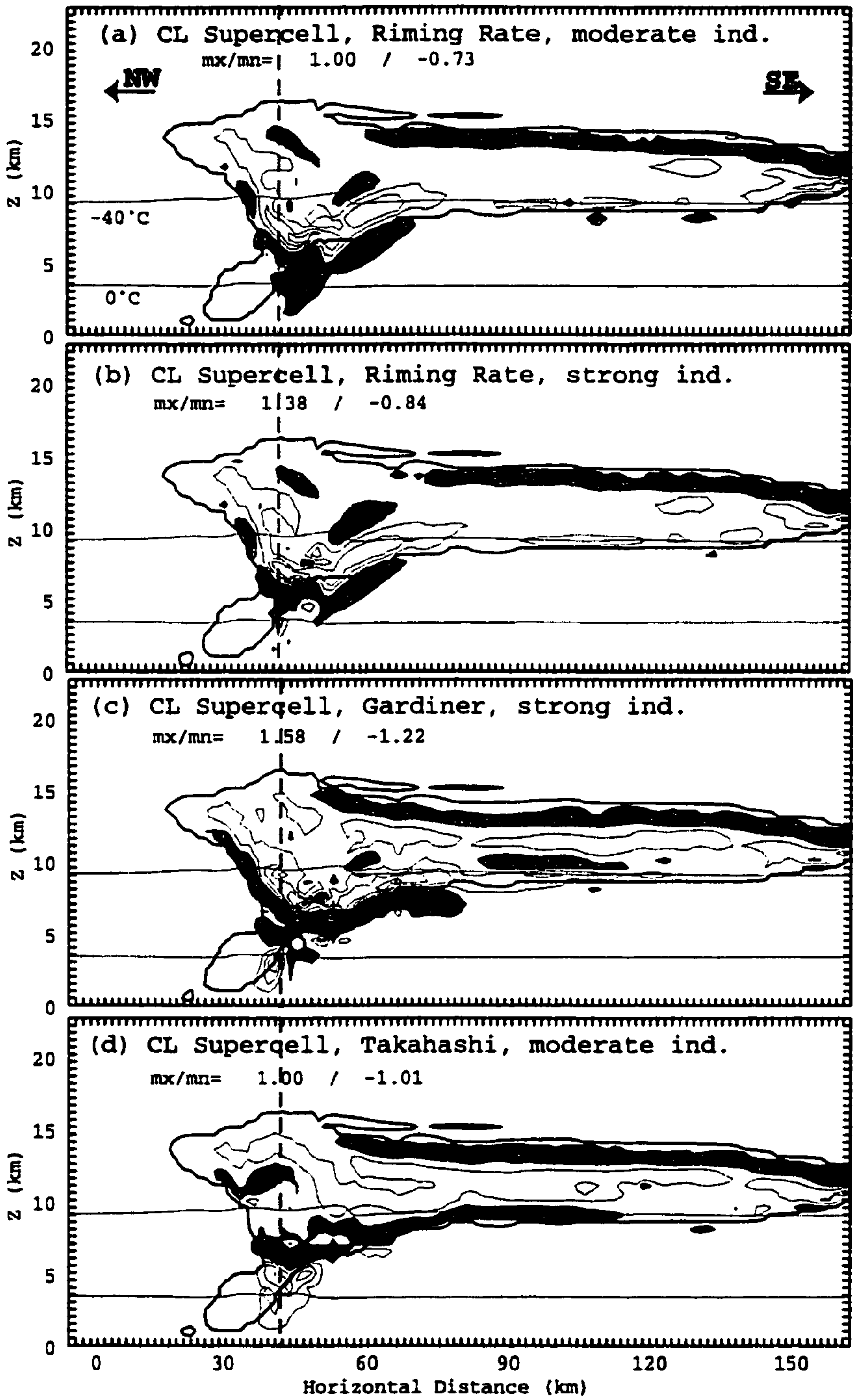

Figure 9.2: Charge density contours (parallel to storm anvil) for the classic supercell storms. The slices are taken through the main storm, just to the northeast of the main updraft. The view is from the southwest at a time of 85 minutes. Negative charge regions are gray. Contour intervals are 0.3 nC m^{-3}, starting at $\pm$0.15. The heavy line outlines the cloud boundary (not including precipitation). Maximum and minimum values for the charge slice are given in each panel.

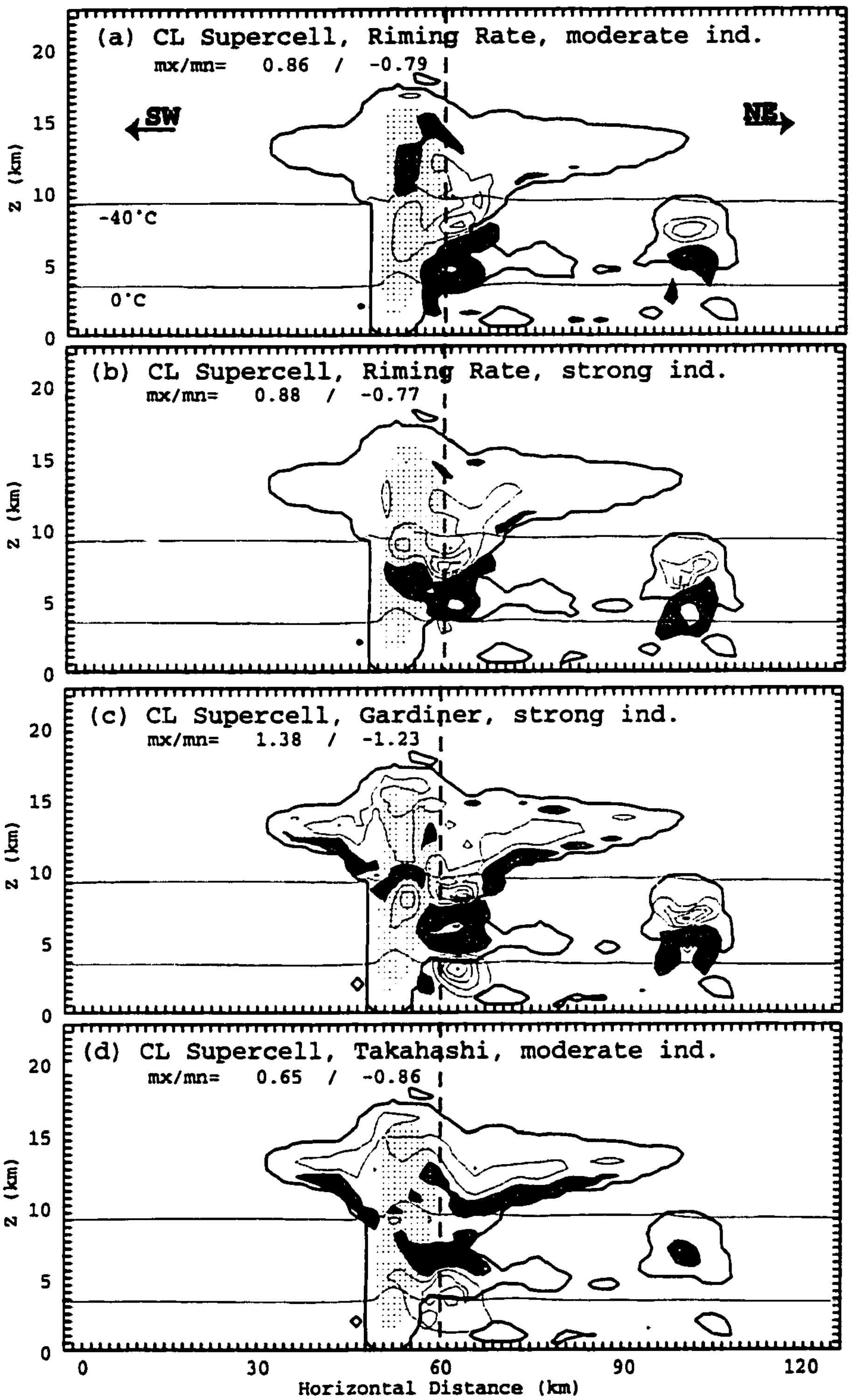

Figure 9.3: Charge density contours (southwest-northeast) for the classic supercell storms. The slices go through the updraft region of the main storm. The view is from the southeast at a time of 85 minutes. Negative charge regions are gray. Contour intervals are 0.3 nC m^{-3}, starting at ± 0.15. The heavy line shows the cloud boundary. Dotted regions indicate updraft of 10 m/s or greater. Maximum and minimum values for the charge slice are given in each panel.

being charged negatively low in the updraft and then being carried up into the updraft exhaust region (see Figure 1.3). The lower part of the convective region had a charge structure more like the case using the Gardiner parameterization (Figure 9.2).

Lightning in the anvil was quite similar for both moderate and strong induction. At about an hour, IC flashes involving the upper negative screening layer started to appear in an isolated region of the anvil. By 80 minutes, the anvil lightning occurred in a much wider region but was still disconnected from lightning in the convective region (Figure 9.1). There were occasional overlaps, but the anvil lightning remained distinct from the convective lightning throughout the simulation.

Overall lightning flash rates were greater with strong inductive charging than with moderate, especially in the weak left-split storm. However, there was a noticeably smaller peak in total lightning segments at 13 km (compare the upper-left and upper-right panels of Figures 9.4 and 9.6; note the different scales). This contrasts with the airmass cases using the riming rate parameterization, which saw an increase in the peak at 13 km when inductive charging was strengthened. The stronger inductive charging also appears to be responsible for the increased number of oscillations in the net charge of the domain (Figure 9.7c and discussed in Chapter 10).

In contrast to the airmass case, increasing the inductive charging strength resulted in some positive ground strikes (instead of negative). The +CG flashes were all close to precipitation in the vicinity of the weak echo region, but not closer than the +CG flashes in the case with the Gardiner parameterization. The +CG flashes appeared to cluster in time (three groups during the 80–100 minute period in Figure 9.7b) and to be correlated to peaks of maximum negative graupel charging by induction. The classic supercell with riming rate noninductive charging and strong induction was the only simulation which had a significant number of +CG flashes when the net charge of the domain was strongly and steadily negative.

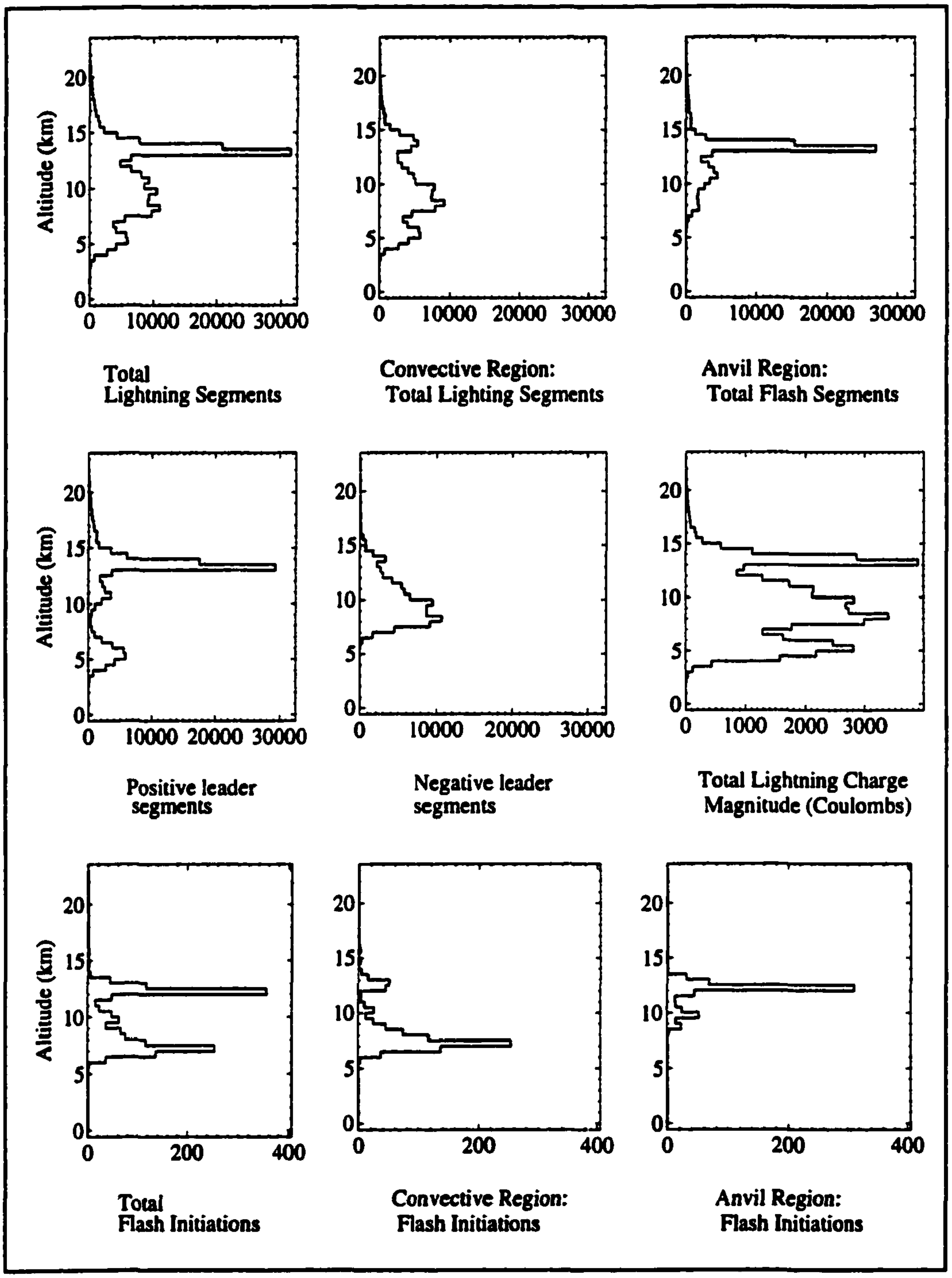

Figure 9.4: Total lightning channel segments and initiations versus height: CL supercell, riming rate, moderate inductive Values are integrated over the whole simulation time. Lightning segments are split into positive and negative leaders or into convective and and anvil regions. Total charge is sum of absolute values of charge deposited by lightning.

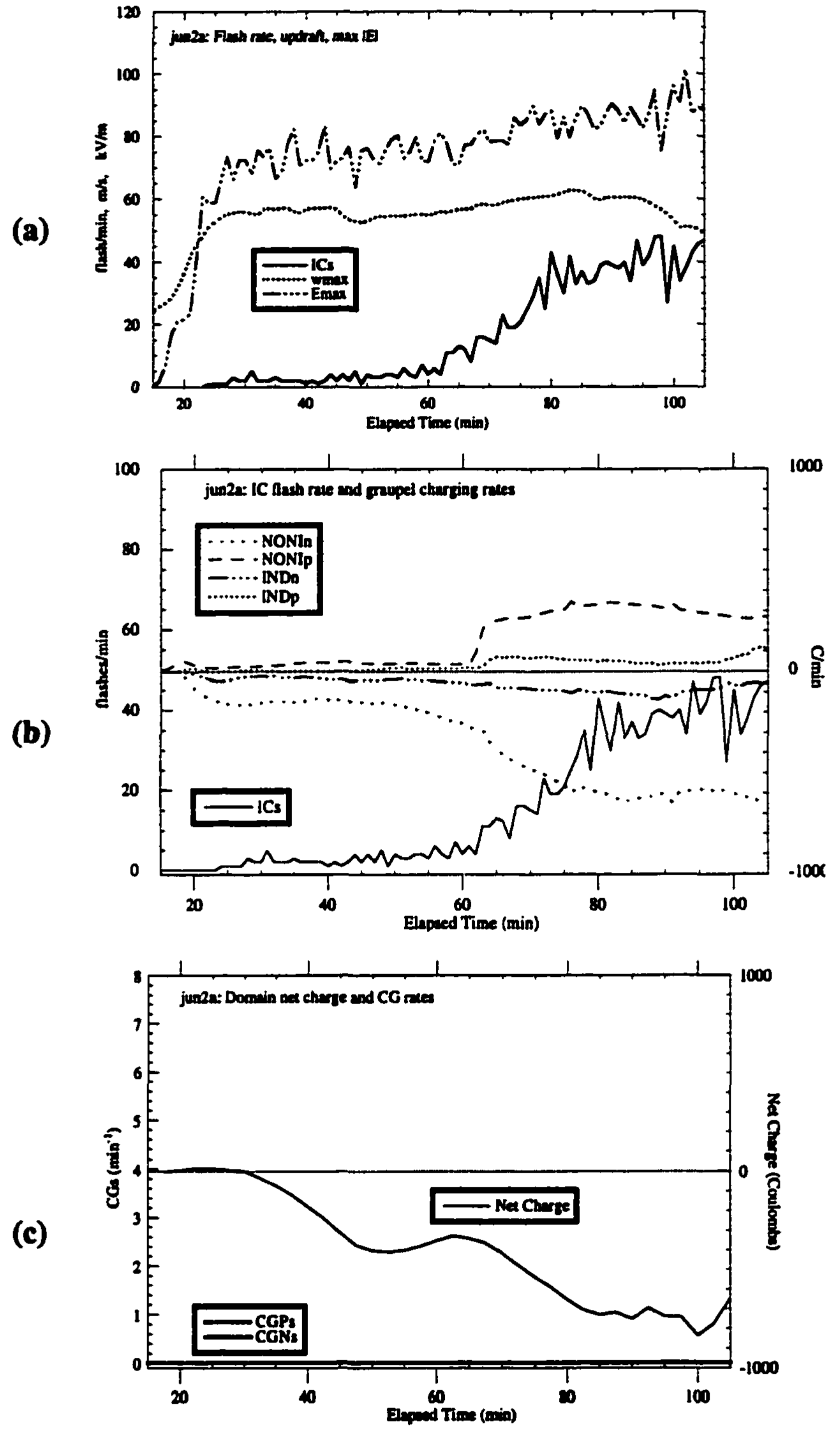

Figure 9.5: Lightning time series plots: CL supercell, riming rate, moderate inductive. (a) IC flash rate (min^{-1}), maximum updraft, and maximum electric field magnitude at one-minute intervals. (b) Domain-integrated noninductive and inductive graupel charging rates (C/min), positive and negative values are summed separately. (c) Domain net charge and CG flash rates. All values are sampled at 1-minute intervals except domain net charge, which has 2.5-minute intervals. (Flash rates are 1-minute totals.)

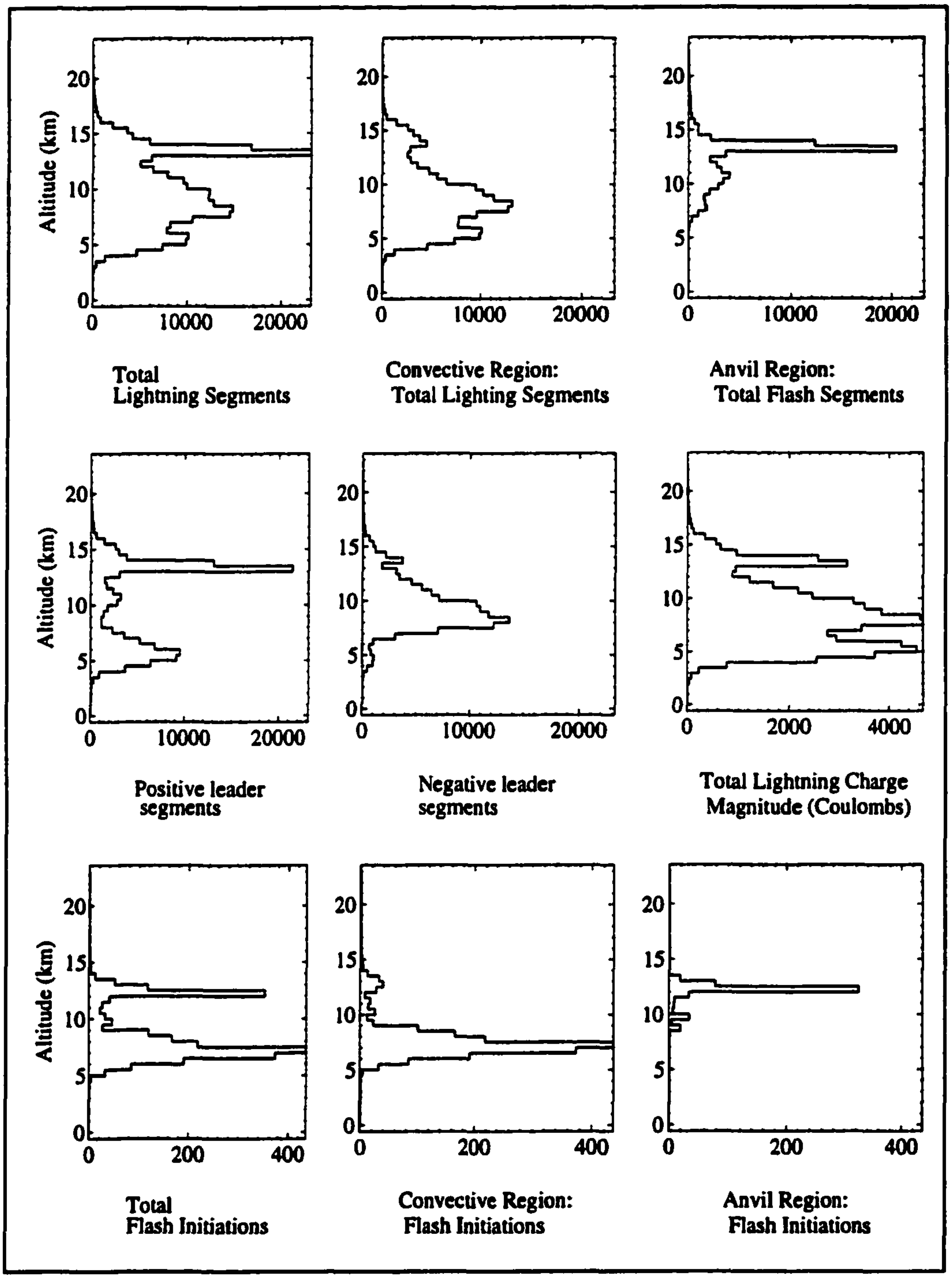

Figure 9.6: Total lightning channel segments and initiations versus height: CL supercell, riming rate, strong inductive. Values are integrated over the whole simulation time. Lightning segments are split into positive and negative leaders or into convective and and anvil regions. Total charge is sum of absolute values of charge deposited by lightning.

(a)

(b)

(c)

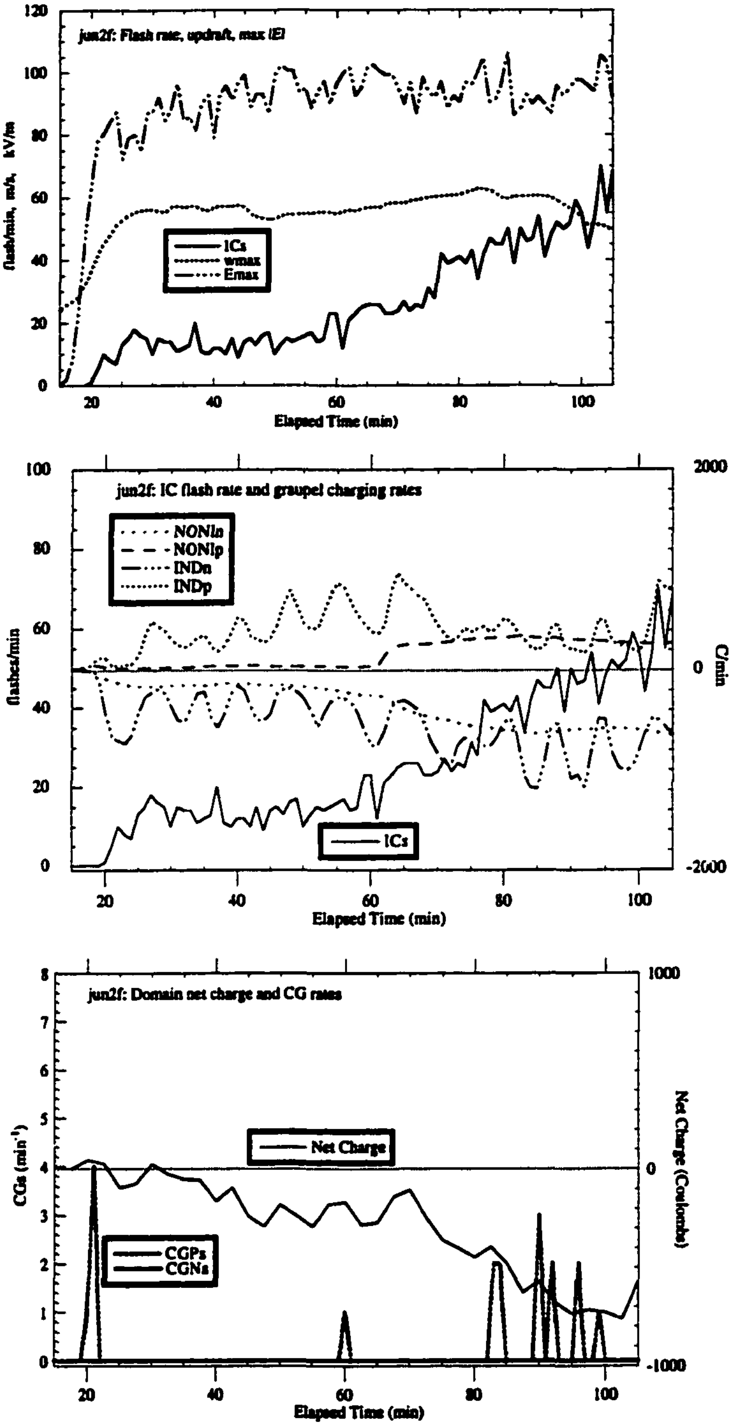

Figure 9.7: Lightning time series plots: CL supercell, riming rate, strong inductive. (a) IC flash rate (min^{-1}), maximum updraft, and maximum electric field magnitude at one-minute intervals. (b) Domain-integrated noninductive and inductive graupel charging rates (C/min), positive and negative values are summed separately. (c) Domain net charge and CG flash rates. All values are sampled at 1-minute intervals except domain net charge, which has 2.5-minute intervals. (Flash rates are 1-minute totals.)

9.3 Gardiner Noninductive Charging

As for the other types of supercell storms, the Gardiner parameterization produced far more +CG flashes than the other two parameterizations did (Table 10.1). Though a few CG flashes occurred early in the storm, the main +CG flash activity started around 65 minutes, while the domain had (decreasingly) net negative charge. The +CG flash rates grew, as the net charge shifted from negative toward zero, and then were relatively steady at 3–5 +CG flashes per minute, while the net charge stayed within about ± 100 C of zero. During the 70–105 minute period, when +CG flashes were very frequent, the net charge in the domain followed an average trend toward more positive values.

All of the +CG flashes produced by the Gardiner parameterization avoided strong surface precipitation. Many of the +CG strikes occurred rather far from the surface precipitation, under the forward flank (over 20 km downshear of the 1 g/kg surface precipitation mixing ratio contour). The vast majority struck where the surface precipitation mixing ratio was less than 2 g/kg, and many occurred where the mixing ratio was less than 1 g/kg.

As the anvil developed, four charge layers became evident there (Figure 9.2c). The upper negative screening layer was carried mostly by cloud ice. The upper positive layer was mainly cloud ice that gained charge in the convective region and advected into the anvil. The lower negative layer was the result of charge deposited by lightning (again mostly carried by cloud ice). The lower positive layer was strongly charged snow crystals, which hid the presence of a negative screening layer on cloud ice at the lower anvil boundary. The first lightning flashes in the anvil region occurred between the upper negative screening layer and upper positive charge layer. Later, flashes also began to occur between the lightning-induced negative layer and the lower positive layer. The anvil charge layers were well stratified, and this resulted in the two distinct peaks for anvil lightning initiations seen in the lower-right panel of Figure 9.8.

Much of the lightning in the anvil tended to occur in the forward half, away from

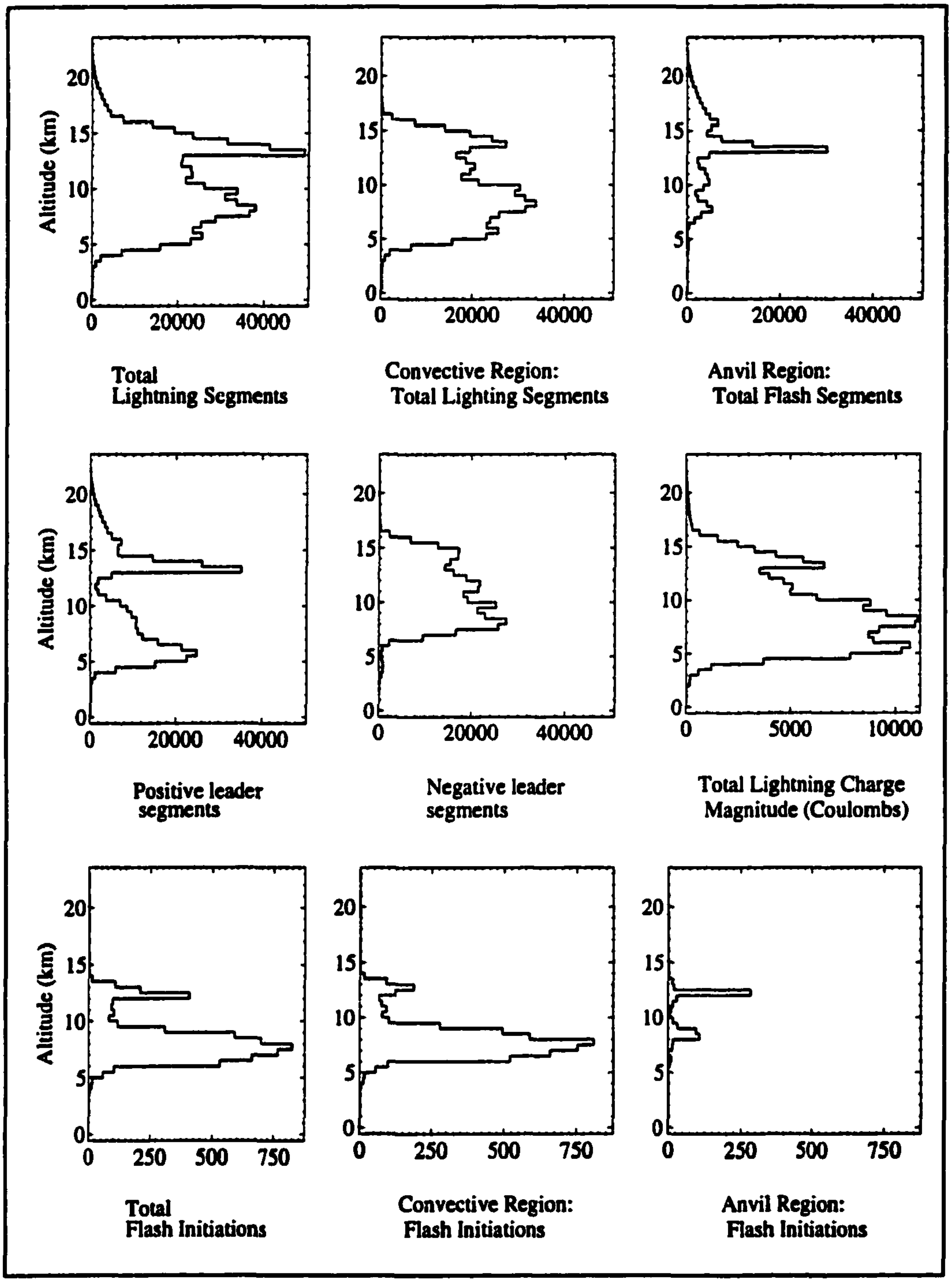

Figure 9.8: Total lightning channel segments and initiations versus height: CL supercell, Gardiner, strong inductive. Values are integrated over the whole simulation time. Lightning segments are split into positive and negative leaders or into convective and and anvil regions. Total charge is sum of absolute values of charge deposited by lightning.

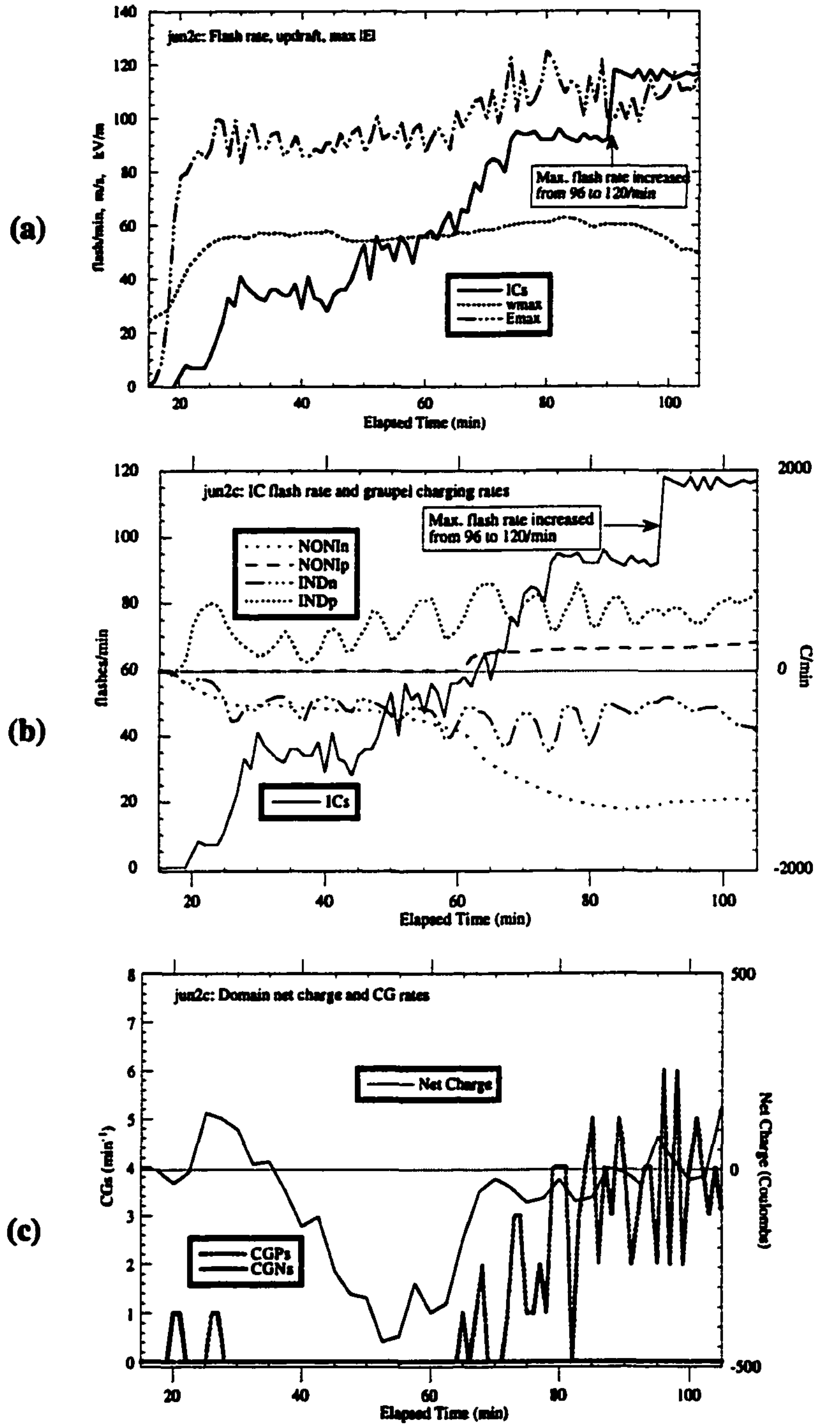

Figure 9.9: Lightning time series plots: CL supercell, Gardiner, strong inductive. (a) IC flash rate (min^{-1}), maximum updraft, and maximum electric field magnitude at one-minute intervals. (b) Domain-integrated noninductive and inductive graupel charging rates (C/min), positive and negative values are summed separately. (c) Domain net charge and CG flash rates. All values are sampled at 1-minute intervals except domain net charge, which has 2.5-minute intervals. (Flash rates are 1-minute totals.)

the updraft and precipitation (Figure 9.1c). As in the simulation with the riming rate parameterization, there was a region of the anvil closer to the precipitation and updraft in which there was a relative minimum of lightning (also apparent in Figure 9.1c). By the end of the simulation, the region of the anvil in which the majority of anvil lightning occurred had moved about halfway out of the model domain.

9.4 Takahashi Noninductive Charging

The classic supercell simulation using the Takahashi parameterization used the moderate inductive setting instead of strong. The reason for choosing weaker induction was that a partial run (30 minutes) with strong inductive charging resulted in dominance of the inductive mechanism, which produced the primary focus of lightning between the lower positive charge and the main negative charge regions. (This was also the reason for using the "$\frac{1}{2}$–strong" inductive charging for the LP supercell simulation with the Takahashi parameterization.) Nevertheless, this simulation of the classic supercell is notable for the −CG flashes produced during the mature stage of the storm. (The Gardiner case had two −CG flashes, but they occurred very early in the simulation.)

As was true for the HP and LP supercell simulations, the lightning produced by the Takahashi parameterization in the classic supercell differed considerably at low levels from that produced by the other two noninductive parameterizations. A small, but distinct peak below 5 km was again present in the vertical distribution of total lightning segments (Figure 9.10, top left). As before, the peak was caused by negative leaders that propagated through the horizontally extended lower region of positive charge (Figures 9.1c and 9.10, center). The peak at 5–6 km in the vertical distribution of flash initiations (Figure 9.10, bottom left) also indicates flashes involving the lower positive charge. The lightning composites in Figure 9.1 show that the Takahashi parameterization produced a wider, more distinct layer of negative leaders at the base of the convective tower than either of the other two noninductive parameterizations.

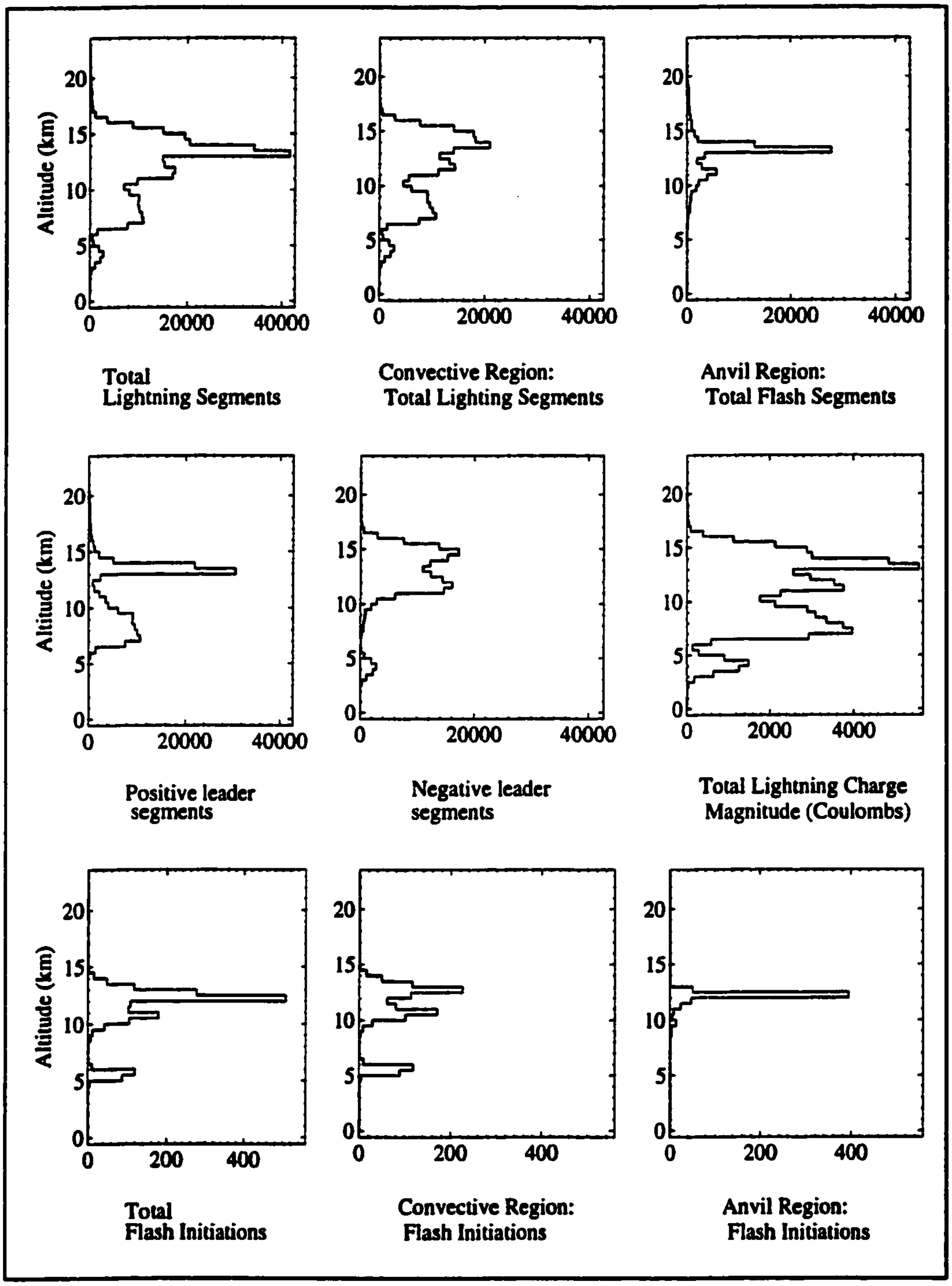

Figure 9.10: Total lightning channel segments and initiations versus height: CL supercell, Takahashi, moderate inductive. Values are integrated over the whole simulation time. Lightning segments are split into positive and negative leaders or into convective and and anvil regions. Total charge is sum of absolute values of charge deposited by lightning.

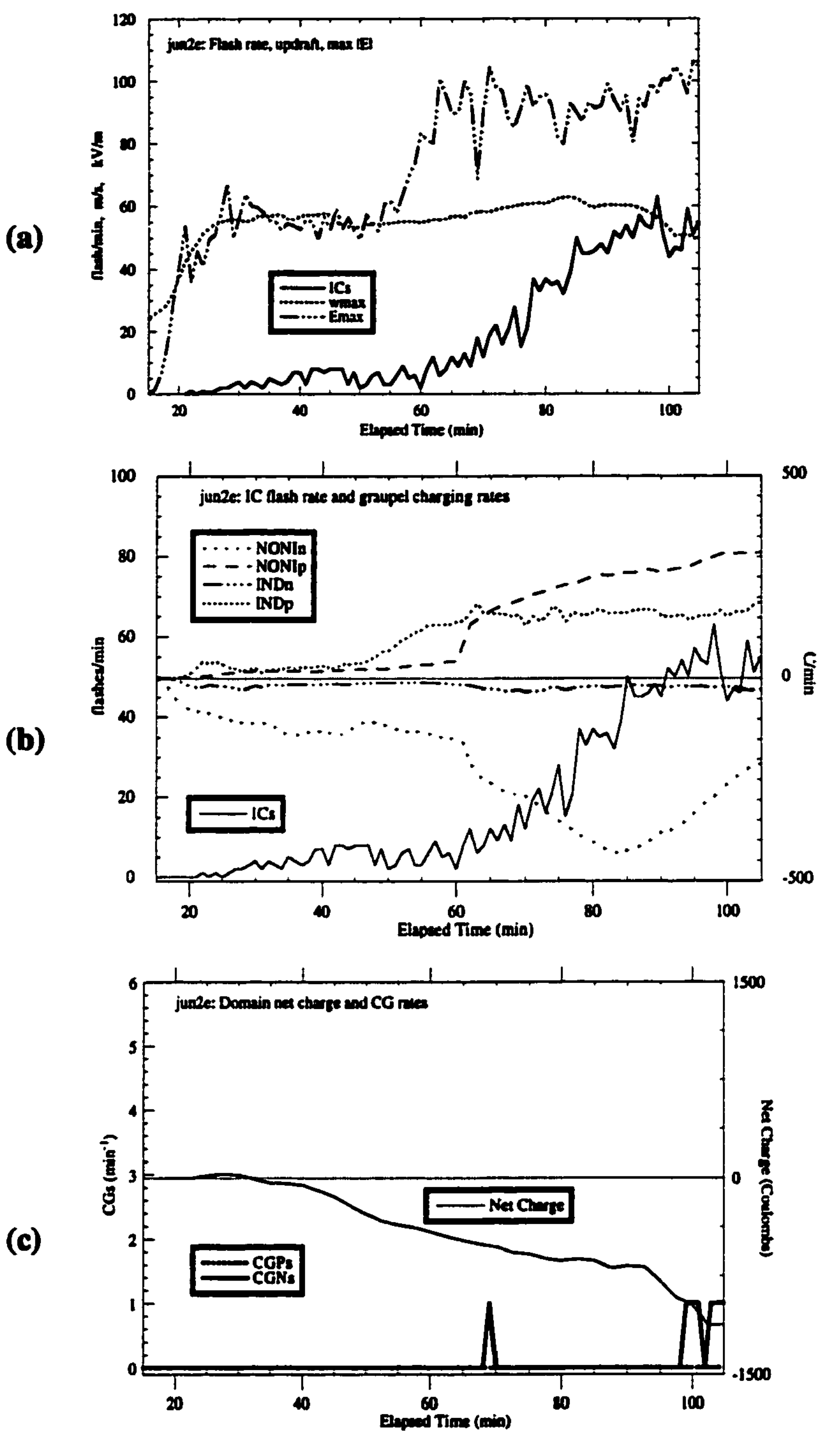

Figure 9.11: Lightning time series plots: CL supercell, Takahashi, moderate inductive. (a) IC flash rate (min^{-1}), maximum updraft, and maximum electric field magnitude at one-minute intervals. (b) Domain-integrated noninductive and inductive graupel charging rates (C/min), positive and negative values are summed separately. (c) Domain net charge and CG flash rates. All values are sampled at 1-minute intervals except domain net charge, which has 2.5-minute intervals. (Flash rates are 1-minute totals.)

Another feature typical of the supercell simulations that used Takahashi parameterization was the strong gap in negative leader segments between 5 and 10 km (Figure 9.10, center). The upper peak in negative leader segments reflects the tendency for the stronger charge densities of the main positive charge to occur at a higher altitude in the convective zone for the Takahashi parameterization. The flash initiations in the convective region exhibited an interesting double peak at the higher altitudes (Figure 9.10, bottom center). The upper peak at 13 km is mainly from flashes between the high-altitude main positive region and the negative charge regions below it in the updraft region. A portion of these regions are seen in Figure 9.2d above the −40°C isotherm at 30–45 km horizontal distance. (Some flash initiations at the 13 km-peak were from flashes with the upper negative screening layer above the downshear side of the convective region, seen in Figure 9.1d.) The second peak at 11 km results from lightning in the last 30 minutes of the simulation (Figure A.17b). A lower part of the charge regions forcing the 11 km peak can be seen just above and below the −40°C isotherm in Figure 9.2d in the forward flank region (about 50–65 km horizontal distance). (These negative and positive charge regions are higher and stronger in the storm a few kilometers to the northeast.)

The main positive and negative regions produced in the convective zone by the other two noninductive parameterizations were at lower altitudes, on average, than those produced by the Takahashi parameterization. Furthermore, the lower altitude of charge regions produced by the other parameterizations also caused flash initiations to peak at lower altitudes than found for the simulation with the Takahashi parameterization (e.g. Figures 9.6 and 9.8, bottom-center panels).

Chapter 10

Discussion and Conclusions

10.1 Summary of Results

This chapter presents a number of relationships based on the simulated storms and electrification mechanisms. However, when comparing simulated electrical behaviors an important caveat to remember is that *the results of all charging separation parameterizations are dependent on the underlying microphysics of the thunderstorm model.* The results presented here are thus dependent on the particular microphysical formulations in the model. Some of the results would very likely have been different if the electrification parameterizations had been used with a different microphysics package. The microphysics package used for this study is unusually detailed and sophisticated, however, and we expect this to have improved the realism of our results.

The discussion here will address a number of aspects of the simulations: First, some general differences and similarities among the results from the different noninductive charging parameterizations are outlined. Second, we discuss some of the variations in the lightning from one storm type to another. The role of a lower positive charge region in −CG flashes is examined in the third subsection, followed by a discussion of the lightning near and above the cloud top. The last subsection discusses the occurrence of positive cloud-to-ground lightning in the model and compares with observations.

10.1.1 Comparison of Noninductive Charging Schemes

The Gardiner noninductive charging parameterization consistently had the strongest negative noninductive charging rates for graupel. Table 10.1 shows that the cases with Gardiner charging had the most IC and +CG flashes of the simulations for the same storm type. The +CG flash rates produced in the supercell storms with Gardiner charging are toward the high end of observations (e.g. Stolzenburg, 1994), suggesting that the charging rates may be higher than generally occur in nature.

The Takahashi parameterization produced the weakest negative noninductive charging rates of graupel, partly because it has a weaker dependence on crystal size and fall speed than the other two noninductive parameterizations. The Takahashi parameterization also tended to have more positive noninductive charging of graupel than the other parameterizations, particularly in regions with low liquid water content and colder than $-15°C$. A consistent feature of the simulations using the Takahashi scheme was the positive charging of graupel in the forward flank region. The wider region of lower positive charge produced by the Takahashi parameterization was evident in the lightning as a distinct strong relative maximum at about 4 km altitude in the vertical distribution of negative leader channels, especially in the supercell storms.

Except for the initial stage of electrification, the riming rate noninductive charging parameterization tended to look like a weaker version of the Gardiner scheme. The structures in the vertical distribution of lightning channels were quite similar in shape and differed from the Gardiner parameterization mainly in magnitude. The HP supercell simulation with the "enhanced" riming rate charging appeared to shift the electrification toward that of the Gardiner version (e.g. compare the net charge of the domain in Figures 7.6c, 7.11c, and 7.8c). However, one particular difference was seen in the supercell anvils: there the Gardiner noninductive charging produced a strong positive layer at the anvil base, but this positive layer was absent or much weaker in the riming rate (and Takahashi) cases.

Table 10.1: Summary of total lightning for each simulation. Totals are shown for 90 minutes and 105 minutes elapsed time from model initiation.

Storm Type	Run[a,b]	IC Totals		−CG Totals		+CG Totals	
		90 min	105 min	90 min	105 min	90 min	105 min
Airmass	RR, mod.	542	951	0	0	0	0
	RR, str.	1225	1956	24	24	0	0
	Gard., mod.	3564	4984	0	0	1	1
	Gard., str.	3625	4992	56	108	2	2
	Gard., str.[c]	2033	3123	140	238	4	4
	Taka., mod.	199	303	5	8	0	0
	Taka., str.	587	900	34	57	2	2
HP Supercell	RR, str.	1927	2995	2	2	2	2
	RR[d], str.	3513	5162	0	0	5	11
	Gard., str.	4168	5775	1	1	47	84
	Taka., str.	1909	3073	6	19	0	0
LP Supercell	RR, str.	1682	2626	24	28	21	21
	Gard., str.	4016	5765	3	3	27	62
	Taka., $\frac{1}{2}$str.	263	555	1	1	1	1
Classic Supercell	RR, mod.	833	1446	0	0	0	0
	RR, str.	1541	2328	0	0	13	18
	Gard., str.	3939	5659	2	2	60	115
	Taka., mod.	949	1730	1	7	0	0

[a]Noninductive charging parameterization: Riming Rate (RR), Gardiner (Gard.), or Takahashi (Taka.) as in Chapter 3.

[b]Inductive charging strength is indicated by "mod." for moderate, "str." for strong, and "$\frac{1}{2}$str." for half-strong.

"moderate" settings: $E_r = 0.07$, $\langle\cos\theta\rangle = 0.2$

"strong" settings: $E_r = 0.015$, $\langle\cos\theta\rangle = 0.5$

"half-strong" settings: $E_r = 0.007$, $\langle\cos\theta\rangle = 0.5$

[c]Used $E_{init} = 150$ kV/m instead of breakeven electric field E_{be} for lightning initiation. All other simulations used $E_{init} = E_{be}$.

[d]Enhanced RR: uses median-volume diameter D_o instead of characteristic diameter ($\mathcal{D}$) for crystal/snow size.

The early electrification produced by the riming rate parameterization differed considerably from that produced by the other two, as seen in the plots of net charge in the domain (e.g., compare Figures 7.6c, 7.8c, and 7.10c): the initial excursions from zero for the riming rate parameterization were always in the opposite direction from the initial excursions produced by the Gardiner and Takahashi parameterizations. In the airmass storms, the riming rate scheme resulted in an initial negative peak in net charge, whereas for the Gardiner and Takahashi versions the initial peak was positive. In the supercell cases, the Gardiner and Takahashi versions had an initial *negative* peak in net charge, but the riming rate versions had an initial *positive* peak. All the simulations with the Takahashi noninductive charging parameterization had the same sign of net charge for the model domain as those with the Gardiner parameterization had. The reasons for the opposite initial excursions between the airmass and supercell storms have not been determined.

One apparent reason the riming rate scheme produced such different initial electrification is that it initially charged graupel positively because of the large cloud water contents (and the correspondingly large rime accretion rates) that existed when the cloud first formed, even in the cold regions at high altitude in the cloud. The riming rate charging scheme thus caused the initial charge structure to be opposite to that produced by the other noninductive charging parameterizations. This reversal of the initial charge structure, in turn, drove the inductive mechanism initially in the opposite direction, as well. In the airmass case, the initial inverted dipole produced a few IC lightning flashes. Observations of first flashes, however, imply a normal dipole structure (P. Krehbiel, personal communication). Thus the inverted dipole seems to be an undesirable feature resulting from the riming rate scheme. Jayaratne (1993) suggested that the laboratory methods used in noninductive charging experiments may result in more positive charging at lower rime accretion rates than would be the case for natural graupel. It is possible that reasonable minor adjustments to the riming rate parameterization would reduce the effect.

10.1.2 Comparison of Storm Types

Differences between the simulated storms are especially evident in the CG lightning activity. All three parameterizations produced significant −CG lightning in the airmass storm when inductive charging was strong. The supercell simulations, however, tended to produce fewer −CG flashes. The supercells also produced more +CG flashes when the riming rate and Gardiner parameterizations were used. The Gardiner parameterization consistently resulted in large numbers of +CG flashes in the supercell storms, but very few −CG flashes. On the other hand, the Takahashi parameterization produced predominantly −CG lightning in all of the storm types except the LP supercell storm, in which it made one CG of each polarity (Table 10.1). The Takahashi parameterization made a total of one +CG flash in the three supercell simulations combined. The LP supercell simulation with the riming rate parameterization was the only simulation to have significant and comparable numbers of both positive and negative CG flashes. Supercell storms can exhibit dominant CG lightning of either polarity (MacGorman, 1993). Therefore, the dominant polarity of simulated CG lightning does not provide a good test of the validity of a particular noninductive charging parameterization.

The intracloud flash totals in Table 10.1 show little variability ($< \pm 3\%$) from one type of supercell to another when the Gardiner parameterization was used. With the riming rate scheme and strong inductive charging the IC totals of the different supercell storms varied by about 20%. Considerably more variation was found for the supercell simulations with the Takahashi parameterization, but each used a different strength of inductive charging. Still, the low IC total for the LP supercell appears to be significant: The LP supercell simulation with the Takahashi parameterization had stronger inductive charging than the corresponding classic supercell, but it nevertheless had fewer than half as many IC flashes.

A general difference between the airmass storms and the supercell storms is seen in the early lightning activity. The time-height contours of lightning segments for the airmass storms (Figures A.1–A.7) show that early lightning in these storms tended to concentrate at altitudes above 10 km. The supercell storms, on the other hand, tended to have early lightning concentrated more at lower altitudes (Figures A.8–A.17). The lack of shear in the airmass storm allowed the updraft to intensify quickly, and graupel formed higher and earlier than in the supercell storms. The higher initial graupel volume also resulted in higher-altitude charge regions. Therefore, the airmass storms tended to have lightning that was initially higher in the storm, because the lightning initiation threshold is smaller at higher altitudes.

The size and shape of the anvil varied considerably from one type of supercell storm to another, and this variability had noticeable effects on the lightning in anvils. The anvil dimensions certainly played a role limiting the extent of lightning flashes. A consistent trend is seen in the vertical distribution of lightning channel segments in the anvil regions: The classic supercell simulations had the largest peaks, the LP supercell simulations had the smallest, and the peaks of the HP supercell simulations fell roughly in the middle. The anvil lightning in the airmass storms was comparable to that in the classic supercells. Furthermore, the LP and classic supercells had a region of anvil lightning that was somewhat distinct from the convective region. The anvil of the HP supercell, however, did not spread far enough from the convective region for a distinctly separate lightning region to be noticeable. Note that all of the anvils eventually extended beyond the model domain. The LP supercell anvil was the most severely affected by the domain boundaries, followed by the classic supercell anvil. Thus, analysis of anvil lightning can be complete only during periods before the anvil reaches the boundary of the domain.

A detailed analysis of the dynamical and electrical differences between the supercell storms is beyond the scope of this study. At this point it must suffice to note that, while the three supercell types have many differences, they also have many similarities. For example, Figures 7.2, 8.1, and 9.1 show overall structures of lightning that tended to be consistent for a given choice of charging options. The convective regions were generally dominated by intracloud flashes between an upper positive charge region and a lower negative charge region. An example of a difference among the supercell storm types is seen in the vertical distributions of negative leader segments for the Gardiner parameterization in Figures 7.7, 8.7, and 9.8 (center-left panel). The HP supercell had a prominent peak at an altitude 12 km (Figure 7.7), but the classic supercell had its strongest peak at about 8 km (Figure 9.8), and the LP supercell had a broader peak at 10–12 km.

10.1.3 The Lower Positive Charge Region and Negative Cloud-to-Ground Lightning

The hypothesis that a lower positive charge is involved in producing −CG lightning has been around for many years (e.g. Clarence and Malan 1957, Williams 1989). Solomon and Baker (1998) demonstrated in their modeling study that the lower positive charge was needed to produce negative cloud-to-ground flashes in their simulations. The results of the present study agree that a relatively strong lower positive charge is needed before −CG flashes can occur.

In the Solomon and Baker (1998) study, the lower positive charge primarily was the result of charge deposited by lightning, and the authors admitted that the lightning charge was artificially enhanced by the geometry of the model. The present study found no evidence that lightning can create a substantial lower positive charge. Furthermore, many observational studies (e.g. Bateman et al. 1999, Marshall and Winn 1982) have reported that precipitation particles carried most of the charge in the lower positive region, and this would not be expected if lightning at somewhat higher altitude were the source.

Williams (1989) reviewed various hypotheses to explain the lower positive charge, including charging by noninductive charge separation during collisions, drop breakup, melting, and collection of ions from corona discharge and lightning. He concluded that the most viable mechanism for development of the lower positive charge was positive noninductive charging of precipitation ice particles, because it provided the best agreement with observations. However, Williams (1989) did not consider inductive charging by rebounding collisions between graupel and cloud droplets. Stolzenburg et al. (1998b), however, mentioned the possibility of inductive graupel-droplet charging being at least partially responsible for the lower positive charge. For the storms simulated in our study, inductive charging between graupel and cloud droplets played an important role in producing a strong lower positive charge. All of the simulations included at least moderate inductive charging. It is clear from our simulations that the riming rate and Gardiner noninductive charging parameterizations alone would not produce a significant lower positive charge in a mature storm. It remains to be seen whether the Takahashi noninductive scheme can produce an appreciable lower positive charge without any help from inductive charging.

10.1.4 Inductive Charging Oscillations

An intriguing behavior in the supercell simulations was the quasi-periodic oscillation of the inductive charging rates when strong inductive charging was employed. The oscillations in the LP supercell storms had longer periods than in the HP or Classic storms (e.g. compare Figures 7.8b and 8.8b). There were no obvious oscillations in the dynamics of the supercells to correlate with the inductive charging. Rather, it appears that the near steady-state character of the updraft structure is important.

The strong, steady updrafts in the supercells can suspend precipitation particles (graupel) aloft as cloud droplets are carried upward. If the graupel is initially charged negatively, then the electric field underneath will have a positive vertical component that causes positive charging of the graupel by induction. If the inductive charging is strong enough, the developing region of positively charged graupel becomes significant enough to cause the vertical electric field component to switch to *negative* at the base of the new positive region. The graupel at the base of the lower positive charge then begins to acquire negative charge from inductive charge transfers with cloud droplets, eventually replacing the lower positive charge with a new lower negative charge. The cycle is self-perpetuating.

Weaker inductive charging is less likely to reverse the polarity of the vertical electric field. The slower oscillations in the LP storms may be related to the slightly weaker updrafts, which would increase the time for charged droplets to be carried upward.

The inductive charging oscillations appear to be related to similar changes in the net charge of the domain, because they occur together and are well correlated (e.g. Figures 7.11b and c). It is unclear what the relationship is, however. A possibility is that it is an artifact of the way charge is treated in the model. When particles evaporate, the charge they carried is no longer tracked and becomes 'lost.' Thus, droplet evaporation could be a substantial charge sink. For example, when graupel gains positive charge, subsequent evaporation of the negatively charged droplets could remove negative charge from the model domain. The shifts in net charge would be expected to lag behind the peaks in inductive charging because of the time delay between maximum inductive charging rates and the evaporation of the charged droplets. The rate of charge loss by evaporating particles is not yet tracked by the model, but it should be addressed in the future to test this speculation.

It is unknown whether such charge oscillations occur in real supercell thunderstorms. Electric field soundings through supercell storm updrafts presented by Stolzenburg et al. (1998a) all indicate positive charge as the lowest significant charge region. If inductive charging were strong enough to periodically reverse the polarity of the lowest significant charge region, one might expect some evidence of strong lower negative charge among the few available updraft soundings. The absence of lower negative charge in those soundings may indicate that the strength of inductive charging has been overestimated by the 'strong' setting used in the simulations.

10.1.5 Lightning in Anvil Screening Layers

All of the simulations presented here predict substantial lightning activity involving negative screening layers at the upper surface of thunderstorms. Taylor et al. (1984)

reported intracloud flashes that formed in the upper part of a storm and were distinct from flashes occurring lower in the storm. These small, high intracloud flashes occurred near the updraft exhaust region and extended into the downstream anvil. In our model simulations, intracloud flashes involving the upper negative screening layer first appear on the downstream side of the updraft.

A peculiar feature of some of the simulated IC flashes involving the negative screening layer of the anvil is the propagation of positive leaders upward and out of the anvil. Figure 9.1 shows this phenomenon in the classic supercell for all of the different charging parameterizations. The positive leaders occasionally propagated 4–5 kilometers above the anvil despite the increase in the threshold electric field for propagation imposed (perhaps artificially) in clear air. If such behavior actually occurs in nature, it may be difficult to detect: Acoustic signals (i.e. thunder) might be weaker because of the high altitude (Holmes et al., 1980), and positive breakdown tends to be less impulsive than negative breakdown and thus radiates much less detectable VHF noise. In the model, positive leaders tended to propagate upward out of the anvil only in or near a region with negative values of electric potential.

The numerics of the model may also affect the propagation of lightning above the storm. The electric potential is calculated in a domain that is the same height as the thunderstorm domain. (Currently, only the lateral boundaries are extended beyond the thunderstorm domain.) The boundary condition imposed at the top is that the vertical gradient in the potential is zero (i.e. a Neumann condition of $\partial\phi/\partial n = -E_z = 0$). The electrical equipotential surfaces are thus required to meet the boundary at right angles, and this adversely affects the accuracy of the solution, especially near the boundary. The influence of the top boundary was seen occasionally when a leader (either positive or negative) propagated upward out of the cloud and then turned to propagate horizontally. A test needs to be made with a higher upper boundary to determine the extent to which the proximity of the domain ceiling has an appreciable effect on the lightning. Limited initial tests of the Poisson equation solver with an early stage of a storm routine found that the accuracy of the initial (full domain) solution was improved more by increasing the width of the domain than by increasing the height.

10.1.6 Positive Cloud-to-Ground Lightning

Positive cloud-to-ground lightning occurred predominantly in the supercell storm simulations that used the Gardiner noninductive charging parameterization. The airmass storm simulation with the Gardiner parameterization and strong inductive charging, on the other hand, produced almost exclusively negative CG flashes. A comparison of the airmass and HP supercell storms with the Gardiner scheme illustrates the differences that led to −CG lightning in the airmass storm and to +CG flashes in the HP supercell. The only environmental difference between the airmass and HP supercell storms was the magnitude of the shear in the 0–5 km layer. In the airmass case, graupel tended to fall through the updraft, with the result that positive inductive charging of graupel was dominant (Figure 6.12b). The airmass storm thus had a strong lower positive charge region which promoted −CG lightning, as described before. In the HP supercell storm, however, the higher wind shear resulted in more graupel falling outside the updraft, so that a more extended graupel volume developed. Although the HP supercell actually had higher rates of positive inductive charging of graupel than the airmass storm, the increase in negative charging (both inductive and noninductive) was much greater, so the total negative charging of graupel became dominant (Figure 7.8b). Furthermore, the airmass storm developed negative net charge in the domain, but the HP supercell had positive net charge (Figures 6.12c and 7.8c) during most of the simulation. Both storms had strong positive and negative charge layers in the forward flanks (Figures 6.4b and 7.3b). Intracloud flashes were regularly initiated between the charge layers in the forward flanks of both storms, but only in the supercell storm did some of those flashes connect to ground to become +CG flashes.

The net charge of the domain appeared to play a role in promoting +CG flashes. In all but one of the simulations that produced +CG flashes, there appears to be a clear association between a positive (or weakly negative) domain net charge with the +CG flashes e.g. in Figures 7.8c, 8.6c, 8.8c, and 9.9c. A causal connection for this relationship can be hypothesized. Analysis of animations of simulations that had a substantial number of +CG flashes revealed that the electric potential became less negative beneath the forward flank before +CG flashes occurred. This shift in potential under the storm could be caused by a net increase of positive charge, which would also affect the shape of the equipotential surfaces. The shift in potential appears to extend the possible range of downward-propagating leaders. If it does so, the difference between IC and CG flashes is probably an outcome of the stochastic stepping process of the lightning propagation parameterization. Forward propagation from the channel tips is expected to have the highest probability, but the combined probability of all sideways steps may be comparable. In other words, there are many choices for propagation direction, and only some of those choices are downward. It seems likely that CG flashes made a critical random step or succession of steps downward at some point whereas the IC flashes in the same region and under similar circumstances did not.

The main exception to the relationship between +CG flashes and the net charge in the domain was the classic supercell with the riming rate noninductive charging parameterization with strong inductive charging (Section 9.2). During the last 30 minutes of that simulation, a number of +CG flashes occurred despite the net charge of the domain being strongly negative (Figure 9.7c). However, all of these +CG flashes occurred in the vicinity of the weak echo region, with none very far into into the forward flank region. The other supercell simulations with significant +CG activity had an appreciable fraction of them occurring farther out in the forward flank region. Thus, a relationship between a positive net charge in the domain with +CG flashes *from the forward flank* appears to hold for all the supercell simulations. Unfortunately, it is not practical to attempt a measurement of the net charge within a real thunderstorm, so this hypothesis is essentially unverifiable by observation.

Also, it was noted in Section 9.2 that the +CG flashes in the supercell simulation with riming rate charging appeared to be associated with inductive charging. Those flashes occurred around the weak echo region, where inductive charging was most active. This suggests that inductive charging may be more important than net charge in the domain for +CG flashes closer to and within the surface precipitation regions. In Section 7.3, a +CG flash occurring in heavy precipitation was also attributed to inductive charging. Therefore, the model results suggest that inductive charging between graupel and droplets can be important for +CG flashes as well as −CG flashes.

The model result that +CG flashes initiate only between oppositely charged regions (positive above negative) appears to be consistent with the observations reported by Carey and Rutledge (1998). Carey and Rutledge found that a corona point sensor indicated negative charge overhead for regions of a storm that tended to produce positive CG flashes (i.e. the lowest significant charge region was negative). Other observations (e.g. Brook et al. 1982, Fuquay 1982) also have suggested that storms producing +CG flashes have a normal dipolar structure, with positive charge over negative. However, the commonly mentioned hypotheses to explain the occurrence of +CG flashes all seem to assume that the lowest charge region above the +CG strike point should be positive. The oft-mentioned tilted dipole (or sheared dipole) hypothesis suggests that positive CG flashes might occur if an upper positive charge layer is shifted away from negative charge below and becomes "exposed to ground." Likewise the "inverted dipole" and "enhanced lower positive charge" hypotheses both assume that a lower positive charge causes +CG lightning. The present results suggest that negative charge is needed below positive charge to initiate most +CG flashes. However, our model results do not preclude the possibility of mountain peaks or tall towers triggering some +CG flashes by initiating a negative leader upward from the ground to a positive charge region overhead.

10.2 Conclusions

The results of this research are quite encouraging. The sophisticated cloud microphysics package combined with detailed electrification and lightning parameterizations represent a unique tool for numerical simulations of thunderstorm electrification and lightning. A wide variety of realistic lightning behaviors were successfully produced, including intracloud flashes in the convective and anvil regions and cloud-to-ground flashes of both positive and negative polarities. The intracloud flashes often exhibited a bilevel structure, consistent with many observations. High-altitude intracloud flashes involving an upper negative electrical screening layer occurred in all of the storm simulations.

Some features of the simulations are less realistic, and this may be a result of limitations in the microphysics and the electrification parameterizations. Each of the noninductive charging parameterizations has results that are in part somewhat unrealistic. The riming rate parameterization tends to result in an initial "inverted dipole" structure. The Gardiner parameterization results in electrification that almost seems too strong, with IC and +CG flash rates at the upper end of observations. The consistently highly stratified lightning structure that results from the Takahashi parameterization appears to be problematic. The charge layers in the model also tend to be thicker than those deduced from electric field soundings, which are often less than 1 km. However, the vertical spacing of 0.5 km is unable to resolve features smaller than 1 km and would thus necessarily result in coarser detail.

The use of a height-varying threshold (breakeven electric field) for lightning initiation appears to be well justified by the results. The resulting vertical profiles of electric field magnitude are very similar to many observed profiles. In contrast, the airmass storm simulation that used a constant value for lightning initiation yielded much larger electric field magnitudes than have been observed at high altitudes. The simulation with constant threshold also had some very unrealistic lightning that branched extensively in clear air in a large volume underneath the anvil. Such lightning behavior is not expected and has not been observed.

The highest densities of lightning activity in the simulated storms occurred in the convective regions. The model also predicted lightning initiation in the storm anvils far downshear (several tens of kilometers) from the main convective region. Though lightning has been observed in those regions of anvils, published observations have not indicated initiation of lightning outside of the convective region. However, observations have tended to focus on the convective regions of storms, so any lightning initiated in anvils may have been overlooked. An electric field sounding presented by Marshall et al. (1989) showed relatively large field magnitudes in an anvil 50 km from the storm core. The maximum electric field magnitudes were close to the breakeven threshold, which suggests that lightning initiation would be possible. Observations that target or specifically include the anvil regions of strong storms are needed to evaluate the realism of the model results.

As mentioned above, the −CG flashes produced by the model are consistent with the hypothesis that a lower positive charge region is needed for negative CG flashes. This hypothesis has been in the literature for many years, although perhaps not widely accepted. The sensitivity tests indicate that inductive charging between graupel and cloud droplets may be important to the development of the lower positive charge. One of the new results of our storm simulations is that a similar hypothesis should apply to positive CG flashes: a *negative* charge region is needed below a positive charge region to promote *positive* CG flashes.

10.3 Future Work

Possibilities abound for the extension of this work. It is easy to outline many unanswered questions concerning this research. Though we believe we have made some progress, much remains to be tackled, such as exploring some of the issues our research has raised, delving into relationships suggested by the simulated storms, and comparing simulated electrical behaviors with observations. All are enough to keep us busy for decades!

One immediate extension of the present work will be to perform a longer supercell simulation to capture its full life-cycle. It would also be interesting to simulate storms in an environment that favors multicell storms, which can produce severe weather and +CG lightning, too. Also, further experimentation with the stochastic lightning model is certainly warranted, especially in the case of cloud-to-ground flashes. Tests should be made with a more physical treatment of the developing bidirectional leader that would allow the channel potential to adjust to maintain charge neutrality.

One of the most exciting new tools in the observation of lightning is the Lightning Mapping Array (LMA) developed at New Mexico School of Mines and Technology (Krehbiel et al., 2000) which reveals lightning behavior in greater detail than available previously and has already documented behavior that had not been suspected. Model 'validation' is always a tricky topic, since no model can ever reproduce more than some general features of a given observed thunderstorm. However, just as radar has been an ideal source of observations for comparison with model microphysical results, the LMA is potentially a very useful tool for testing the realism of the lightning produced in the model.

Bibliography

Aufdermauer, A. N. and D. A. Johnson, 1972: Charge separation due to riming in an electric field. *Q. J. R. Meteorol. Soc.*, **98**, 369–382.

Baker, B., M. B. Baker, E. R. Jayaratne, J. Latham, and C. P. R. Saunders, 1987: The influence of diffusional growth rate on the charge transfer accompanying rebounding collisions between ice crystals and hailstones. *Q. J. R. Meteorol. Soc.*, **113**, 1193–1215.

Barclay, A. L., P. J. Sweeney, L. A. Dissado, and G. C. Stevens, 1990: Stochastic modelling of electrical treeing: fractal and statistical characteristics. *J. Physics D*, **23**, 1536–45.

Bateman, M. B., T. C. Marshall, M. Stolzenburg, and W. D. Rust, 1999: Precipitation charge and size measurements indise a New Mexico mountain thunderstorm. *J. Geophys. Res.*, **104**, 9643–9653.

Brook, M., M. Nakano, P. Krehbiel and T. Takeuti, 1982: The electrical structure of the Hokuriku winter thunderstorms, *J. Geophys. Res.*, **87**, 1207–15.

Brooks, I. M. and C. P. R. Saunders, 1994: An experimental investigation of the inductive mechanism of thunderstorm electrification. *J. Geophys. Res.*, **99**, 10627–10632.

Brooks, I. M. and C. P. R. Saunders, 1995: Thunderstorm charging: laboratory expeiments clarified. *Atmos. Res.*, **39**, 263–273.

Brooks, I. M., C. P. R. Saunders, R. P. Mitzeva, S. L. Peck, 1997: The effect on thunderstorm charging of the rate of rime accretion by graupel. *Atmos. Res.*, **43**, 277–295.

Carey, L. D. and S. A. Rutledge, 1998: Electrical and multiparameter radar observations of a severe hailstorm. *J. Geophys. Res.*, **103**, 13979–14000.

Chiu, C., 1978: Numerical study of cloud electrification in an axisymmetric, time-dependent cloud model. *J. Geophys. Res.*, **83**, 5025–5049.

Clarence, N. D., and D. J. Malan, 1957: Preliminary discharge processes in lightning flashes to ground. *Q. J. R. Meteorol. Soc.*, **83**, 161–172.

Doswell, C. A., III, and D. W. Burgess, 1993: Tornadoes and tornadic storms: A review of conceptual models. In *The Tornado: Its Structure, Dynamics, Prediction, and Hazards*, Geophys. Monogr. 79, Amer. Geophys. Union, Washington, D.C., pp. 161–72.

Dye, J. E., J. J. Jones, W. P. Winn, T. A. Cerni, B. Gardiner, D. Lamb, R. L. Pitter, J. Hallett, and C. P. R. Saunders, 1986: Early electrification and precipitation development in a small, isolated Montana cumulonimbus. *J. Geophys. Res.*, **91**, 1231–1247.

Elster, J., and H. Geitel, 1885: Über die Electrizitäts-Entwicklung bei der Regenbildung. (On the development of electricity by rain formation) *Ann. Phys. Chem.*, **25**, 121–131.

Ferrier, B. S., 1994: A double-moment multiple-phase four-class bulk ice scheme. Part I: Description. *J. Atmos. Sci.*, **51**, 249–280.

Fowler, H. A., J. E. Devaney, J. G. Hagedorn, F. E. Sullivan, 1998: Dielectric breakdown in a simplified parallel model. *Computers in Physics*, **12**, n. 5, 478–487.

Fukuta, N. and Q. J. Lu, 1995: The surface structure and properties of atmospheric ice crystals. *Atmos. Res.*, **38**, 101–108.

Fuquay, D. M., 1982: Positive cloud-to-ground lightning in summer thunderstorms. *J. Geophys. Res.*, **87**, 7131–40.

Gaskell, W., 1981: A laboratory study of the inductive theory of thunderstorm electrification, *Q. J. R. Meteorol. Soc.*, **107**, 955-966.

Gilmore, M. S. and L. J. Wicker, 1998: Supercells simulated in the 2 June 1995 West Texas panhandle environments. *Preprints*, 19th Conference on Severe Local Storms, Minneapolis, MN, Amer. Meteor. Soc., 242–245.

Gilmore, M. S., 2000: *Observed and Simulated 2-3 June 1995 West Texas Panhandle Supercells*. Ph.D. diss., Texas A & M, 250 pp.

Griffiths, R. F. and C. T. Phelps, 1976: The effects of air pressure and water vapoout content on the propagation of positive corona streamers and their implications to lightning initiation. *Q. J. R. Meteorol. Soc.*, **102**, 419–426.

Hager, W. W., 1998: A discrete model for the lightning discharge. *J. Comp. Physics*, **144**, 137–150.

Helsdon, J. H., Jr. and R. D. Farley, 1987: A numerical modeling study of a Montana thunderstorm: 2. Model results versus observations involving electrical aspects. J. Geophys. Res., **92**, 5661–75.

Helsdon, J. H., Jr., G. Wu, and R. D. Farley, 1992: An intracloud lightning parameterization scheme for a storm electrification model. *J. Geophys. Res.*, **97**, 5865–5884.

Helsdon, J. H., Jr., S. Gattaleeradapan, and R. D. Farley, 1999: And examination of the convective charging hypothesis. *Proceedings, 11th International Conference on Atmospheric Electricity*, Gunthersville, Alabama, U.S.A., 288–291.

Holmes, C. R., E. W. Szymanski, S. J. Szymanski, and C. B. Moore, 1980: Radar and acoustic stndy of lightning. *J. Geophys. Res.*, **85**, 7517–7532.

Jayaratne, E. R., C. P. R. Saunders, and J. Hallett, 1983: Laboratory studies of the charging of soft hail during ice crystal interactions. *Q. J. R. Meteorol. Soc.*, **109**, 609–630.

Jayaratne, E. R., 1993: The heat balance of a riming graupel pellet and the charge separation during ice-ice collisions. *J. Atmos. Sci.*, **50**, 3185–3193.

Jayaratne, E. R., 1998: Density and surface temperatue of graupel and the charge separation during ice crystal interactions. *J. Geophys. Res.*, **103**, 13957–13961.

Jennings, S. G., 1975: Electric charging of water dops in polarizing electric fields, *J. Electrost.*, **1**, 15–25.

Kasemir, H. W., 1960: A contribution to the electrostatic theory of a lightning discharge. *J. Geophys. Res.*, **65**, 1873–1878.

Klemp, J. B., 1987: Dynamics of tornadic thunderstorms. *Ann. Rev. Fluid Mech.*, **19**, 369–402.

Krehbiel, P. R., 1986: The electrical structure of thunderstorms. In *The Earth's Electrical Environment*, National Acad. Press, Washington, D.C. pp. 90–113.

Krehbiel, P. R., R. J. Thomas, W. Rison, T. Hamlin, J. Harlin, and M. Davis, 1999: Three-dimensional lightning mapping observations during MEaPRS in central Oklahoma. *Proceedings, 11th International Conference on Atmospheric Electricity*, Gunthersville, Alabama, U.S.A., 376–379.

Krehbiel, P. R., R. J. Thomas, W. Rison, T. Hamlin, J. Harlin, and M. Davis, 2000: GPS-bases mapping system reveals lightning inside storms. *Eos, Transactions, Amer. Geophys. Union*, **81**, n. 3, 21-25.

Kuettner, J. P., Z. Levin, and J. D. Sartor, 1981: Thunderstorm electrification—Inductive or non-inductive? *J. Atmos. Sci.*, **38**, 2470–2484.

Leonard, B. P., 1991: The ULTIMATE conservative difference scheme applied to unsteady one-dimensional advection. *Comput. Methods Appl. Mech. Eng.*, **88**, 17–74.

Lin, Y.-L., R. D. Farley, and H. D. Orville, 1983: Bulk parameterization of the snow field in a cloud model. *J. Climat Appl. Meteor.*, **22**, 1065–1092.

MacGorman, D. R., A. A. Few, and T. L. Teer, 1981: Layered lightning activity. *J. Geophys. Res.*, **86**, 9900–9910.

MacGorman, D. R., D. W. Burgess, V. Mazur, W. D. Rust, W. L. Taylor, and B. C. Johnson, 1989: Lightning rates relative to tornadic storm evolution on 22 May 1981, *J. Atmos. Sci.*, **46**, 221–250.

MacGorman, D. R., 1993: Lightning in tornadic storms: A review, in *The Tornado: Its Structure, Dynamics, Prediction, and Hazards.* C. Church, D. Burgess, R. Davies-Jones, and C. Doswell, eds., Geophys. Monogr. 79, Amer. Geophys. Union, pp. 173–82.

MacGorman, D. R., and W. D. Rust, 1998: The electrical nature of storms. Oxford University Press.

MacGorman, D. R., J. M. Straka, and C. L. Ziegler, 1998: A lightning parameterization for numerical cloud models. *Preprints*, 19th Conference on Severe Local Storms, AMS pp. 348–351.

Marshall, T. C., and W. P. Winn, 1982: Measurements of charged preciptation in a New Mexico thunderstorm: Lower positive charge centers. *J. Geophys. Res.*, **87**, 7141–7157.

Marshall, T. C., W. D. Rust, W. P. Winn, and K. E. Gilbert, 1989: Electrical structure in two thunderstorm anvil clouds. *J. Geophys. Res.*, **94**, 2171–2181.

Marshall, T. C., M. P. McCarthy, and W. D. Rust, 1995: Electric field magnitudes and lightning initiation in thunderstorms. *J. Geophys. Res.*, **100**, n. D4, 7097–7103.

Masuelli, S., M. A. Pulido, C. M. Scavuzzo, and G. M. Caranti, 1998: Graupel trajectories and charging: A numerical approach for cloud electrification studies. *Q. J. R. Meteorol. Soc.*, **124**, 1329–1341.

Mazur, V. and L. Ruhnke, 1998: Model of electric charges in thunderstorms and associated lightning. *J. Geophys. Res.*, **103**, n. D18, 23299–23308.

Moller, A. R., C. A. Doswell III, and R. Przybylinski, 1990: High-precipitation supercells: A conceptual model and documentation. Preprints *16th Conf. on Severe Local Storms*, Kananaskis Park, AB, Canada, Amer. Meteor. Soc., 52–57.

Niemeyer, L., L. Pietronero, and H. J. Weismann, 1984: Fractal dimension of dielectric breakdown. *Phys. Rev. Let.*, **52**, n. 12, 1033–1036.

Orville, R. E., 1994: Cloud-to-ground lightning flash characteristics in the contiguous United States: 1989–91. *J. Geophys. Res*, **99**, 10833–41.

Petrov, N. I. and G. N. Petrova, 1993: Physical mechanisms for intracloud lightning discharges. *Technical Physics*, **38**, 287–290.

Petrov, N. I. and G. N. Petrova, 1999: Physical mechanisms for the development of lightning discharges between a thundercloud and the ionosphere. *Technical Physics*, **44**, 472–475.

Pietronero, L. and H. J. Wiesmann, 1988: From physical dielectric breakdown to the stochastic fractal model. *Zeitschrift Phys. B*, **70**, 87–93.

Proctor, D. E., R. Uytenbogaardt, and B. M. Meredith, 1988: VHF radio pictures of lightning flashes to ground. *J. Geophys. Res.*, **93**, 12683–12727.

Randell, S. C., S. A. Rutledge, R. D. Farley, and J. H. Helsdon Jr., 1994: A modeling study of the early electrical development of tropical convection: Continental and oceanic (monsoon) storms. *Mon. Wea. Rev.*, **122**, 1852–1877.

Rasmussen, E. N., J. M. Straka, R. Davies-Jones, C. A. Doswell III, F. H. Carr, M. D. Eilts, and D. R. MacGorman, 1994: Verifications of the Origins of Rotation in Tornadoes Experiment: VORTEX. *Bull. Amer. Meteor. Soc.*, **75**, 995–1006.

Rasmussen, E. N. and J. M. Straka, 1998: Variations in supercell morphology. Part I: Observations of the role of upper-level storm-relative flow. *Mon. Weath. Rev.*, **126**, 2406–2421.

Rawlins, F., 1982: A numerical study of thunderstorm electrification using a three dimensional model incorporating the ice phase. *Q. J. R. Meteorol. Soc.*, **108**, 779–800.

Rust, W. D. and C. B. Moore, 1974: Electrical conditions near the bases of thunderclouds over New Mexico. *Q. J. R. Meteorol. Soc.*, **100**, 450–468.

Sartor, J. D., 1981: Induction Charging of Clouds. *J. Atmos. Sci.*, **38**, 218–220.

Saunders, C. P. R., W. D. Keith, R. P. Mitzeva, 1991: The effect of liquid water on thunderstorm charging. *J. Geophys. Res.*, **96**, 11007–11017.

Saunders, C. P. R., and S. L. Peck, 1998: Laboratory studies of the influence of the rime accretion rate on charge transfer during crystal/graupel collisions. *J. Geophys. Res.*, **103**, 13949–13956.

Saunders, C. P. R., E. E. Avila, S. L. Peck, N. E. Castellano, and G. G. Aguirre Varela, 1999a: Vapor and heat supply to riming graupel: Effect on charging. *Proceedings, 11th International Conference on Atmospheric Electricity*, Gunthersville, Alabama, U.S.A., 268–271.

Saunders, C. P. R., E. E. Avila, S. L. Peck, N. E. Castellano, and G. G. Aguirre Varela, 1999b: A laboratory study of the effects of rime ice accretion and heating on charge transfer during ice crystal/graupel collisions. *Atmos. Res.*, **51**, 99–117.

Scavuzzo, C. M. and G. M. Caranti, 1996: Thunderstorm electrification analysis: The dependence on the temperature-LWC diagram. *J. Atmos. Sci.*, **53**, 349–358.

Scavuzzo, C. M., S. Masuelli, G. M. Caranti, and E. R. Williams, 1998: A numerical study of thundercloud electrification by graupel-crystal collisions. *J. Geophys. Res.*, **103**, 13963–13973.

Shao, X. M. and P. R. Krehbiel, 1996: The spatial and temporal development of intracloud lightning. *J. Geophys. Res.*, **101**, n. D21, 26641–2,668.

Sohncke, L., 1885: Der Ursprung der Gewitter-Elektrizität und der gewöhnlichen Electrizität der Atmosphäre (The origins of thunderstorm electricity and the everyday electricity of the atmosphere). Verlag Fischer.

Solomon, R. and M. B. Baker, 1994: Electrification of New Mexico thunderstorms. *Mon. Weath. Rev.*, **122**, 1878–1886.

Solomon, R. and M. B. Baker, 1996: A one-dimensional lightning parameterization. *J. Geophys. Res.*, **101**, 14983–14990.

Solomon, R. and M. B. Baker, 1998: Lightning flash rate and type in convective storms. *J. Geophys. Res.*, **103**, n. D12, 14041–14057.

Stolzenburg, M., 1994: Observations of high ground flash densities of positive lightning in summertime thunderstorms. *Mon. Weath. Rev.*, **122**, 1740–1750.

Stolzenburg, M, T. C. Marshall, and W. D. Rust, 1998a: Electrical structure in thunderstorm convective regions 2. Isolated Storms. *J. Geophys. Res.*, **103**, n. D12, 14079–14096.

Stolzenburg, M, T. C. Marshall, and W. D. Rust, 1998b: Electrical structure in thunderstorm convective regions 3. Synthesis. *J. Geophys. Res.*, **103**, n. D12, 14097–14108.

Straka, J. M. and J. R. Anderson, 1993: Numerical simulations of microburst-producing storms: Some results from storms observed during COHMEX. *J. Atmos. Sci.*, **50**, 1329–1348.

Straka, J. M.. MacGorman, D. R., C. L. Ziegler, and E. N. Rasmussen, 1998: Early electrification and lightning in simulations of airmass, multicell, and supercell storms. *Preprints*, 19th Conference on Severe Local Storms, AMS pp. 697–700.

Takahashi, T., 1978: Riming electrification as a charge generation mechanism in thunderstorms. *J. Atmos. Sci.*, **35**, 1536–1548.

Taylor, W. L., E. A. Brandes, W. D. Rust, And D. R. MacGorman, 1984: Lightning activity and severe storm structure. *Geophys. Res. Lett.*, **11**, 545–548.

Trembeck, C. J., J. Powell, W. R. Cotton, and R. A. Pielke, 1987: The forward-in-time upstream advection scheme: Extension to higher orders. *Mon. Weath. Rev.*, **115**, 540–555.

Weisman, M. L. and J. B. Klemp, 1984: The structure and classification of numerically simulated convetive storms in directionally varying wind shears. *Mon. Weath. Rev.*, **112**, 2479–2498.

Wiesmann, H. J., 1988: Realistic models of dielectric breakdown. *Fractals' Physical Origin and Properties*, ed., L. Pietronero, Plenum, New York, 243–257.

Wiesmann, H. J. and H. R. Zeller, 1986: A fractal model of dielectric breakdown and prebreakdown in solid dielectrics. *J. Appl. Phys.*, **60**, 1770–1773.

Williams, E. R., C. M. Cooke, and K. A. Wright, 1985: Electrical discharge propagation in and around space charge clouds. *J. Geophys. Res.*, **90**, 6054–6070.

Williams, E. R., 1989: The tripole structure of thunderstorms. *J. Geophys. Res.*, **94**, 13151–13167.

Williams, E. R., R. Zhang, and J. Rydock, 1991: Mixed-phase microphysics and cloud electrification. *J. Atmos. Sci.*, **48**, 2195–2203.

Williams, E. R. and R. Zhang, 1996: Density of rime in laboratory simulations of thunderstorm microphysics and electrification. *J. Geophys. Res.*, **101**, 29715–29719.

Wojcik, W. A., 1994: *An Examination of Thunderstorm Charging Mechanisms Using the IAS 2D Storm Electrification Model.* Master's thesis, So. Dakota Schl. Mines Technol., Rapid City, 113 pp.

Ziegler, C. L., 1985: Retrieval of thermal and microphysical variables in observed convective storms. Part I: Model development and preliminary testing. *J. Atmos. Sci.*, **42**, 1487-1509.

Ziegler, C. L., P. S. Ray, and D. R. MacGorman, 1986: Relations of kinematics, microphysics and electrification in an isolated mountain thunderstorm. *J. Atmos. Sci.*, **43**, 2098–2114.

Ziegler, C. L., D. R. MacGorman, J. E. Dye, and P. S. Ray, 1991: A model evaluation of non-inductive graupel-ice chargin in the early electrification of a mountain thunderstorm. *J. Geophys. Res.*, **96**, 12833–12855.

Ziegler, C. L. and D. R. MacGorman, 1994: Observed lightning morphology relative to modeled space charge and electric field distributions in a tornadic storm. *J. Atmos. Sci.*, **51**, 833–851.

Appendix A

Lightning Time-Height Contours

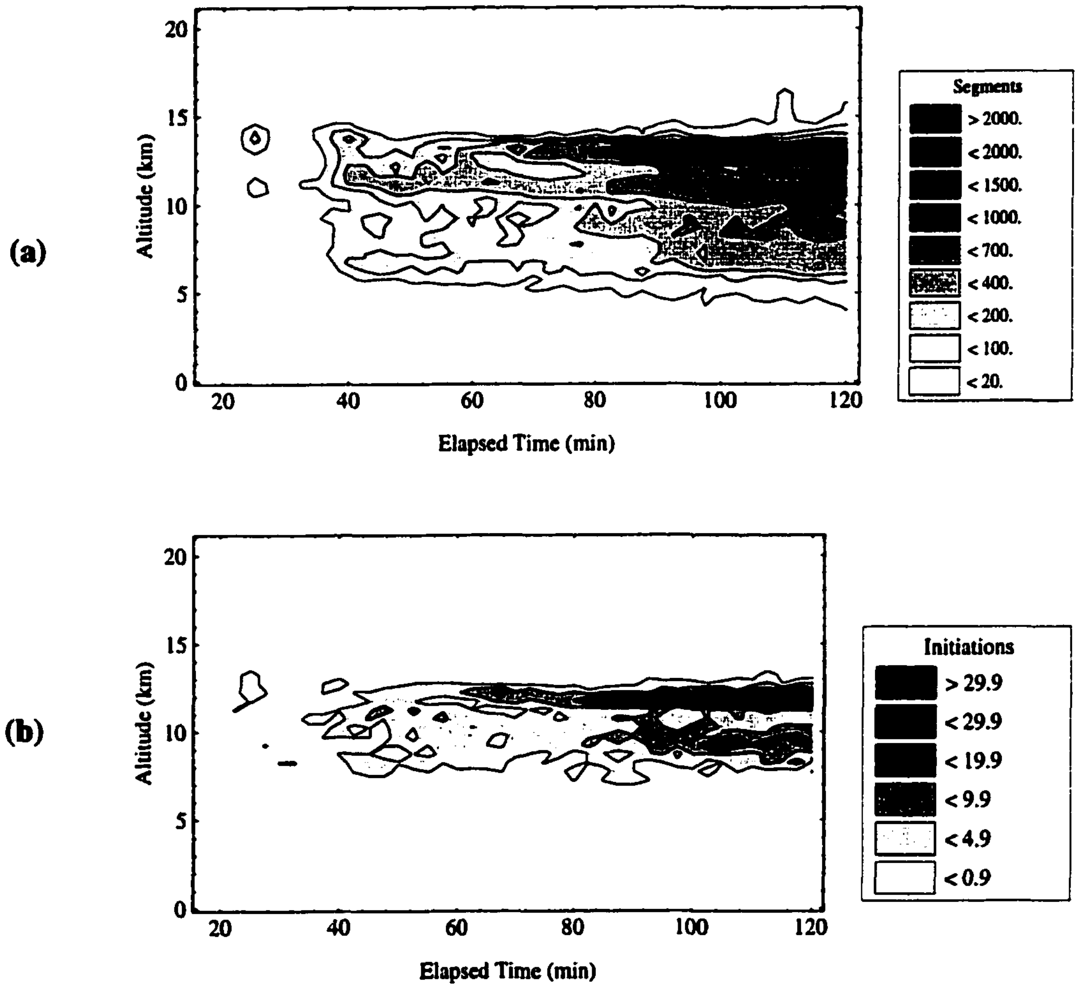

Figure A.1: Lightning channel segments and initiations versus altitude and time: airmass, riming rate, moderate induction. Horizontally integrated (a) lightning segment counts and (b) initiations for each level. Time intervals are 2.5 minutes. (i.e. number per 2.5 minutes.)

(a)

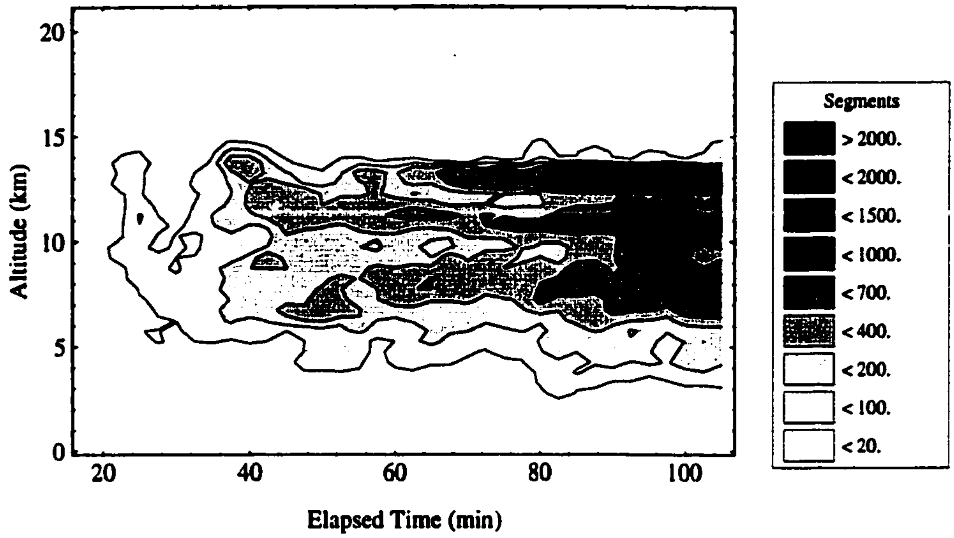

(b)

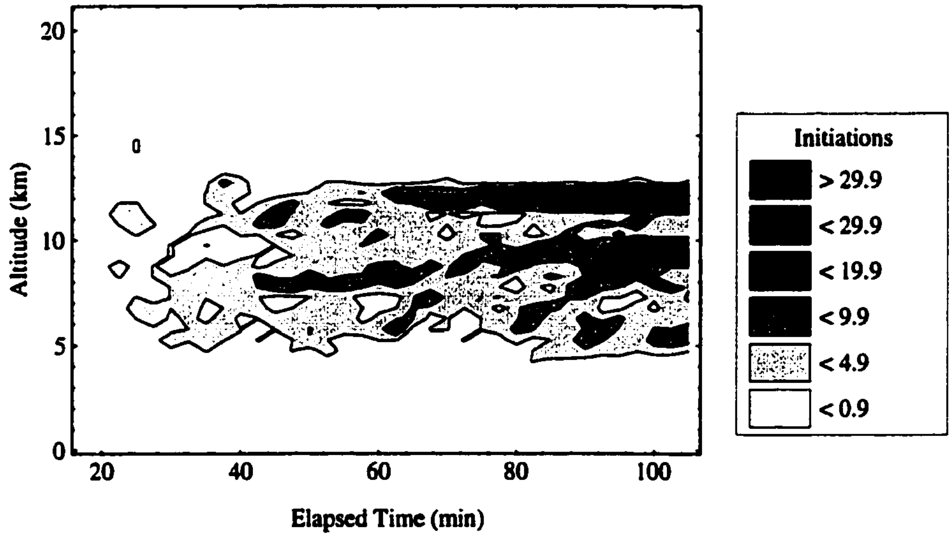

Figure A.2: Lightning channel segments and initiations versus altitude and time: airmass, riming rate, strong induction. Horizontally integrated (a) lightning segment counts and (b) initiations for each level. Time intervals are 2.5 minutes. (i.e. number per 2.5 minutes.)

(a)

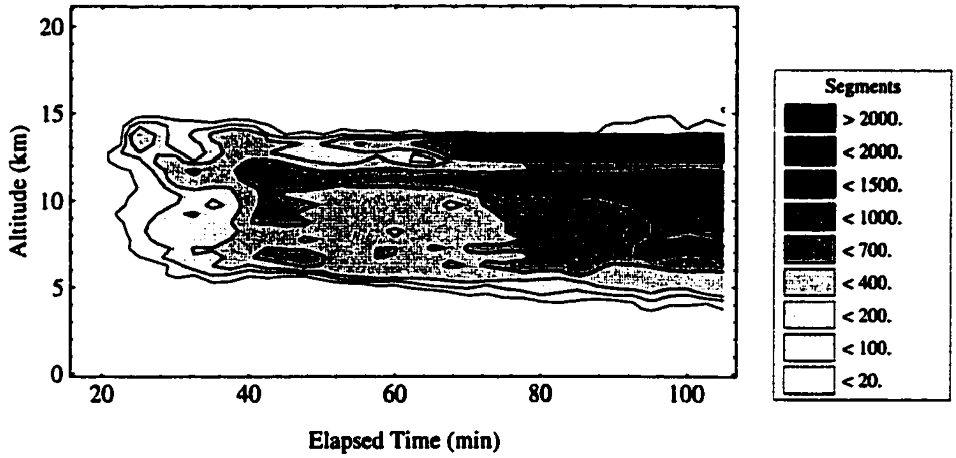

(b)

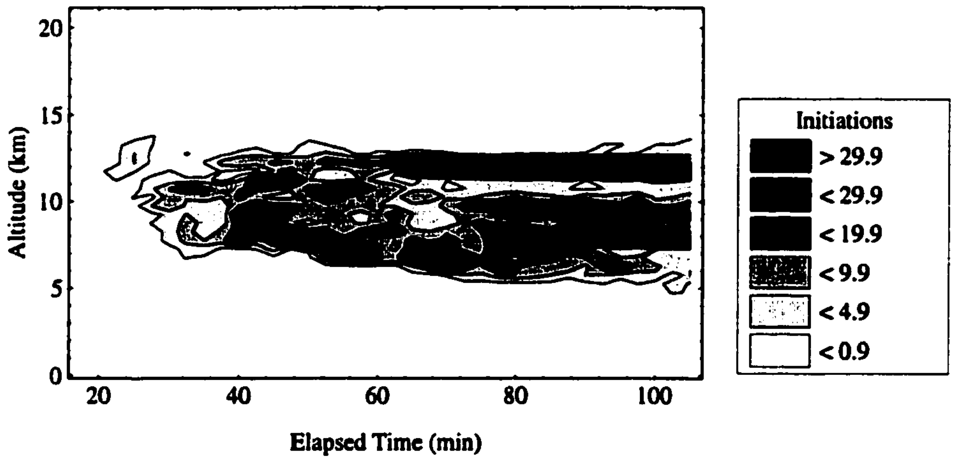

Figure A.3: Lightning channel segments and initiations versus altitude and time: airmass, Gardiner, moderate induction. Horizontally integrated (a) lightning segment counts and (b) initiations for each level. Time intervals are 2.5 minutes. (i.e. number per 2.5 minutes.)

(a)

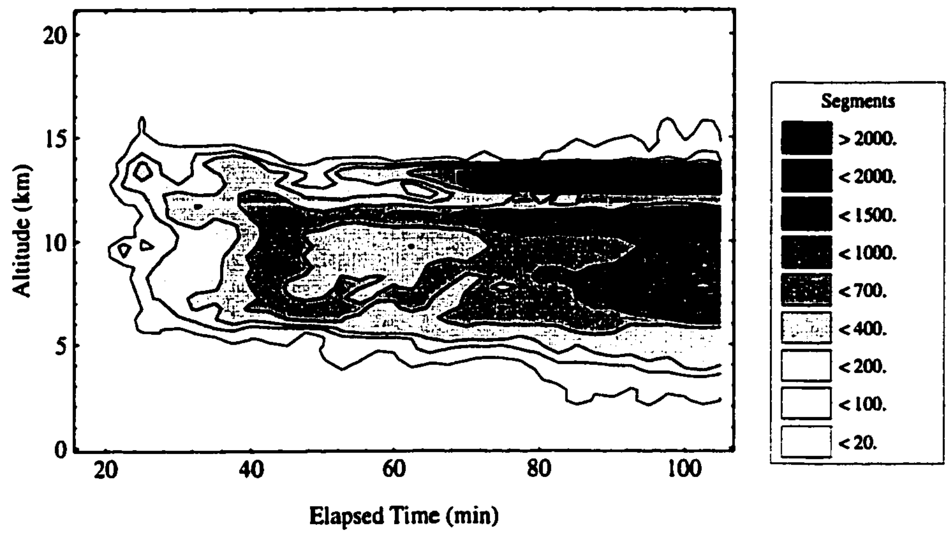

(b)

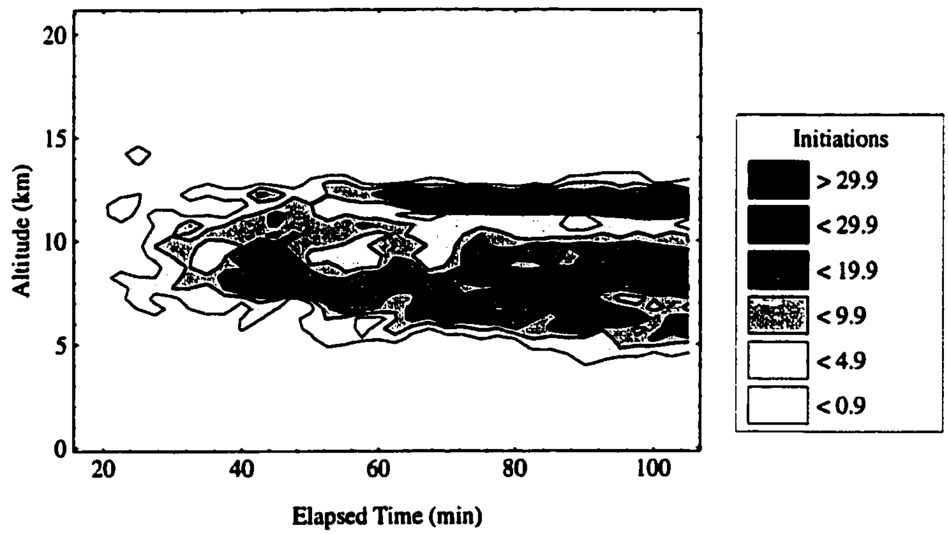

Figure A.4: Lightning channel segments and initiations versus altitude and time: airmass, Gardiner, strong induction. Horizontally integrated (a) lightning segment counts and (b) initiations for each level. Time intervals are 2.5 minutes. (i.e. number per 2.5 minutes.)

(a)

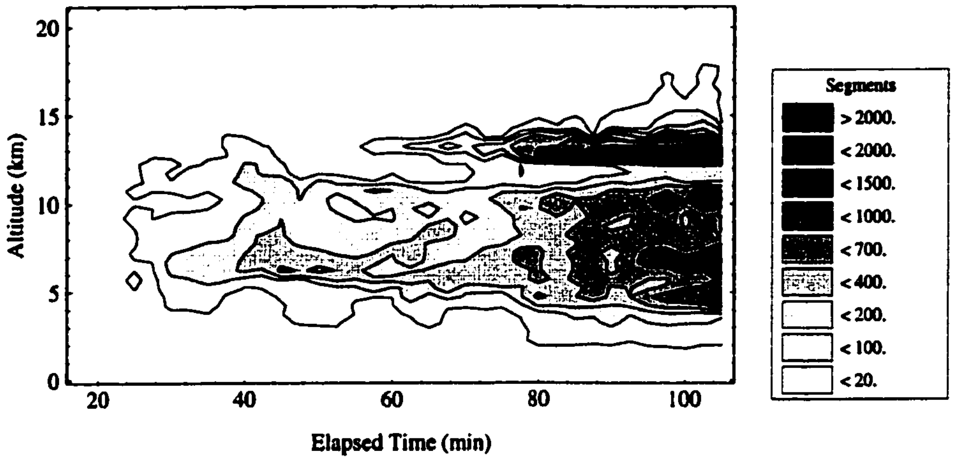

(b)

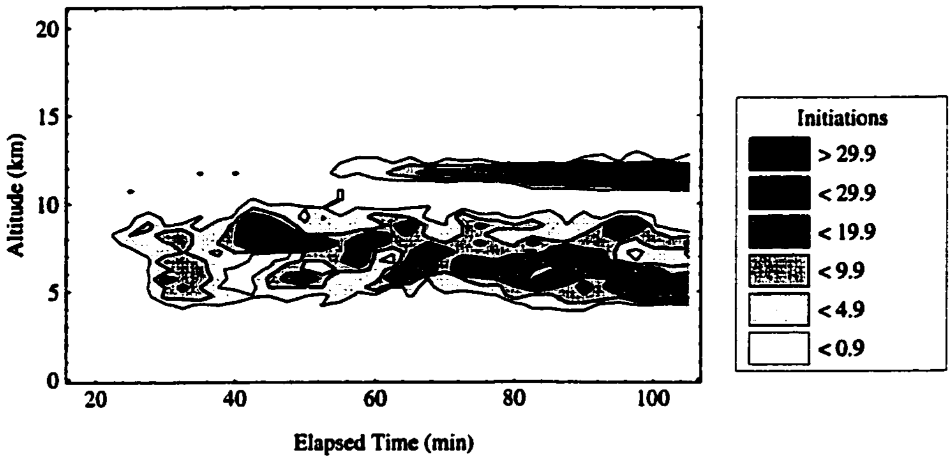

Figure A.5: Lightning channel segments and initiations versus altitude and time: airmass, Gardiner, strong induction, uniform $E_{\mathrm{init}} = 150\,\mathrm{kV/m}$. Horizontally integrated (a) lightning segment counts and (b) initiations for each level. Time intervals are 2.5 minutes. (i.e. number per 2.5 minutes.)

(a)

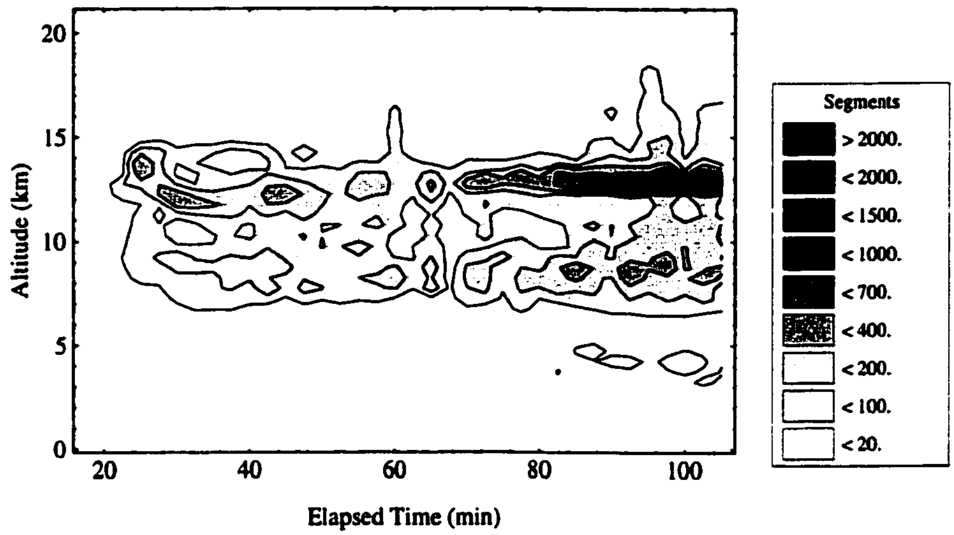

(b)

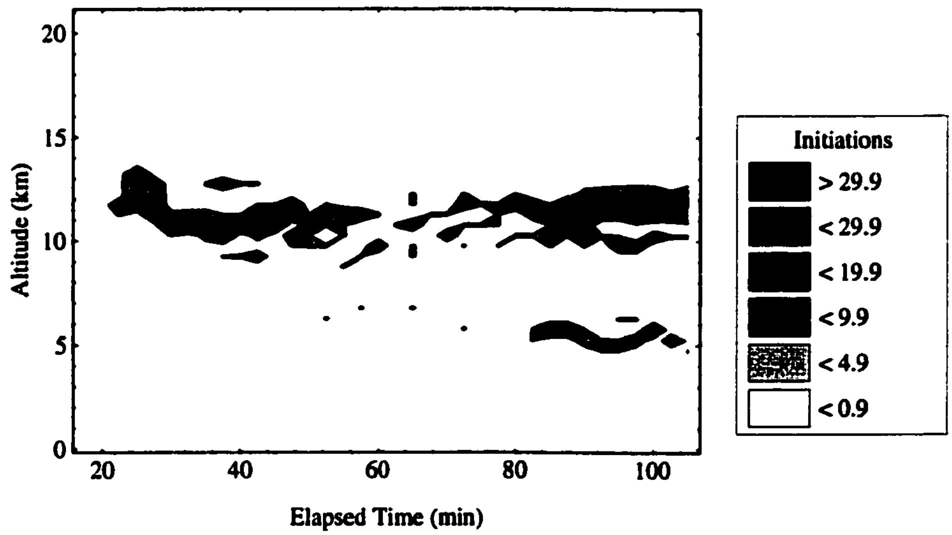

Figure A.6: Lightning channel segments and initiations versus altitude and time: airmass, Takahashi, moderate induction. Horizontally integrated (a) lightning segment counts and (b) initiations for each level. Time intervals are 2.5 minutes. (i.e. number per 2.5 minutes.)

(a)

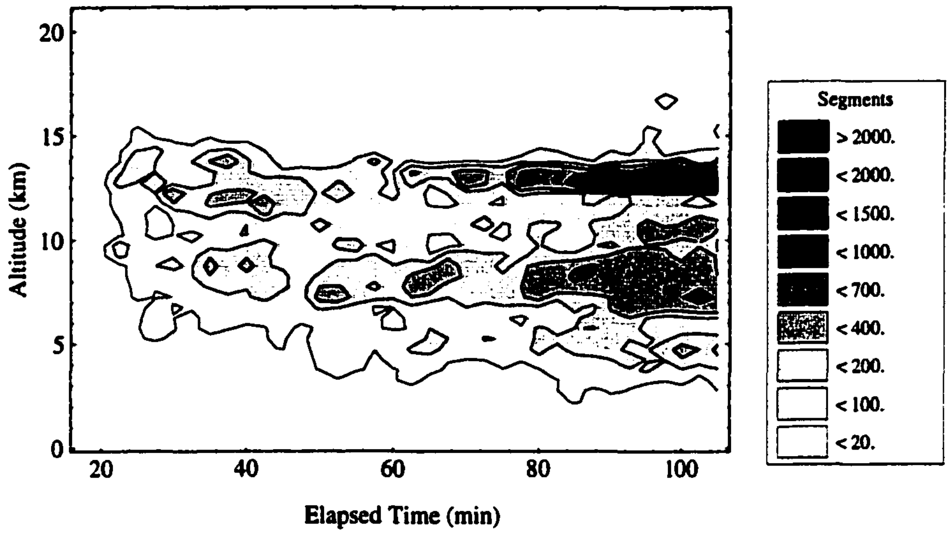

(b)

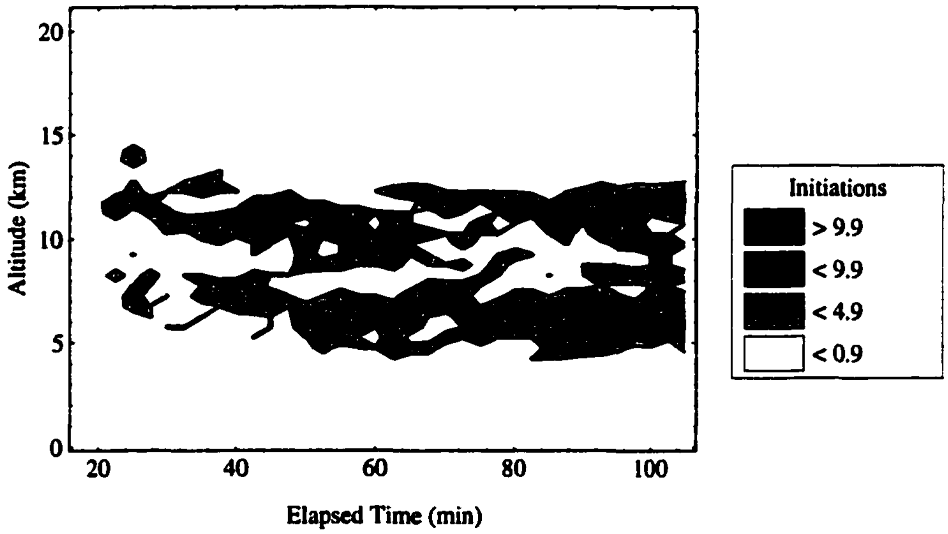

Figure A.7: Lightning channel segments and initiations versus altitude and time: airmass, Takahashi, strong induction. Horizontally integrated (a) lightning segment counts and (b) initiations for each level. Time intervals are 2.5 minutes. (i.e. number per 2.5 minutes.)

(a)

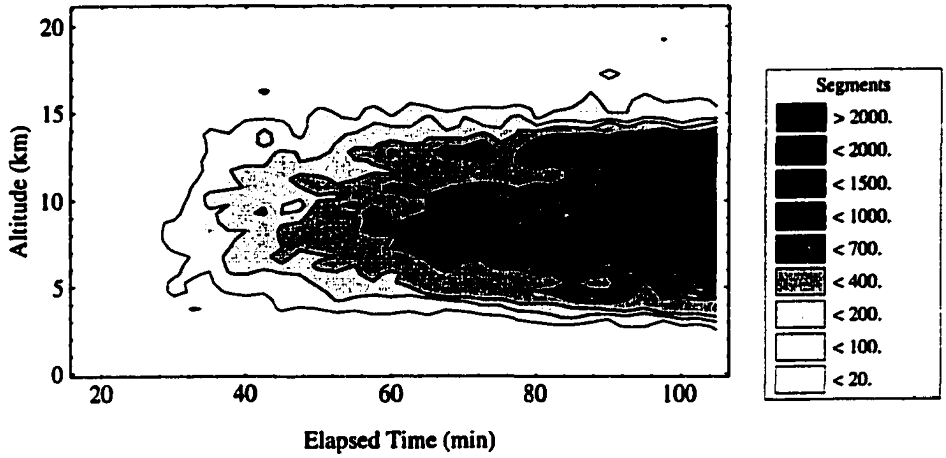

(b)

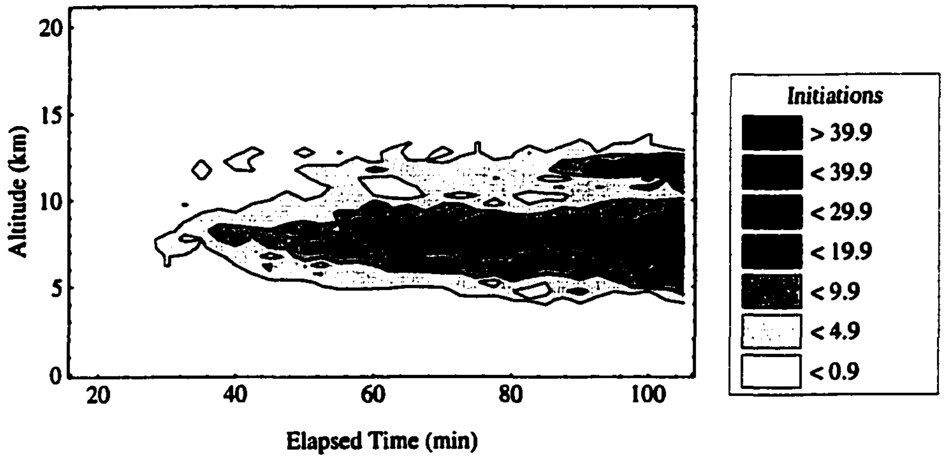

Figure A.8: Lightning channel segments and initiations versus altitude and time for HP supercell (riming rate, strong ind.). Horizontally integrated (a) lightning segment counts and (b) initiations for each level. Time intervals are 2.5 minutes. (i.e. number per 2.5 minutes.)

(a)

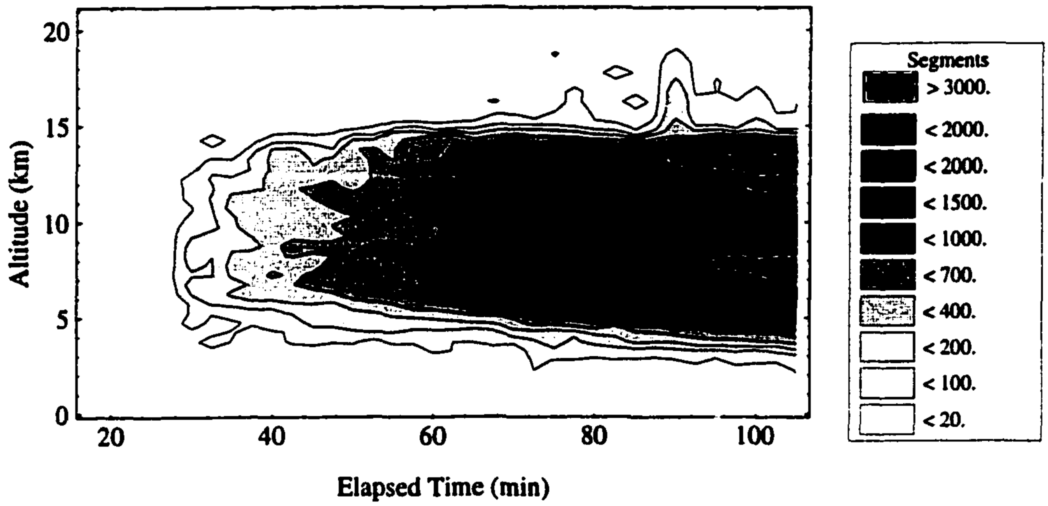

(b)

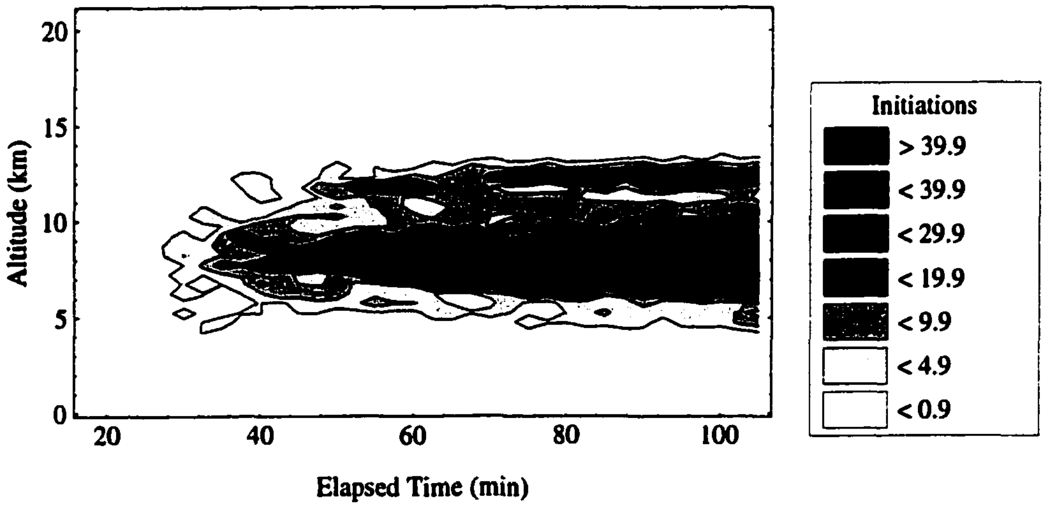

Figure A.9: Lightning channel segments and initiations versus altitude and time for HP supercell (Gardiner, strong ind.). Horizontally integrated (a) lightning segment counts and (b) initiations for each level. Time intervals are 2.5 minutes. (i.e. number per 2.5 minutes.)

(a)

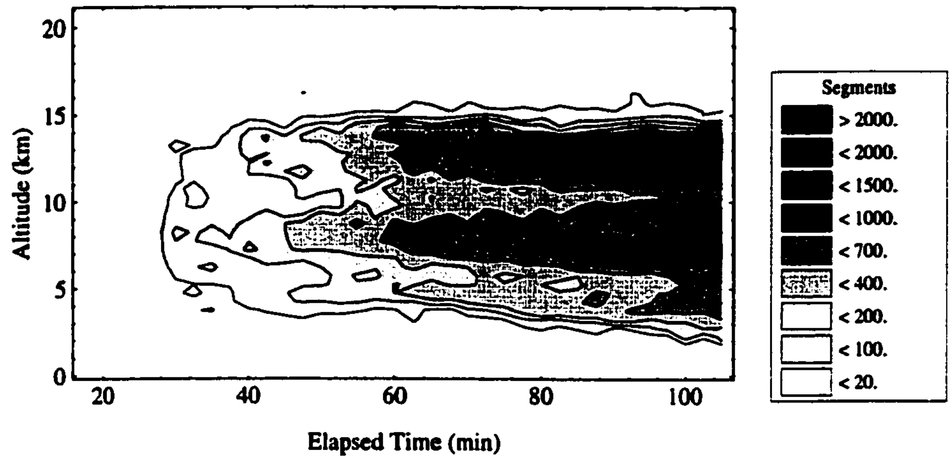

(b)

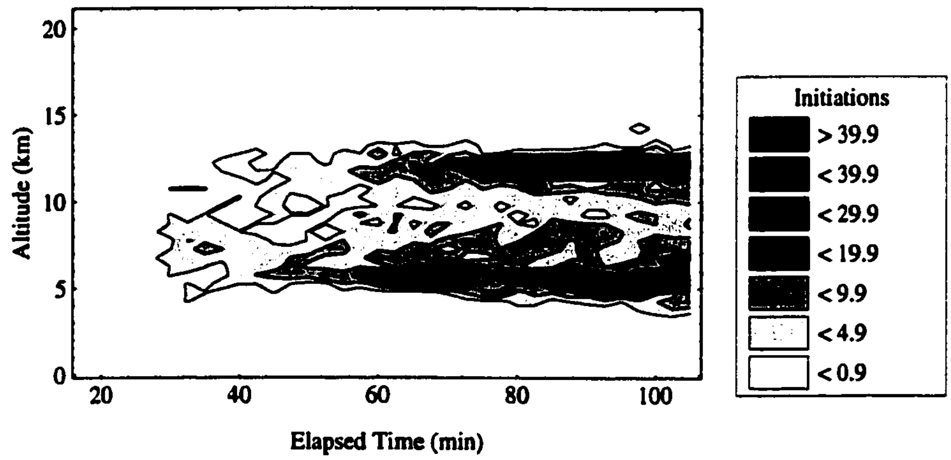

Figure A.10: Lightning channel segments and initiations versus altitude and time for HP supercell (Takahashi, strong ind.). Horizontally integrated (a) lightning segment counts and (b) initiations for each level. Time intervals are 2.5 minutes. (i.e. number per 2.5 minutes.)

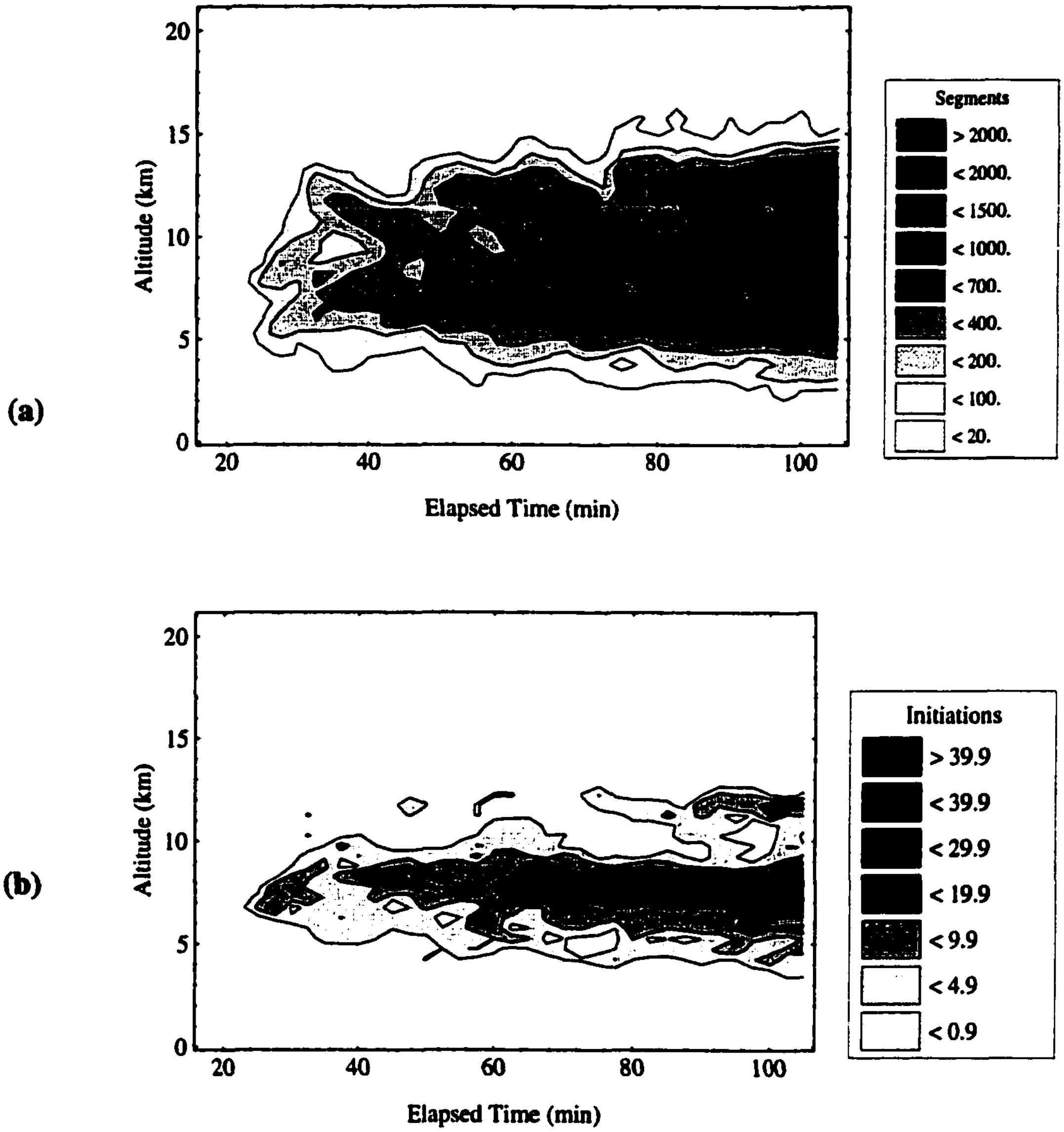

Figure A.11: Lightning channel segments and initiations versus altitude and time for LP supercell (riming rate, strong ind.). Horizontally integrated (a) lightning segment counts and (b) initiations for each level. Time intervals are 2.5 minutes. (i.e. number per 2.5 minutes.)

(a)

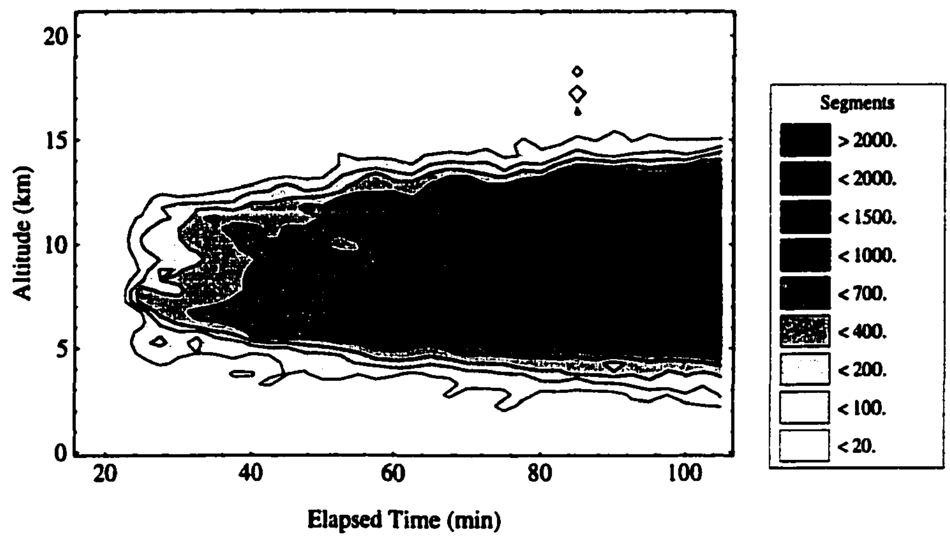

(b)

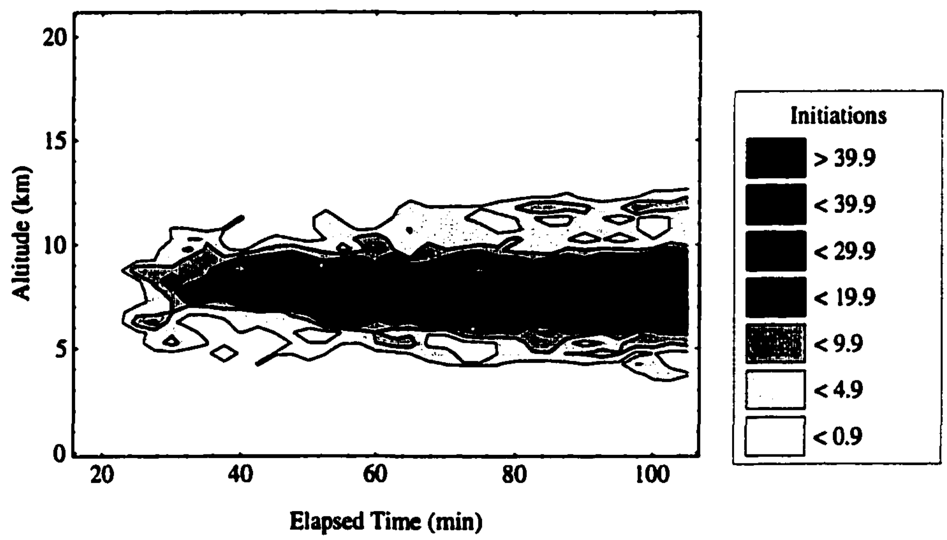

Figure A.12: Lightning channel segments and initiations versus altitude and time for LP supercell (Gardiner, strong ind.). Horizontally integrated (a) lightning segment counts and (b) initiations for each level. Time intervals are 2.5 minutes. (i.e. number per 2.5 minutes.)

(a)

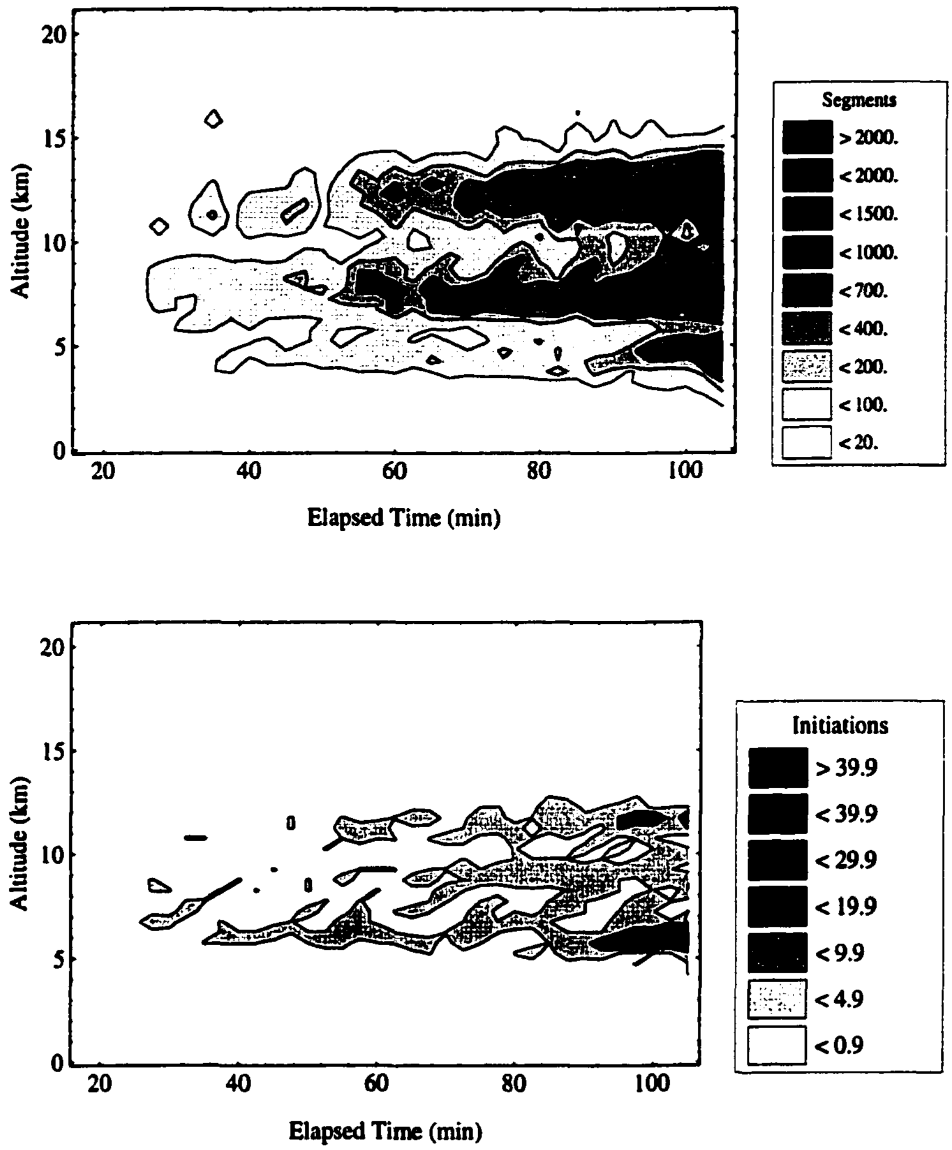

(b)

Figure A.13: Lightning channel segments and initiations versus altitude and time for LP supercell (Takahashi, half-strong ind.). Horizontally integrated (a) lightning segment counts and (b) initiations for each level. Time intervals are 2.5 minutes. (i.e. number per 2.5 minutes.)

(a)

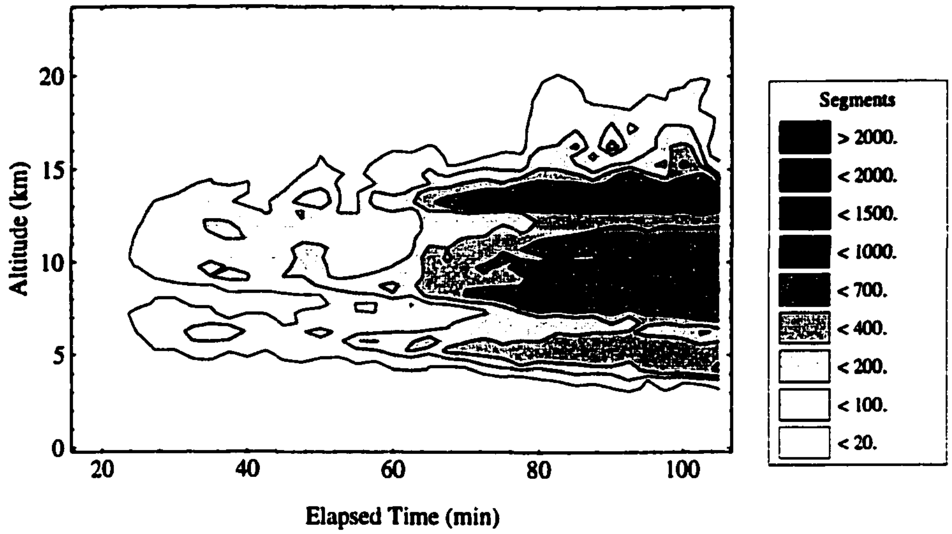

(b)

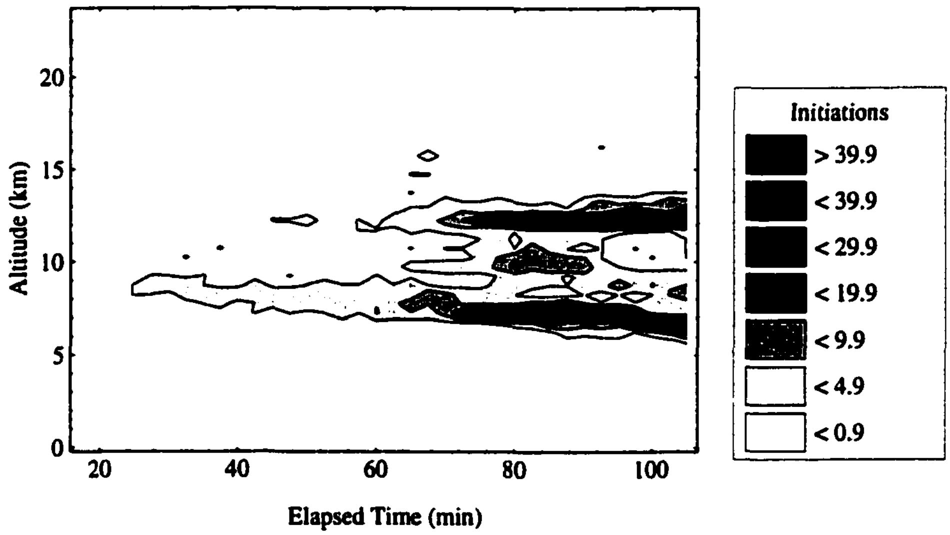

Figure A.14: Lightning channel segments and initiations versus altitude and time for CL supercell (Riming Rate, moderate ind.). Horizontally integrated (a) lightning segment counts and (b) initiations for each level. Time intervals are 2.5 minutes. (i.e. number per 2.5 minutes.)

(a)

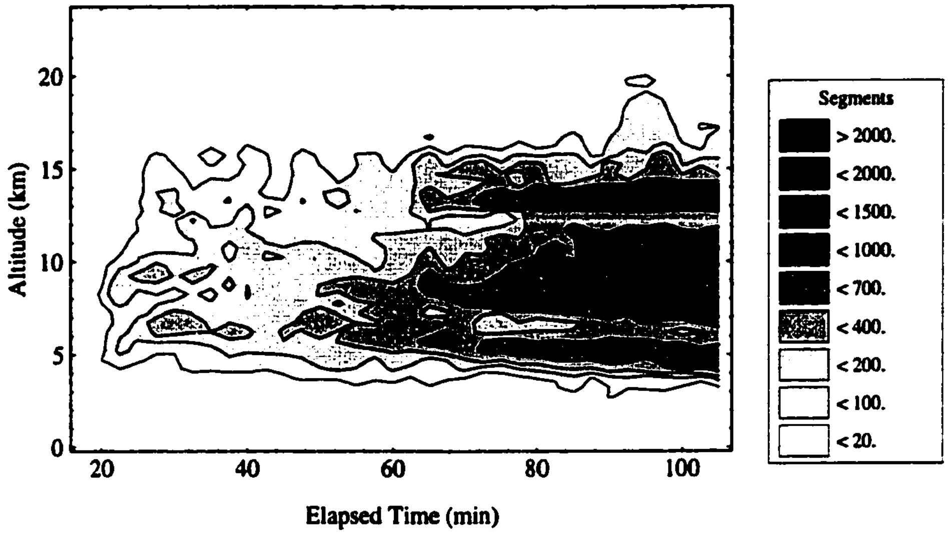

(b)

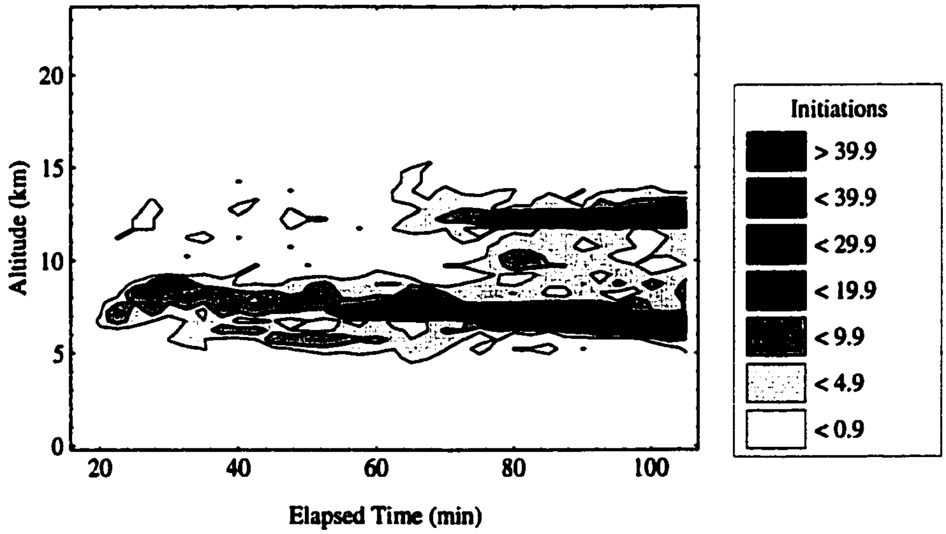

Figure A.15: Lightning channel segments and initiations versus altitude and time for CL supercell (Riming Rate, strong ind.). Horizontally integrated (a) lightning segment counts and (b) initiations for each level. Time intervals are 2.5 minutes. (i.e. number per 2.5 minutes.)

(a)

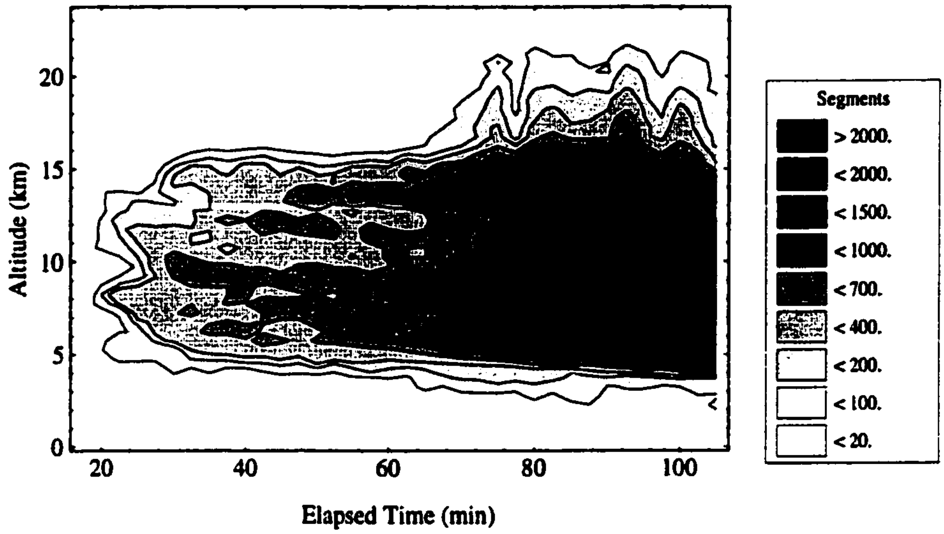

(b)

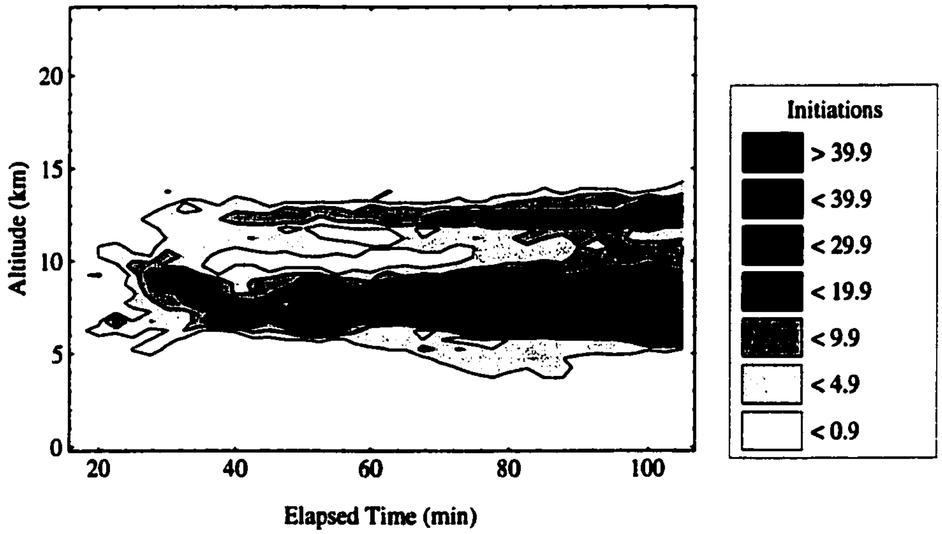

Figure A.16: Lightning channel segments and initiations versus altitude and time for CL supercell (Gardiner, strong ind.). Horizontally integrated (a) lightning segment counts and (b) initiations for each level. Time intervals are 2.5 minutes. (i.e. number per 2.5 minutes.)

(a)

(b)

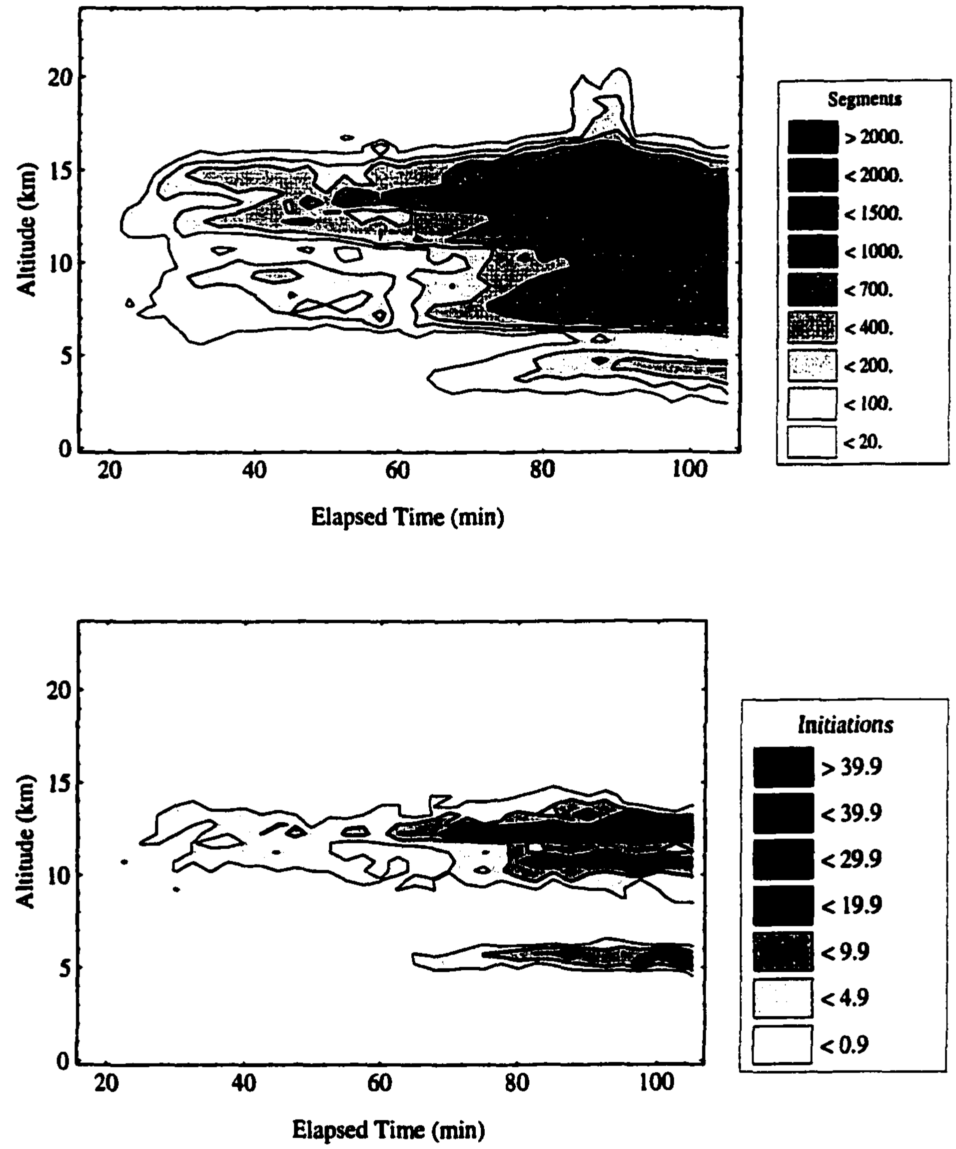

Figure A.17: Lightning channel segments and initiations versus altitude and time for CL supercell (Takahashi, moderate ind.). Horizontally integrated (a) lightning segment counts and (b) initiations for each level. Time intervals are 2.5 minutes. (i.e. number per 2.5 minutes.)

Appendix B

Lightning Discharge Magnitude Histograms

(a)

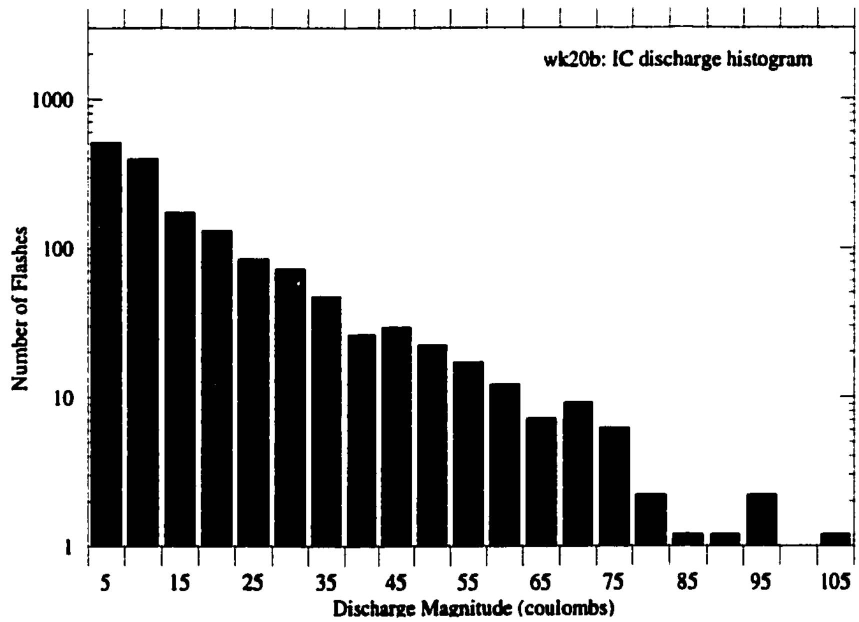

Figure B.1: Histogram of IC discharge magnitudes: airmass, riming rate, moderate induction.

(a)

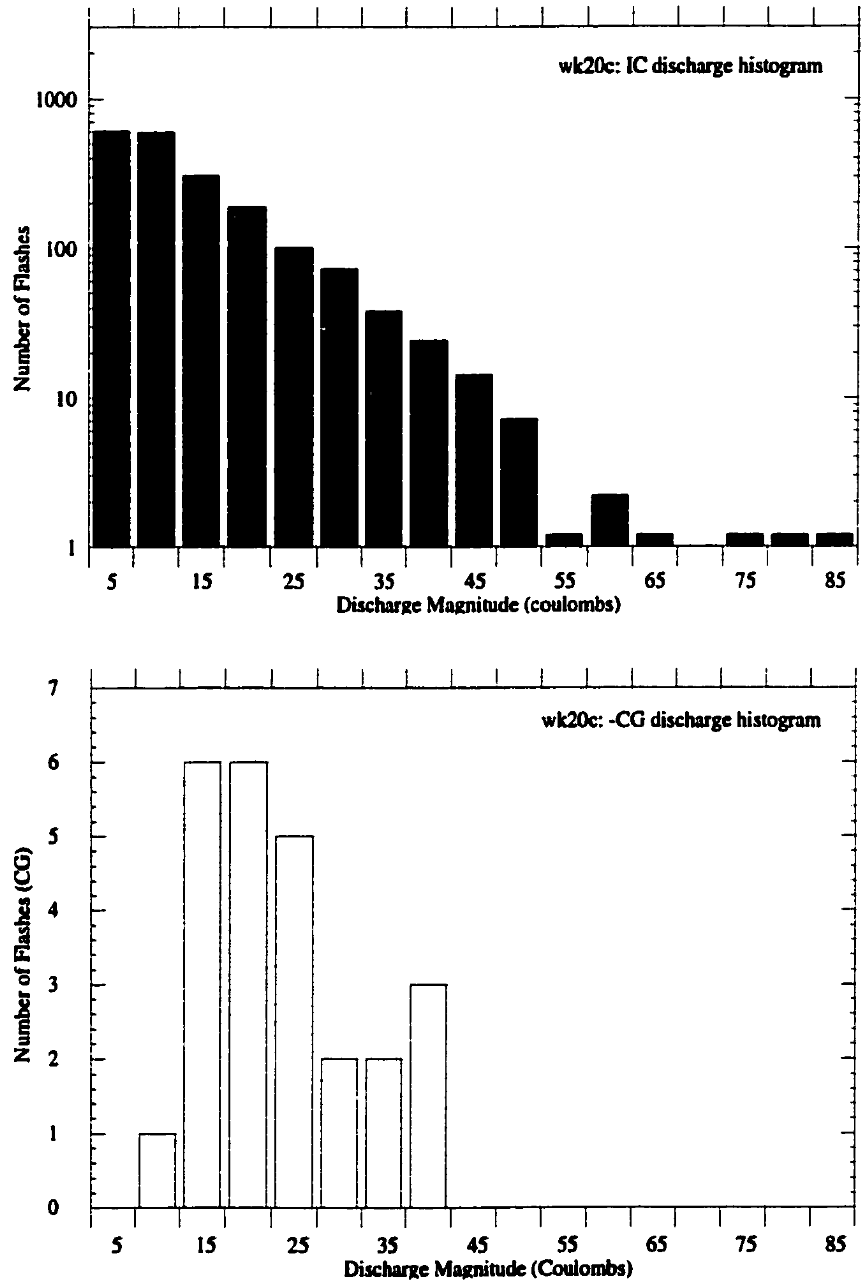

(b)

Figure B.2: Histogram of (a) IC and (b) CG discharge magnitudes: airmass, riming rate, strong induction.

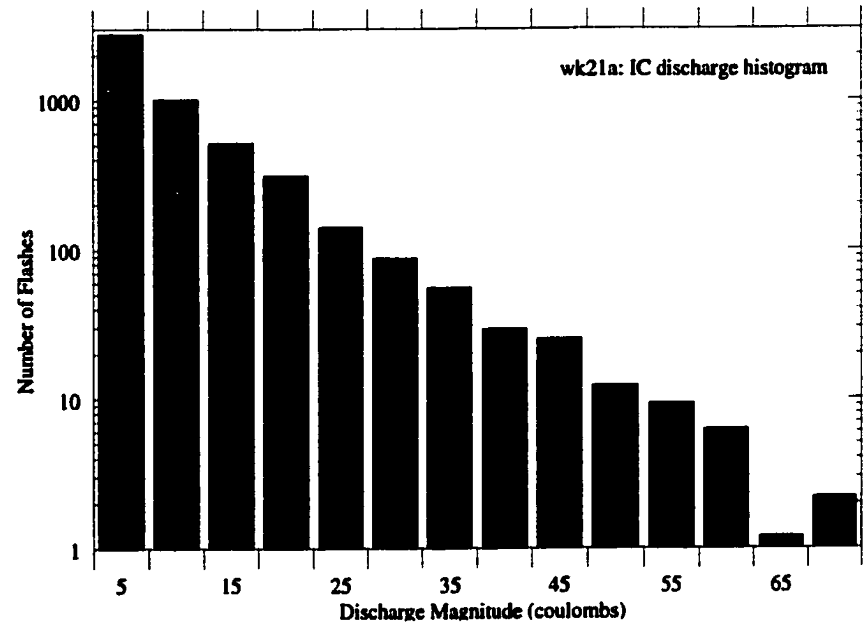

(a)

Figure B.3: Histogram of IC discharge magnitudes: airmass, Gardiner, moderate induction.

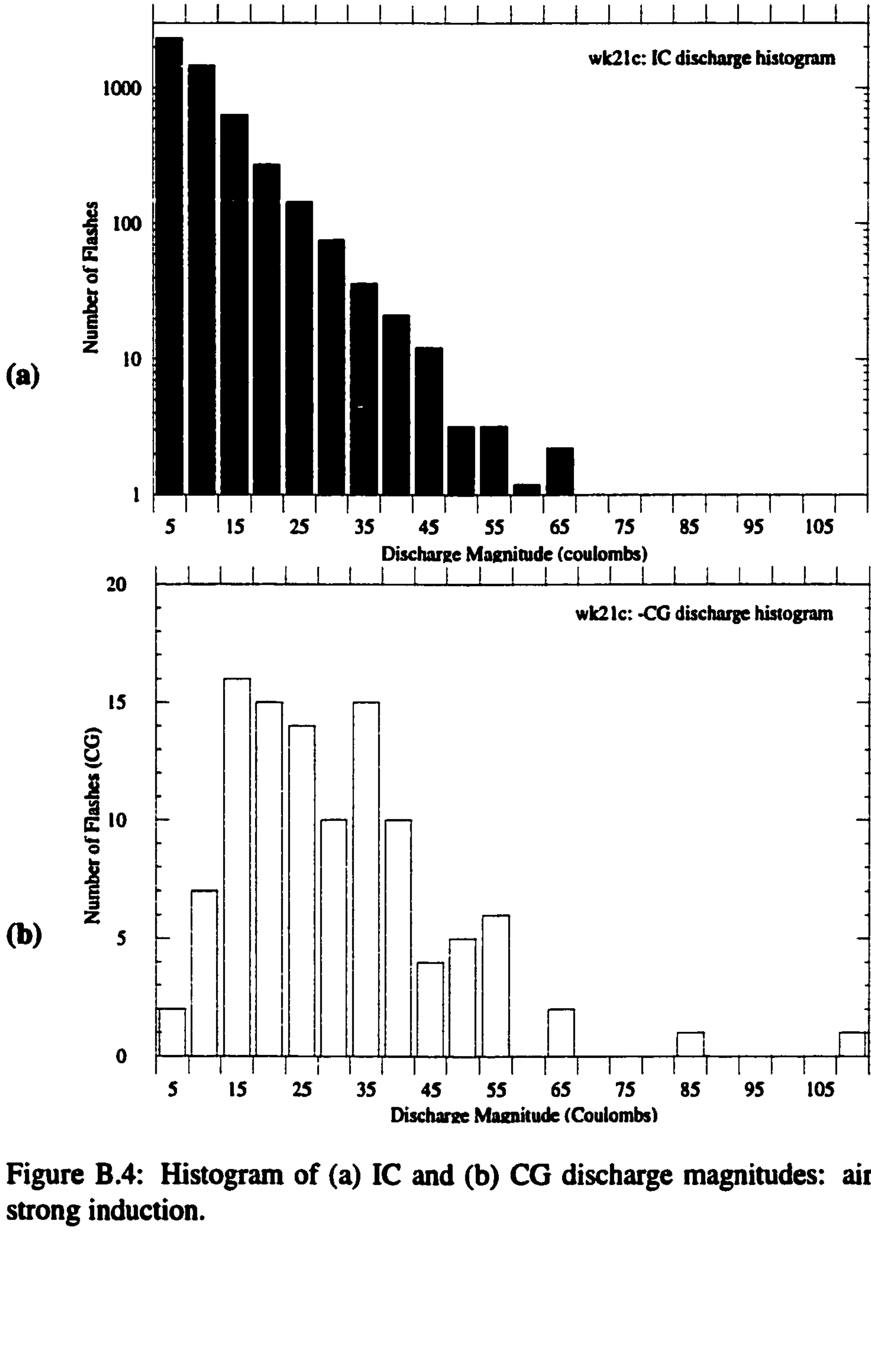

Figure B.4: Histogram of (a) IC and (b) CG discharge magnitudes: airmass, Gardiner, strong induction.

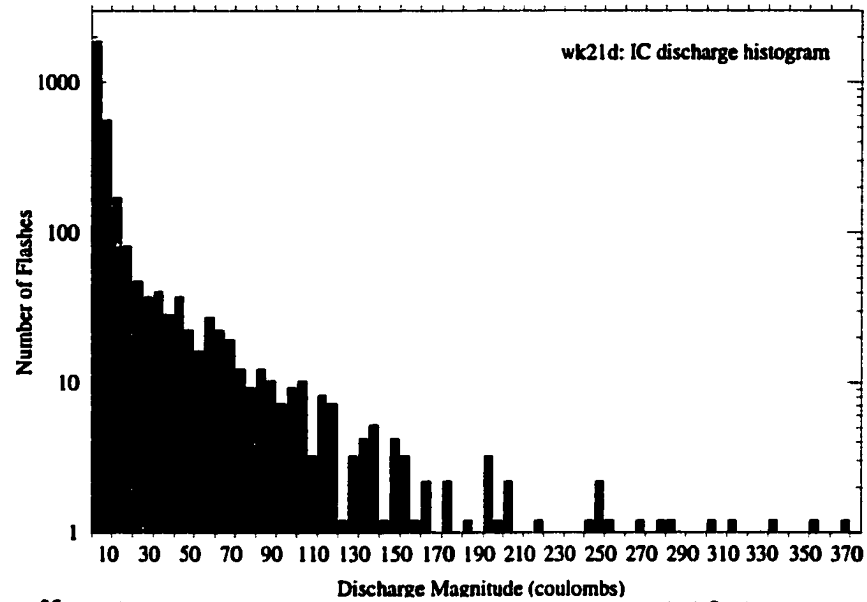

(a)

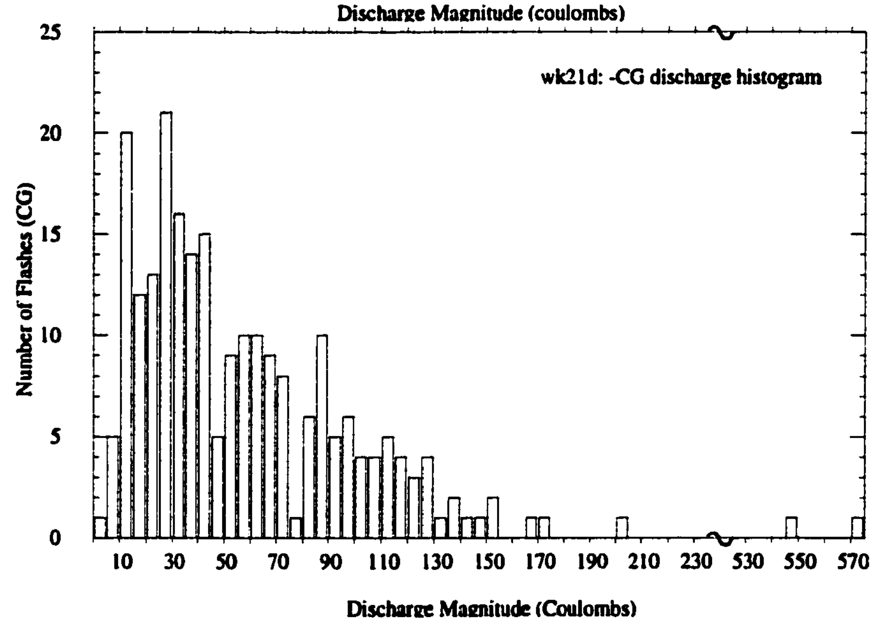

(b)

Figure B.5: Histograms of (a) IC and (b) CG discharge magnitudes: airmass, Gardiner, strong induction, uniform $E_{\text{init}} = 150\,\text{kV/m}$.

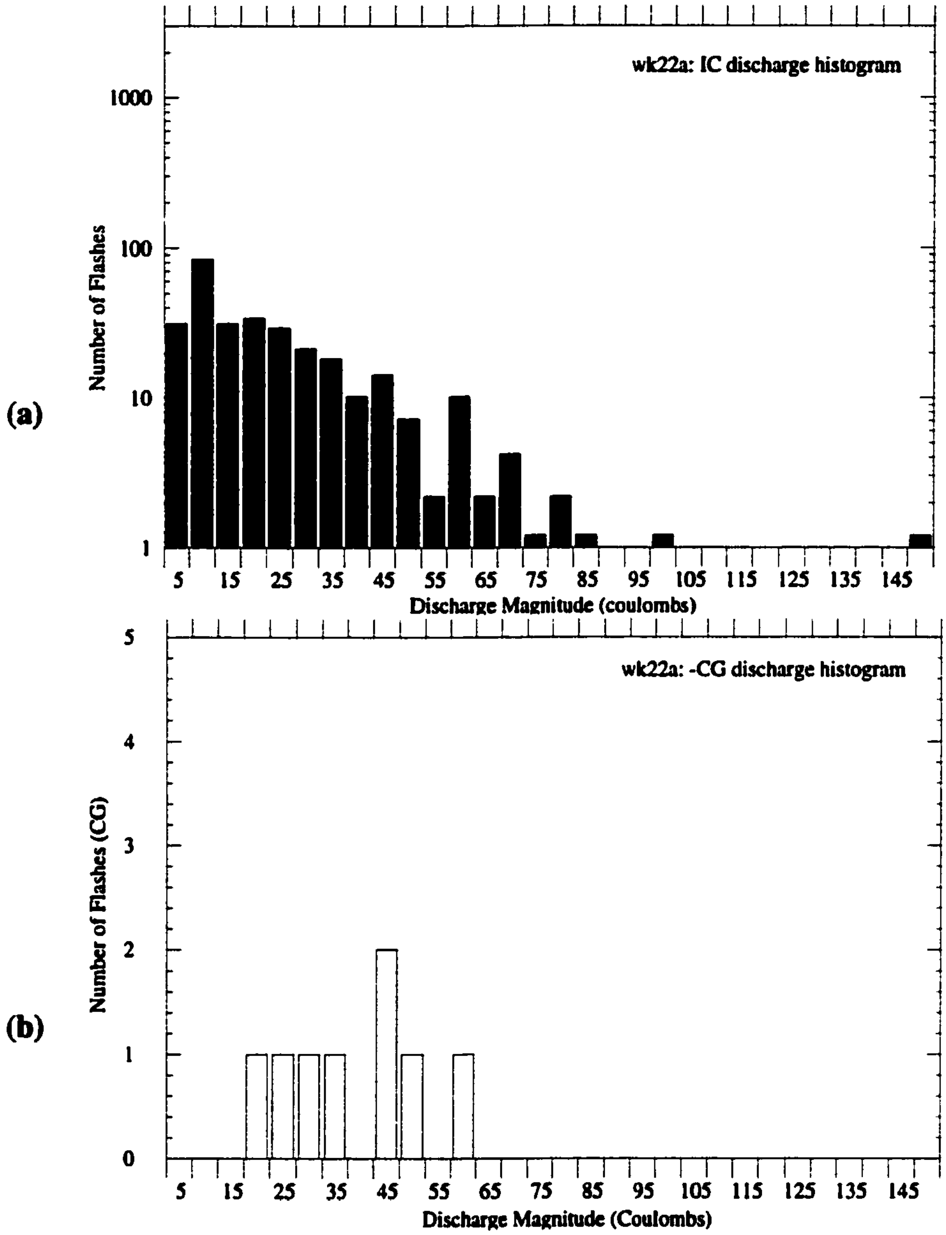

Figure B.6: Histograms of (a) IC and (b) CG discharge magnitudes: airmass, Takahashi, moderate induction.

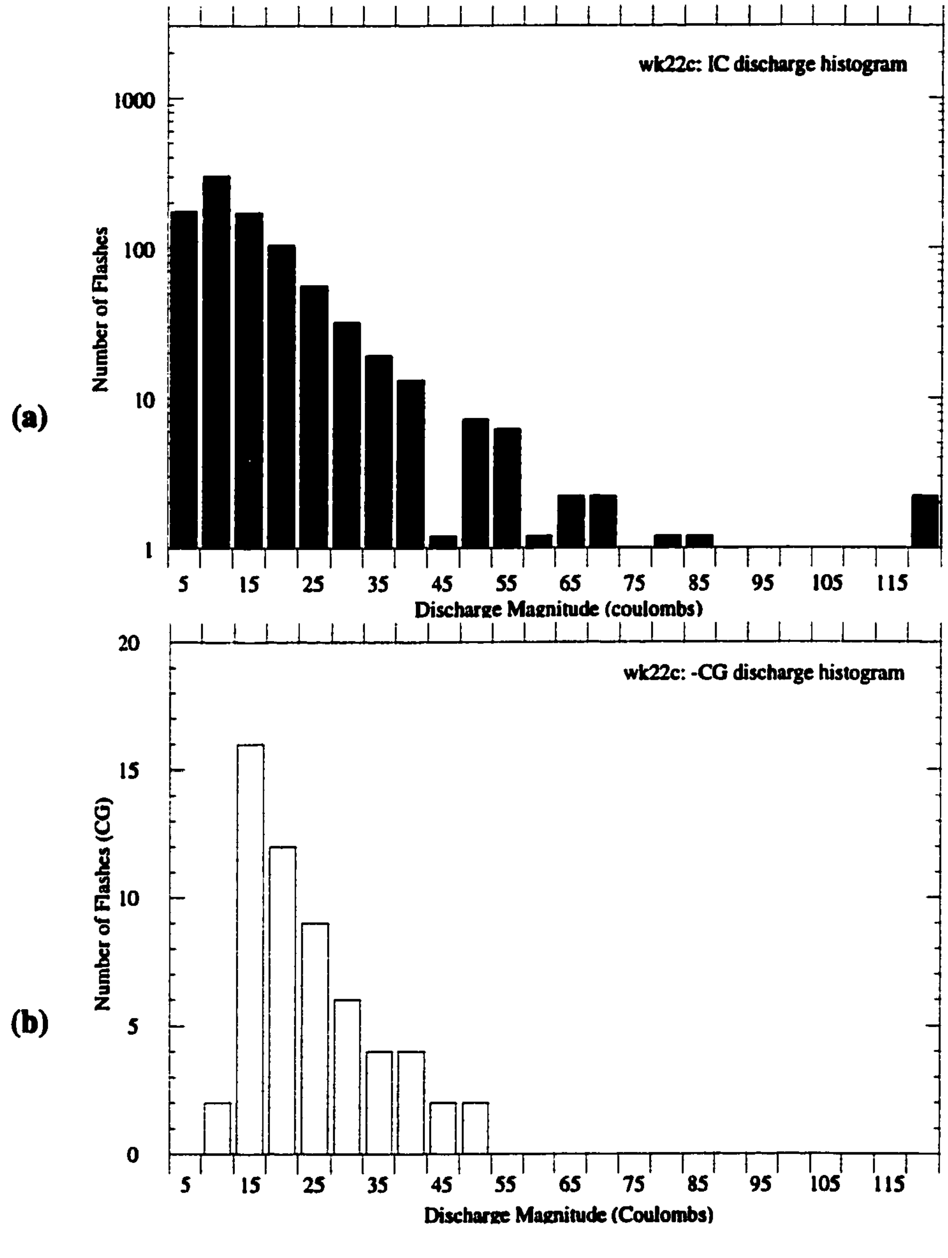

Figure B.7: Histograms of (a) IC and (b) CG discharge magnitudes: airmass, Takahashi, strong induction.

(a)

(b)

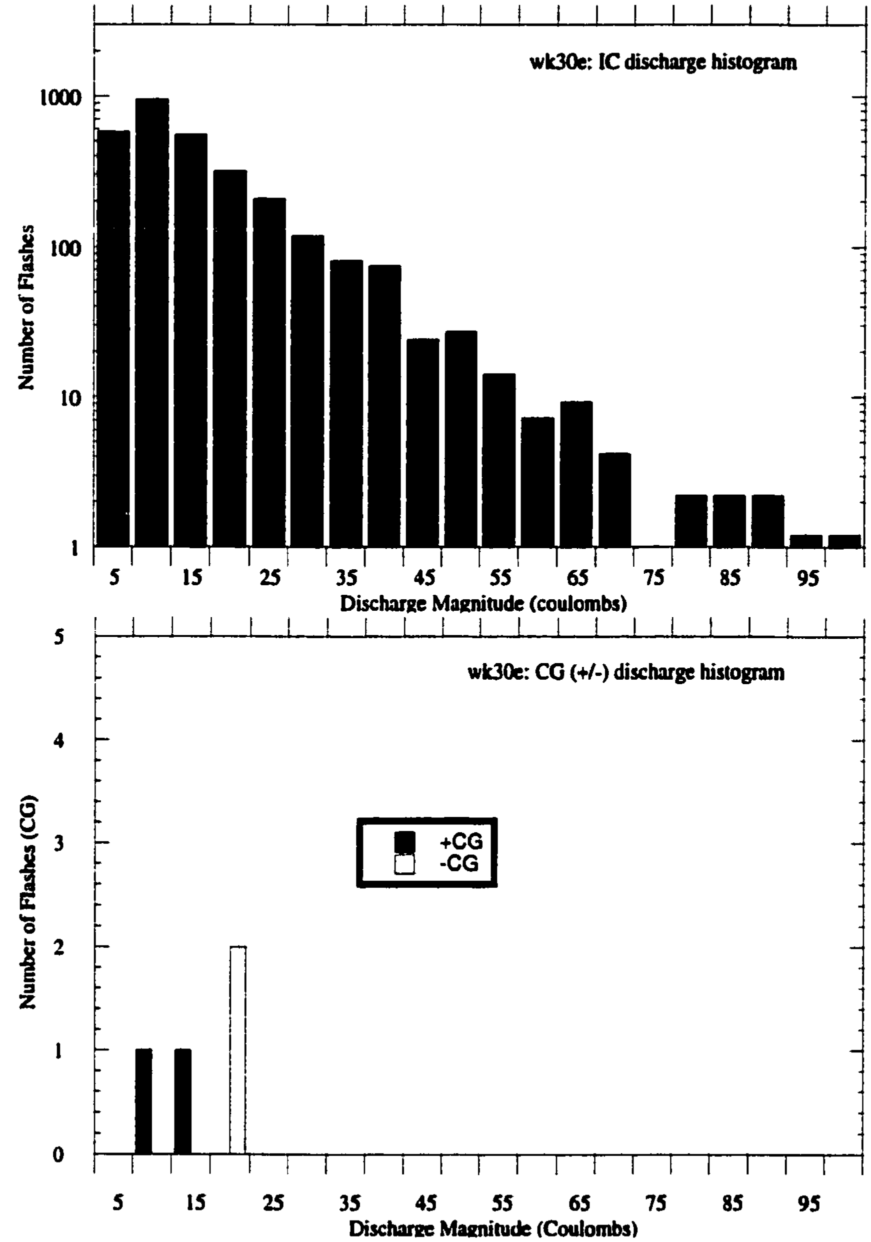

Figure B.8: Histograms of (a) IC and (b) CG discharge magnitudes: HP supercell, Riming Rate, strong induction.

(a)

(b)

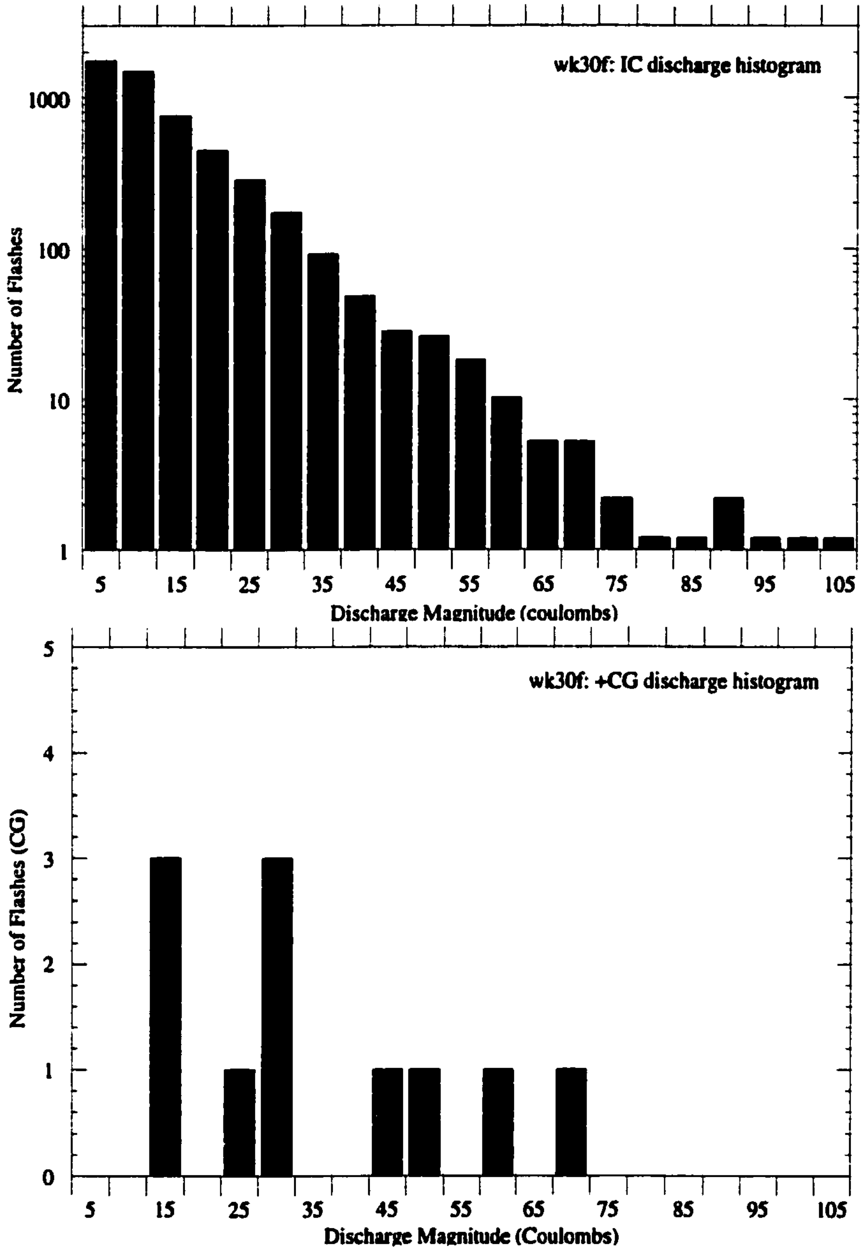

Figure B.9: Histograms of (a) IC and (b) CG discharge magnitudes: HP supercell, enhanced Riming Rate, strong induction.

(a)

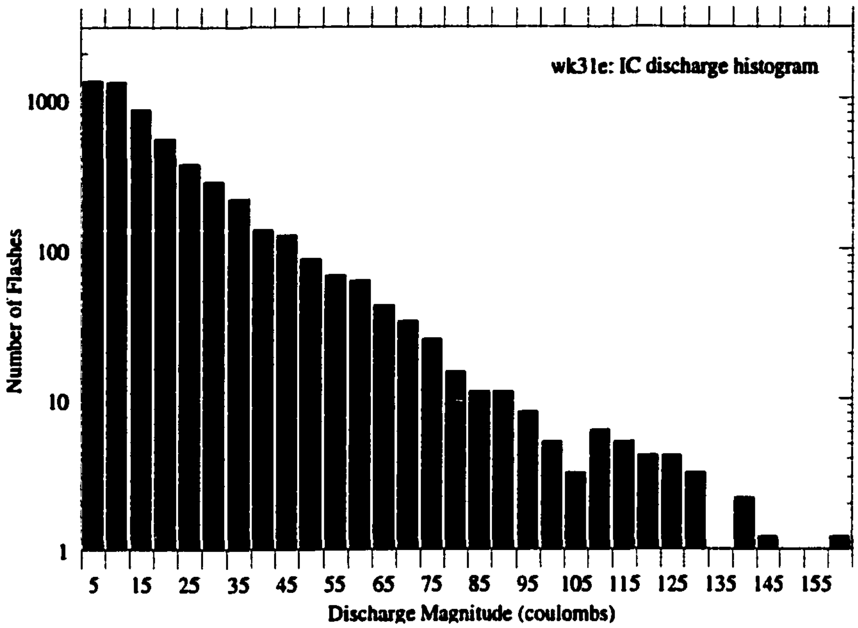

(b)

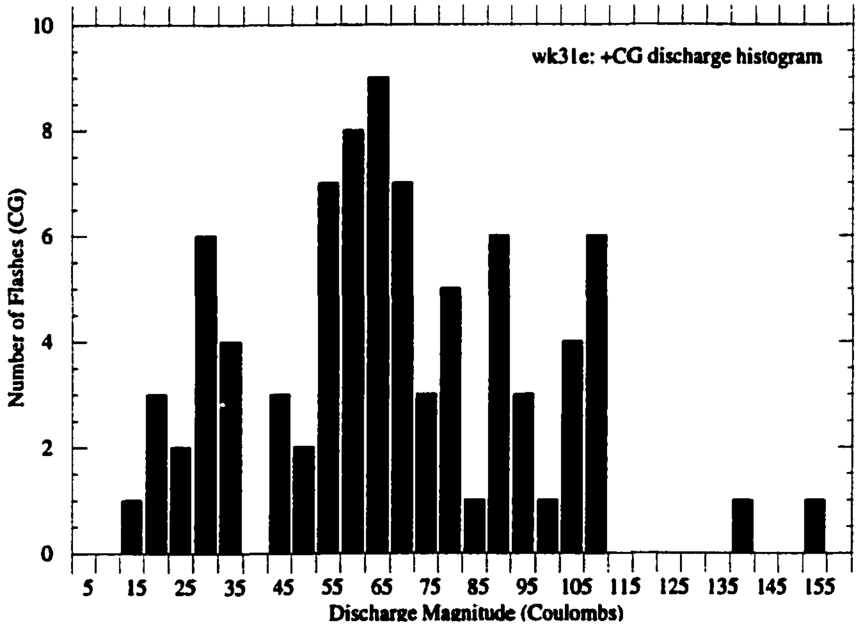

Figure B.10: Histograms of (a) IC and (b) CG discharge magnitudes: HP supercell, Gardiner, strong induction.

(a)

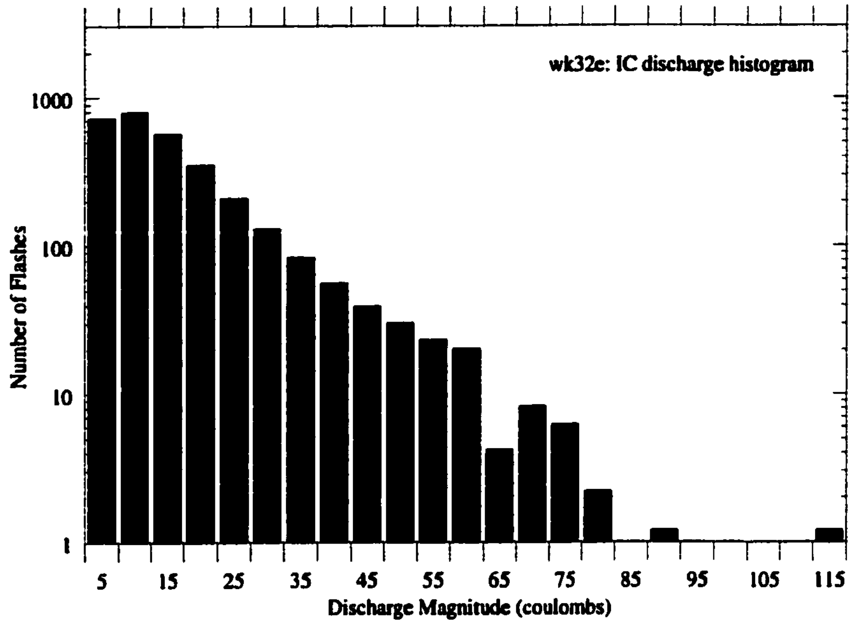

(b)

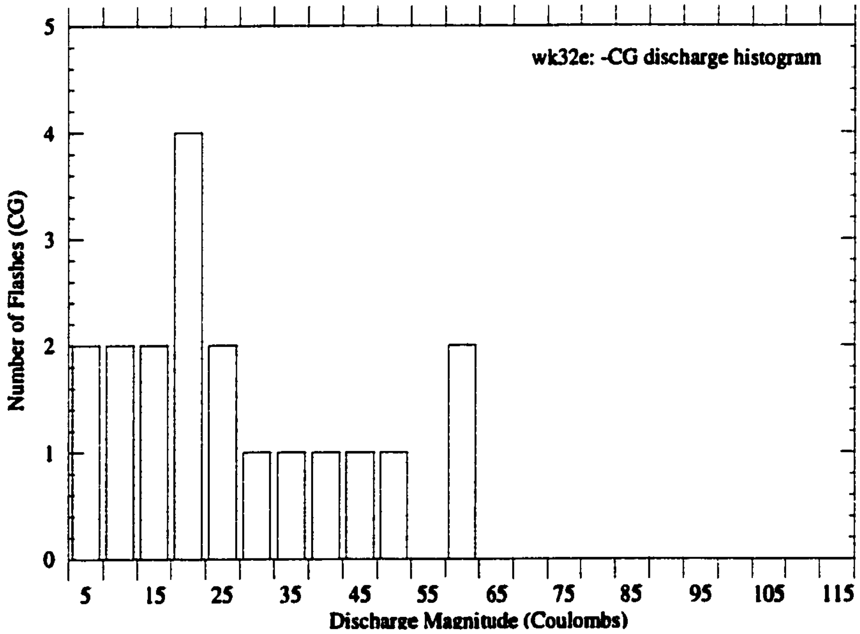

Figure B.11: Histograms of (a) IC and (b) CG discharge magnitudes: HP supercell, Takahashi, strong induction.

(a)

(b)

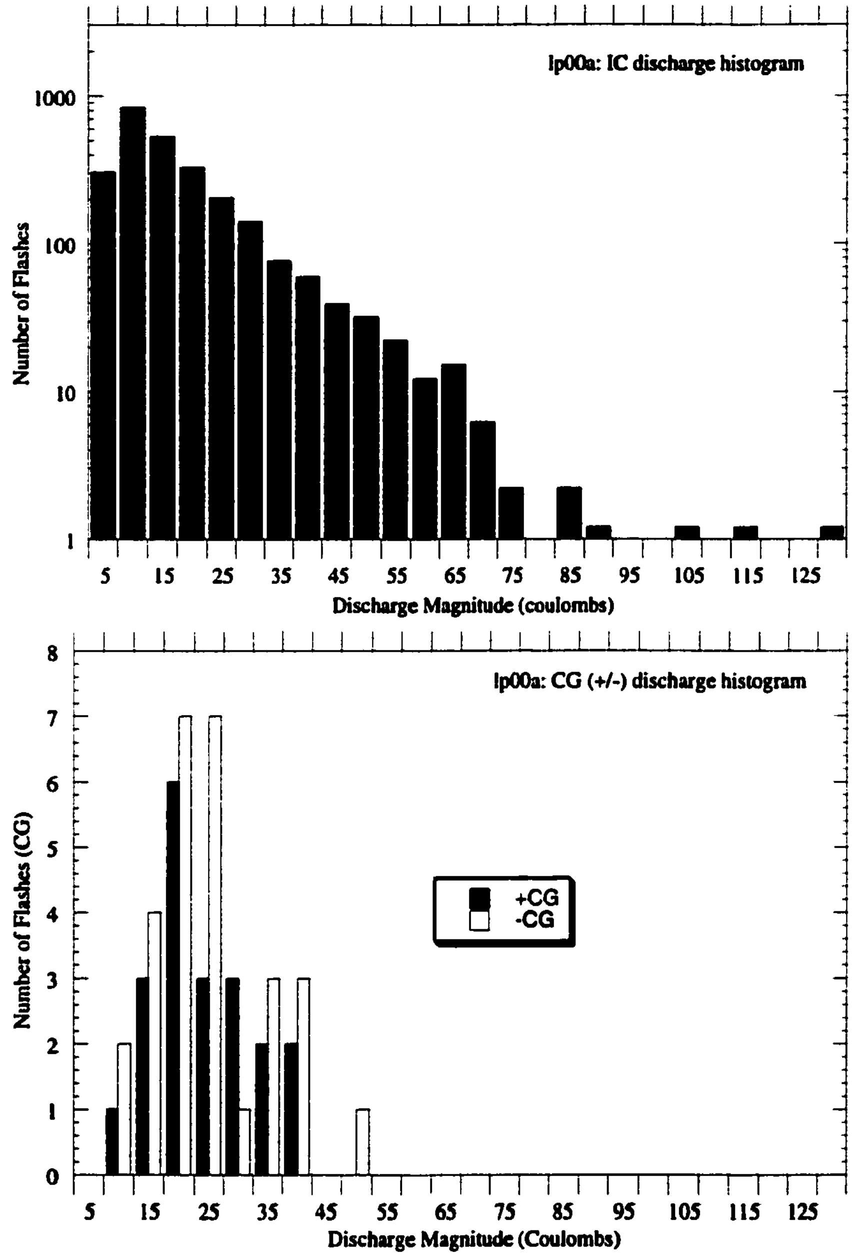

Figure B.12: Histograms of (a) IC and (b) CG discharge magnitudes: LP supercell, Riming Rate, strong induction.

(a)

(b)

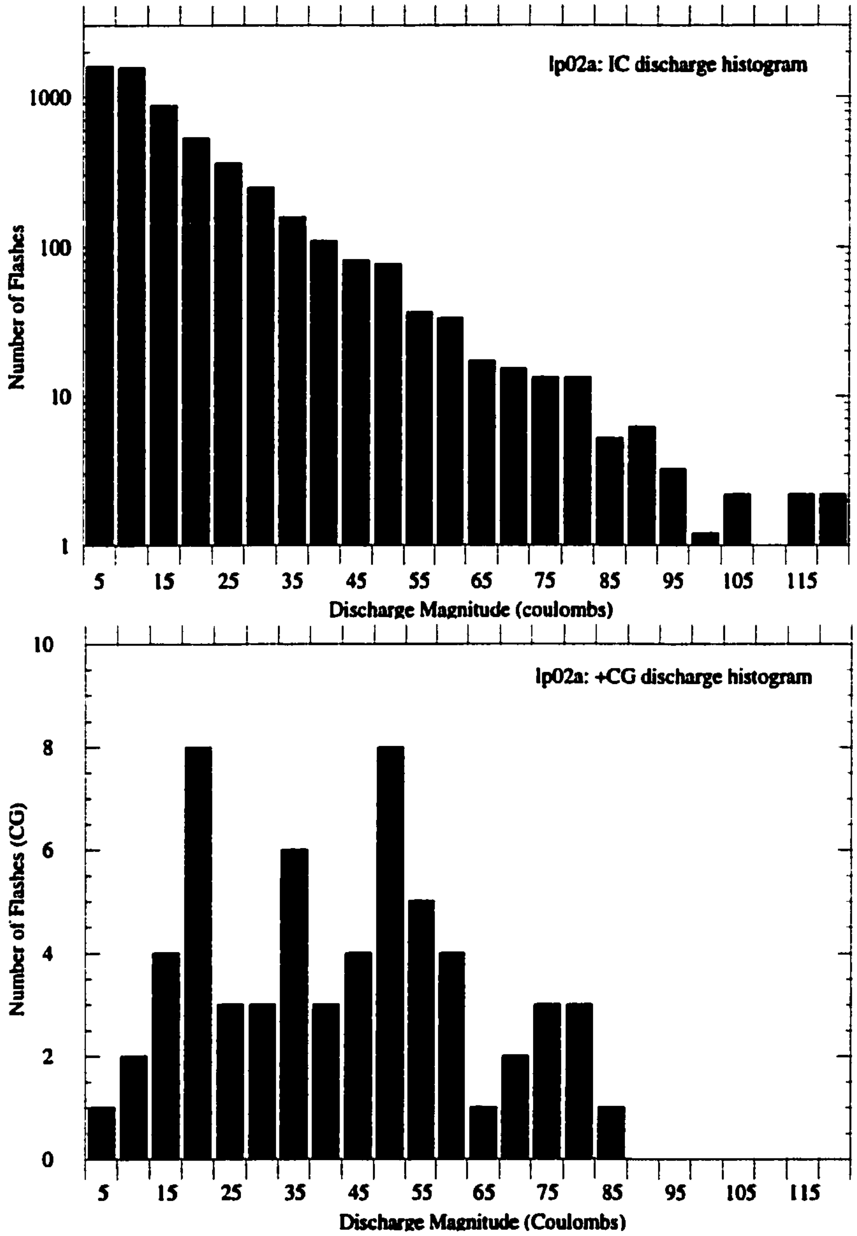

Figure B.13: Histograms of (a) IC and (b) CG discharge magnitudes: LP supercell, Gardiner, strong induction.

(a)

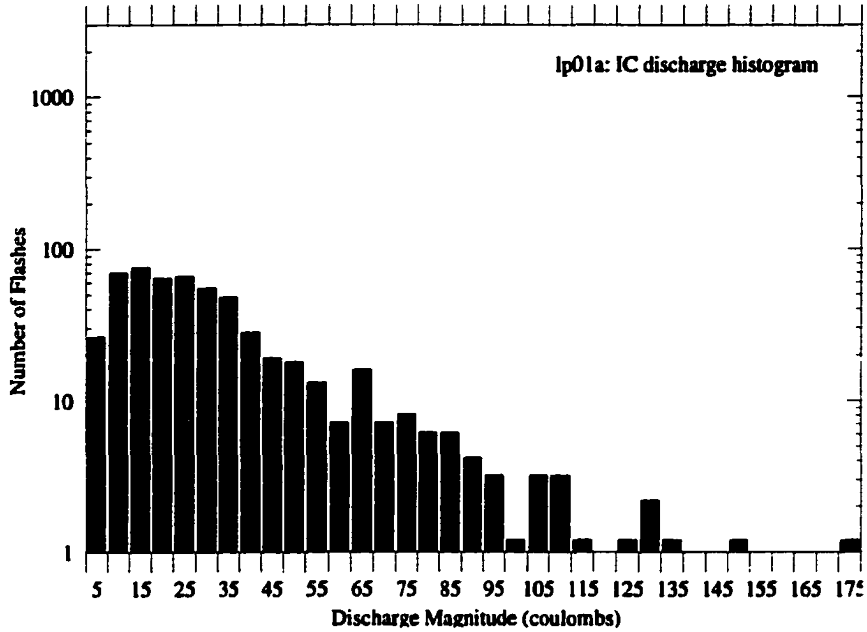

Figure B.14: Histogram of IC discharge magnitudes: LP supercell, Takahashi, half-strong inductiong. (The storm produced one −CG flash and one +CG flash.)

(a)

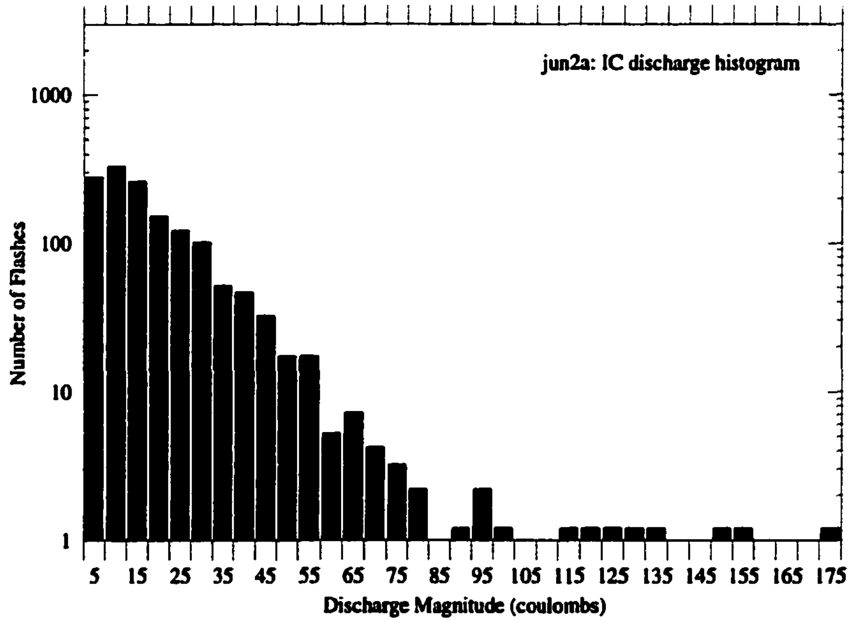

Figure B.15: Histograms of IC discharge magnitude: CL supercell, Riming Rate, moderate induction.

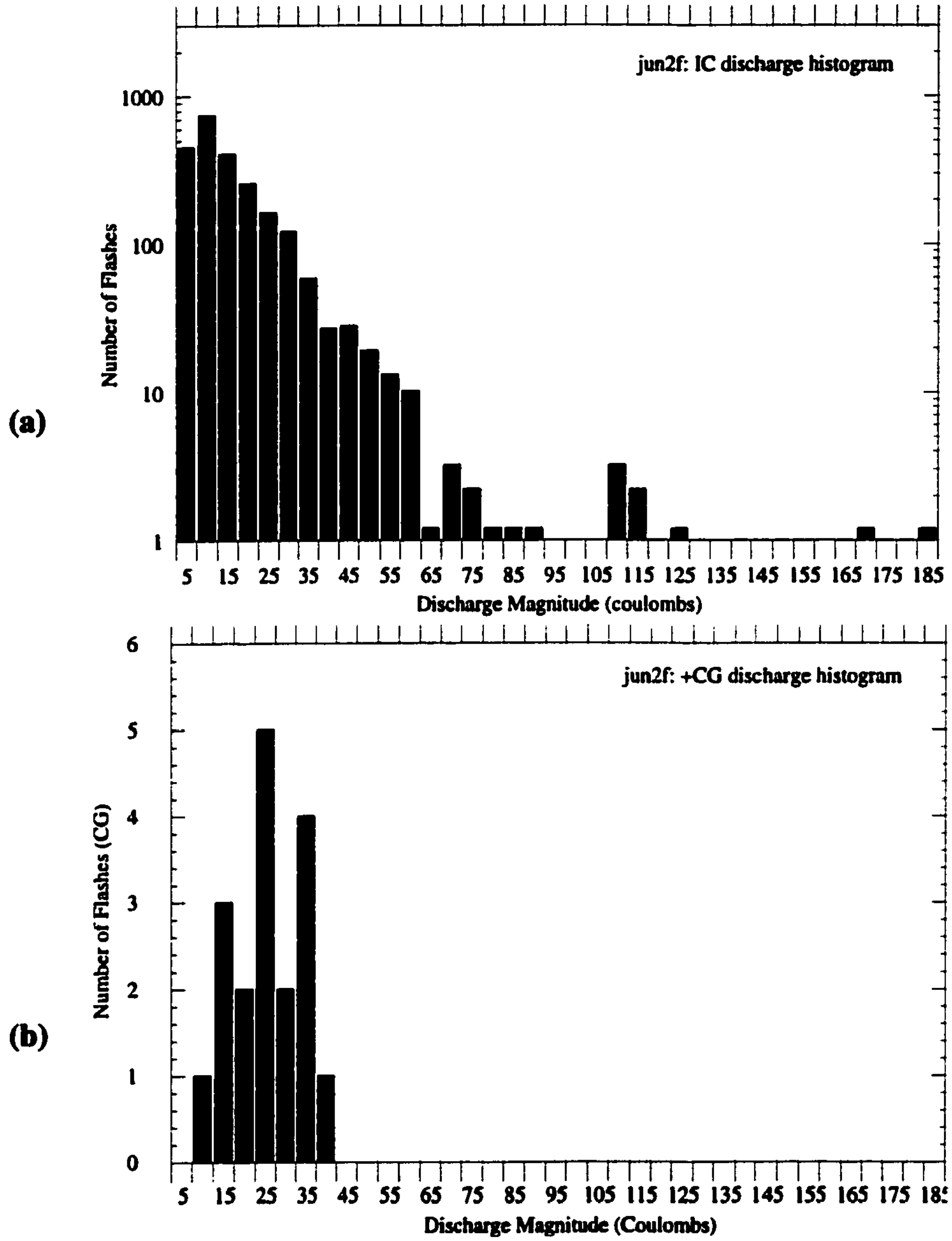

Figure B.16: Histograms of (a) IC and (b) CG discharge magnitudes: CL supercell, Riming Rate, moderate induction.

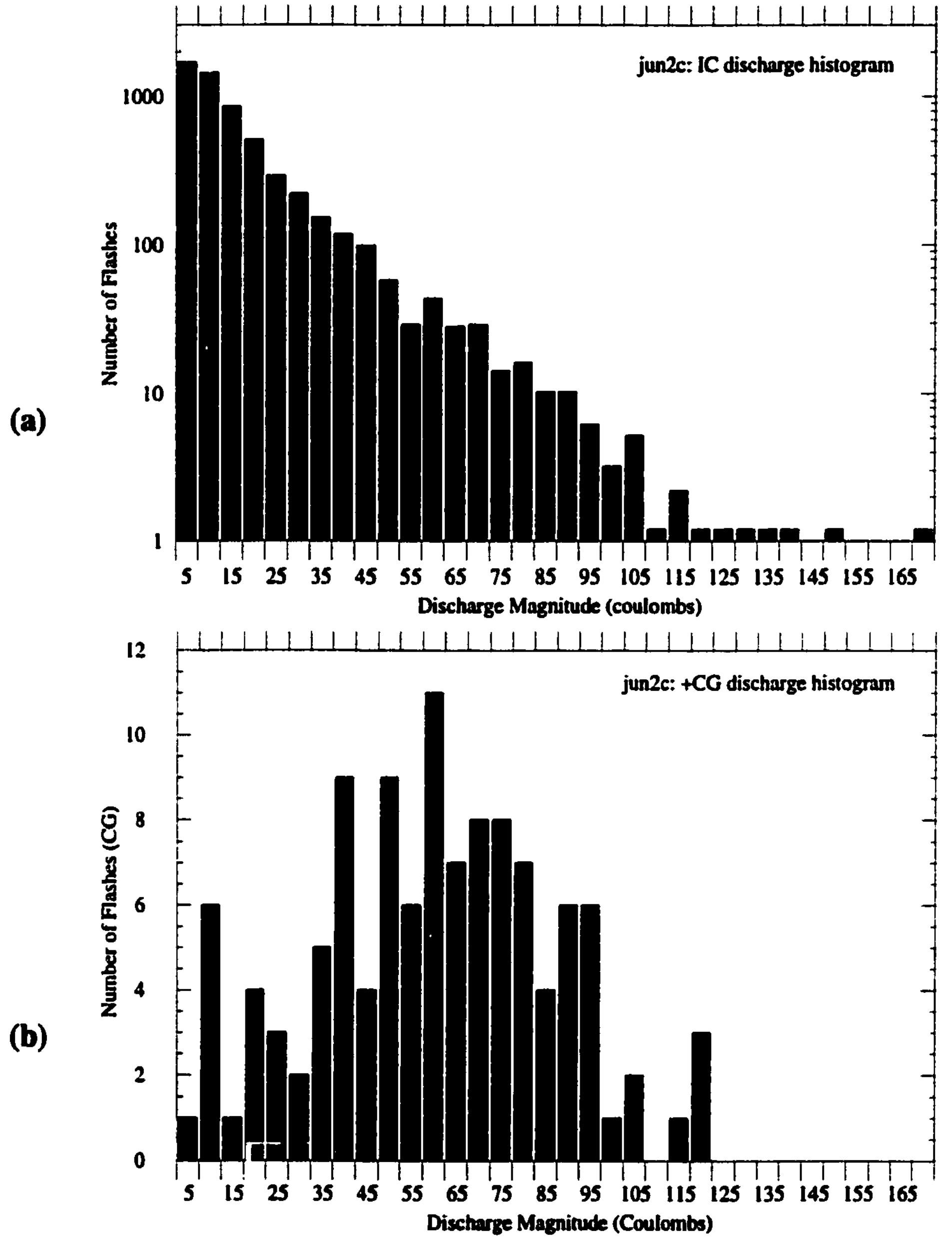

Figure B.17: Histograms of (a) IC and (b) CG discharge magnitudes: CL supercell, Gardiner, strong induction.

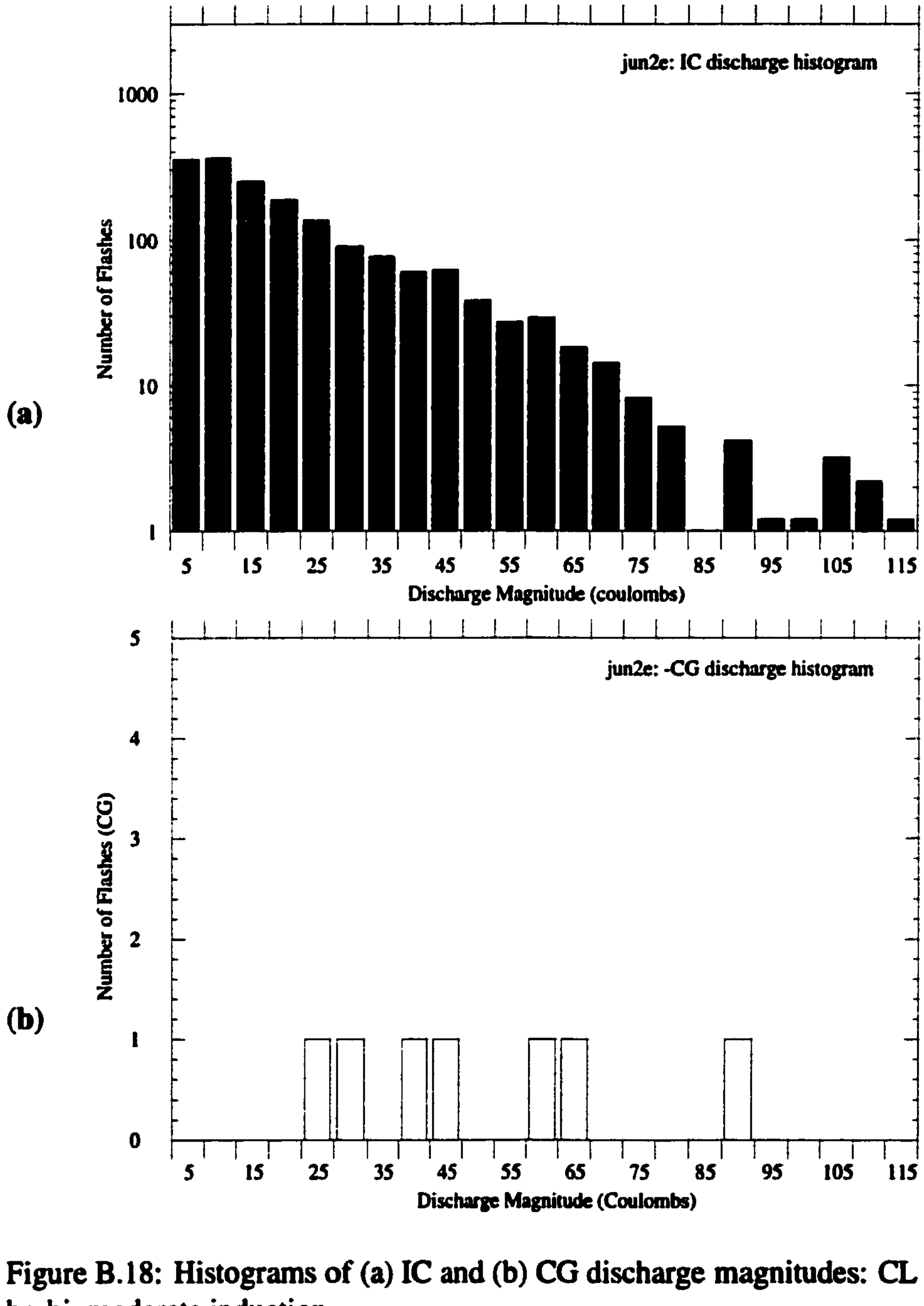

Figure B.18: Histograms of (a) IC and (b) CG discharge magnitudes: CL supercell, Takahashi, moderate induction.

Appendix C

Takahashi Lookup Table

Table C.1: Lookup table from Wojcik (1994) of Takahashi (1978) laboratory results for noninductive ice-ice charge transfer (units of fC).

Temperature (°C)

Liquid Water Content ($g\ m^{-3}$)	0.00	-1.00	-2.00	-3.00	-4.00	-5.00	-6.00	-7.00	-8.00	-9.00	-10.00	-11.00	-12.00	-13.00	-14.00	-15.00
30.00	31.35	31.02	30.69	30.36	30.03	29.70	29.37	29.04	28.71	28.38	28.05	27.72	27.39	27.06	26.73	26.73
20.00	31.35	31.35	31.02	30.69	30.03	29.70	29.04	28.71	28.38	28.05	27.72	27.39	27.06	26.73	26.40	26.40
10.00	31.35	31.35	30.36	30.03	30.03	29.04	28.71	28.05	27.39	27.06	26.73	26.40	25.41	24.75	24.42	24.09
9.00	31.35	31.35	31.02	31.02	30.36	30.03	29.37	29.04	28.38	27.39	26.73	25.74	25.41	24.42	23.76	23.43
8.00	31.68	31.35	31.02	30.36	30.03	29.04	28.71	28.38	27.39	27.06	26.73	25.41	24.42	23.76	23.10	22.44
7.00	32.01	32.01	31.68	30.69	30.36	29.37	28.71	28.05	27.39	27.06	26.07	25.08	23.76	23.10	21.78	20.79
6.00	32.01	32.01	31.68	31.35	30.69	29.37	28.71	27.72	27.06	26.40	25.08	24.09	23.10	21.45	19.80	19.47
5.00	32.34	32.34	32.01	31.68	30.36	29.37	28.38	27.39	26.73	25.41	23.76	22.77	20.13	19.14	18.48	17.49
4.00	36.30	33.00	32.01	31.35	30.69	29.70	29.71	27.39	25.74	23.43	21.45	19.80	18.15	16.83	14.85	4.95
3.00	39.60	36.30	33.00	31.35	30.69	30.03	28.05	26.40	23.10	20.46	18.15	16.50	3.30	0.00	-0.33	-1.32
2.00	49.50	49.50	42.90	42.90	33.00	31.35	28.05	24.75	16.50	0.99	-6.60	-16.50	-19.80	-26.40	-33.00	-33.00
1.00	52.80	52.80	56.10	59.40	52.80	49.50	42.90	33.00	19.80	9.90	0.00	-4.95	-11.55	-13.20	-14.85	-14.85
0.90	49.50	52.80	56.10	59.40	62.70	66.00	52.80	46.20	39.60	26.40	3.30	-0.99	-9.90	-9.90	-9.90	-9.99
0.80	46.20	52.80	56.10	59.40	62.70	56.10	42.90	39.60	33.00	19.80	9.90	0.99	-1.98	-4.29	-6.60	-8.25
0.70	42.90	49.50	52.80	56.10	59.40	56.10	46.20	42.90	36.30	23.10	16.50	3.30	0.00	-1.98	-3.30	-3.30
0.60	33.00	36.30	39.60	46.20	52.80	56.10	52.80	46.20	39.60	29.70	21.45	16.50	2.97	0.00	-1.32	-2.31
0.50	31.02	33.00	36.30	39.60	47.20	49.50	49.50	42.90	39.60	33.00	26.40	21.45	16.50	3.30	0.33	-0.33
0.40	26.40	29.70	32.34	36.30	39.60	39.60	42.90	42.90	39.60	36.30	33.00	28.71	26.40	22.44	19.47	9.90
0.30	19.80	23.10	26.40	28.71	31.35	33.00	36.30	36.30	33.00	31.02	28.71	27.39	26.40	23.43	20.79	17.82
0.20	13.20	15.18	17.16	19.80	22.44	24.09	25.08	26.40	27.39	27.39	27.06	26.73	25.74	24.42	23.10	21.45
0.10	4.95	6.93	9.24	10.56	11.88	13.20	14.85	16.50	16.50	18.15	19.14	18.81	18.81	18.48	17.82	16.83
0.09	3.30	6.60	7.59	9.90	11.22	12.21	13.20	14.85	15.84	16.50	16.50	16.83	16.83	16.83	16.50	16.50
0.08	1.65	4.95	6.60	8.25	9.90	11.55	13.20	14.85	15.18	15.51	15.84	15.84	16.17	15.84	15.84	15.51
0.07	0.00	2.64	4.95	7.26	9.24	10.23	11.22	11.22	11.88	12.54	13.20	13.86	14.85	15.18	14.85	14.85
0.06	0.00	0.33	3.30	5.61	7.59	8.91	9.90	10.23	12.21	12.87	13.53	13.53	13.53	13.86	13.86	13.53
0.05	0.00	0.00	0.33	2.97	5.61	7.26	8.91	9.90	10.56	11.22	11.88	11.88	12.21	12.54	12.54	12.54
0.04	0.00	0.00	0.00	0.33	2.64	4.29	6.60	7.59	9.24	9.57	10.23	10.89	11.22	11.22	11.22	11.22
0.03	0.00	0.00	0.00	0.00	0.33	0.33	2.31	4.29	6.27	6.93	7.59	8.25	8.91	9.24	9.57	9.57
0.02	0.00	0.00	0.00	0.00	0.00	0.00	0.00	0.00	0.00	0.66	2.64	3.30	4.62	5.28	5.94	5.94
0.01	0.00	0.00	0.00	0.00	0.00	0.00	0.00	0.00	0.00	0.00	0.00	0.00	0.00	0.00	0.00	0.00

Table C.1 (continued)

Liquid Water Content ($g\ m^{-3}$)	Temperature (°C)														
	-16.00	-17.00	-18.00	-19.00	-20.00	-21.00	-22.00	-23.00	-24.00	-25.00	-26.00	-27.00	-28.00	-29.00	-30.00
30.00	26.40	26.07	25.41	24.75	24.42	24.42	24.09	24.09	23.76	23.76	23.76	23.76	23.43	23.43	23.43
20.00	25.74	25.41	25.08	24.75	24.42	24.09	23.76	23.43	23.10	23.10	22.77	22.44	22.11	21.78	21.45
10.00	23.43	22.77	22.11	21.45	20.46	20.13	19.80	19.80	19.47	19.47	19.14	18.81	18.15	18.15	18.15
9.00	22.44	21.45	20.79	20.46	19.80	19.47	19.47	18.81	18.48	18.15	17.82	17.49	17.49	17.16	17.16
8.00	21.12	20.13	19.80	19.47	18.81	18.48	18.15	17.82	17.16	16.83	16.50	16.50	16.50	14.85	14.85
7.00	19.47	19.14	18.81	18.48	17.82	17.16	16.83	16.50	16.50	14.85	14.85	13.20	11.55	9.90	9.90
6.00	19.14	17.82	17.49	17.16	16.50	14.85	13.20	11.55	8.25	6.60	6.60	6.60	6.60	6.60	6.60
5.00	16.83	16.50	13.20	6.60	4.95	4.29	3.30	3.30	2.97	2.97	2.64	2.64	2.31	2.31	2.31
4.00	3.30	2.64	1.65	1.32	0.66	0.00	0.00	0.00	0.00	0.00	0.00	0.00	0.00	0.00	0.00
3.00	-2.97	-3.30	-3.30	-3.30	-3.30	-3.30	-6.60	-9.90	-6.60	-6.60	-6.60	-6.60	-4.95	-4.95	-3.30
2.00	-29.70	-28.10	-26.40	-24.80	-23.10	-21.50	-19.80	-18.20	-17.50	-16.50	-16.50	-16.50	-15.80	-9.99	-9.99
1.00	-14.85	-13.20	-13.20	-13.20	-13.20	-13.20	-13.20	-11.55	-11.55	-9.90	-9.90	-8.25	-4.95	-4.95	-3.30
0.90	-9.99	-9.99	-9.99	-9.99	-9.99	-9.99	-9.99	-9.99	-9.99	-9.90	-9.90	-8.25	-4.95	-3.63	-2.97
0.80	-9.99	-9.99	-9.99	-9.99	-9.90	-9.90	-9.90	-9.90	-9.90	-9.90	-8.25	-6.60	-3.30	-2.97	-2.97
0.70	-4.95	-6.60	-6.60	-6.60	-6.60	-6.60	-6.60	-6.60	-6.60	-4.95	-4.29	-3.30	-2.97	-2.64	-2.64
0.60	-2.97	-3.30	-3.30	-3.30	-3.30	-3.30	-3.30	-3.30	-3.30	-3.30	-3.30	-3.30	-2.97	-2.97	-2.64
0.50	-0.99	-1.65	-1.98	-2.31	-2.64	-2.64	-2.64	-2.64	-2.64	-2.64	-2.64	-2.64	-2.64	-2.31	-2.31
0.40	0.00	-0.33	-0.99	-1.32	-1.98	-2.31	-2.31	-2.31	-1.98	-1.98	-1.98	-1.98	-1.98	-1.98	-1.65
0.30	9.90	3.30	1.65	0.00	-0.66	-0.66	-0.66	-0.99	-0.99	-1.32	-1.32	-1.32	-1.32	-1.32	-1.32
0.20	19.47	17.16	9.90	6.60	3.30	2.64	0.99	0.00	0.00	-0.33	-0.66	-0.66	-0.66	-0.66	-0.66
0.10	16.17	15.51	14.85	13.86	13.20	11.88	10.56	9.57	8.58	7.59	6.60	3.63	2.97	2.31	1.65
0.09	15.84	15.18	14.85	14.19	13.20	12.21	10.89	9.90	8.91	7.92	6.93	4.95	3.30	2.31	1.98
0.08	15.18	14.85	14.52	13.86	12.87	11.88	10.89	10.23	9.24	7.59	7.26	6.60	4.62	2.31	1.65
0.07	14.52	14.19	13.86	13.20	12.54	11.88	10.89	10.23	9.24	8.25	7.59	6.60	4.29	2.64	0.99
0.06	13.53	13.20	13.20	12.54	11.88	11.55	10.89	9.90	9.24	8.25	7.26	6.60	4.29	3.30	0.66
0.05	12.21	12.21	11.88	11.55	11.22	10.56	9.90	9.24	8.91	7.59	6.93	5.61	3.30	0.99	0.00
0.04	10.89	10.89	10.89	10.56	9.90	9.57	8.91	8.25	7.59	6.60	5.28	3.63	0.99	0.00	0.00
0.03	9.57	9.57	8.91	8.58	8.25	7.59	6.93	6.27	5.61	4.29	2.64	0.33	0.00	0.00	0.00
0.02	6.27	5.94	5.61	5.28	4.95	4.29	3.96	2.97	0.66	0.00	0.00	0.00	0.00	0.00	0.00
0.01	0.00	0.00	0.00	0.00	0.00	0.00	0.00	0.00	0.00	0.00	0.00	0.00	0.00	0.00	0.00